FERROELECTRIC-PHOTOCATALYST NANOCOMPOSITE THIN FILMS FOR ENHANCED PHOTOCATALYTIC ACTIVITY

Adriana Augurio

Submitted in partial fulfilment of the requirements of the Degree of Doctor of Philosophy

School of Engineering and Material Science

Queen Mary University of London

DECLARATION

I, Adriana Augurio, confirm that the research included within this thesis is my own work or that where it has been carried out in the collaboration with or supported by others, that this is duly acknowledged below and my contribution indicated. Previously published material is also acknowledged below.

I attest that I have exercised reasonable care to ensure that the work is original, and does not to the best of my knowledge break any UK law, infringe any third party's copyright or other Intellectual Property Right, or contain any confidential material.

I accept that the College has the right to use plagiarism detection software to check the electronic version of the thesis.

I confirm that this thesis has not been previously submitted for the award of a degree by this or any other university.

The copyright of this thesis rests with the author and no quotation from it or information derived from it may be published without the prior written consent of the author.

Adriana Augurio

April 2022

ABSTRACT

Photoelectrochemical (PEC) water splitting has recently gained particular attention as promising method to produce hydrogen through the conversion of solar light into chemical energy. A key challenge for this application is to reduce the high level of electron-hole recombination, which can significantly affect the efficiency of a PEC system. Ferroelectric polarization has emerged as new strategy to facilitate the separation of electron-hole pairs, driving them towards the opposite direction and consequently enhancing the water splitting performance. In this thesis, the influence of ferroelectric polarization on the photoelectrochemical properties of bare nanostructured $BaTiO_3$ as well as nanostructured $BaTiO_3$ combined with Fe_2O_3 photocatalyst is explored.

Nanostructured $BaTiO_3$ thin films are synthesized and employed as photoanodes for photocatalytic studies. Porous barium titanate (pBTO) thin films show a controllable porosity by tuning organic/inorganic ratios. Importantly, the switching of ferroelectric domains in pBTO thin films is still observed in the porous structures. The presence of porosity in pBTO thin films leads to a clear improvement of the PEC response. By electrochemical (EC) poling, the tuning of PEC performance of pBTO thin films via ferroelectric polarization is also demonstrated. In addition, the influence of oxygen vacancies on EC poling of pBTO thin films, prepared in different annealing conditions (O_2, air, N_2) is investigated, revealing that higher concentrations of oxygen vacancies limit the ability of these films to be controlled *via* poling.

Lastly, Fe_2O_3/pBTO thin films are developed and studied. The composite film shows higher photocurrent density than pBTO and Fe_2O_3 and this is ascribed to the improved charge injection and separation in Fe_2O_3/pBTO. The possibility of achieving PEC

performance enhancements in Fe_2O_3/pBTO by controlling ferroelectric polarisation is also demonstrated.

This research reveals the role of ferroelectricity on the photocatalytic activity enhancements in nanostructured $BaTiO_3$ and Fe_2O_3-$BaTiO_3$ films, which could benefit future work on ferroelectric photocatalysts.

ACKNOWLEDGEMENTS

I would first like to thank my supervisor, Dr Joe Briscoe, for his continuous assistance and guidance throughout my PhD journey. His insightful feedback and brilliant suggestions have encouraged me at every stage of this research project, pushing me to sharpen my thinking. I will always be deeply grateful for the opportunity to have been part of his research group. Thank you for your valuable support and belief in me.

I would like also to express my gratitude to Maurizio Leo, Dr Russell Bailey and Dr Richard Whiteley for their technical support with material characterization and lab work. I would like also to thank all my collaborators, especially Qian Guo, Dr Vishal Panchal and Dr Alberto Alvarez Fernandez. My sincere thanks go to all my colleagues for their help and for all the laughs in the lab during the past four years. It was a great pleasure to work with you.

In addition, I would like to thank my family for their encouragement and sympathetic ear all through my studies. You always will be my anchor. I would like to thank also my cat Marie, who always cheered me up, especially during the pandemic. Finally, my special thanks go to Riccardo, who has always been there for me with a great deal of strength and patience. All the ups and downs, fun and adventures we shared together during the past four years have made my study and life in the UK a memorable time.

PUBLICATIONS AND PRESENTATIONS

Publications

- Du T., Sinclair R. R., Kosasih U. F., Macdonald J. T., Mohan L., **Augurio A.**, Ahli H., Lin C., Xu S., Xu W., Binions R., Ducati C., Durrant R. J., Briscoe J., and McLachlan A. M., "Aerosol Assisted Solvent Treatment: A Universal Method for Performance and Stability Enhancements in Perovskite Solar Cells, *Advanced Energy Materials*, 2021
- **Augurio A.**, Alvarez-Fernandez A., Panchal V., Pittenger B., De Wolf P., Guldin S., and Briscoe J., "Controlled porosity in ferroelectric $BaTiO_3$ photoanodes", *ACS Applied Materials & Interfaces*, 2022
- **Augurio A.**, Forrester C. and Briscoe J., "Role of oxygen vacancies in the poling of $BaTiO_3$ photoanode"- to be submitted
- **Augurio A.**, Guo Q., Forrester C., Sobrido Jorge A., Briscoe J., "Fe_2O_3-$BaTiO_3$ nanocomposite films for ferroelectric polarization-based enhancement of photocatalytic activity"- in preparation

Presentations

- 7^{th} Solar Fuels Network Symposium, School of Divinity, St. John's College, Cambridge, UK (28^{th}-29^{th} March 2019)-**Poster presentation**
- London Energy Materials & Devices Hub, University College London, London, UK (6^{th} June 2019)-**Oral presentation**
- MRS Fall Meeting & Exhibit, Boston, Massachusetts (1^{st}- 6^{th} December 2019)-**Poster presentation**

- UK Solar Fuels Network-SuperSolar Early Career Researcher Meeting, online event (28th April 2021)-**Oral presentation**
- International solar fuels conference 2021, online event (26th -29th July 2021)-**Poster presentation**
- Smart NanoMaterials 2021-Advances, Innovation and Applications, hybrid online (7th-10th December 2021)-**Oral presentation**

CONTENTS

LIST OF FIGURES

LIST OF TABLES

1 INTRODUCTION

1.1 The global energy transformation

"You are here today to write the script for a new future. A future of hope and promise – we need the world to know that we are headed to a low-emissions, climate-resilient future, and that there is no going back". With these words, Ban Ki-Moon, the United Nations Secretary-General, opened the 21st Conference of the Parties (COP21) of the United Nations Framework Convention on Climate Change (UNFCCC), which was held in Paris in December 2015[1]. The outcome of this event was the "Paris agreement", which establish the first-ever deal to legally bind governments for cooperation on climate change mitigation. The Paris Agreement does indeed highlight the urgency of a global energy transition to limit global temperature increase below 2 °C[2,3]. Above this target value, the consequence of climate change will be irreversible and catastrophic, as stated by climate scientists, social scientists and policymakers.

Therefore, in order to reach this future ambitious goal, the International Energy Agency (IEA) and the International Renewable Energy Agency (IRENA) clarified the essential requirements of an energy sector transition that would be in accordance with the target to keep the increase of global temperature to well below 2 °C [4].

The total greenhouse gas (GHG) emissions (expressed as gigatons of carbon dioxide, Gt CO_2, or " carbon emissions") which are attributed to the use and supply of fossil fuels, play an essential role in this global warming and in particular, two-thirds of all GHG are represented by energy-related carbon dioxide (CO_2) emissions[4].

The analysis, reported in the REmap case, shows that it is necessary to reduce CO_2 emissions by 85 % between 2015 and 2050 and drop CO_2 emissions by more than 70 % compared to the Reference Case in 2050. This future perspective produces an annual decline of CO_2 emissions by 0.6 Gt on absolute terms, leading to 9.7 Gt of energy CO_2 emissions per year in 2050 (Figure 1.1).

Moreover, the trend represented by the Reference Case, shows the future scenario of the energy use if the world continues to adopt policies that are currently in place. According to the Reference Case, energy CO_2 emissions rises by 6 % from 33 Gt in 2015 to 35 Gt in 2050[4](Figure 1.1).

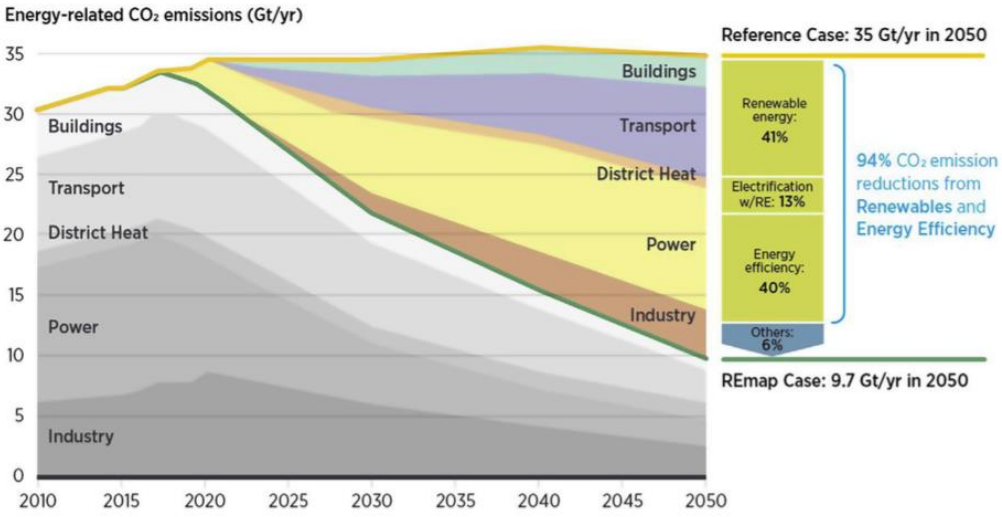

Figure 1.1 Study developed by IEA and IRENA on the potential CO_2 emissions reduction in the Reference Case and Remap between 2010-2050[4].

Therefore, a transition away from fossil fuels to low-carbon solutions is an essential requirement to meet the agreed Paris Climate target of well below 2 °C. A promising strategy to potentially achieve 94 % of CO_2 emission reductions by 2050, is the development of higher energy efficiency and higher share of renewable energy[4].

1.2 Renewable energy

Energy resources can be divided into three categories: fossil fuels, renewable resources and nuclear resources. Renewable energy resources, known often as "alternative sources of energy", can be used to produce clean energy: solar energy, wind energy, biomass energy, geothermal energy. The share of renewable energy resources is expected to increase very significantly in the coming years. In particular, Table 1.1 reports the global renewable energy scenario by 2040. Approximately half of the global energy supply will come from renewables in 2040, according to the European Renewable Energy Council[5].

Table 1.1 Scenario of global renewable energy by 2040[5].

Global renewable energy scenario by 2040					
	2001	2010	2020	2030	2040
Total consumption (million ton oil equivalent)	10,038	10,549	11,425	12,352	13,310
Biomass	1,080	1,313	1,791	2,483	3,271
Large hydro	22.7	266	309	341	358
Geothermal	43.2	86	186	333	493
Small hydro	9.5	19	49	106	189
Wind	4.7	44	266	542	688
Solar thermal	4.1	15	66	244	480
Photovoltaic	0.2	2	24	221	784
Solar thermal electricity	0.1	0.4	3	16	68
Marine (tidal/ wave/ocean)	0.05	0.1	0.4	3	20
Total RES	1,365.5	1,745.5	2,694.4	4,289	6,351
Renewable energy source contribution (%)	13.6	16.6	23.6	34.7	47.7

1.2.1 Solar energy

Renewable resources are not all equal. As shown in Figure 1.2, the annual flow of energy from the sun overcomes all the other resources combined by orders of magnitude. Wind energy and Biomass could probably be secondary alternative resources to meet the planet's energy requirements, but none of them could alone satisfy the world demand[6]. Therefore, the low-carbon energy transition for the well-being of the planet should be essentially solar-based.

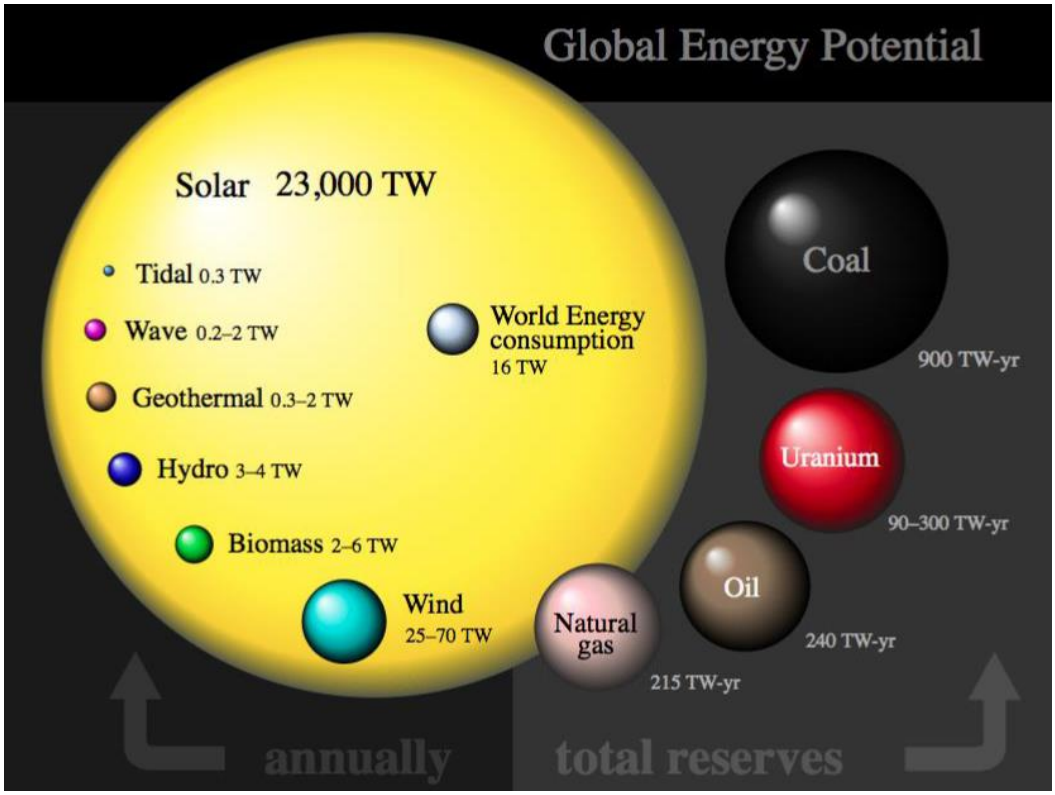

Figure 1.2 Comparison between finite and renewable planetary energy resources measured in TW/years[6].

However, even if solar energy seems a promising solution toward sustainable energy consumption, the fluctuation of sunlight intensity at the earth's surface related to the season and weather conditions and the diffuse nature of solar energy is a serious challenge for the inclusion of the photovoltaic technology in the electricity network. This imposes great advances for the development of a viable solar energy storage solution. For these reasons, the investigation of new methods for solar fuel generation that can significantly compete with fossil fuels has great importance[6].

1.3 Hydrogen fuel

Hydrogen presents great potential as energy vector candidate for solar energy storage, considering that it is sustainable, non-toxic and the most abundant element in the universe. H_2 can be produced from both renewable resources (*e.g.* hydro, wind, wave, solar biomass and geothermal energy) and non-renewable ones (*e.g.* coal, natural gas and nuclear energy sources), ensuring an adaptive production that relies on the resources available in a given country[7]. However, more than 95 % of H_2 production is currently based on the fossil fuels industry (*e.g.* steam methane reforming), which has a significant carbon impact. Hydrogen can also be generated by water electrolysis, where electricity is used in electrolysers for the splitting of water in hydrogen and oxygen, known as water splitting. However, water electrolysis requires 5 times more energy input than steam reforming and this energy may be generated from fossil fuels[8]. Thus, it is expected that only 4 % will be produced via water electrolysis in 2050[9] (Figure 1.3).

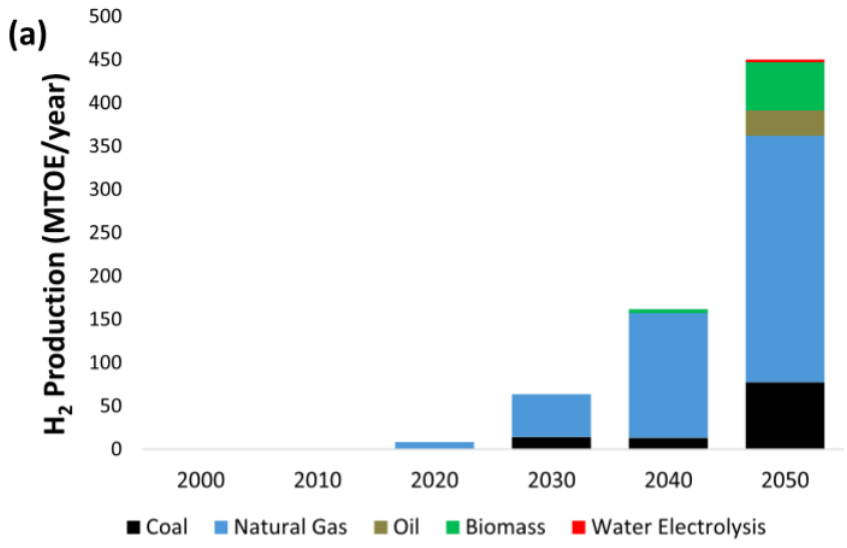

Figure 1.3 Energy model for the global H_2 production between 2000 and 2050[9].

Therefore, methods for the production of clean hydrogen from natural resources such as water and sunlight are necessary to develop a sustainable economy in the long term. Figure 1.4 shows an example of a sustainable energy path for hydrogen generation based on the combination of solar energy with water using solar water splitting. According to the system reported in Figure 1.4, after introducing water in a solar water splitting module, it is converted into hydrogen, which can be used in high-efficiency power production systems (e.g. fuel cells) to produce electricity. Moreover, when hydrogen is combined with carbon dioxide, obtained from the atmosphere or natural gas burning plants, methanol and synthetic natural gas can be produced. The development of those processes would offer numerous advantages in terms of a sustainable energy revolution. A route to realising solar water splitting is water photoelectrolysis where hydrogen and oxygen are generated at the semiconductor/water interface in a system named photoelectrochemical cell[10]. This technology is the focus of this PhD thesis and will be explained in more detail in Chapter 2.

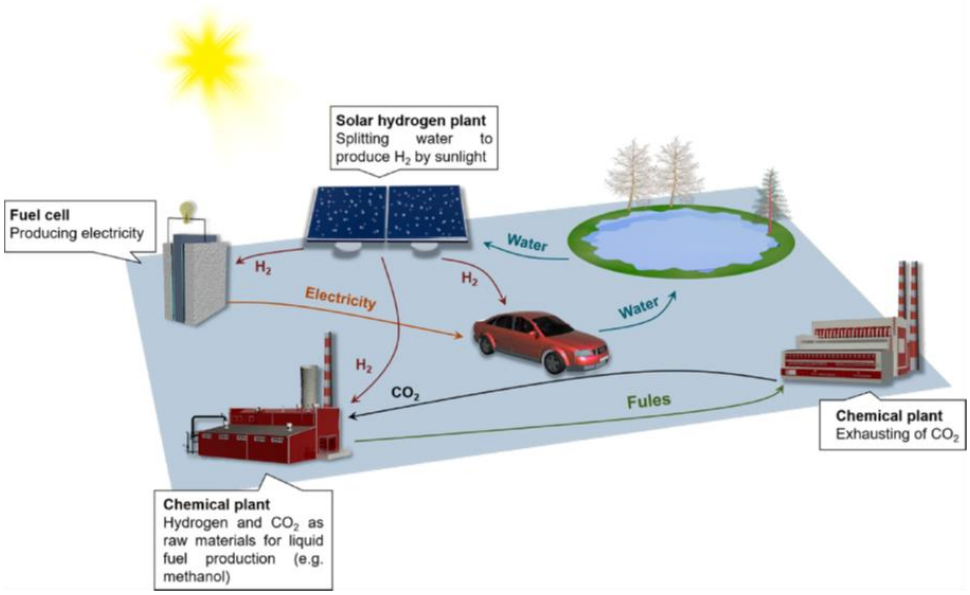

Figure 1.4 Sustainable hydrogen fuel cycle based on photocatalytic water splitting[11].

1.4 Thesis structure

This thesis is organized into seven chapters and they are summarised below:

1. **Chapter 1:** This chapter offers an overview of the research background and a summary of the thesis structure.
2. **Chapter 2:** Literature review. An overview of semiconductor photocatalysis and ferroelectric materials as semiconductors is reported. The basic mechanism and the devices based on semiconductor photocatalysts have been reviewed, focusing also on the factors influencing photocatalytic efficiency and the strategies adopted for its improvement. The definition, basic principle and beneficial properties of ferroelectric materials in photocatalysis have been reviewed. Moreover, the semiconductor materials used in this work have been introduced.
3. **Chapter 3:** This chapter reports the experimental details of material synthesis and characterisation methods used in this project.
4. **Chapter 4:** This chapter is focused on the development of nanostructured ferroelectric $BaTiO_3$ thin films and the study of their PEC performance enhancement due to ferroelectric polarisation. Two different synthesis methods for the preparation of nanostructured and porous $BaTiO_3$ ferroelectric thin films have been explored – hydrothermal synthesis and sol-gel synthesis of porous $BaTiO_3$ – with only porous $BaTiO_3$ films considered for the rest of this research project. The ferroelectric behaviour of porous $BaTiO_3$ (pBTO) thin films is verified. The relationship between porosity and PEC performance in pBTO thin films is studied. The influence of ferroelectric polarisation on the PEC response of pBTO films *via* electrochemical (EC) poling is investigated and explained.

5. **Chapter 5:** This chapter investigates the effect of EC poling pre-treatment on pBTO thin films with different content of oxygen vacancies induced by the annealing atmospheres (O_2, air, N_2). The correlation between annealing condition and oxygen vacancies is verified. The structure, composition and optical properties of the pBTO films, annealed in O_2, air and N_2 atmospheres (pBTO-O_2, pBTO-air and pBTO-N_2) are studied. The effect of EC poling on the composition and PEC performance of pBTO-O_2, pBTO-air and pBTO-N_2 is investigated, demonstrating that the high migration of oxygen vacancies in pBTO films can significantly affect the control of their PEC performance *via* ferroelectric polarisation.
6. **Chapter 6:** This chapter outlines the development of Fe_2O_3/pBTO as a ferroelectric/photocatalyst composite system, investigating the enhancement of PEC response in the composite film *via* ferroelectric polarisation of $BaTiO_3$. The successful preparation of Fe_2O_3/pBTO film is demonstrated. The advantage of combining ferroelectric pBTO with Fe_2O_3 as photocatalyst on the PEC performance is discussed. The possibility of controlling the PEC response in Fe_2O_3/pBTO *via* ferroelectric polarisation, without affecting the film composition, is demonstrated
7. **Chapter 7:** This chapter offers a summary of conclusions and suggests future work to pursue to follow on from the current project.

REFERENCES

1. Falkner, R. The Paris agreement and the new logic of international climate politics. *Int. Aff.* **92**, 1107–1125 (2016).

2. Jackson, R. B., Friedlingstein, P., Canadell, J. G. & Andrew, R. M. Two or Three Degrees: CO_2 emissions and Global Temperature Impacts. *Summer Issue Bridg. Energy, Environ. Clim. Chang.* **45**, 16–21 (2015).

3. Jackson, R. B., Friedlingstein, P., Canadell, J. G. & Andrew, R. M. Two or Three Degrees CO_2 Emissions and Global Temperature Impacts. *Natl. Acad. Eng.* **2**, 43–47 (2015).

4. Gielen, D. *et al.* The role of renewable energy in the global energy transformation. *Energy Strateg. Rev.* **24**, 38–50 (2019).

5. Panwar, N. L., Kaushik, S. C. & Kothari, S. Role of renewable energy sources in environmental protection: A review. *Renew. Sustain. Energy Rev.* **15**, 1513–1524 (2011).

6. Perez, R. & Perez, M. A Fundamental Look At Energy Reserves For The Planet. *Int. Energy Agency SHC Program. Sol. Updat.* **50**, 4–6 (2009).

7. Abe, J. O., Popoola, A. P. I., Ajenifuja, E. & Popoola, O. M. Hydrogen energy, economy and storage: Review and recommendation. *Int. J. Hydrogen Energy* **44**, 15072–15086 (2019).

8. Abbasi, T. & Abbasi, S. A. ‘Renewable’ hydrogen: Prospects and challenges. *Renew. Sustain. Energy Rev.* **15**, 3034–3040 (2011).

9. Chapman, A. *et al.* A review of four case studies assessing the potential for hydrogen penetration of the future energy system. *Int. J. Hydrogen Energy* **44**, 6371–6382 (2019).

10. Grätzel, M. Photoelectrochemical cells. *Nature* **414**, 338–344 (2001).

11. Wang, Q. & Domen, K. Particulate Photocatalysts for Light-Driven Water Splitting: Mechanisms, Challenges, and Design Strategies. *Chem. Rev.* **120**, 919–985 (2020).

2 LITERATURE REVIEW

2.1 Semiconductor photocatalysis

Since the pioneering work of Fujishima and Honda in 1972[1], photocatalytic technologies based on semiconductors, including photo-generation of electricity and photoelectrochemical production of renewable hydrogen from water[2,3], have been largely explored, aiming to overcome the environmental issues correlated to the remediation of hazardous waste and the control of toxic air contaminants[4]. In this context, the role of photocatalysis is to initiate or accelerate specific redox reactions by means of semiconductor materials as catalysts. Various semiconducting oxide materials (TiO_2, $BiVO_4$, WO_3 and Fe_2O_3) have been used for many photocatalytic applications[5–7] but significant challenges still persist for realistic commercialisation. Extremely important is the improvement of degradation or energy conversion efficiency, which is significantly influenced for example by the energy band mismatch of the semiconductor materials and the effective charge separation and transfer. The latter lie at the core of the entire photocatalysis process[8]. The main applications of photocatalysis are photocatalytic degradation of organic pollutants and solar water splitting. In the following sections, the

basic mechanism of solar water splitting will be described in more detail, as it is the application chosen in this thesis.

2.1.1 Electronic band structure of semiconductors

In solid-state physics, the electrical conductivity is described in terms of energy band structures. Molecular orbitals occupied by electrons are condensed at given energy levels, rather than forming discrete energy states. These continuum energy levels create broad bands of allowed energy separated by gaps of forbidden energies, known as bandgaps (E_g)[9]. The highest occupied energy band is defined as the valence band (VB) while the lowest unoccupied energy band is termed as conduction band (CB). Thus, the bandgap can be also defined as the energy difference between the CB and the VB[10] and it regulates the electrical properties of the materials. To determine the conductivity of a solid, partial occupancy of the conduction band is required. This can be obtained by promoting an electron from the valence band to the conduction band, which consequently leaves a positively charged hole in the valence band[11]. When the bandgap is too large ($E_g > 4$ eV), the electrons cannot reach the CB, thus the material is defined as an insulator. If the bandgap is sufficiently small ($E_g < 4$ eV) to allow the excitation of an electron in the CB upon absorption of heat or photons, the material is known as a semiconductor[12]. In the case of conductive materials (metals), the conduction and valence bands are instead already overlapping or partially filled. The band structure of metals, semiconductors and insulators is illustrated in Figure 2.1.

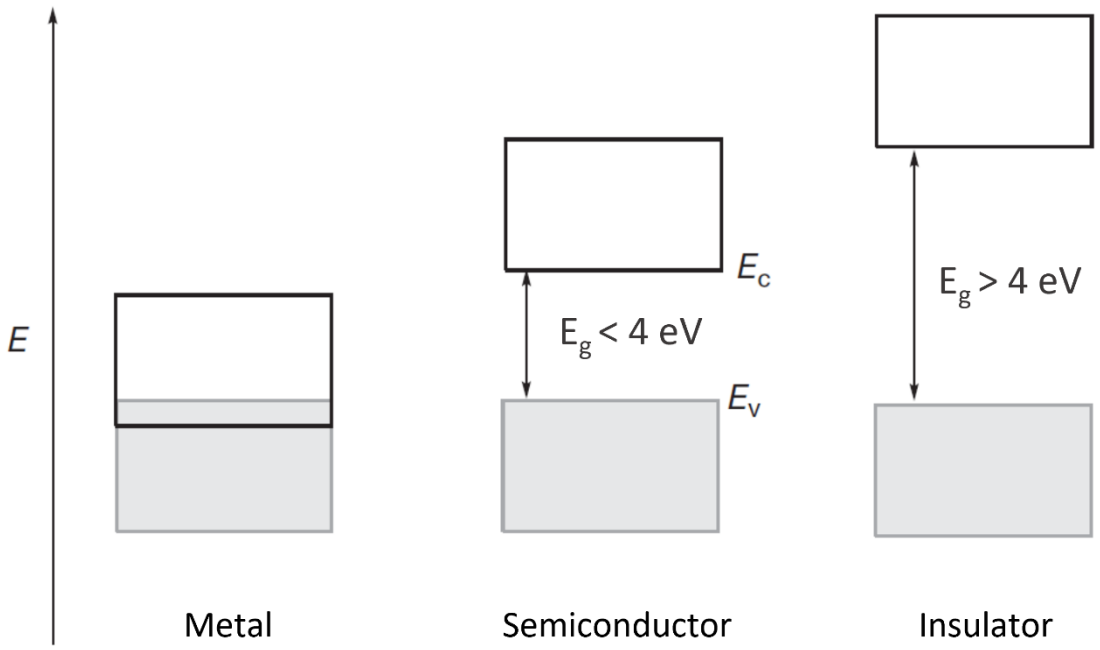

Figure 2.1 Band configuration in metal, semiconductor and insulator: in metals, an occupied band overlaps with an unoccupied one. A material is defined as a semiconductor and an insulator, if the bandgap is less or more than 4 eV, respectively[9].

Related to the electronic properties of semiconductors is the definition of the Fermi Level (E_F), which is based on the Fermi-Dirac distribution, describing the probability of occupying an electronic state. The Fermi Level is the energy level at which the probability of electron occupation is 50 %[9]. This energy also relates to the electrochemical potential (μ) of the semiconductor[13]. Generally, an intrinsic semiconductor has E_F in the middle of the bandgap, where the density of electrons (n_i) is equal to the density of holes (p_i), which can be expressed by the following equations[14]:

$$\boldsymbol{n_i = N_c \exp(-\frac{E_c - E_{f,n}}{kT})} \qquad 2.1$$

$$\boldsymbol{p_i = N_V \exp(-\frac{E_V - E_{f,p}}{kT})} \quad 2.2$$

where k is the Boltzmann constant, T is absolute temperature, N_c and N_v correspond to the density of energy states at conduction and valence band, E_c and E_v are the energy conduction and valence band, $E_{f,n}$ and $E_{f,p}$ are the Fermi levels of electrons and holes, respectively.

Considering that $n_i = n_p$ in an intrinsic semiconductor, equations 2.1 and 2.2 can be rearranged as follow:

$$\boldsymbol{n_i p_i = n_i^2 = N_c N_V \exp(-\frac{E_c - E_V}{kT}) = N_c N_V \exp(-\frac{E_g}{kT})} \quad 2.3$$

However, in the case of extrinsic semiconductors when impurities are present or introduced via doping, the Fermi level can be shifted by altering the density of electrons or holes. Thus, in an n-type material where electrons are the majority carriers, E_F is located near the conduction band (CB) while E_F lies just above the valence band (VB) in p-type materials where holes are the majority carriers[15] (Figure 2.2).

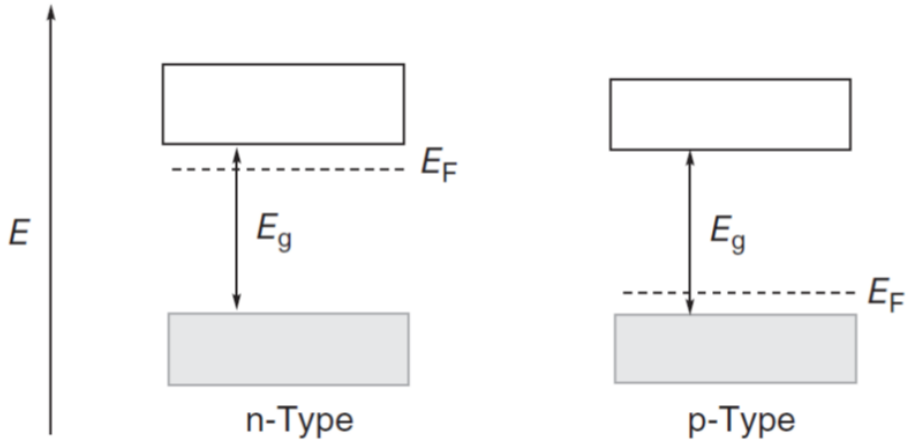

Figure 2.2 Band configuration in n-type and p-type semiconductors, where the Fermi level E_F is located close to the valence (p-type) and conduction (n-type) band[9].

2.1.2 Solar water splitting

The process that involves semiconductor materials for solar water splitting is based on the absorption of light by a semiconductor photocatalyst, inducing the generation of an electron-hole pair, which can be transferred to the catalytically active sites at the semiconductor surface where chemical transformations are driven[16] (Figure 2.3a). The main reactions that describe solar water splitting in basic conditions are summarized below[17]:

$$\boldsymbol{Photocatalyst} \xrightarrow{hv} \boldsymbol{e_{cb}^{-} + h_{vb}^{+}} \qquad 2.4$$

$$\boldsymbol{2OH^{-} \rightarrow H_2O + \frac{1}{2}O_2 + 2e^{-}} \text{ (Anode)} \qquad 2.5$$

$$2H_2O + 2e^- \rightarrow H_2 + 2OH^-$$ (Cathode) 2.6

$$H_2O \rightarrow H_2 + \frac{1}{2} O_2$$ (Overall reaction) 2.7

A fundamental requirement for e^- - h^+ pair formation and consequently to generate solar water splitting in a semiconductor is that the energy of the incident light must be equal to or larger than the bandgap (E_g) of the semiconductor[18]. The bandgap energies of typical semiconductors applied for photoelectrochemical H_2O splitting are illustrated in Figure 2.3b, where the wide and narrow bandgap materials can be used as top and bottom absorbers, respectively. This refers to a tandem PEC cell, where sunlight passes first through the wide bandgap 'top' photoelectrode, and then into the narrower bandgap 'bottom' photoelectrode[19].

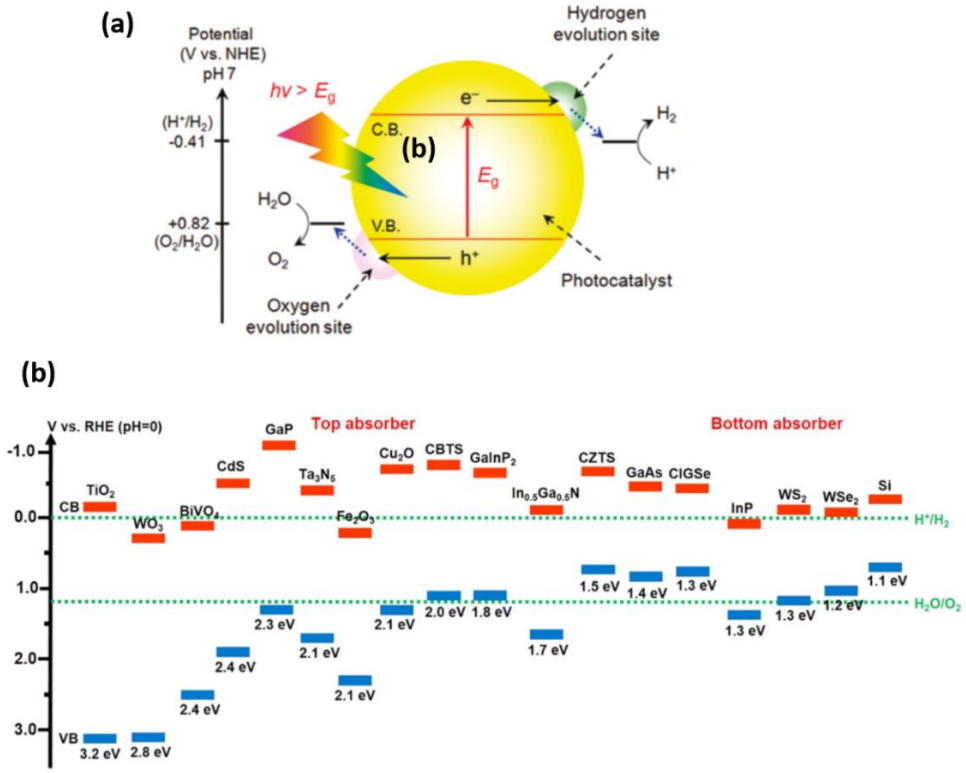

Figure 2.3 (a) Schematic mechanism of the principle of photocatalytic water splitting in a semiconductor, referred to the normal hydrogen electrode (NHE): (1) photo-generation of electron and hole pairs, under sunlight irradiation; (2) spatial separation of electron-hole pair and their distribution to the surface of semiconductor; (3) reactions of photo-reduction and photo-oxidation on the semiconductor's surface active sites[20]; (b) Band edge positions and energy bandgap of semiconductors in the aqueous electrolyte at pH=0, referred to the reversible hydrogen electrode (RHE)[17].

2.1.2.1 Device designs for solar water splitting

The relevant systems adopted for solar water splitting can be divided into three major categories: photocatalytic (PC) system, photoelectrochemical (PEC) cell, and photovoltaic-electrolysis (PV+E), as shown in Figure 2.4.

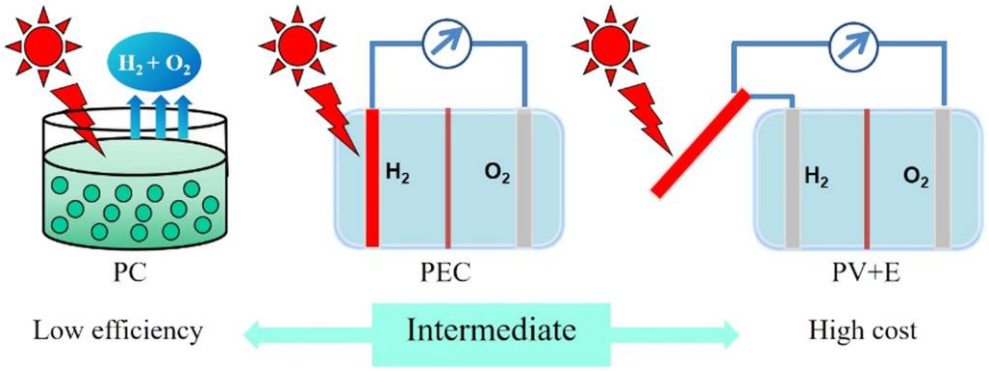

Figure 2.4 Schematic of the three types of solar water splitting system: PC system, PEC cell and PV+E approach[21].

PV+E is a straightforward strategy that involves two existing developed technologies: a photovoltaic (PV) cell and a water electrolyzer. Even if high solar-to-hydrogen (STH) conversion efficiencies over 10 %[22-29] have been reported for PV+E, this route is still too expensive compared to the traditional methods that adopt fossil fuels[28] and further enhancement in the efficiency is also more limited. Thus, alternative and low-cost routes for the generation of solar hydrogen must be considered. PC approach is a simple and low-cost process for potential solar hydrogen production. However, this route leads to an STH efficiency typically at least one order of magnitude lower (< 1 %), and can potentially generate an explosive mixture of H_2 and O_2, requiring an external high cost for the separation of the products to avoid back reactions[30]. Therefore, the PEC system, which lies intermediate between PV+E and PC, is a more valid alternative, offering a high STH efficiency at an affordable cost[31-33]. The PEC system includes the light absorption and electrochemical process of a PV+E system via a direct semiconductor/electrolyte interface to limit the cost, showing also a distinct advantage over PC system because the H_2 and O_2 evolution half-reactions occur on two different electrodes and are separated physically. Recently, it has been demonstrated that the PEC system possesses

substantially lower overall system cost with respect to the PV+E approach, and can become economically competitive with existing fossil-fuel derived hydrogen upon improvement in the efficiency and lifetime to > 10 % and > 5 years, respectively[33-35].

A simple PEC configuration for water splitting using a two-electrode system includes the following components: the photoelectrode based on a semiconductor photocatalyst, the counter electrode, which is generally Pt or graphite and the electrolyte, which lies in between the two electrodes to improve the electrical conductivity, keeping the required pH value, as shown in Figure 2.5. A typical PEC water splitting system based on n-type and p-type semiconductor photoelectrodes is shown in Figure 2.5. The fundamental process which occurs in those PEC water splitting systems can be described by two separate half-reactions: oxidation of water to O_2 at the photoanode and the reduction of water to H_2 at the photocathode.

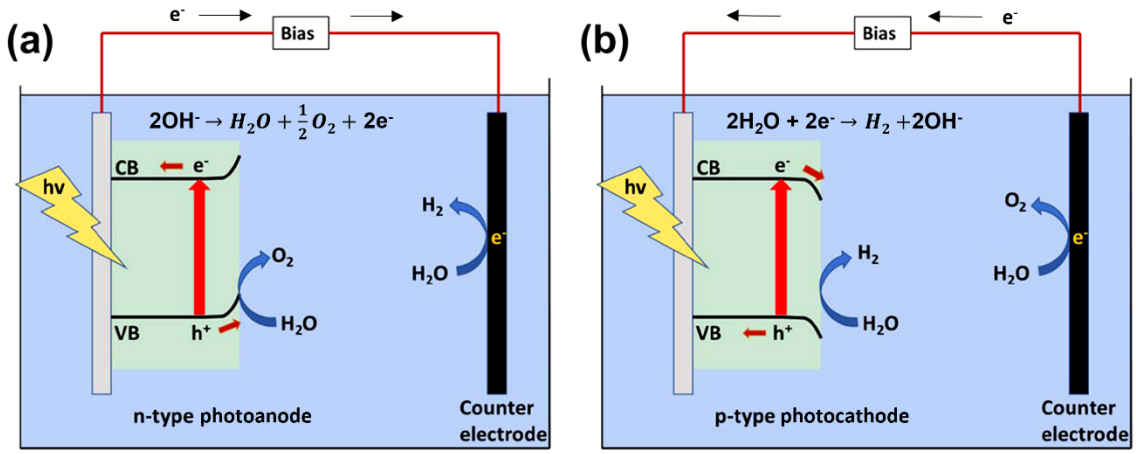

Figure 2.5 Schematic of PEC water splitting systems using n-type semiconductor photoanode (a) and p-type semiconductor photocathode (b)[36].

In the n-type semiconductor photoanode under illumination, photo-excited electrons and holes are generated in the conduction band and valence band, respectively. By applying an anodic potential through an external circuit, these electrons are driven via the real Ohmic contact toward an electrical connection on the surface of the counter electrode to reduce water to H_2. In the meantime, the holes are transferred to the semiconductor surface, promoting the oxidation of water to O_2. On the other hand, in the case a of p-type semiconductor photocathode, the electrons move to the semiconductor surface, where they reduce water to H_2 while the holes are transferred to the counter electrode via an external circuit to oxidize water to O_2[36].

Since overall water splitting consists of two half-reactions (oxidation and reduction reactions), it is necessary to use a dual-electrode system for this application. Tandem PEC water splitting system, consisting of the spatially separated p-type photocathode and n-type photoanode, is commonly used to achieve unassisted overall water splitting. Moreover, considering that the oxidation and reduction reaction sites are spatially separated in a tandem system, O_2 and H_2 products can be easily collected[21].

2.1.3 Semiconductor/electrolyte interface

The study of the semiconductor/liquid junction (SCLJ) is a unique feature of semiconductors which makes their photoelectrochemistry particularly interesting. Prior to contact with the electrolyte (*i.e.* before the equilibration process), the Fermi level of the semiconductor is not located at the same level as the electrochemical potential of the electrolyte[37], as shown in Figure 2.6.

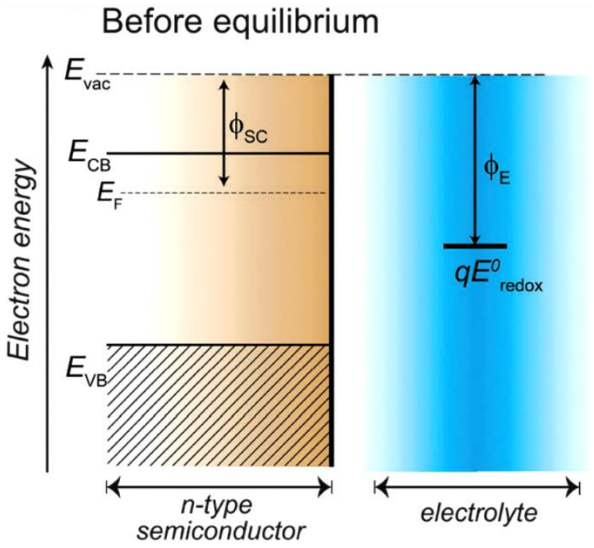

Figure 2.6 Schematic of band structure at semiconductor/liquid junction (SCLJ) of n-type semiconductors before equilibrium (adapted from[37]). The parameters included in the figure are specified as follows: Fermi level (E_F), the bottom of the conduction band (E_{CB}) and top of the valence band (E_{VB}), redox potential of the electrolyte (E^0_{redox}), local vacuum level (E_{vac}), work function of the semiconductor (Φ_{SC}) and the redox electrolyte (Φ_E).

When a semiconductor material comes in contact with an electrolyte in the dark, the formation of the junction requires that one or both energy levels should move in order to reach equilibrium (Figure 2.7).

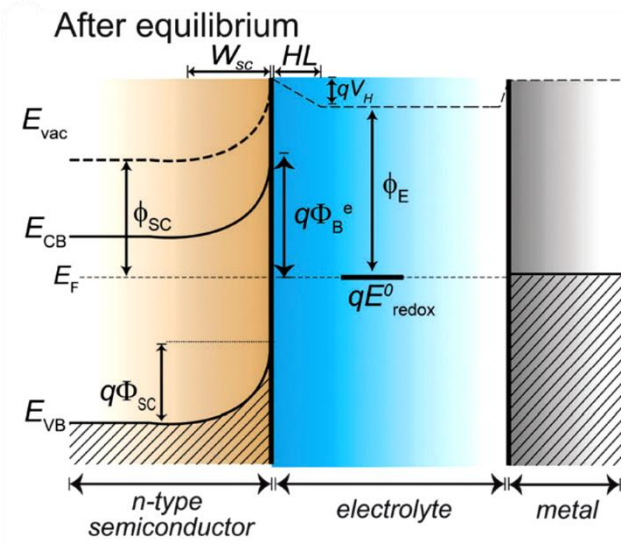

Figure 2.7 Schematic of band structure at semiconductor/liquid junction (SCLJ) of n-type semiconductors after equilibrium (Adapted from[37]). The additional parameters included in the figure are defined as follows: barrier height ($q\Phi^e_B$), depletion layer (W_{SC}), Helmholtz layer (HL), the potential drop through the Helmholtz layer (V_H).

Considering that the charge density of the electrolyte is usually several orders of magnitude higher than that of the semiconductor, electrons will move in or out the semiconductor, aligning the chemical potential of the electrons with the electrochemical potential of the electrolyte, until an equilibrium is reached. For semiconductors, the chemical potential of electrons is determined at the Fermi level (E_F), whereas for liquid electrolytes it is given by the redox couples present in the solution (E^0_{redox}). In the case of an n-type semiconductor which has a Fermi level higher than the electrolyte redox potential, upon contact electron transfer from the semiconductor to the electrolyte occurs. The remaining positive ions in the n-type semiconductor induce the formation of a positive space charge region (SCR), which bends the conduction band (CB) and valence

band (VB) edges of the semiconductor upwards[37]. Conversely, in a p-type semiconductor where the Fermi level is lower than the redox potential of the electrolyte, the charge equilibration induces the generation of a negative SCR in the semiconductor that bends the bands downward. In this section, only the case of an n-type semiconductor will be shown as only photoanodes will be considered in the rest of this PhD thesis. The band bending at the semiconductor/electrolyte interface is described by $q\Phi_{SC}$, resulting in a potential barrier against electron (n-type) or hole (p-type) flux into the electrolyte. The SCR, the width of which can be from a few tens of angstroms to several microns, is also known as the depletion layer (W_{SC}) since it is depleted of the majority of carriers. As shown in Figure 2.6, this band bending can be controlled upon application of an electrical bias to the semiconductor, and thus a bias that flattens the band edges is applied. Because the band edges are flat after the application of this potential, it is defined as the flat band potential E_{fb}. E_{fb} indicates the actual position of the Fermi level of the semiconductor with respect to the reference electrode before equilibrium. Thus, E_{fb} can be determined using Mott-Schottky analysis, giving a reliable estimation of the CB or VB edge positions and thus providing insight into the thermodynamic capability of the semiconductor to reduce/oxidize a given species upon illumination. In response to the charge transfer between semiconductor and electrolyte, a charge layer in the electrolyte adjacent to the semiconductor surface is formed, known as Helmoholtz layer (HL). This layer possesses opposite sign to the charge induced in the semiconductor, and it is made by ions from the electrolyte, adsorbed on the semiconductor surface with a width of few angstroms[37].

Under illumination, photons with energy greater than the semiconductor bandgap can be absorbed inducing the formation of electron–hole pairs, separated by the electric field in

the depletion layer, which can be selectively moved to the SCLJ or the Ohmic rear contact using the external circuit to the counter electrode (Figure 2.8).

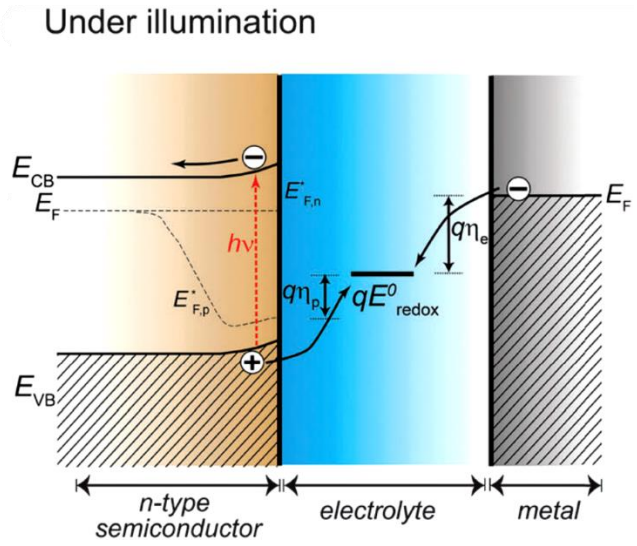

Figure 2.8 Schematic of band structure at semiconductor/liquid junction (SCLJ) of n-type semiconductors after illumination (Adapted from[37]). The additional parameters reported in the figure are defined as follows: the quasi-Fermi level for electrons ($E_{F,n}^*$) and holes ($E_{F,p}^*$), the photopotential (E_{ph}), and the overpotentials for the reduction (η_e) and oxidation (η_p) reactions.

The Fermi level rises under illumination with the photopotential E_{ph}. Under illumination, the native Fermi level splits into two quasi-Fermi levels, of which one is associated with the concentration of electrons ($E_{F,n}^*$) and the other to the holes ($E_{F,p}^*$). If the free energy of the photogenerated carriers is appropriate, reduction (electrons) and oxidation (holes) of the redox species in solution will be moved at the different (opposite) electrode/electrolyte interfaces. As shown in Figure 2.8, these oxidation and reduction reactions commonly need overpotential (η_p,η_e) to effectively drive the processes, as despite being thermodynamically favoured, they are kinetically slow[37]. If only one redox

couple exists, the oxidation and reduction on the photoelectrodes can constantly regenerate the redox couple through the conversion of solar energy into electric power, considering the constant flow of carriers via the external circuit. On the other hand, when two redox couples are present, two different reactions can take place on the photoelectrodes, generating an evident change in the electrolyte composition. Thus, solar energy can be stored directly in the chemical bonds of the new compounds. This PEC cell is known as photosynthetic cell, which can be adopted for solar fuel production[37].

2.1.4 Definition of efficiencies in solar water splitting

Generally, to investigate the PEC performance of a semiconductor photocatalyst, the onset potentials and the photocurrent densities at the redox potential of O_2/H_2O (1.23 vs RHE) for photoanodes and at the redox potential of H^+/H_2 (0 vs RHE) for photocathode are compared. However, considering that the product of solar water splitting is hydrogen, solar-to-hydrogen conversion efficiency (STH) is the most important parameter to consider for the calculation of the solar water splitting efficiency in devices. It can be expressed by the following equation:

$$\eta_{STH} = \left[\frac{\Phi_{H_2}(mol\ s^{-1}\ m^{-2})\ x\ G^0_{f,H_2}(kJ\ mol^{-1})}{P_{light}(W\ m^{-2})}\right]_{AM\ 1.5G} \quad 2.8$$

where Φ_{H2} is the hydrogen gas production rate, $G^0_{f,H2}$ is the Gibbs free energy of hydrogen gas (237 kJ mol−1 at 25 °C) and P_{light} is the total solar irradiation input. The light source should match the solar spectrum of air mass 1.5 global (AM 1.5 G)[38].

Considering that 100% of the current may not contribute to the redox reaction, Faradaic efficiency must be included in the equation. Faradaic efficiency (η_F) is defined as the

efficiency of passing charges contributing to the desired electrochemical reaction, expressed as the ratio of the measured product quantity and the theoretical value derived by passing charges. Thus, STH can also be calculated by the following equation:

$$\eta_{STH} = \left[\frac{j_{SC}(mA\ cm^{-2})\ x\ 1.23\ V\ x\ \eta_F}{P_{light}(mW\ m^{-2})}\right]_{AM\ 1.5G} \quad 2.9$$

where usually j_{SC} can be substituted by the externally measured current density at zero applied potential under steady-state conditions, which is equivalent to short circuit conditions[21]. Comparing equation 2.8 and 2.9, it can be noted that equation 2.8 is based on the calculation of the power output (numerator) by the direct measurement of the true H_2 production rate using an analytical method (e.g. gas chromatography or mass spectrometry) while equation 2.9 calculates that power as the product of voltage, current, and the Faradaic efficiency for hydrogen evolution.

Besides STH efficiency, to calculate the performance of a single photoelectrode independently, where extra applied potential is often required from a second photoelectrode or external power supply, applied bias photon to current conversion efficiency (ABPE) can be used. Using certain j_{SC} and η_F, ABPE can be expressed as follow:

$$\mathbf{ABPE} = \left[\frac{j_{SC}(mA\ cm^{-2})\ x\ (1.23\ V - V_{app})\ x\ \eta_F}{P_{light}(mW\ m^{-2})}\right]_{AM\ 1.5G} \quad 2.10$$

where V_{app} corresponds to the applied potential between the photoelectrode and counter electrode. Moreover, the efficiency calculation of electrons/holes converted from photons at individual wavelengths of light on a single photoelectrode needs to be considered.

Thus, incident photon-to-current efficiency (IPCE) or external quantum efficiency (EQE) can be introduced as follows:

$$\mathbf{IPCE}(\boldsymbol{\lambda}) = \mathbf{EQE}(\boldsymbol{\lambda}) = \frac{\boldsymbol{electron\ flux}\ (\boldsymbol{cm^{-2}\ s^{-1}})}{\boldsymbol{photon\ flux}\ (\boldsymbol{cm^{-2}s^{-1}})} \qquad 2.11$$

$$= \frac{\left|\boldsymbol{j_{ph}}(\boldsymbol{mA\ cm^{-2}}\right|\boldsymbol{x\ hc}(\boldsymbol{V\ nm})}{\boldsymbol{P_{\lambda}}(\boldsymbol{mW\ cm^{-2}})\boldsymbol{x\ \lambda}(\boldsymbol{nm})}$$

where λ is the single wavelength light source, P_λ is the power of irradiation, h is Plank's constant, c is the speed of light, and j_{ph} is the photocurrent density. To obtain IPCE, a monochromator and a three-electrode configuration are essential, so j_{ph} at the identical applied potential with individual wavelengths of light can be calculated accurately. Integrating the IPCE values obtained with the standard AM 1.5 G solar spectrum, the total photocurrent density upon solar illumination can be extrapolated as follows:

$$\boldsymbol{J_{AM\ 1.5}} = \int (\boldsymbol{IPCE_{\lambda}\ x\ \Phi_{\lambda} x\ e})\boldsymbol{d\lambda} \qquad 2.12$$

where e is the elementary electronic charge (C) and Φ_λ is the photon flux of irradiation (m^2 s)[17]. It can be noted that STH and IPCE are related: if no applied bias is used in the IPCE measurement, the integration of IPCE over the entire solar spectrum can provide an estimation of the maximum possible STH.

2.1.5 Semiconductor photoanode requirements

In order to maximize the PEC efficiency, photoanodes (n-type materials) for solar water splitting should meet the specific requirements, which will be described in the following sections.

2.1.5.1 Stability, low cost and abundance

Firstly, the stability of a photoanode in aqueous environments under oxidation conditions is an essential parameter to control for photocatalytic applications. Indeed, the decomposition or the formation of an oxide layer on the surface of semiconductors can have a great impact on the charge transfer to the electrolyte[39]. Secondly, considering the current development of sustainable material and resource shortage, the materials used for solar water splitting must be low cost and abundant. Many metal oxides, including for example TiO_2 and Fe_2O_3, meet these requirements along with a good stablity in aqueous solutions[40]. Thus, they are promising materials as photoanodes for solar water splitting.

2.1.5.2 Band position

An important feature of a photocatalyst for solar water splitting is that the energy bands of the semiconductor should straddle the redox potentials of water in order to obtain overall water splitting. In particular, the bottom level of the conduction band must be more negative than the redox potential of H^+/H_2 (0V versus normal hydrogen electrode (NHE)), while the top level of the valence band must be more positive than the redox potential of O_2/H_2O (1.23 V)[41]. A schematic example of a photocatalyst with a desirable bandgap structure for water splitting is illustrated in Figure 2.9. However, as explained in 2.1.2.1, each photoelectrode (photoanode and photocathode) is responsible for the appropriate half-reaction of water splitting. Consequently, the photoanode needs to have the top level of the valence band more positive than the redox potential of O_2/H_2O while the photocathode should have the bottom of the conduction band above H^+/H_2 energy level.

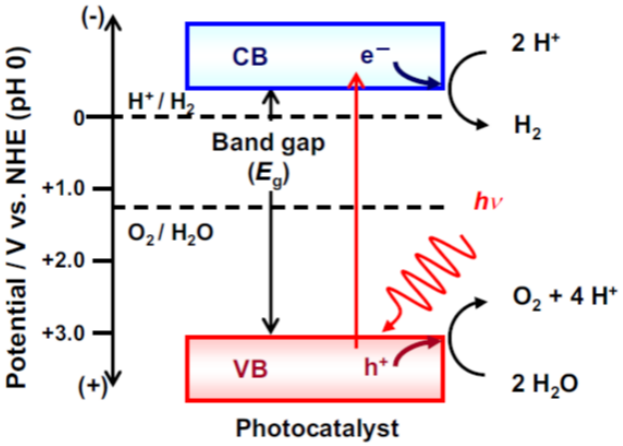

Figure 2.9 Schematic of band structure for solar water splitting[41].

2.1.5.3 Light absorption

To generate electron-hole pairs upon illumination, the semiconductor photocatalyst has to absorb photons in the solar spectrum, the energy of which has to be at least equal to the bandgap E_g. Considering water splitting kinetic overpotentials and thermodynamic losses, it has been found that the optimal bandgap should lie in the range 1.9-3.1 eV, with an optimal value about 2 eV[39,42]. A semiconductor which possesses such a bandgap would absorb photons with wavelengths below 620 nm and ideally would lead to solar-to-hydrogen efficiency of 16.8 %[39]. Figure 2.10 shows the photocurrent density and solar-to-hydrogen efficiency corresponding to some metal oxide used as photoanodes. It can be noted that hematite (α-Fe_2O_3), which usually has a bandgap of 2.15 eV, can reach a theoretical solar-to-hydrogen effiency of *ca.* 15 %, which makes it a promising candidate as n-type photoanode[43]. Besides a small bandgap, α-Fe_2O_3 possesses a suitable position of valance band (VB) and conduction band (CB), which is an important requirement for water oxidation.

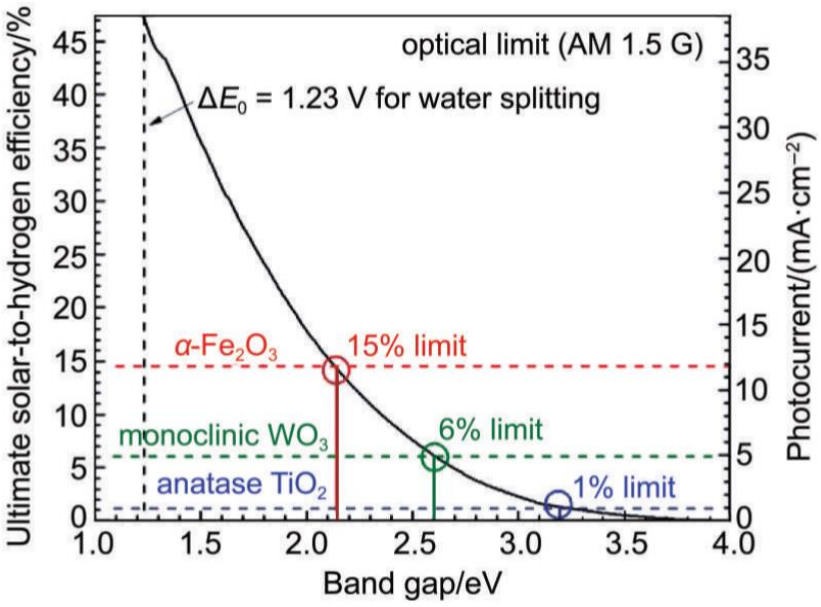

Figure 2.10 Photocurrent density and solar to hydrogen efficiency, relative to some metal oxide materials used as photoanodes[43].

2.1.5.4 Electron-hole pair recombination

If an electron (from an electron-hole pair) promoted in the conduction band returns to an energy state in the valence band, recombination of the electron-hole pair can occur, causing a net loss in charge carrier density and consequently a reduction in photocurrent and also the water splitting efficiency. When a photoanode is in contact with an electrolyte, electron-hole pair recombination can take place within the bulk of the semiconductor, within the space charge layer, or at its surface, as shown in Figure 2.11. Generally, recombination in the space charge layer can be neglected compared to bulk and surface recombination, considering that the electric field induced by the band bending leads to electron-hole pairs separation. Moreover, the presence of defects in the material (*e.g.* impurities, structural defects, grain boundaries) can create discrete energy levels within the bandgap, facilitating carrier recombination since the carrier lifetime is

inversely proportional to the defect density in the material[44]. These trapping levels generally lie near the middle of the bandgap. This is critical in polycrystalline oxides, which are prepared at low temperature and thus possessing more defects. Moreover, the crystallinity of semiconductor materials is related to charge recombination: the recombination probability is reduced when the crystallinity of a photocatalyst is increased, because the density of crystal defects is reduced with higher crystallinity[45]. Recombination also takes place at the surface of the semiconductor photoanode due to the presence of intra band gap electronic states located at the semiconductor/electrolyte interface, acting as preferred recombination centers[46]. For example, they can arise in response to ion adsorption or surface reconstruction. The presence of such states significantly affects the kinetics of the water oxidation reaction.

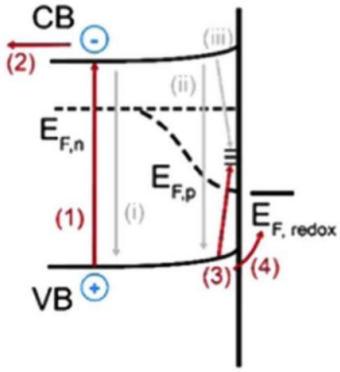

Figure 2.11 Schematic of band structure of n-type semiconductor under illumination where the steps involved are indicated as follows: (1) electron-hole pair generation by light excitation, (2) extraction of electron through back contact, (3) hole transfer to semiconductor surface and then (4) to the electrolyte; (i) bulk recombination, (ii) surface recombination and (iii) electron trap by surface states can take place. Adapted from[21].

2.1.6 Strategies to improve semiconductor photoanodes

To improve PEC performance of photoanodes for solar water splitting, different strategies have been adopted which can be classified in three different approaches: (1) control bulk recombination, (2) heterostructuring and (3) improving surface kinetics. These approaches will be described in more detail in the following sections, focusing on the state-of-art examples from literature, which are more relevant to this PhD thesis.

2.1.6.1 Control of bulk recombination

As introduced in 2.1.5.2, the control of electron-hole pair recombination is particularly important as it leads to a net loss in the photocurrent and PEC water splitting performance. Among the various strategies used to limit bulk recombination, increasing the n-type doping of photoanodes is a very convenient way that has been explored. Indeed, the Fermi level position within the bandgap can be moved closer to the bottom of the conduction band (CB) through doping, compared to an undoped material. This will increase the flat band potential and consequently the band bending at photoanode/electrolyte interface, leading to an enhancement in the charge transfer. It has been reported that in hematite doped with transition metal (*e.g.* Ti, Sn, Al)[47-49] the overall photocurrent significantly increases with respect to the undoped material. Doping of metal oxide photoanodes using oxygen vacancies, which are known as donor species[50,51] is also quite common. The effect of oxygen vacancies on the PEC performance of $BaTiO_3$ photoanodes, presented in this thesis, will be described in Chaper 4.

Another strategy recently adopted is the internal electric field to reduce the charge carrier recombination rate. The use of ferroelectric materials has been proven an efficient solution to improve charge carrier separation, thanks to the spontaneous ferroelectric

polarisation, which induces band bending at the material's surface, facilitating water oxidation and reduction reactions[52]. The role of ferroelectric material in photocatalysis, reporting relevant state-of-art example from literature, will be explored in 2.2.10 and in particular the influence of both ferroelectric $BaTiO_3$ and ferroelectric/photocatalyst $BaTiO_3$/α-Fe_2O_3 thin films on the their PEC performance will be described in detail in Chapters 4, 5 and 6.

Moreover, nanostructuring is a widely used strategy to compensate the small carrier diffusion lengths[53,54]. Using this approach, the distance carriers must travel is reduced without significantly diminishing the total volume of the material, so the same quantity of light is absorbed. Thus, the recombination rate is reduced as holes reach the surface before recombining. Figure 2.12 shows a comparison between Fe_2O_3 thin films with planar and nanostructured configuration, highlighting how the charge recombination can be reduced in nanostructured Fe_2O_3 thin films. The control and investigation of nanostructured $BaTiO_3$ thin films in relation to their photoelectrochemical properties will be explored in detail in Chapter 4.

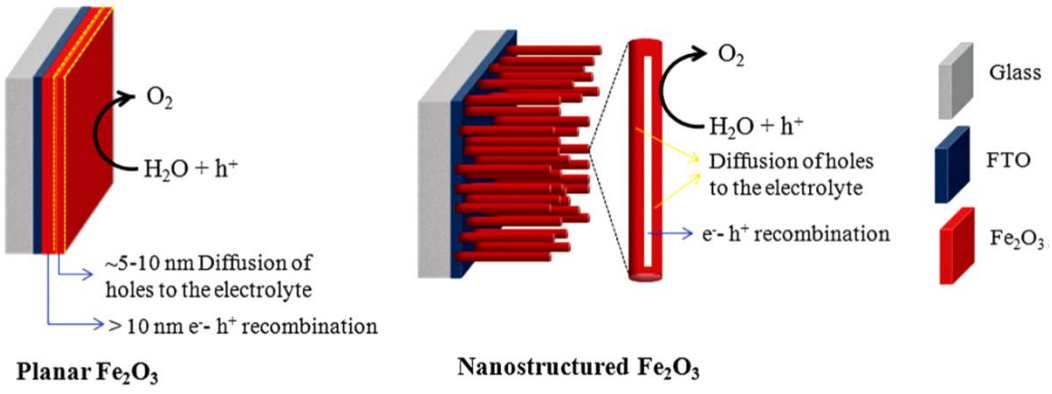

Figure 2.12 Comparison of planar Fe_2O_3 and nanostructure Fe_2O_3 in terms of charge carrier recombination[55].

Also, the inclusion of interfacial layers between the substrate and the photoanode material have been reported as an additional method to limit the recombination rate since it acts as potential barrier to prevent back injection of the holes from the photoanode to the substrate[56]. In this PhD thesis, compact titanium dioxide ($cTiO_2$) layer will be used as blocking layer at the interface of $BaTiO_3$ film and FTO glass substrate.

2.1.6.2 Heterostructuring

The combination of a semiconductor material with a small bandgap with one possessing a wide bandgap, forming heterostructures has been reported as an effective method to enhance the absorption efficiency of the entire system for solar water splittiing[57]. The case of ferroelectric $BaTiO_3$, which is the material with larger E_g (3.2 eV) combined with photocatalyst Fe_2O_3 as small E_g material (2.1 eV) will be considered in Chapter 6, discussing the advantages derived from this combined system.

2.1.6.3 Improving surface kinetics

It is known that the water oxidation reaction could be challenging because of the high kinetic overpotential required with respect to that for the water reduction reaction. In this context, cocatalysts materials have been adopted to reduce the overpotential necessary to oxidize water[58], thus the water oxidation kinetics are improved. Different types of materials, including iridium oxide[59], cobalt oxide[60], mixed cobalt-nickel-iron oxides[61], have been used as cocatalysts for photoanodes. Figure 2.13 shows the improvement in the photoelectrochemical performance of a photoanode, after addition of cocatalyst on the surface.

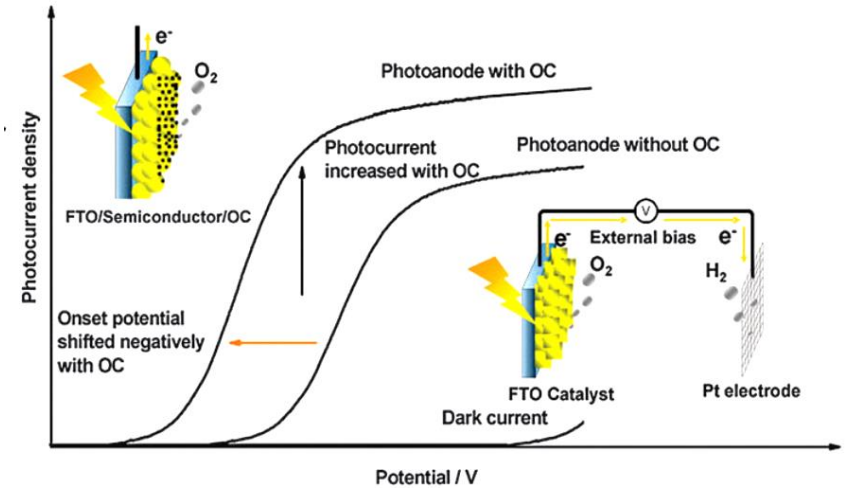

Figure 2.13 Schematic on the role of oxidation cocatalyst (OC) in PEC water splitting systems[55].

To overcome the high recombination rate of holes at the surface of some photoanodes (e.g. α-Fe_2O_3) caused by intra bandgap trapping states, the deposition of overlayers on the photoanode surface to passivate such trapping states has been used as alternative strategy to improve the surface kinetics. These layers are defined passivating overlayers, which differ from the cocatalysts as they do not have catalytic activity if used alone[62]. Several studies have been reported on the deposition of thin overlayers of Al_2O_3, In_2O_3 and TiO_2 on hematite, which successfully reduce the required applied bias potential[63,64]. The mechanism of a passivation layer in the improvement of water oxidation performance is illustrated in Figure 2.14.

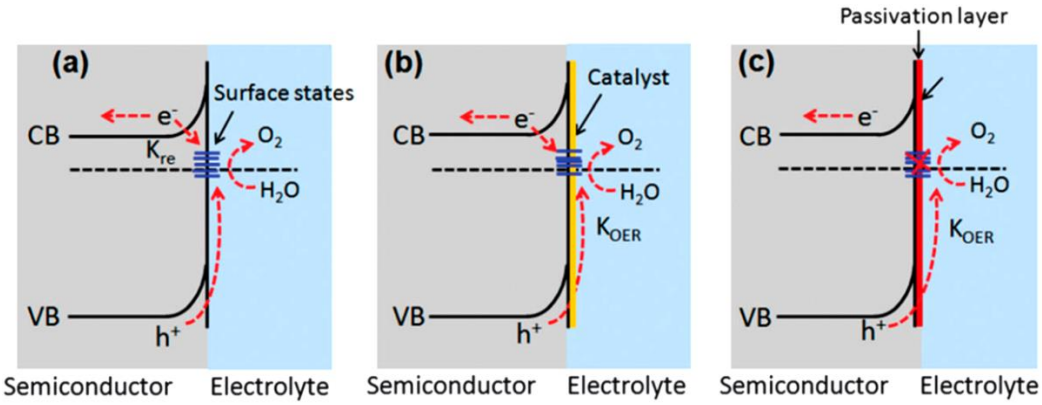

Figure 2.14 Band structure of an n-type semiconductor photoanode in the presence and the absence of passivation layers in a PEC cell. (a) High charge recombination at surface defects and inefficient water oxidation by the photogenerated holes. (b) Use of an OER catalyst layer, facilitating hole transfer to the electrolyte to enhance water oxidation; (c) use of thin non-catalytic passivation layers which suppress surface recombination, improving water oxidation[55].

2.2 Ferroelectric materials as semiconductors

2.2.1 Ferroelectricity: definition and origin

Ferroelectricity refers to a polar crystal that exhibits a spontaneous electric polarization **P**, which can be switched by applying a suitable electric field **E**[65]. The origin of the name "ferroelectrics" derives from the analogy with ferromagnetics, where the magnetization **M** can be reversed by a magnetic field **H**. However, ferroelectrics are all solids and non-metallic, so they are also known as Seignette-electrics, after the discovery of P. de la Seignette around 1655, who first prepared Rochelle salt as a laxative. Even if Seignette did not discover the ferroelectric phenomena, Rochelle salt is the first known ferroelectric crystal. Indeed, the discovery of ferroelectricity is commonly assigned to Valasek, who

recognized in 1920 that the polarization of Rochelle salt can be reversed by the application of an external electric field[66].

2.2.2 Crystal symmetry in ferroelectric materials

The origin of ferroelectricity derives from crystal symmetry. Generally, crystals are classified into seven systems: triclinic (the least symmetrical), monoclinic, orthorhombic, tetragonal, trigonal, hexagonal, and cubic (the most symmetrical). Depending on their symmetry, these systems are subdivided in 32 crystal classes or point groups. Among them, 11 crystal classes possess a centre of symmetry[65]. For definition, a crystal is centrosymmetric if the movement of each point, indicated by coordinates x,y,z to a new point at -x,-y,-z does not determine a recognizable difference. Therefore, centrosymmetric crystals are nonpolar and consequently do not exhibit a finite polarization or dipole moment[67]. All the remaining 21 non-centrosymmetric crystal classes (except one) show polarization upon application of mechanical stress or exhibit strain by the application of an electric field. This effect is known as piezoelectric effect and thus, these crystal classes are defined as piezoelectrics. Among the 20 piezoelectric crystal classes, 10 possess a unique polar axis and show electric polarization in the absence of an electric field, known as spontaneous polarization. The latter changes with temperature and is associated to the thermal expansion of the crystal lattice. Materials that satisfy these conditions are defined as pyroelectrics[68]. The subgroup of the pyroelectric class, which includes only the crystals capable of reversing their spontaneous polarization by application of an electric field, is defined as the ferroelectric class[65]. The relationship between ferroelectrics, pyroelectrics and piezoelectrics, included in the non-centrosymmetric point groups, is reported in Figure 2.15.

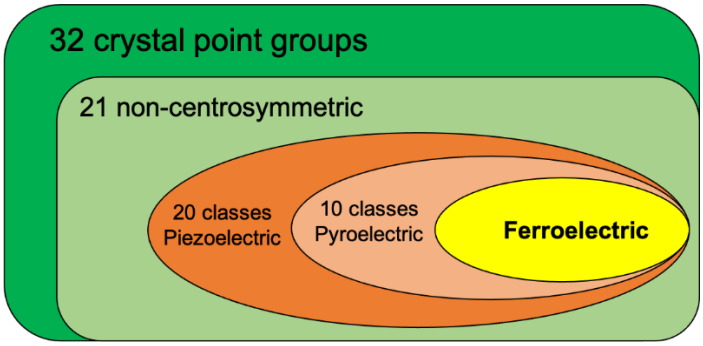

Figure 2.15 Subdivision of 32 crystal classes in 11 centrosymmetric and 21 non-centrosymmetric groups, of which 20 classess exhibit piezoelectric effect and 10 classess possess also pyroelectricity; only a subgroup of those 10 classes show ferroelectricity.

2.2.3 Dipole moments, spontaneous polarization and Curie Temperature

As in all ordinary dielectric materials, the electrical properties of ferroelectrics arise from the dipole moments, generated after application of an electric field **E**. Considering a dipole, which consists of a positive and negative charge, q, separated by a distance **x**, the electric dipole moment is defined as:

$$\boldsymbol{p = qx} \qquad \textbf{2.13}$$

Therefore, the spontaneous polarization $\mathbf{P}_s$ corresponds to the density of electric moments, in analogy with the magnetization for magnetic materials:

$$\boldsymbol{P_s = \frac{\sum_n p_n}{V}} \qquad \textbf{2.14}$$

or the dipole moment per unit volume[68], as reported in 2.14.

In a typical ferroelectric material, the spontaneous polarization $\mathbf{P}_s$ only exists over a limited range of temperatures. Increasing the temperature T, a point is reached where the transition from the polar, ferroelectric phase to a nonpolar, paraelectric phase occurs. The temperature at which the polar state disappears continuously or discontinuously is defined as the Curie Temperature (T_C)[65,69].

In addition, the approach to T_C is associated with an anomalously high dielectric constant or permittivity $\boldsymbol{\varepsilon}$. According to the Curie-Weiss law, the dependence of permittivity ε on temperature above T_C can be described as:

$$\boldsymbol{\varepsilon} = \frac{\boldsymbol{C}}{(\boldsymbol{T} - \boldsymbol{T_0})} \qquad \textbf{2.15}$$

where C is called the Curie Weiss constant and T_0 is termed the Curie Weiss temperature, which is equal to T_C only for the case of a continuous phase transition[67]. The typical plots of P_s and $\boldsymbol{\varepsilon}$ as function of temperature for ferroelectric materials around T_C are reported in Figure 2.16. As shown in Figure 2.16, P_s drops (discontinuously or continuously) to zero at T_C while $\boldsymbol{\varepsilon}$ increases to a sharp peak (with a discontinuous or continuous step) as the temperature decreases[69].

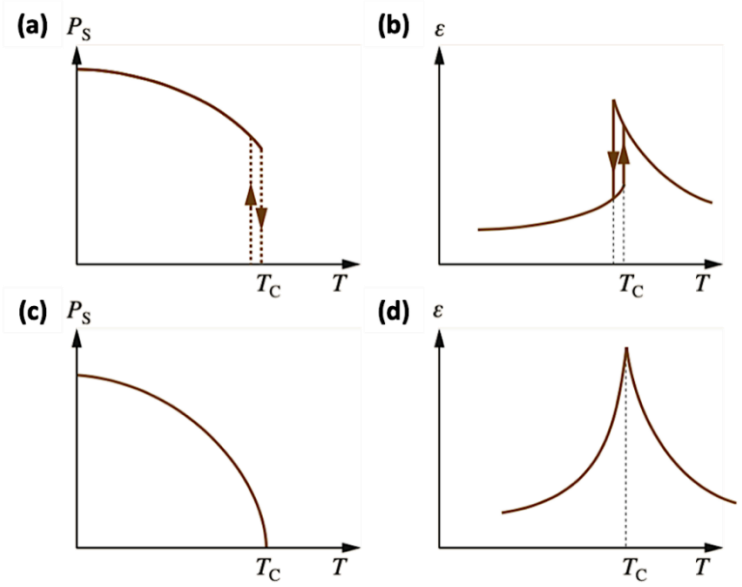

Figure 2.16 Temperature-dependent spontaneous polarization and permittivity for a discontinuous (a, b) and a continuous (c, d) phase transition (adapted from[69]).

2.2.4 Polarization reversal

As defined in 2.2.1, the primary feature of ferroelectrics is that the spontaneous polarization can be reversed, at least partially, when an electric field **E** is applied. The first demonstration of polarization reversal was obtained by the observation of dielectric hysteresis[70]. Indeed, the hysteresis loop is currently used to identify ferroelectric materials.

Figure 2.17 shows the relationship between polarization **P** and applied electric field **E** observed in ferroelectrics and described by a hysteresis loop. At low **E** fields, the polarization **P** increases linearly with the field considering that **E** is not large enough to induce the orientation of the domains (portion 1-2). When the field **E** raises more than the low-field range, the polarization **P** increases nonlinearly, because the electric dipoles start to orient toward the direction of the field (portion 2-3). At very high fields, polarization

will approach a state of saturation which corresponds to the portion 3-4, where most electric dipoles are aligned toward the direction of the applied field **E**. Extrapolating the linear portion 3-4 back to the abscissa, the saturation value of the spontaneous polarization $\mathbf{P}_s$ is obtained. When the **E** field is decreased to zero, the polarization will drop down (portion 4-5) but does not become 0, leaving a remanent polarization $\mathbf{P}_r$. The electric field **E**, required to reduce the polarization to zero (portion 5-6) is called the coercive field $\mathbf{E}_c$. The area within the loop is a measure of the energy necessary to twice reverse the polarization. When the applied electric field **E** is increased above $\mathbf{E}_c$, a reverse saturation polarization $-\mathbf{P}_s$ is eventually developed (portion 6-7). When the field **E** return to zero, a negative remanent polarization $-\mathbf{P}_r$ is obtained (portion 7-8). A further raising in the **E** field, increases the polarization first from $-\mathbf{P}_r$ to zero at $\mathbf{E}_c$ and then to $+\mathbf{P}_s$, completing the ferroelectric hysteresis loop[67,69,65].

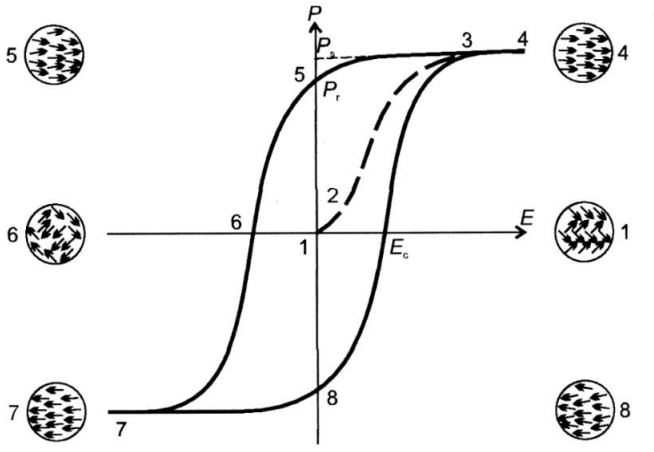

Figure 2.17 Typical hysteresis loop of ferroelectric material[71].

2.2.5 Depolarization field, domain structure and poling

The arising of spontaneous polarization $\mathbf{P_s}$ will induce bound charges on the surface of ferroelectric materials[72]. Generally, if those charges are left uncompensated within ferroelectrics, an electric field that opposes the spontaneous polarization $\mathbf{P}_s$, named as the depolarization field $\mathbf{E}_{dep}$, is generated[73]. The magnitude of $\mathbf{E}_{dep}$ is given by:

$$\boldsymbol{E_{dep}} = -\frac{\boldsymbol{P}}{\boldsymbol{\varepsilon_0 \varepsilon_{ferro}}} \qquad 2.16$$

where $\mathbf{P}$ is the ferroelectric polarization, $\boldsymbol{\varepsilon}_0$ and $\boldsymbol{\varepsilon_{ferro}}$ correspond to the vacuum permittivity and static dielectric constant of the material, respectively[73]. It is extremely rare to identify a ferroelectric material where the polarisation is uniformly oriented across the whole single crystal, considering that this would lead to a very large $\mathbf{E}_{dep}$[75]. On the contrary, a more typical ferroelectric material will develop multiple oppositely oriented regions, known as domains, separated by boundaries defined as domains walls to minimize the total electrostatic energy of the system, which can be defined as:

$$\boldsymbol{W_{tot} = W_M + W_E + W_{DW} + W_S = min} \qquad \mathbf{2.17}$$

where W_M is the strain related elastic energy, generated from the crystalline anisotropy and spontaneous polarization, W_E correspond to the elastic energy derived from $\mathbf{E}_{dep}$, W_{DW} is associated to the domain wall energy and W_S is the surface energy[73].

The domain walls are named after the angle between the adjacent polarization vectors. Generally, two kinds of domain walls can be generated in tetragonal structured ferroelectrics: 180° domain walls and non-180° domain walls (also defined the 90° domain walls). 180° domains walls can induce the reduction of the electric energy W_E

while non-180° domain walls can allow the release of elastic energy W_M. The final domain configuration is determined by minimizing the total energy, which lead to a more stable crystal.

Considering a multi-domain structured ferroelectric material, the randomly oriented electric dipoles will cancel each other, giving a zero net polarization (Figure 2.18 a). When an external electric field greater than or equal to $\mathbf{E}_c$ is applied, the domain walls will move and the randomly oriented polarisation vectors will be oriented along a uniform direction of the electric field (Figure 2.18 b). This process is known as poling, which induces domain switching in the ferroelectric material. Consequently, the net polarisation of the materials will be parallel to the direction of the applied electric field. When the electric field is removed, the presence of some domains that conserve the orientation will still be observed, leading to the remnant polarisation (Figure 2.18 c).

By definition, the C+ domains show $\mathbf{P}_s$ that points toward the surface (upward polarization or $\mathbf{P}_{up}$) while C- domains show $\mathbf{P}_s$ that points toward the bulk (downward polarization or $\mathbf{P}_{down}$)[73].

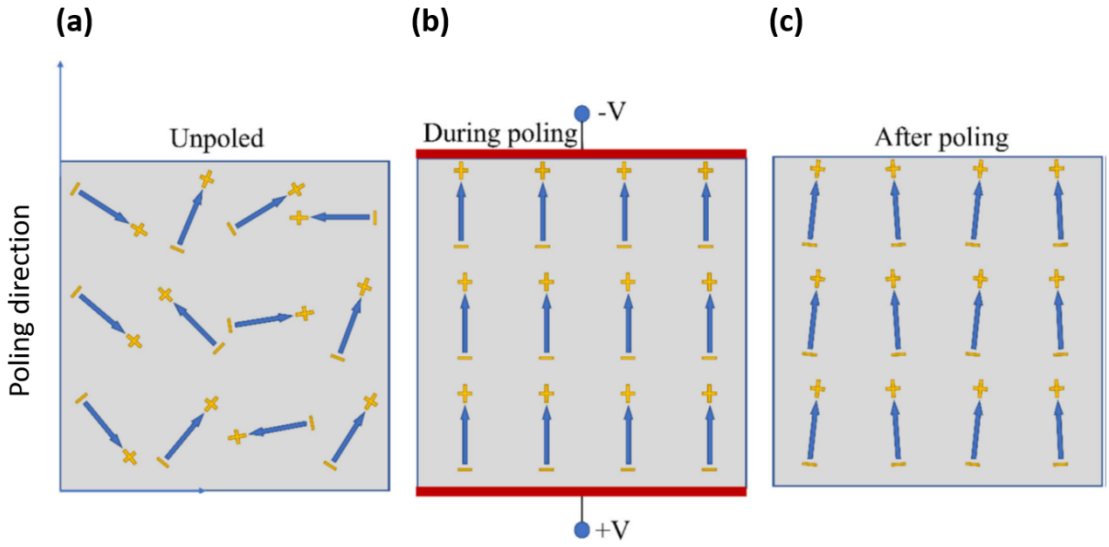

Figure 2.18 Mechanism of poling process: (a) before poling, the domains are randomely oriented, giving a zero net polarisation; (b) during poling, the domains align with the electric field direction and, (c) after poling, a remnant polarisation can still be observed. Figure adapted from ref[76].

2.2.6 Screening mechanisms

The $\mathbf{E}_{dep}$, generated in response to $\mathbf{P}_s$, will induce the movement of mobile charge carriers and defects in the ferroelectric material to neutralise the surface bound charges. This process is known as internal screening. In addition, if ionic species or polar molecules are absorbed onto the ferroelectric material surface, external screening can occur[77]. The presence of internal or external screening is related to the material. Indeed, in a ferroelectric material that contains a large number of defects internal screening is predominant due to the availability of mobile electrons and holes. On the contrary, in a ferroelectric material with a low number of defects and consequently lack of mobile free carriers, external screening is favoured[77]. Figure 2.19 shows the polarization bound charge and the relative screening mechanism in ferroelectrics.

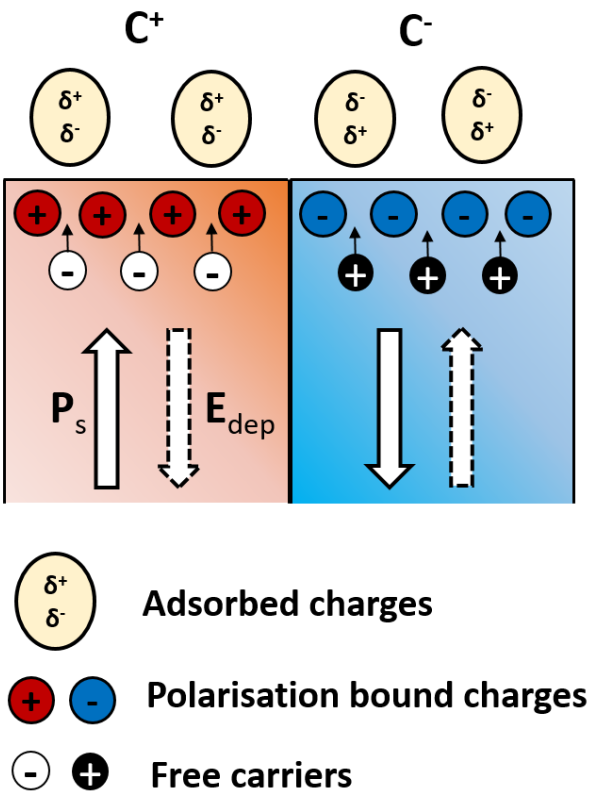

Figure 2.19 Schematic of polarisation directions and carrier movement in a ferroelectric material. To obtain charge compensation induced by the spontaneous polarisation P_s, any free carriers or defects in the ferroelectric material will screen the surface charge (internal screening); any polar molecules or ions will generate charge compensation if adsorbed on the surface.

2.2.7 Band bending in ferroelectrics

Although the carrier concentration and consequently the conductivity may be low, ferroelectric materials can be considered as wide bandgap semiconductors and thus their photo-physical and chemical properties are often comparable to their conventional semiconductor counterparts. However, the internal and external screening, which arises in response to the ferroelectric polarisation, induces some important differences, in

particular related to the band bending at the interface between the electrolyte and the ferroelectric material, illustrated schematically in Figure 2.20. Specifically, at C^+ faces, the positive polarisation induces the accumulation of electrons for screening and this leads to downward band bending. On the other hand, at C^- faces, the negative polarisation favour hole accumulation, which generates upward band bending (Figure 2.20)[78].

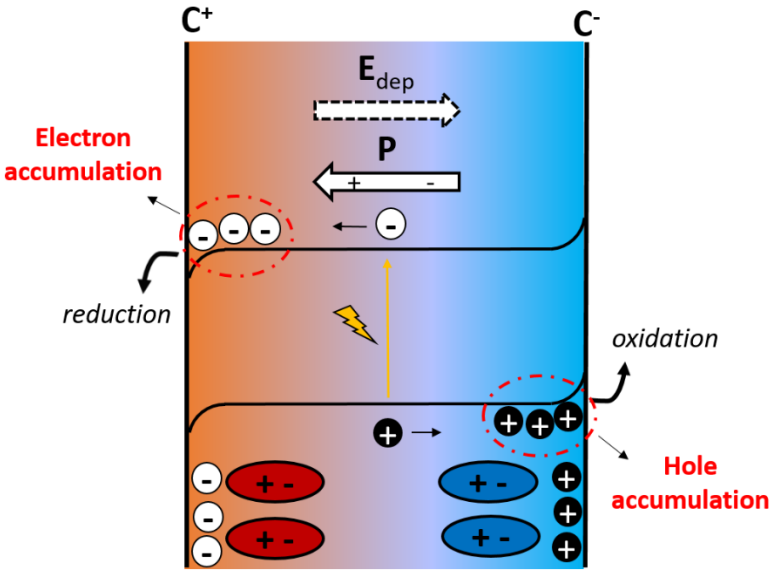

Figure 2.20 Schematic mechanism of band bending at ferroelectric/electrolyte interface, induced by the movement of internal free charges and defects. A driving force for the separation of photogenerated electrons and holes at the surface of the ferroelectric is produced as a result of the band bending.

As a consequence, the near-surface areas at the ferroelectric surfaces are equivalent to the space-charge region (SCR) present in conventional semiconductors, previously detailed 2.1.3. However, compared to typical semiconductors, the band bending in ferroelectrics occurs also under inert atmospheres and it is due to the movement of free carriers and defects to the material surface for screening of the spontaneous polarisation, as shown in

Figure 2.20. It has been observed that this kind of band bending in ferroelectric materials prevails even when they are immersed in an electrolyte and it can assume values of several hundred meV or greater, which is in the same magnitude order of the bend bending at most p/n junctions and semiconductor/electrolyte interfaces[79,80]. As a consequence, the band bending in ferroelectrics can favor the drastic reduction in the recombination of photogenerated electrons-holes near the surface, proving a driving force for their effective separation.

2.2.8 Size effect on ferroelectric behaviour

It is well known that ferroelectric materials possess a correlation between their size and the relative ferroelectric properties. In particular, when the dimensions of ferroelectrics are reduced to the nanometer scale, the dielectric properties will significantly differ from the bulk and thus size effects will arise in response to the size-driven instability in the polar phase, which can lead to the suppression of ferroelectric behaviour below a critical size[81]. It has been reported that the values of the 'critical size' change among different ferroelectrics as well as the same ferroelectric materials, possessing different forms (bulk ceramics, particles or thin films). For example, research works have found that $BaTiO_3$ ceramic present a critical size of around 400 nm[82] while for $BaTiO_3$ thin films it a much smaller critical size of ~ 5 nm has been recently reported[83].

The origin of size effects can be related to intrinsic and extrinsic factors. The intrinsic factors include the depolarization field effects due to the formation of a single domain[84] and the absence of long-range cooperative interaction[82]. Indeed, the density of domain walls and the energy associated with the domain wall formation is strongly influenced by the size of ferroelectrics. When the volume of a ferroelectric sample decreases, the energy

associated with domain wall formation increases and thus the stabilization of the ferroelectric material is affected. As a consequence of this reduction in size, ferroelectrics change their configuration from polydomain to single domain below a critical size. For example, this effect is observed in barium titanate particles that possess a size below around 100 nm. As a consequence, the depolarisation field associated with the ferroelectric sample increases in response to the generation of single domains and thus, if it is left uncompensated (no internal/external screening occurs), the ferroelectricity of the sample will be destroyed.

The other intrinsic factor that influences the ferroelectric properties is related to the dipole interactions over a long-range. Indeed, long-range interactions between the polar units are needed to generate a homogeneous spontaneous polarization and consequently to support ferroelectric phase formation. However, the interactions are limited by some correlation lengths. Ginzburg-Landau theory demonstrates that there exist size constraints below which the ferroelectric domain structure collapses. To demonstrate this in detail, the free energy of an inhomogeneous ferroelectric particle has been analysed over a range of sizes, using the polarization as a key parameter in the modelling. The polarisation can be related to the correlation length, defined as the average coordination distance for polarisation fluctuations in the material. In the case of large correlation length, the dipoles present in the crystal will interact over long distances within the lattice. Extrapolating the length values, the differences in the coupling strength present at the bulk and surface of the material can be obtained. If the coupling strength at the surface is lower than the one present in the body of the sample, the surface will be disordered with respect to the bulk. Thus, a reduction in size of the ferroelectric material implies that the disorder in the system significantly changes the ferroelectric phase stability.

Besides the intrinsic factors, extrinsic factors due to the effects of material processing (e.g. modification of the microstructures or defects) may significantly contribute to the size effect in ferroelectrics[82]. For example, the presence of hydroxyl ions, which commonly exist as defects in the lattice of $BaTiO_3$ may affect the long-range polar ordering which controls the ferroelectric phase transition[85]. Therefore, the size effect need to be carefully considered during the design and development of ferroelectric materials.

2.2.9 Photochemistry of ferroelectrics

The surface photochemistry of ferroelectrics had remained mostly unexplored until around 2000 when Giocondi and Rohrer published a series of research works on the variations of photochemical properties of $BaTiO_3$[79,86,87], showing clearly the role of internal polarisation of $BaTiO_3$ on the behaviour of photogenerated charge carriers. They observed that upon UV light illumination, in a $BaTiO_3$ single crystal when submerged in $AgNO_3$ and $Pb(C_2H_3O_2)$ solutions, solid deposits of Ag and PbO_2 accumulated on the surface of domains with opposite polarisation (C^+, C^-), where oxidation and reduction reactions are separated. This was related to the ferroelectric polarisation which induces band bending at ferroelectric surface, described in 2.2.7: in particular, at C^- domain where hole accumulation promotes upward band bending the oxidation of Pb^{2+} to Pb^{4+} was favorited while electron accumulation induces downward band bending at C^+ domains, where consequently the reduction reaction of Ag^+ to Ag was facilitated. Figure 2.21 summarizes this process, showing indeed that the silver is reduced on positive C^+ domains while lead is oxidized on negative C^- domains. Thus, this suggests that the ferroelectric polarisation induces the separation of redox reactions at different locations. The oxidation and reduction reactions that occurs at different domains can be expressed as:

$$Ag^{+} + e^{-} = Ag \qquad 2.18$$

$$Pb^{2+} + 2H_2O + 2h^{+} = PbO_2 + 4H^{+} \qquad 2.19$$

The same phenomenon has been also demonstrated for $BaTiO_3$ microcrystals or ceramics[87,88].

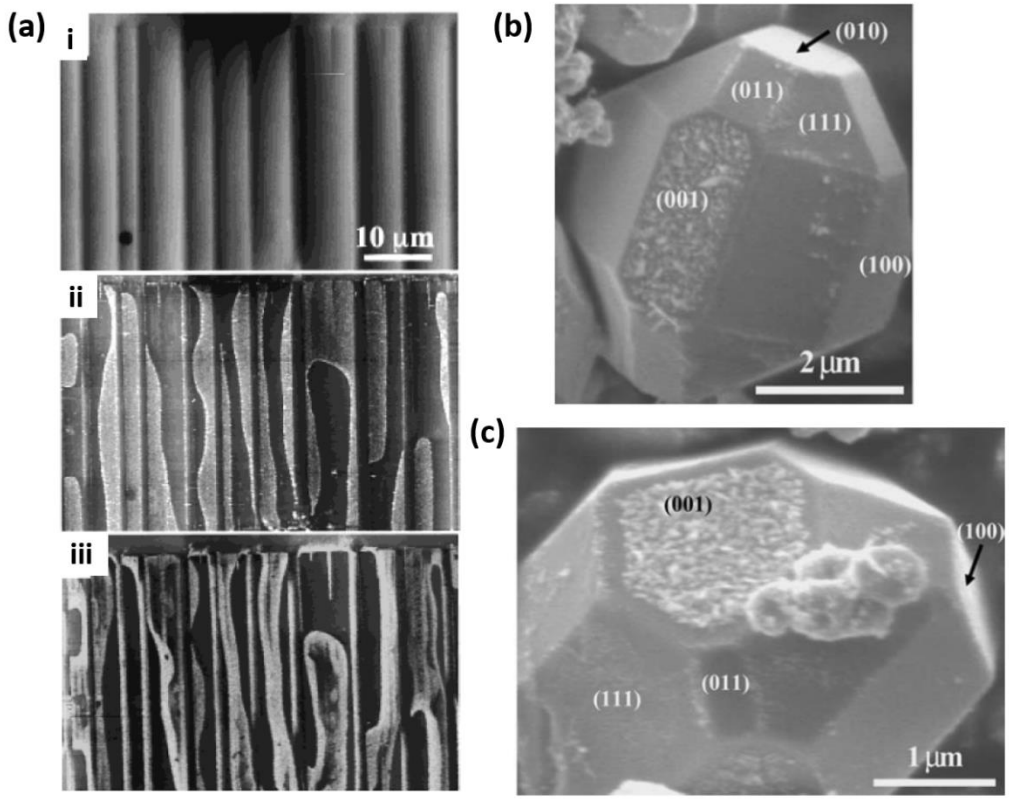

Figure 2.21 (a)Topography of {001} $BaTiO_3$ single crystal surface, obtained by atomic force microscopy (AFM): (i) clean surfaces before the redox reactions, (ii) the same surface area after illumination in an $AgNO_3$ aqueous solution and (iii) after illumination in a lead acetate aqueous solution; SEM image of $BaTiO_3$ crystal after

the reaction with (b) $AgNO_3$ and (c) $Pb(C_2H_3O_2)$, where the presence of Ag and Pb reduction and oxidation products are observed. Adapted from[89].

Rohrer and coworkers also investigated the photochemical reduction of Ag using $Ba_{1-x}Sr_xTiO_3$ solid solution, varying x=0-1.0[90]. They found that even if the reduction of Ag on $BaTiO_3$ was spatially selective and correlated with the orientations of the underlying ferroelectric domains, increasing the amount of strontium, the reduced silver become more spatially homogeneous because of the non-ferroelectric properties of $SrTiO_3$. This provides significant evidence that the spatial selectivity of redox reactions is strongly connected to the ferroelectric behaviour. The formation of these selective patterns associated with the redox products was also demonstrated in different ferroelectric materials, including $Pb(Zr,Ti)O_3$[91], $LiNbO_3$[92] and $BiFeO_3$[93]. The latter possesses a narrow band gap (from 2 to 3 eV), which allows visible light absorption. Indeed, Schultz *et al.* have reported the spatially selective reduction of silver from an aqueous solution on the surface of $BiFeO_3$ ceramic, under visible light illumination[94].

2.2.10 Role of ferroelectric materials in photocatalysis

The peculiar properties of ferroelectric materials related to their ferroelectric polarisation which influence the spatial separation of oxidation and reduction sites makes them particularly attractive for photocatalytic applications. Indeed, the presence of ferroelectric field increases charge carrier lifetime by limiting their recombination[95,96].

Despite the interesting early fundamental research works demonstrating the spatial separation of redox products on ferroelectric surfaces, there have only been a limited

number of studies on utilising ferroelectrics as photocatalysts for practical applications, such as for photocatalytic dye degradation and for photocatalytic water splitting.

2.2.10.1 Photocatalytic dye degradation

Among the few studies showing the use of ferroelectric materials for photocatalytic dye degradation, Cui *et al.* reported the photocatalytic degradation of $BaTiO_3$ by Rhodamine B (RhB), used as degradation target upon UV-visible light illumination[88]. The authors produced $BaTiO_3$ powder with higher tetragonal content and, therefore, enhanced ferroelectricity by thermal treatment of the as-received $BaTiO_3$, which was predominantly cubic and consequently non-ferroelectric. The smaller particle size of the as-received $BaTiO_3$ sample compared to the annealed one induced the suppression of ferroelectricity and stabilization of the cubic phase at room temperature. This effect was explained in more detail in 2.2.8. The results obtained showed a three times improvement of the decolorization rate in the ferroelectric $BaTiO_3$ compared to the non-ferroelectric one (Figure 2.22 a,b). It was related to the ferroelectric behaviour of the sample which creates a tightly bound layer of dye molecules as well as induces the separation of the photogenerated charge carriers via the internal screening. Moreover, after photochemical deposition of nanostructured Ag on ferroelectric $BaTiO_3$ surface, an additional enhancement in the photocatalytic activity was observed, which was attributed to both improved charge separation due to the ferroelectricity of $BaTiO_3$ and enhanced visible light absorption through surface plasmon resonance (SPR). Successively, Yang and coworkers investigated the effect of ferroelectric polarisation on the photodecolourisation rates of RhB on $BaTiO_3$ nanoparticles of different sizes (down to 7.5 nm) at 30 and 80 °C (Figure 2.22 c,d). Using 7.5 nm $BaTiO_3$ nanoparticles as photocatalyst, a reduction in the decolorization rate of RhB under UV light illumination by ∼12 % was observed, when

the temperature was increased from 30 to 80 °C. This was correlated to a P_s close to zero due to a reduced T_C in very small nanoparticles. On the contrary, no such reduction in rate was observed at different temperatures when large $BaTiO_3$ nanoparticles (500 nm) were used as photocatalysts, because only a small reduction in P_s would be experienced until the T_C of 120 °C is reached. Considering the strong temperature dependence of the polarisation in 7.5 nm $BaTiO_3$ nanoparticles, their ferroelectric polarisation promotes the photogenerated charge carriers' separation, improving the overall efficiency of their photocatalytic properties[96]. Besides $BaTiO_3$, the enhanced photocatalytic activity for dye degradation has also been observed using other ferroelectric materials, such as $LiNbO_3$ nanopowder[91]and $BiFeO_3$ nanoparticles[97].

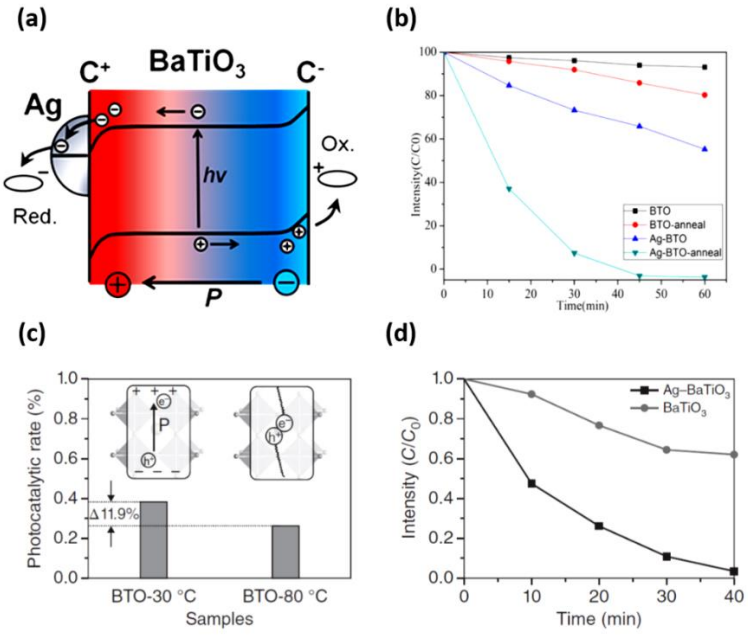

Figure 2.22 (a) Schematic on band bending in ferroelectric $BaTiO_3$ in response to the movement of free carriers; (b) Photodecolorization curves of RhB using different catalysts under solar simulator, where ferroelectric BTO (after annealing) shows higher activity, when combined with Ag nanoparticles[88]; (c) Photocatalytic

performance of $BaTiO_3$ nanoparticles at 30 and 80°C and relationship with the spontaneous polarisation, affecting the photocatalytic activity; (d) RhB photodegradation induced by $BaTiO_3$ and Ag-$BaTiO_3$ under UV illumination[96].

2.2.10.2 Photocatalytic water splitting

Among various ferroelectric materials, $BaTiO_3$ is a promising candidate for photocatalytic water splitting, considering that it has conduction and valence bands at very similar energy to those in TiO_2 (-0.5 and 2.7 V vs NHE, respectively), which is thermodynamically suited for water oxidation and proton reduction[98]. In 1976, Nasby and Quinn first studied photoelectrochemical water splitting on $BaTiO_3$ single crystals[99]. They reported that under UV light illumination, $BaTiO_3$ electrode generates photocurrents of around 101 μA (illuminated area of 0.18 cm^2), remaining stable under applied potential. Even if the influence of ferroelectric polarisation on the PEC performance (e.g. via poling) was not directly investigated in this early research work, they demonstrate that $BaTiO_3$ photoanodes can generate very small photocurrents even without an applied voltage, contrary to TiO_2 single crystal photoanodes[99]. After this pioneering work by Nasby and Quinn, few studies were reported in the following years on single ferroelectric materials for water splitting[100]. More recently, the use of epitaxial $BiFeO_3$ thin films for water splitting upon simulated solar light was explored[101]. Ji *et al.* have reported a slight shift of the onset potential (by 0.016 V) after poling of the film and also they showed that the oxidation and reduction reactions could be promoted according with the polarisation direction[101]. Despite the limited values of photocurrents (about 10 $\mu A/cm^2$) obtained in this work, it demonstrates that upon careful design, a single ferroelectric material could be used to obtain water splitting, where the products of redox reactions are spatially separated on the ferroelectric material surface. Cao *et al.* showed a

significant photocurrent enhancement from 0 to 10 mA/cm^2 at 0 V vs Ag/AgCl in $BiFeO_3$ polycrystalline films upon variation of the poling bias from -8 V to +8 V. The authors correlated this enhancement with the upward band bending at semiconductor/electrolyte interface, arising from the ferroelectric polarization[102].

Rioult *et al.* investigated the influence of internal electric polarisation on the photoelectrochemical response of epitaxial ferroelectric $BaTiO_3$ thin films. The authors showed that the measured photocurrent of the ferroelectric layer is more than doubled after +8 V electrochemical poling, compared to the unpoled state, observing also a reduction of the onset potential by ~ 0.2 V for the poled sample[103]. The manipulation of photoelectrochemical performance by ferroelectric polarisation was also demonstrated in vertically aligned epitaxial ferroelectric $KNbO_3$ nanowires. Li *et al.* showed that when the $KNbO_3$ film is downward polarised, the photocurrent density enhances to 11.5 μAcm^{-2} at 0 V vs. Ag/AgCl under illumination, which is 10-fold larger than that of the same sample upward polarised[104]. More recently, Singh and co-authors showed the tuning of PEC response in Ag/Nb-doped $SrTiO_3$ nanoporous films by poling treatment. The ferroelectricity was achieved in $SrTiO_3$ nanoporous films due to strain induced by the nanocomposite approach. As reported in Figure 2.23 b, an enhancement in the photocurrent density (130 μAcm^{-2} at 1 V vs Ag/AgCl) and the reduction of onset potential by 20 mV were observed in the positively poled sample, compared to the unpoled counterpart, showing a photocurrent of 93 μAcm^{-2} at 1 V vs Ag/AgCl and an onset potential at -0.74 V vs Ag/AgCl (Figure 2.23a). On the contrary, the negatively poled sample shows a reduction of photocurrent to 40 μAcm^{-2} at 1 V vs Ag/AgCl with a 20 mV increase in the onset potential (Figure 2.23 c). This demonstrates that the photoelectrochemical performance of Ag/Nb-doped $SrTiO_3$ nanoporous films can be

effectively controlled by ferroelectric polarisation. The corresponding band diagram of $SrTiO_3$ films before and after poling is reported in Figure 2.23 d. The authors attributed the improvement in the photoelectrochemical performance of the $SrTiO_3$ nanoporous films after positive poling to the enlarged width of the space charge region (W_{sc}), which drives more holes toward the semiconductor interface, facilitating the interfacial charge transfer[105].

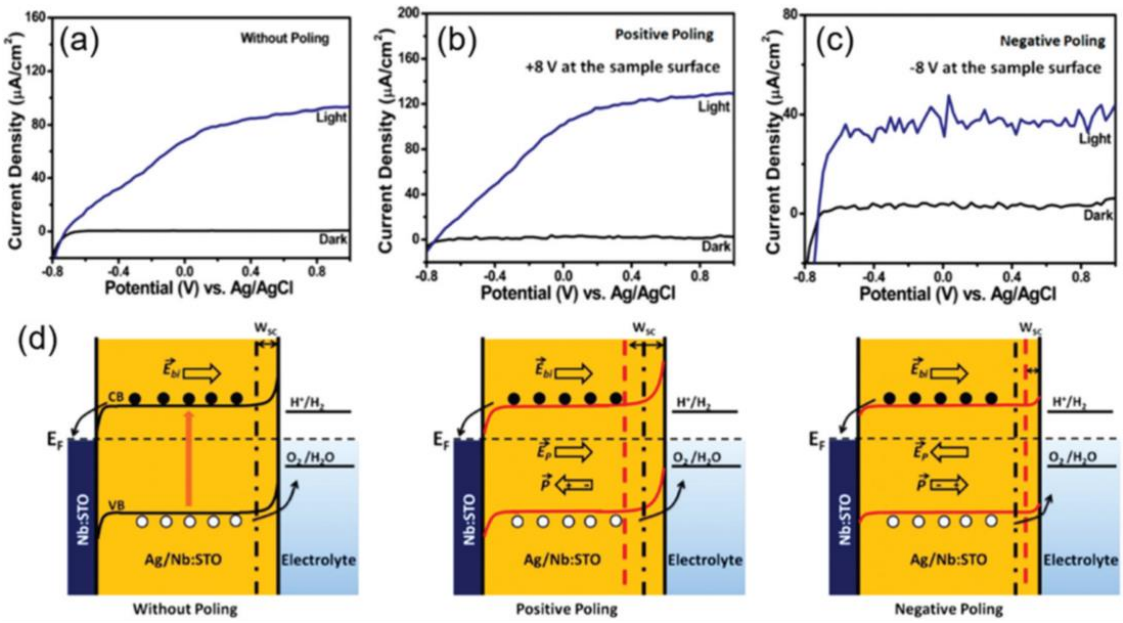

Figure 2.23 J-V curves of Ag/Nb-doped $SrTiO_3$ nanoporous films unpoled (a), positively poled (b), and negatively poled (c); corresponding schematic of band diagram before and after poling (d).

2.2.10.2.1 Ferroelectric/non-ferroelectric heterostructures

Considering the beneficial properties of ferroelectric materials in photocatalysis, recent research works have been focusing on the combination of ferroelectrics with other more efficient traditional photocatalysts (e.g. Fe_2O_3, $BiVO_4$ and WO_3). Indeed, it is known that very few ferroelectric materials are visible light absorbers, thus such a ferroelectric/non-

ferroelectric heterostructure is a promising solution to exploit the attractive properties of both the ferroelectric material (improved charge carrier separation) alongside a suitable non-ferroelectric semiconductor (visible light absorption, good charge mobility, photoconductivity etc.).

Early studies have reported that TiO_2 coated on BTO substrate induces the silver photoelectrochemical reduction in preferred sites of the thin film, indicating that the ferroelectric field influence the charge separation on TiO_2 surface up to 100 nm thick[94,106]. However, by increasing the thickness of the thin film, the photocatalyst effectively screens the ferroelectric polarization, which affects the charge dynamics and photocatalytic activity[107]. Enhancement in the PEC performance have been also found using different ferroelectrics as substrates (e.g. $LiNbO_3$[108], $PbTiO_3$[109]).

Successively, various research works have focused on $BaTiO_3/TiO_2$ heterostructures, considering the favorable band energy alignment which does not inhibit the charge transfer. For example, Li and coworkers investigated the influence of ferroelectric polarization on photocatalytic water splitting activity using $BaTiO_3/TiO_2$ core-shell photocatalysts, showing photocatalytic hydrogen production rates much greater than those obtained using bare TiO_2 or $BaTiO_3$[110]. The authors suggested that the ferroelectric core could improve the charge separation thanks to the spontaneous polarisation and the movement of free carriers in the ferroelectric material is related to the band bending at the $BaTiO_3/TiO_2$ interface. Moreover, photoelectrochemical water splitting on $TiO_2/BaTiO_3$ core/shell nanowire photoelectrodes has recently shown to lead a 67 % photocurrent density enhancement than the bare TiO_2 nanowires[111] (Figure 2.24 a,b).

Even if $BaTiO_3/TiO_2$ heterostructures offer an excellent proof of principle, these materials possess a wide bandgap which limits the light absorption to the UV region, which limit their capabilities in photocatalysis. Thus, other heterostructures have been recently investigated, such as $BaTiO_3/\alpha$-Fe_2O_3 core/shell structures, which showed an enhanced decolourisation of RhB compared to the bare $BaTiO_3$ and significantly faster than the bare α-Fe_2O_3 (Figure 2.24 c,d). This improvement in the photocatalytic activity of $BaTiO_3/\alpha$-Fe_2O_3 heterostructure was related to heterojunction band alignment and ferroelectric internal field, which allow efficient carriers separation at the ferroelectric-semiconductor interface[112].

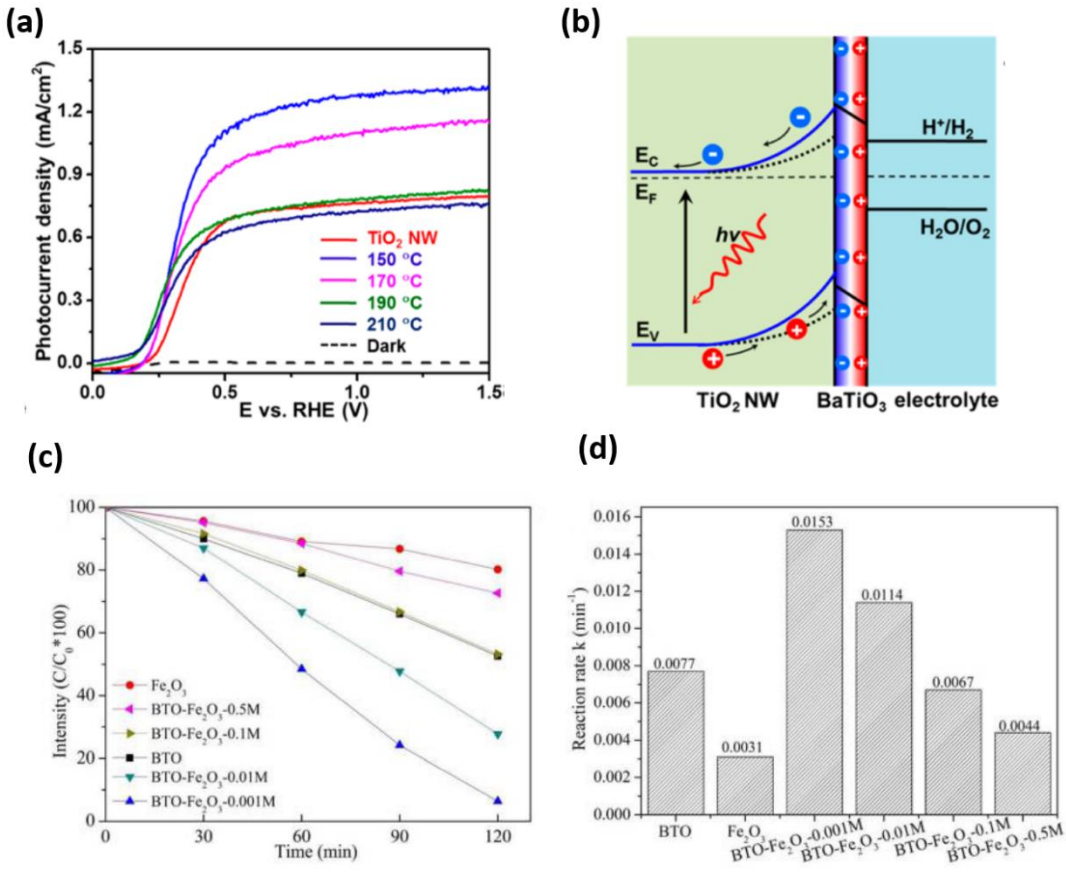

Figure 2.24 Photocurrent density-potential (J-V) curves of TiO_2 NWs and 150-210 °C TiO_2/BTO NWs (a) and corresponding schematic of TiO_2/BTO-electrolyte

interface (b)[111]; Photodecolorization profiles of RhB using different photocatalysts under simulated sunlight (c) and the calculated reaction rates of different photocatalysts (d).

Moreover, heterostructures based on $BiFeO_3$ have attracted great interest, considering the beneficial PEC properties of this ferroelectric material, due to its narrow bandgap[113]. The spatial selective deposition of Ag was again observed on the surfaces of TiO_2 thin films on $BiFeO_3$ as substrate[114]. The authors showed maximum heights of deposited silver in the range of 60 to 100 nm for TiO_2 films with thickness of 10 and 20 nm. However, when the TiO_2 film is 80 nm thick, the heights of deposited silver do not exceed 20 nm. This demonstrates a direct correlation between amount of silver reduced and thickness of TiO_2 film: increasing the TiO_2 film thickness, the amount of silver reduced is decreased. Figure 2.25 a,b,c shows the silver reduction heights in $TiO_2/BiFeO_3$ with TiO_2 thickness of 10 nm. Owing to the ferroelectric polarization, $BiFeO_3/TiO_2$ core/shell nanopowders generated a fast dye photodegradation compared to both bare TiO_2 and $BiFeO_3$ samples, degrading almost 70 % of the initial dye in the same conditions[115].

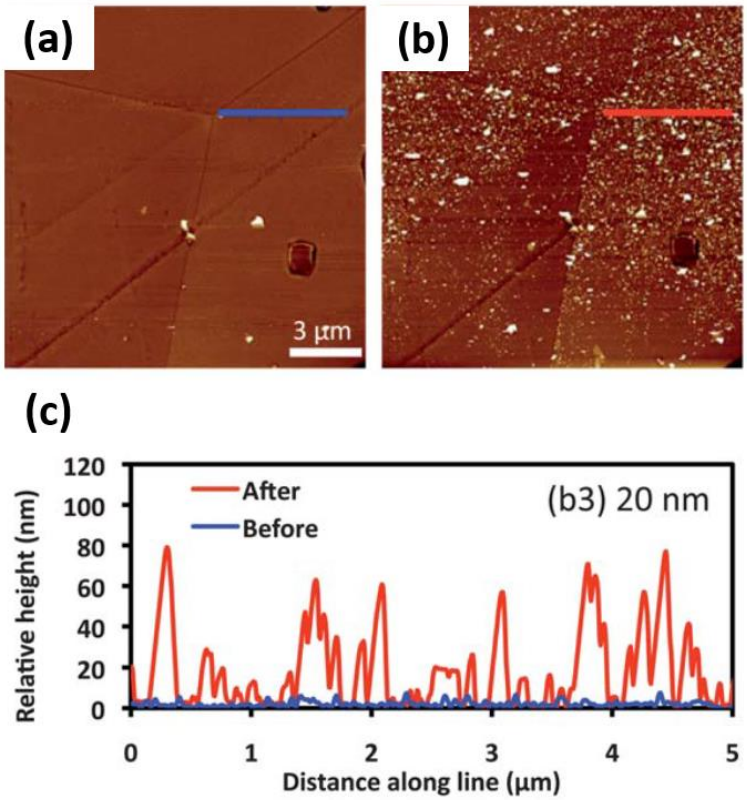

Figure 2.25 AFM topographic images of $TiO_2/BiFeO_3$ with TiO_2 thickness of 20 nm before (a) and after (b) reaction; comparison of silver reduction heights at the same locations (c).

However, even if a clear improvement in the PEC performance is observed in all these heterostructures, only few research works on ferroelectric-photocatalyst hybrid systems demonstrated how ferroelectric polarisation influence photocatalytic activity, investigating the effect of poling pre-treatment on ferroelectric-photocatalyst system. Without this evidence, it is very difficult to prove that the ferroelectric polarisation is the cause of the enhancement in the photoelectrochemical performance rather than just the effect arising from heterojunction formation.

Among the few examples that evaluated the effect of poling in ferroelectric-photocatalyst system, the research work from Yang and co-authors, which was introduced previously in this section, shows that the ferroelectric polarisation in $TiO_2/BaTiO_3$ core/shell nanowire photoelectrode can be switched using external electric field poling, inducing an improvement or decrease of PEC performance according to the polarisation direction[111], as shown in Figure 2.26 a,b. More recently, He *et al*. investigated the role of ferroelectric polarisation in the enhancement of PEC performance of the Fe_2O_3/PZT system[116]. The obtained Fe_2O_3/PZT films presented a remarkable improvement in the photoelectrochemical performance, reaching a photocurrent density of 1 mA/cm^2 at 1.23 V vs RHE, which is 10 times that of the bare Fe_2O_3 photoanode. To demonstrate the direct influence of ferroelectric polarisation in this PEC improvement, the authors reported that the Fe_2O_3/PZT films obviously enhance their PEC response after positive poling compared to the unpoled state, with also a negative shifting of their onset potential. On the contrary, the photocurrent density of Fe_2O_3/PZT films was decreased and the onset potential had a positive shift after negative poling (Figure 2.26 c). This demonstrates that the PEC response of Fe_2O_3/PZT can be regulated by tuning the ferroelectric polarisation orientation. The mechanism proposed by the authors, involved in the improvement of PEC performance after positive poling, is shown in Figure 2.26 d[116].

Despite these studies clearly demonstrating the possibility to tune the PEC performance by poling, they do not investigate the effect of poling on the chemical composition of the ferroelectric-photocatalyst film. In case of sample alteration due to poling treatment, variations in the PEC performance may arise, which give consequently unreliable results.

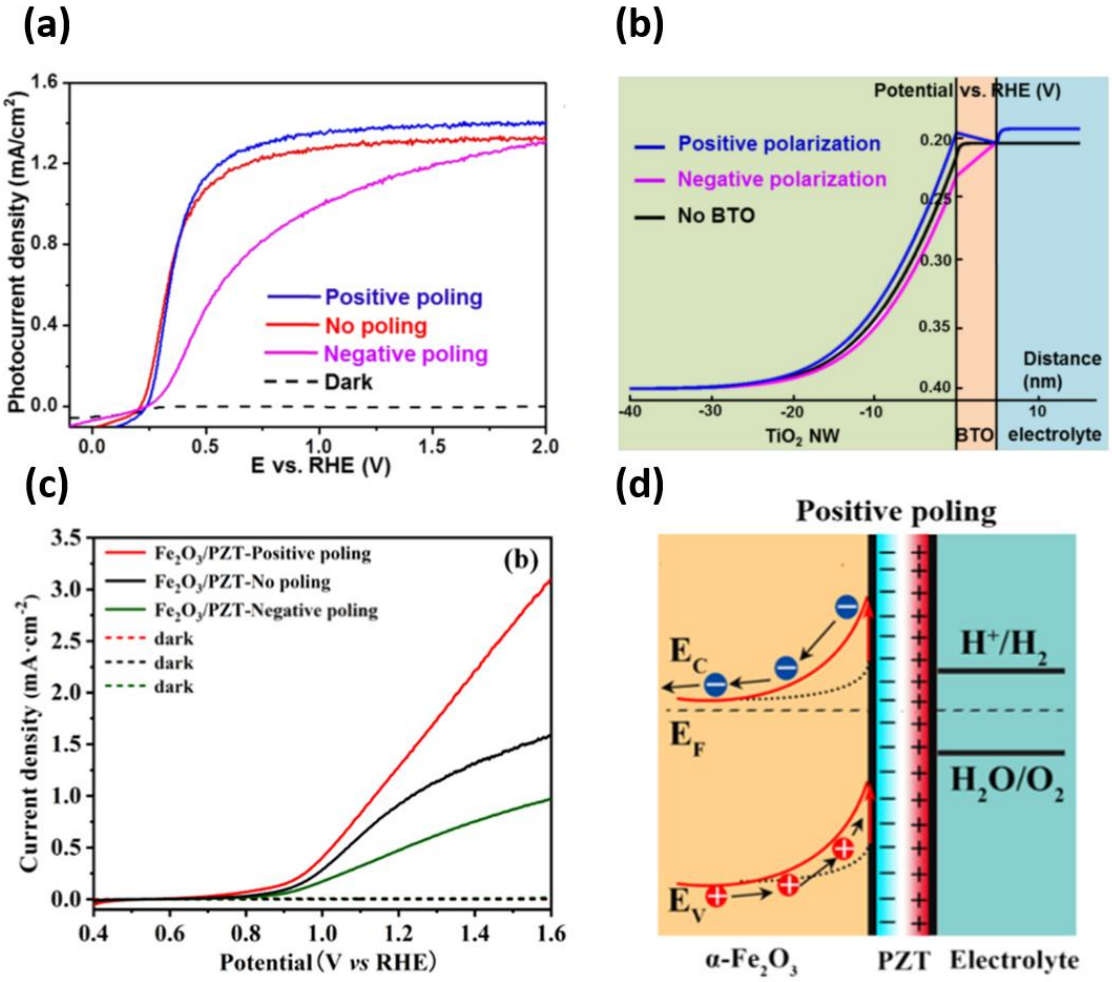

Figure 2.26 Current density-voltage curves of the unpoled, positively poled and negatively poled 150 °C $TiO_2/BaTiO_3$ nanowires (a), Potential distribution of 150 °C TiO_2/5 nm BTO/NaOH heterojunction, showing that the spontaneous polarization in $BaTiO_3$ shell lead to an upward band bending of TiO_2 core, facilitating thecharge separation in TiO_2 (b)[111]; LSV curves of Fe_2O_3/PZT under illumination, measured before and after poling (c) schematic mechanism of adjusting the PEC response by tuning polarization direction during positive poling (d)[116].

2.3 Semiconductor materials used in this project

2.3.1 Barium Titanate ($BaTiO_3$)

Barium titanate (BTO) is the first ferroelectric material with a perovskite structure to be reported[117]. BTO has the general formula of ABX_3, where the Ba^{2+} cations are positioned on the A-sites and Ti^{4+} on the B-sites while the X-sites are filled by O^-. Figure 2.27 a shows the relative position of each ion within a single unit cell in BTO. In particular, eight Ba^{2+} are located on the corners at (0 0 0), (0 0 1), (0 1 0), (1 0 0), (1 0 1), (1 1 0), (0 1 1) (1 1 1). When BTO has cubic symmetry, the Ti^{4+} cations are in the center at (1/2, 1/2, 1/2) while six O^{2-} anions are positioned at the center of the four faces at (0, 1/2, 1/2); (1/2, 0, 1/2); (1/2, 1/2, 0). Ionic bonds are generated between Ba^{2+} and TiO_3 group, while Ti and O atoms are covalently bonded. BTO has a stable tetragonal symmetry (P4mm) at room temperature and consequently non-centrosymmetric, where the displacement of the titanium ions from the center of the unit cell along the elongated axis (c-axis), generates a net dipole moment **P** (Figure 2.27 a), which is responsible of the ferroelectric properties in BTO. The other two axes a and b have the same length in the tetragonal phase. Above the Curie temperature (T_C) at 120 °C, the unit cell of BTO has cubic symmetry (Pm3m), which is centrosymmetric and therefore is paraelectric[117] (Figure 2.27 b). The Curie temperature can increase in case of strained BTO thin films, stabilizing the ferroelectric phase in BTO[117]. Generally, the tensile strain in the [0 0 1] direction can enhance the tetragonal distortion and lead to the stabilisation of the ferroelectric tetragonal phase, including to high temperatures. Conversely, compressive strain in [0 0 1] can stabilise paraelectric cubic phase at room temperature. BTO can also undergo to a series of ferroelectric to ferroelectric transitions from tetragonal to orthorhombic (Bmm2), which

is observed at 5 °C and from orthorhombic to rhombohedral (R3m) at -90 °C. It can be also noted that **P** is parallel to the edge of the crystal unit cell for tetragonal phase, while for the orthorhombic (a = c < b) and rhombohedral (a = c = b) phases it is parallel to the face diagonal and the body diagonal, respectively (Figure 2.27 b)[122].

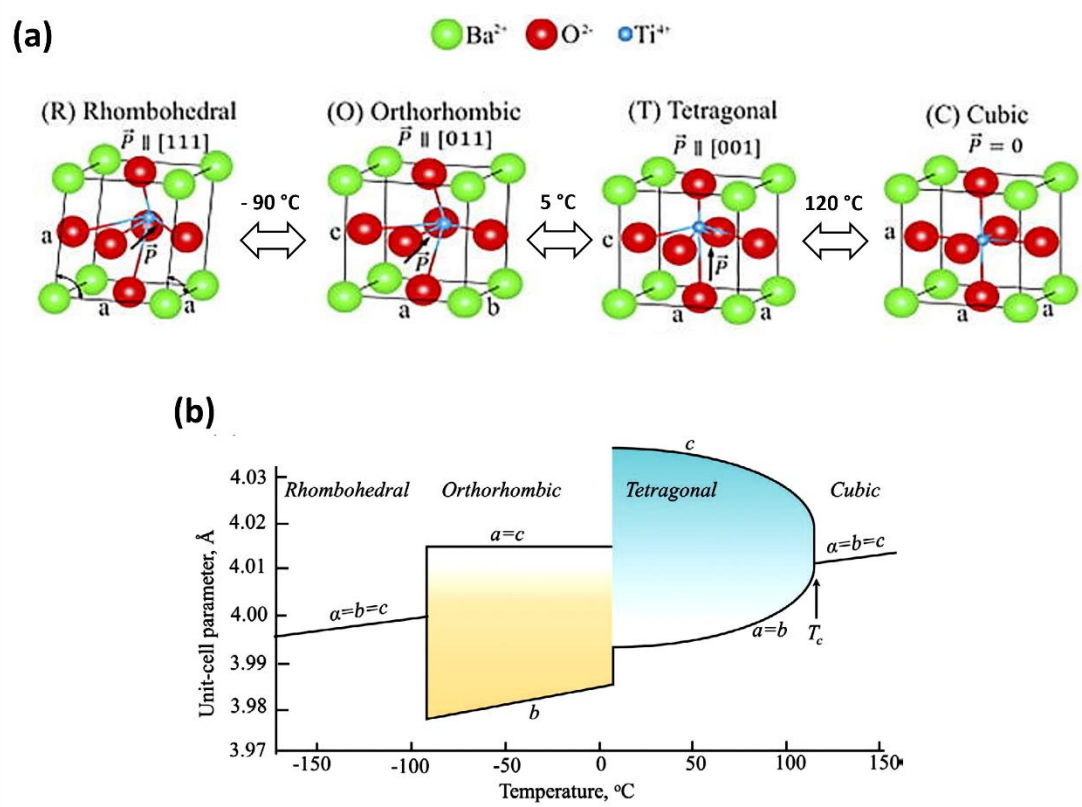

Figure 2.27 Crystalline structure of BTO above and below the Curie temperature and the relative unit cell distorsion[121] (a); Variation of the unit-cell parameter with temperature for the different $BaTiO_3$ phases[122] (b).

The band gap of $BaTiO_3$ bulk is reported to be around 3.2 eV. However, decreasing the particle size of $BaTiO_3$ (< 11.5 nm), it was observed that the band gap increased (~3.47 eV) for the particle size of 6.7 nm[120]. Moreover, the synthesis methodology can induce variations in the band gap energies: for example, $BaTiO_3$ thin films prepared by sol-gel

method show a band gap of 3.7 e V[121]. Owing to its low toxicity, ease of preparation and excellent ferroelectric properties, BTO has been largely used as photocatalyst as reported in the previous sections[122].

2.3.2 Hematite (α-Fe_2O_3)

Iron oxides are the most abundant mineral on Earth and they constitute the primary source of iron. Among them, hematite (α-Fe_2O_3) is the most stable phase. Hematite has been largely used for photocatalytic applications. The hematite structure possesses two formula units per unit cell: the trigonal–hexagonal and the primitive rhombohedral unit cells (Figure 2.28 a,b)[55]. Iron and oxygen atoms are arranged in a trigonal–hexagonal unit cell structure with space group R3c and lattice parameters a = b = 0.5034 nm, and c = 1.375 nm, with six formula units per unit cell. For the rhombohedral unit cell, α_{rh} = 0.5427 nm and α= 55.3°.

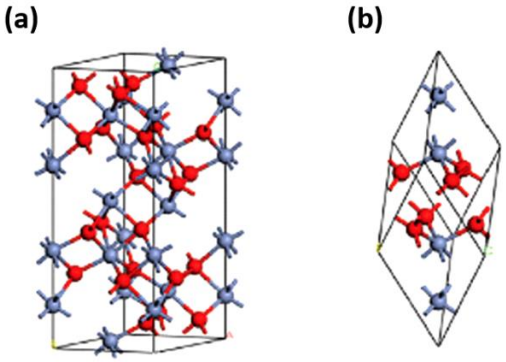

Figure 2.28 Schematic illustration of the crystal structure of hematite: (a) hexagonal unit cell and (b) rhombohedral primitive cell[54].

Hematite (α-Fe_2O_3) is a very promising n-type semiconductor for photo-electrochemical water splitting thanks to its widespread availability, extraordinary chemical stability and

good visible light absorption[123], due to its bandgap of 2.1 eV. However, hematite has not yet maximized its theoretical photoelectrochemical performance, because it is affected by various intrinsic factors such as long penetration depth of visible light, a very short excited-state lifetime (~10^{-12} s)[25], combined with the poor minority charge carrier mobility (0.2 cm^2 V^{-1} s^{-1})[124]. Therefore, most of the photogenerated charge carriers undergo recombination before reaching the material's surface. Thus, different strategies have been recently used to improve the efficiency of hematite-based photoelectrodes, including nanostructuring and use of internal electric field, which have been adopted in this PhD thesis.

2.4 Research aim and objectives

The aim of the research reported in this thesis is to investigate the effect of ferroelectric polarisation on the photoelectrochemical (PEC) properties of nanostructured ferroelectric $BaTiO_3$ thin films and subsequently to combine ferroelectric $BaTiO_3$ and photocatalyst Fe_2O_3 (Fe_2O_3/$BaTiO_3$) films to enhance the PEC performance for solar water splitting. The design approach used for the fabrication of Fe_2O_3/$BaTiO_3$ photoanode is based on the incorporation of nanostructured ferroelectric $BaTiO_3$ in parallel with Fe_2O_3, as more efficient photoactive material, rather than in series. This design aims to prevent charge transfer between photocatalyst and ferroelectric material. Combining the ferroelectric and photocatalyst materials in parallel at nanoscale, the electric field generated by the ferroelectric $BaTiO_3$ can be coupled to the photocatalyst Fe_2O_3, which harvests the majority of incident light. This facilitates the separation of photogenerated charges without any charge transport through the ferroelectric material (Figure 2.29).

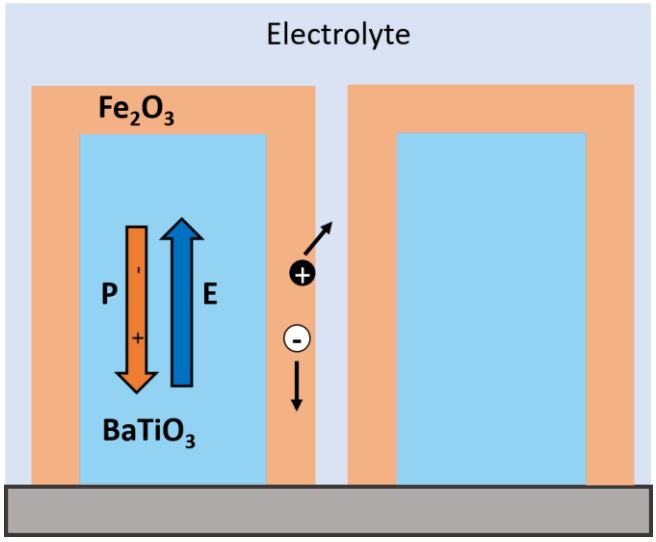

Figure 2.29 Schematic design structure of Fe_2O_3 photocatalyst coated onto ferroelectric $BaTiO_3$ in parallel at the nanoscale.

Thus, the main objectives of this work are:

1. Identify an appropriate design for the development of nanostructured $BaTiO_3$ thin films, allowing the successful integration with Fe_2O_3 photocatalyst.

2. Investigate the effect of ferroelectric polarisation on the PEC properties of nanostructured $BaTiO_3$ films as photoanode.

3. Combine $BaTiO_3$ films with Fe_2O_3 photocatalyst and study the influence of ferroelectric polarisation from $BaTiO_3$ films on the PEC performance of the overall composite $Fe_2O_3/BaTiO_3$ photoanode.

2.5 Summary

This literature review section has touched upon the mechanism behind solar water splitting as well as the different cell configurations based on semiconductor photocatalysts for solar water splitting. The main factors influencing photocatalytic efficiency and the strategies used for its improvement have been discussed. The origin, basic principles and unique properties of ferroelectric materials in photocatalysis have been described, discussing relevant examples for this PhD thesis. Moreover, the semiconductor materials that will be studied in this thesis have been introduced and the aim/objectives of this work have been clearly defined.

Thus, it has been shown that ferroelectrics are promising for photocatalysis due to enhancements in charge carrier separation but they mostly have wide bandgaps. Some attempts to use narrower bandgaps ferroelectrics have been made, as well as being combined with photocatalysts. But the studies are fairly limited and very few have clearly proved that a ferroelectric can directly influence a coupled photocatalyst to give an enhanced photoelectrochemical response. Therefore, this PhD thesis will focus on the effect of ferroelectricity on the photoelectrochemical properties of bare $BaTiO_3$ films as well as $BaTiO_3$ combined with Fe_2O_3 photocatalyst, as explained in more detail in 2.4.

REFERENCES

1. Fujishima, A. & Honda, K. Electrochemical Photolysis of Water at a Semiconductor Electrode. *Nature* **238**, 38–40 (1972).

2. Grätzel, M. Photoelectrochemical cells. *Nature* **414**, 338–344 (2001).

3. Kudo, A. & Miseki, Y. Heterogeneous photocatalyst materials for water splitting. *Chem. Soc. Rev.* **38**, 253–278 (2009).

4. Hoffmann, M. R., Martin, S. T., Choi, W. & Bahnemann, D. W. Environmental Applications of Semiconductor Photocatalysis. *Chem. Rev.* **95**, 69–96 (1995).

5. Chen, X. & Mao, S. S. Titanium dioxide nanomaterials: Synthesis, properties, modifications and applications. *Chem. Rev.* **107**, 2891–2959 (2007).

6. Kay, A., Cesar, I. & Grätzel, M. New benchmark for water photooxidation by nanostructured α-Fe2O3 films. *J. Am. Chem. Soc.* **128**, 15714–15721 (2006).

7. Kudo, A., Omori, K. & Kato, H. A novel aqueous process for preparation of crystal form-controlled and highly crystalline BiVO4 powder from layered vanadates at room temperature and its photocatalytic and photophysical properties. *J. Am. Chem. Soc.* **121**, 11459–11467 (1999).

8. Li, L., Salvador, P. A. & Rohrer, G. S. Photocatalysts with internal electric fields. *Nanoscale* **6**, 24–42 (2014).

9. Smestad, G. Photoelectrochemistry. in Semiconductor Photocatalysis: Principles and Applications 55–84 (2015).

10. Wert, C. A. & Thomson, R. M. *Physics of Solids*. (McGraw-Hill, 1970).

11. Mayers, H. P. *Introductory Solid State Physics*. (CRC Press, 1997).

12. Callister, W. & Rethwisch, D. Materials Science and Engineering: An introduction. (2007).

13. Roy, N. B. Fundamentals of Classical and Statistical Thermodynamics. (Wiley, 2002).

14. Brennan, K. F. The Physics of Semiconductors: With Applications to Optoelectronic Devices. (Cambridge University Press, 1999).

15. Guijarro, N., Le Formal, F. & Sivula, K. Artificial Photosynthesis with Semiconductor-Liquid Junctions. *Chem. Light* **8**, 30–40 (2015).

16. Djurišić, A. B., Leung, Y. H. & Ching Ng, A. M. Strategies for improving the efficiency of semiconductor metal oxide photocatalysis. *Mater. Horizons* **1**, 400–410 (2014).

17. Kment, S. *et al*. Photoanodes based on TiO2 and α-Fe2O3 for solar water splitting-superior role of 1D nanoarchitectures and of combined heterostructures. *Chem. Soc. Rev.* **46**, 3716–3769 (2017).

18. Sivula, K. & Van De Krol, R. Semiconducting materials for photoelectrochemical energy conversion. *Nat. Rev. Mater.* **1**, (2016).

19. Chen, Q., Fan, G., Fu, H., Li, Z. & Zou, Z. Tandem photoelectrochemical cells for solar water splitting. *Adv. Phys. X* **3**, 863–884 (2018).

20. Maeda, K. & Domen, K. Photocatalytic water splitting: Recent progress and future challenges. *J. Phys. Chem. Lett.* **1**, 2655–2661 (2010).

21. Chu, S. *et al.* Roadmap on solar water splitting : current status and future prospects Roadmap on solar water splitting : current status. *Nano Futur.* **1**, (2017).

22. Luo, J. *et al.* Water photolysis at 12.3 % efficiency via perovskite photovoltaics and Earth-abundant catalysts. *Science (80-.).* **345**, 1593–1596 (2014).

23. Nakamura, A. *et al.* A 24.4 % solar to hydrogen energy conversion efficiency by combining concentrator photovoltaic modules and electrochemical cells. *Appl. Phys. Express* **8**, (2015).

24. Cox, C. R., Lee, J. Z., Nocera, D. G. & Buonassisi, T. Ten-percent solar-to-fuel conversion with nonprecious materials. *Proc. Natl. Acad. Sci. U. S. A.* **111**, 14057–14061 (2014).

25. Jacobsson, T. J., Fjällström, V., Sahlberg, M., Edoff, M. & Edvinsson, T. A monolithic device for solar water splitting based on series interconnected thin film absorbers reaching over 10 % solar-to-hydrogen efficiency. *Energy Environ. Sci.* **6**, 3676–3683 (2013).

26. Peharz, G., Dimroth, F. & Wittstadt, U. Solar hydrogen production by water splitting with a conversion efficiency of 18 %. *Int. J. Hydrogen Energy* **32**, 3248–3252 (2007).

27. Licht, S. *et al.* Over 18 % solar energy conversion to generation of hydrogen fuel; theory and experiment for efficient solar water splitting. *Int. J. Hydrogen Energy* **26**, 653–659 (2001).

28. Khaselev, O., Bansal, A. & Turner, J. A. High-efficiency integrated multijunction photovoltaic/electrolysis systems for hydrogen production. *Int. J. Hydrogen Energy* **26**, 127–132 (2001).

29. Nowotny, J. *et al.* Sustainable practices: Solar hydrogen fuel and education program on sustainable energy systems. *Int. J. Hydrogen Energy* **39**, 4151–4157 (2014).

30. Fabian, D. M. *et al.* Particle suspension reactors and materials for solar-driven water splitting. *Energy Environ. Sci.* **8**, 2825–2850 (2015).

31. Ager, J. W., Shaner, M. R., Walczak, K. A., Sharp, I. D. & Ardo, S. Experimental demonstrations of spontaneous, solar-driven photoelectrochemical water splitting. *Energy Environ. Sci.* **8**, 2811–2824 (2015).

32. McKone, J. R., Lewis, N. S. & Gray, H. B. Will solar-driven water-splitting devices see the light of day? *Chem. Mater.* **26**, 407–414 (2014).

33. Pinaud, B. A. *et al.* Technical and economic feasibility of centralized facilities for solar hydrogen production via photocatalysis and photoelectrochemistry. *Energy Environ. Sci.* **6**, 1983–2002 (2013).

34. Shaner, M. R., Atwater, H. A., Lewis, N. S. & McFarland, E. W. A comparative technoeconomic analysis of renewable hydrogen production using solar energy. *Energy Environ. Sci.* **9**, 2354–2371 (2016).

35. Sathre, R. *et al.* Life-cycle net energy assessment of large-scale hydrogen production via photoelectrochemical water splitting. *Energy Environ. Sci.* **7**, 3264–3278 (2014).

36. Kalanur, S. S., Duy, L. T. & Seo, H. Recent Progress in Photoelectrochemical Water Splitting Activity of WO3 Photoanodes. Topics in Catalysis vol. 61 (Springer US, 2018).

37. Guijarro, N., Prévot, M. S. & Sivula, K. Surface modification of semiconductor photoelectrodes. *Phys. Chem. Chem. Phys.* **17**, 15655–15674 (2015).

38. Montoya, J. H. *et al.* Materials for solar fuels and chemicals. *Nat. Mater.* **16**, 70–81 (2016).

39. Van De Krol, R., Liang, Y. & Schoonman, J. Solar hydrogen production with nanostructured metal oxides. *J. Mater. Chem.* **18**, 2311–2320 (2008).

40. Sivula, K., Le Formal, F. & Grätzel, M. Solar water splitting: Progress using hematite (α-Fe 2O3) photoelectrodes. *ChemSusChem* **4**, 432–449 (2011).

41. Hisatomi, T., Takanabe, K. & Domen, K. Photocatalytic Water-Splitting Reaction from Catalytic and Kinetic Perspectives. *Catal. Letters* **145**, 95–108 (2015).

42. Walter, M. G. *et al.* Solar water splitting cells. *Chem. Rev.* **110**, 6446–6473 (2010).

43. Qiu, W. T. *et al.* Effective strategies towards high-performance photoanodes for photoelectrochemical water splitting. *Wuli Huaxue Xuebao/ Acta Phys. - Chim. Sin.* **33**, 80–102 (2017).

44. Sze, S. M. & Ng, K. K. Physics and Properties of Semiconductors-A Review. *Phys. Semicond. Devices* 5–75 (2006).

45. Marschall, R. Semiconductor composites: Strategies for enhancing charge carrier separation to improve photocatalytic activity. *Adv. Funct. Mater.* **24**, 2421–2440 (2014).

46. Peter, L. M., Wijayantha, K. G. U. & Tahir, A. A. Kinetics of light-driven oxygen evolution at α-Fe2O3 electrodes. *Faraday Discuss.* **155**, 309–322 (2012).

47. Zhao, B. *et al.* Electrical transport properties of Ti-doped Fe_2O_3(0001) epitaxial films. *Phys. Rev. B - Condens. Matter Mater. Phys.* **84**, 1–9 (2011).

48. Hahn, N. T. & Mullins, C. B. Photoelectrochemical performance of nanostructured Ti- and Sn-doped α-Fe2O3 photoanodes. *Chem. Mater.* **22**, 6474–6482 (2010).

49. Shinde, S. S., Bansode, R. A., Bhosale, C. H. & Rajpure, K. Y. Physical properties of hematite α-Fe_2O_3 thin films: Application to photoelectrochemical solar cells. *J. Semicond.* **32**, (2011).

50. Ling, Y. *et al.* The Influence of Oxygen Content on the Thermal Activation of Hematite Nanowires. *Angew. Chemie* **124**, 4150–4155 (2012).

51. Yang, T. Y. *et al.* A new hematite photoanode doping strategy for solar water splitting: Oxygen vacancy generation. *Phys. Chem. Chem. Phys.* **15**, 2117–2124 (2013).

52. Fang, L., You, L. & Liu, J.-M. Ferroelectrics in Photocatalysis. *Ferroelectr. Mater. Energy Appl.* 265–309 (2018).

53. Cummings, C. Y., Marken, F., Peter, L. M., Wijayantha, K. G. U. & Tahir, A. A. New Insights into Water Splitting at Mesoporous a-Fe_2O_3 Films: A study by Modulated Transmittance and Impedance Spectroscopies. *J. Am. Chem. Soc.* **134**, 1228–1234 (2012).

54. Kay, A., Cesar, I. & Grätzel, M. New benchmark for water photooxidation by nanostructured α-Fe_2O_3 films. *J. Am. Chem. Soc.* **128**, 15714–15721 (2006).

55. Tamirat, A. G., Rick, J., Dubale, A. A., Su, W. N. & Hwang, B. J. Using hematite for photoelectrochemical water splitting: A review of current progress and challenges. *Nanoscale Horizons* **1**, 243–267 (2016).

56. Hisatomi, T. *et al.* Enhancement in the performance of ultrathin hematite photoanode for water splitting by an oxide underlayer. *Adv. Mater.* **24**, 2699–2702 (2012).

57. Hwang, Y. J., Boukai, A. & Yang, P. High density n-S/n-TiO_2 core/shell nanowire arrays with enhanced photoactivit. *Nano Lett.* **9**, 410–415 (2009).

58. Sivula, K. Metal oxide photoelectrodes for solar fuel production, surface traps, and catalysis. *J. Phys. Chem. Lett.* **4**, 1624–1633 (2013).

59. Tilley, S. D., Cornuz, M., Sivula, K. & Grätzel, M. Light-inducedwater splitting with hematite: Improved nanostructure and iridium oxide catalysis. *Angew. Chemie - Int. Ed.* **49**, 6405–6408 (2010).

60. Riha, S. C. *et al.* Atomic layer deposition of a submonolayer catalyst for the enhanced photoelectrochemical performance of water oxidation with hematite. *ACS Nano* **7**, 2396–2405 (2013).

61. Du, C. *et al.* Hematite-based water splitting with low turn-on voltages. *Angew. Chemie - Int. Ed.* **52**, 12692–12695 (2013).

62. Steier, L. *et al.* Understanding the role of underlayers and overlayers in thin film hematite photoanodes. *Adv. Funct. Mater.* **24**, 7681–7688 (2014).

63. Le Formal, F., Sivula, K. & Grätzel, M. The transient photocurrent and photovoltage behavior of a hematite photoanode under working conditions and the influence of surface treatments. *J. Phys. Chem. C* **116**, 26707–26720 (2012).

64. Le Formal, F. *et al.* Passivating surface states on water splitting hematite photoanodes with alumina overlayers. *Chem. Sci.* **2**, 737–743 (2011).

65. Lines, M. E. & Glass, A. M. Principles and Applications of Ferroelectrics and Related Materials. (Oxford University Press, 1997).

66. Valasek, J. Piezo-Electric and Allied Phenomena in Rochelle Salt. *Phys. Rev.* **17**, (1921).

67. Kao, C. K. Ferroelectrics, Piezoelectrics, and Pyroelectrics. in *Dielectric Phenomena in Solids* 213–282 (Elsevier Inc., 2004).

68. David S. Schmool. Dielectric Materials. in Solid State Physics - From the Material Properties of Solids to Nanotechnologies 447–482 (2016).

69. Whatmore, R. Ferroelectric Materials. in *Springer Handbook of Electronic and Photonic Materials* (eds. Kasap, S. & Capper, P.) 589–614 (Springer International Publishing, 2017). doi:10.1007/978-3-319-48933-9.

70. Valasek, J. Piezoelectric and Allied Phenomena in Rochelle Salt. *Phys. Rev.* **15**, 537–538 (1920).

71. Vilarinho, P. Functional Materials : Properties , Processing and Applications. (2005).

72. Conklin, D., Park, T. H., Nanayakkara, S., Therien, M. J. & Bonnell, D. A. Controlling polarization dependent reactions to fabricate multi-component functional nanostructures. *Adv. Funct. Mater.* **21**, 4712–4718 (2011).

73. Tiwari, D. & Dunn, S. Photochemistry on a polarisable semi-conductor: What do we understand today? *J. Mater. Sci.* **44**, 5063–5079 (2009).

74. Zhao, D. *et al.* Depolarization of multidomani ferroelectric materials. *Nat. Commun.* 1–11 (2019) doi:10.1038/s41467-019-10530-4.

75. Eng, L. M. Nanoscale domain engineering and characterization of ferroelectric domains. *Nanotechnology* **10**, 405–411 (1999).

76. Sharma, S., Kumar, R., Talha, M. & Vaish, R. Design of spatially varying electrical poling for enhanced piezoelectricity in $Pb(Mg_{1/3}Nb_{2/3})O_3$–$0.35PbTiO_3$. *Int. J. Mech. Mater. Des.* **17**, 99–118 (2021).

77. Briscoe, J. & Dunn, S. Piezoelectricity and Ferroelectricity. in *Piezoelectricity and Ferroelectricity* vol. 3 3–17 (2014).

78. Yang, W. *et al.* Ferroelectric Polarization-Enhanced Photoelectrochemical Water Splitting in TiO_2-$BaTiO_3$ Core-Shell Nanowire Photoanodes. *Nano Lett.* **15**, 7574–7580 (2015).

79. Dunn, S. & Tiwari, D. Influence of ferroelectricity on the photoelectric effect of LiNbO3. *Appl. Phys. Lett.* **93**, 2006–2009 (2008).

80. Höfer, A. *et al.* Persistence of surface domain structures for a bulk ferroelectric above T C. *Phys. Rev. Lett.* **108**, 1–4 (2012).

81. Akdogan, E. K., Rawn, C. J., Porter, W. D., Payzant, E. A. & Safari, A. Size effects in $PbTiO_3$ nanocrystals: Effect of particle size on spontaneous polarization and strains. *J. Appl. Phys.* **97**, (2005).

82. Frey, M. & Payne, D. Grain-size effect on structure and phase transformations for barium titanate. *Phys. Rev. B - Condens. Matter Mater. Phys.* **54**, 3158–3168 (1996).

83. Polking, M. J. *et al.* Ferroelectric order in individual nanometre-scale crystals. *Nat. Mater.* **11**, 700–709 (2012).

84. Shih, W. Y., Shih, W. H. & Aksay, I. A. Size dependence of the ferroelectric transition of small $BaTiO_3$ particles: Effect of depolarization. *Phys. Rev. B* **50**, 15575–15585 (1994).

85. Gruverman, A. & Kholkin, A. Nanoscale ferroelectrics: Processing, characterization and future trends. *Reports Prog. Phys.* **69**, 2443–2474 (2006).

86. Giocondi, J. L. & Rohrer, G. S. Spatial separation of photochemical oxidation and reduction reactions on the surface of ferroelectric $BaTiO_3$. *J. Phys. Chem. B* **105**, 8275–8277 (2001).

87. Giocondi, J. L. & Rohrer, G. S. Spatially Selective Photochemical Reduction of Silver on the Surface of Ferroelectric Barium Titanate. *Chem. Mater.* **13**, 241–242 (2001).

88. Cui, Y., Briscoe, J. & Dunn, S. Effect of ferroelectricity on solar-light-driven photocatalytic activity of $BaTiO_3$ - Influence on the carrier separation and stern layer formation. *Chem. Mater.* **25**, 4215–4223 (2013).

89. Giocondi, J. L. & Rohrer, G. S. The influence of the dipolar field effect on the photochemical reactivity of $Sr_2Nb_2O_7$ and $BaTiO_3$ microcrystals. *Top. Catal.* **49**, 18–23 (2008).

90. Bhardwaj, A., Burbure, N. V., Gamalski, A. & Rohrer, G. S. Composition dependence of the photochemical reduction of ag by Ba 1-xSrxTiO3. *Chem. Mater.* **22**, 3527–3534 (2010).

91. Jones, P. M. & Dunn, S. Photo-reduction of silver salts on highly heterogeneous lead zirconate titanate. *Nanotechnology* **18**, (2007).

92. Liu, X., Kitamura, K., Terabe, K., Hatano, H. & Ohashi, N. Photocatalytic nanoparticle deposition on LiNbO3 nanodomain patterns via photovoltaic effect. *Appl. Phys. Lett.* **91**, 1–4 (2007).

93. Schultz, A. M., Zhang, Y., Salvador, P. A. & Rohrer, G. S. Effect of crystal and domain orientation on the visible-light photochemical reduction of Ag on $BiFeO_3$. *ACS Appl. Mater. Interfaces* **3**, 1562–1567 (2011).

94. Burbure, N. V., Salvador, P. A. & Rohrer, G. S. Photochemical reactivity of titania films on $BaTiO_3$ substrates: Influence of titania phase and orientation. *Chem. Mater.* **22**, 5831–5837 (2010).

95. Morris, M. R., Pendlebury, S. R., Hong, J., Dunn, S. & Durrant, J. R. Effect of Internal Electric Fields on Charge Carrier Dynamics in a Ferroelectric Material for Solar Energy Conversion. *Adv. Mater.* 7123–7128 (2016).

96. Su, R. *et al.* Silver-modified nanosized ferroelectrics as a novel photocatalyst. *Small* **11**, 202–207 (2015).

97. Gao, F. *et al.* Visible-light photocatalytic properties of weak magnetic $BiFeO_3$ nanoparticles. *Adv. Mater.* **19**, 2889–2892 (2007).

98. Fujisawa, J. ichi, Eda, T. & Hanaya, M. Comparative study of conduction-band and valence-band edges of TiO_2, $SrTiO_3$, and $BaTiO_3$ by ionization potential measurements. *Chem. Phys. Lett.* **685**, 23–26 (2017).

99. Nasby, R. D. & Quinn, R. K. Photoassisted electrolysis of water using a $BaTiO_3$ electrode. *Mater. Res. Bull.* **11**, 985–992 (1976).

100. Khan, M. A., Nadeem, M. A. & Idriss, H. Ferroelectric polarization effect on surface chemistry and photo-catalytic activity: A review. *Surf. Sci. Rep.* **71**, 1–31 (2016).

101. Ji, W., Yao, K., Lim, Y. F., Liang, Y. C. & Suwardi, A. Epitaxial ferroelectric $BiFeO_3$ thin films for unassisted photocatalytic water splitting. *Appl. Phys. Lett.* **103**, 1–5 (2013).

102. Cao, D., Wang, Z., Wen, L., Mi, Y. & Lei, Y. Switchable Charge-Transfer in the Photoelectrochemical Energy-Conversion Process of Ferroelectric $BiFeO_3$ Photoelectrodes. *Angew. Chemie - Int. Ed.* 1–6 (2014).

103. Rioult, M. *et al.* Tailoring the photocurrent in $BaTiO_3$/Nb:$SrTiO_3$ photoanodes by controlled ferroelectric polarization. *Appl. Phys. Lett.* **107**, 1–5 (2015).

104. Li, S. *et al.* Manipulation of charge transfer in vertically aligned epitaxial ferroelectric $KNbO_3$ nanowire array photoelectrodes. *Nano Energy* **35**, 92–100 (2017).

105. Singh, S., Sangle, A. L., Wu, T., Khare, N. & MacManus-Driscoll, J. L. Growth of Doped $SrTiO_3$ Ferroelectric Nanoporous Thin Films and Tuning of Photoelectrochemical Properties with Switchable Ferroelectric Polarization. *ACS Appl. Mater. Interfaces* **11**, 45683–45691 (2019).

106. Giocondi, J. L. & Rohrer, G. S. Spatial separation of photochemical oxidation and reduction reactions on the surface of ferroelectric $BaTiO_3$. *J. Phys. Chem. B* **105**, (2001).

107. Burbure, N. V., Salvador, P. A. & Rohrer, G. S. Influence of dipolar fields on the photochemical reactivity of thin titania films on $BaTiO_3$ substrates. *J. Am. Ceram. Soc.* **89**, 2943–2945 (2006).

108. Inoue, Y., Sato, K. & Suzuki, S. Polarization effects upon adsorptive and catalytic properties. 2. Surface electrical conductivity of NiO deposited on $LiNbO_3$ and its changes upon gas adsorption. *J. Phys. Chem.* **89**, 2827–2831 (1985).

109. Li, L. *et al.* Visible Light Photochemical Activity of Heterostructured $PbTiO_3/TiO_2$ core-shell particles. *J. Mater. Chem. C* **3**, 10715–10722 (2015).

110. Li, L., Liu, X., Zhang, Y., Salvador, P. A. & Rohrer, G. S. Heterostructured $(Ba,Sr)TiO_3/TiO_2$ core/shell photocatalysts: Influence of processing and structure on hydrogen production. *Int. J. Hydrogen Energy* **38**, 6948–6959 (2013).

111. Yang, W. *et al.* Ferroelectric Polarization-Enhanced Photoelectrochemical Water Splitting in TiO_2-$BaTiO_3$ Core-Shell Nanowire Photoanodes. *Nano Lett.* **15**, 7574–7580 (2015).

112. Cui, Y., Briscoe, J., Wang, Y., Tarakina, N. V. & Dunn, S. Enhanced Photocatalytic Activity of Heterostructured Ferroelectric $BaTiO_3/\alpha$-Fe_2O_3 and the Significance of Interface Morphology Control. *ACS Appl. Mater. Interfaces* **9**, 24518–24526 (2017).

113. Zhu, C., Chen, Z., Zhong, C. & Lu, Z. Facile synthesis of - $BiFeO_3$ nanosheets with enhanced visible-light photocatalytic activity. *J. Mater. Sci. Mater. Electron.* **29**, 4817–4829 (2018).

114. Zhang, Y., Schultz, A. M., Salvador, P. A. & Rohrer, G. S. Spatially selective visible light photocatalytic activity of $TiO_2/BiFeO_3$ heterostructures. *J. Mater. Chem.* **21**, 4168–4174 (2011).

115. Li, S., Lin, Y. H., Zhang, B. P., Li, J. F. & Nan, C. W. $BiFeO_3/TiO_2$ core-shell structured nanocomposites as visible-active photocatalysts and their optical response mechanism. *J. Appl. Phys.* **105**, 3–8 (2009).

116. He, X. *et al.* Novel Fe_2O_3/PZT nanorods for ferroelectric polarization-enhanced photoelectrochemical water splitting. *Energy and Fuels* **34**, 16927–16935 (2020).

117. Vijatović, M. M., Bobić, J. D. & Stojanović, B. D. History and challenges of barium titanate: Part I. *Sci. Sinter.* **40**, 155–165 (2008).

118. Smith, M. B., Page, K., Siegrist, T. & Et, A. Crystal structure and the paraelectric-to-ferroelectric phase transition of nanoscale $BaTiO_3$. *J. Am. Chem. Soc.* **130**, 6955–6963 (2008).

119. Suzuki, K. & Kijima, K. Optical band gap of barium titanate nanoparticles prepared by RF-plasma chemical vapor deposition. *Japanese J. Appl. Physics, Part 1 Regul. Pap. Short Notes Rev. Pap.* **44**, 2081–2082 (2005).

120. Sharma, H. B. Structural and optical properties of sol-gel derived barium titanate thin film. *Int. J. Mod. Phys. B* **21**, 1837–1849 (2007).

121. M. Acosta, N. Novak, V. Rojas, S. Patel, R. Vaish, J. Koruza, G. A. Rossetti Jr., J. Rödel, *Applied Physics Reviews* **4**, 041305 (2017).

122. Karvounis, A., Timpu, F., Vogler-Neuling, V. V., Savo, R. & Grange, R. Barium Titanate Nanostructures and Thin Films for Photonics. *Adv. Opt. Mater.* **8**, (2020).

123. Kennedy, J. H. & Frese, K. W. Photooxidation of Water at α-Fe_2O_3 Electrodes. *J. Electrochem. Soc.* **125**, 709–714 (1978).

124. Sivula, K., Le Formal, F. & Grätzel, M. Solar water splitting: Progress using hematite (α-Fe_2O_3) photoelectrodes. *ChemSusChem* **4**, 432–449 (2011).

3 EXPERIMENTAL METHODS

3.1 Materials preparation and methods

3.1.1 Barium Titanate thin films

3.1.1.1 Nanostructured Barium Titanate thin film growth

Nanostructured Barium Titanate (BTO) thin films were prepared by hydrothermal conversion of amorphous sol-gel TiO_2 in BTO thin films[1,2]. The hydrothermal conversion of TiO_2 into crystalline $BaTiO_3$ thin films involves dissolution-precipitation reactions and ion diffusion (Ba^{2+}, OH^-) at the same time. The hydrothermal reaction mechanism can be summarized as follows:

$$\boldsymbol{Ba^{2+} + TiO_2 + 2OH^- \rightleftharpoons BaTiO_3 + H_2O} \quad 3.1$$

where Ti^{4+} ions in the TiO_2 film react with Ba^{2+} and OH^- ions present in the alkaline solution until an equilibrium is reached between the $BaTiO_3$ thin films and TiO_2 films[3].

The synthesis of nanostructured BTO thin films comprises the following steps: (1) preparation of $Ba(OH)_2$ and TiO_2 precursor solutions, (2) amorphous sol-gel TiO_2 thin films deposition, (3) hydrothermal treatment.

3.1.1.1.1 Preparation of $Ba(OH)_2$ and TiO_2 precursor solutions

Hereafter, all chemicals were purchased from Sigma-Aldrich unless otherwise stated. 0.25 M, 0.3 M, 0.4 M $Ba(OH)_2 \cdot 8H_2O$ precursor solutions (pH ≥ 12) were prepared by dissolving 27.76 g, 33.31 g and 44.41 g respectively in 352 ml of deionized (DI) water at room temperature (RT) under stirring. TiO_2 precursor solution was prepared from titanium isopropoxide (0.2 M) solution in ethanol, with the addition of HCl (0.02 M) at RT under stirring.

3.1.1.1.2 Amorphous sol-gel TiO_2 thin film deposition

In this thesis, fluorine-doped tin oxide coated float glass (Sigma Aldrich, SKU 735167-1EA, L × W × thickness 300 mm × 300 mm × 2.2 mm, surface resistivity ~7 Ω/sq) is used as a substrate for film deposition. Before the deposition process, 1×2 cm^2 FTO glass substrates were sonicated sequentially in deionized (DI) water, acetone, and 2-propanol for 15 minutes each. Between each step, FTO glass substrates were blown with nitrogen, to remove any possible dust/particulates deposited. After that, the prepared TiO_2 precursor solution was deposited by spin-coating on FTO glass at 4000 rpm for 30 s and subsequently, the TiO_2 gel films were prebaked at 120 °C for 10 min. This procedure was repeated to obtain two, five and seven layers of TiO_2 gel films. The prebaking temperature of TiO_2 gel films is important for the successful preparation of $BaTiO_3$ thin films: it has been reported that when the prebaking temperature is above 250 °C, the TiO_2 films seem not successfully crystallized and therefore not suited for hydrothermal reaction[2].

3.1.1.1.3 Hydrothermal treatment

The amorphous sol-gel TiO_2 films were held vertically on a dedicated sample holder for this hydrothermal reaction and then set into a Teflon vessel. After that, the $Ba(OH)_2$ solution was poured into the Teflon vessel, which was then placed in the stainless steel autoclave reactor. The latter was transferred into an electric oven (Memmert) for the hydrothermal treatment at 210 °C for 3 h. After the holding period, the heater was switched off and the autoclave reactor was cooled down at room temperature (RT). Then, the BTO thin films were rinsed in boiling DI water and then they were washed with ethanol and dried with compressed air.

3.1.1.2 Porous Barium Titanate thin films preparation process

Considering that the morphology of the as-prepared nanostructured BTO thin films was not easily controlled as well as the photocatalytic performance of such films was low as discussed in Chapter 4, a second approach was adopted to prepare porous Barium Titanate (pBTO) thin films. Porous Barium Titanate (pBTO) thin films were synthesized by a soft template-assisted sol-gel method[4,5]. The preparation of pBTO thin films involves the following 3 steps: (1) preparation of precursor solution, (2) thin films deposition and (3) thermal treatment.

3.1.1.2.1 Preparation of precursor solution

To prepare pBTO precursor solutions, different quantities of block copolymer (BCP) Pluronic-P123 (0.2 g, 2 g, 3.5 g, 5 g; BASF Corporation) were dissolved in absolute ethanol (3.8 ml) at 40°C, under stirring. Then, barium acetate (0.46 g); (Thermo Fisher Scientific) was added into glacial acetic acid (3 ml); (Thermo Fisher Scientific) at 50°C under stirring, until complete solubilisation. After the solution was cooled down to RT,

an equimolar amount of titanium butoxide (0.61 g) was added dropwise to the barium acetate solution. The solution was kept stirring for 30 min at RT. After the Pluronic-P123 solution was cooled down to RT, it was added dropwise under stirring to obtain the final solution. The mixture was kept stirring for 1h at RT.

3.1.1.2.2 Thin film deposition

Before the deposition process, 1×2 cm^2 FTO glass substrates were cleaned using the procedure reported in 3.1.1.1.2. To prevent charge recombination at the interface between the pBTO layer and FTO glass[6], pBTO thin films were grown on compact titanium dioxide ($cTiO_2$) used as a blocking layer. TiO_2 precursor solution was prepared using the procedure detailed in 3.1.1.1.1. The as-prepared TiO_2 precursor solution was deposited by spin-coating (4000 rpm, 30 s) and it was heated up at 120 °C for 10 min and then 500 °C for 30 min[1]. After the deposition of the $cTiO_2$ layer on FTO substrates, 70 µl of the prepared barium titanate precursor solutions were deposited by spin-coating on FTO glass at 500 rpm, 5 s (1^{st} step) and then 3000 rpm, 30 s (2^{nd} step), successively. In this thesis, a digitally-controlled spin coater (G3P Spin Coater, Specialty Coating Systems Inc.) was used, equipped with a vacuum specimen stage to secure the substrate during spinning and a control system to program spin velocity and duration.

3.1.1.2.3 Thermal treatment

After the deposition process, the thermal treatment was performed to convert the as-deposited gel-thin films into crystallized pBTO thin films. The thermal treatment process comprises three steps: (1) Drying, (2) Pyrolysis (3) Sintering[7]. The drying process involves the evaporation of the solvent by spin-coating and heating. After that, the pyrolysis step at a higher temperature is necessary to remove all the polymers in the

material before crystallization to limit the formation of defects in the films. During the sintering step which requires a higher temperature than pyrolysis, the amorphous films are transformed into crystallized films through the nucleation-and-growth process[8].

In this thesis, after spin-coating deposition, the thin films obtained were placed on a hot plate at 90 °C for 1 min for drying and then 350 °C for 4 min for pyrolysis. Afterwards, they were cooled down at RT. Then, the thin films were transferred into a box furnace (Lenton Furnace, model UAF 14/5) and annealed at 750 °C for 10 min for the crystallization into BTO and then cooled to 30 °C, with a ramp rate of 5 °C/min.

The same procedure was also used for the synthesis of pBTO thin films using different atmospheres. In this case, the pBTO thin films were annealed in O_2, air or N_2 conditions in a tube furnace (Lenton Furnace, model LTF 12/100/940) at 750 °C for 10 min and then cooled down at RT at 30 °C, with a ramp rate of 5 °C/min and controlling the gas flow (2 L/min).

3.1.2 Hematite-Barium Titanate nanocomposite thin films

3.1.2.1 Hydrothermal growth of hematite Nanorods on porous Barium Titanate

In this thesis, pBTO-5 thin films, synthesized by the soft template-assisted sol-gel method detailed in 3.1.1.2, were used as substrates for the hydrothermal growth of hematite (Fe_2O_3) nanorods, which were prepared by Qian Guo, PhD student from Dr Ana Sobrido's research group. For the synthesis of hematite nanorods, the obtained pBTO thin films were placed in an autoclave reactor, containing 0.15 M of $FeCl_3$ and 1 M $NaNO_3$ solution. Then, the autoclave reactor was transferred into an oven and heated up at 100 °C for 1 h. After cooling down at RT, the as-prepared FeOOH deposited pBTO-5 samples were

thoroughly rinsed with DI water followed by annealing at 800 °C for 10 min with a speed rate of 10 °C/min to convert the FeOOH into hematite. The same experimental procedure is used for the preparation of hematite thin films on FTO glass as a substrate, which are be used as control samples in this thesis.

3.1.3 Sample abbreviations

To identify the different samples produced in this section and described in more detail in the following chapters, the sample notation is illustrated in Table 3.1.

Table 3.1 List of the samples used in this thesis with the relative notation assigned.

Material	Notation	Description
Nanostructured $BaTiO_3$	0.25 M BTO	0.25 M $Ba(OH)_2$, 1 layer of TiO_2
	0.3 M BTO	0.3 M $Ba(OH)_2$, 1 layer of TiO_2
	0.4 M BTO	0.4 M $Ba(OH)_2$, 1 layer of TiO_2
	0.25 M BTO-2L	0.25 M $Ba(OH)_2$, 2 layers of TiO_2
	0.25 M BTO-5L	0.25 M $Ba(OH)_2$, 5 layers of TiO_2
	0.25 M BTO-7L	0.25 M $Ba(OH)_2$, 7 layers of TiO_2
Porous $BaTiO_3$	pBTO-0.2	0.2 g BCP, $cTiO_2$
	pBTO-2	2 g BCP, $cTiO_2$
	pBTO-3.5	3.5 g BCP, $cTiO_2$
	pBTO-5	5 g BCP, $cTiO_2$
	pBTO-air	5 g BCP, $cTiO_2$, air ambient
	pBTO-N_2	5 g BCP, $cTiO_2$, N_2 ambient
	pBTO-O_2	5 g BCP, $cTiO_2$, O_2 ambient
Fe_2O_3	Fe_2O_3/pBTO-5	Fe_2O_3, 5 g BCP, $cTiO_2$
	Fe_2O_3	Bare Fe_2O_3

3.1.4 Electrochemical (EC) poling pretreatment

In this thesis, all the thin films prepared were used as photoanodes. Thus, to investigate the effect of ferroelectric polarization on their photoelectrochemical performance, electrochemical (EC) poling pretreatment was carried out on pBTO thin films and Fe_2O_3/pBTO-5 samples using a two-electrodes cell configuration: the sample and a platinum wire were used as the working electrode (WE) and counter electrode (CE), respectively.

The choice of the voltage value to apply for the EC poling depends on the coercive field of the ferroelectric material. However, it is necessary to consider that eventual potential losses can be experienced because the external field is not directly applied between the surface and the bottom of the ferroelectric thin film. Recently, it has been demonstrated that macroscopic poling of $BiFeO_3$ thin films is obtained by applying poling potentials higher than 5 V[9]. Thus, for macroscopic poling, an electrolyte with a large electrochemical window is required, where no chemical reactions are observed in a potential range [-10 V, +10 V]. Therefore, in this thesis, the EC poling was conducted in a non-aqueous electrolyte solution (0.1 M $LiClO_4$ in propylene carbonate) using a two-electrodes cell, where the sample and platinum electrode were used as the working and counter electrodes respectively. Potentials of +8 V/-8 V were alternatively applied on the platinum electrode for 5 steps (10 s each) using a Keithley 2400 source-measure unit to apply the voltage, while the sample was held at 0 V. The last potential was +8 V or -8 V to obtain a remnant $\mathbf{P}_{down}$ or $\mathbf{P}_{up}$, respectively. The +/-8 V applied voltage was selected according to previous research works[10,11], where ferroelectric films prepared in similar conditions were poled using the above voltage. It should be noted that it is difficult to

know the precise electric field that is applied across the film itself in these conditions, since there will be voltage drops across the electrolyte, interfaces, etc. The current flow between the sample and counter electrode was monitored to be not higher than 1 mA to avoid damaging the sample[10,11]. The schematic of the EC poling procedure used in this thesis is illustrated in Figure 3.1. After EC poling, the thin films were washed with DI water, acetone, and ethanol and dried in air before performing Linear Sweep Voltammetry (LSV) measurements.

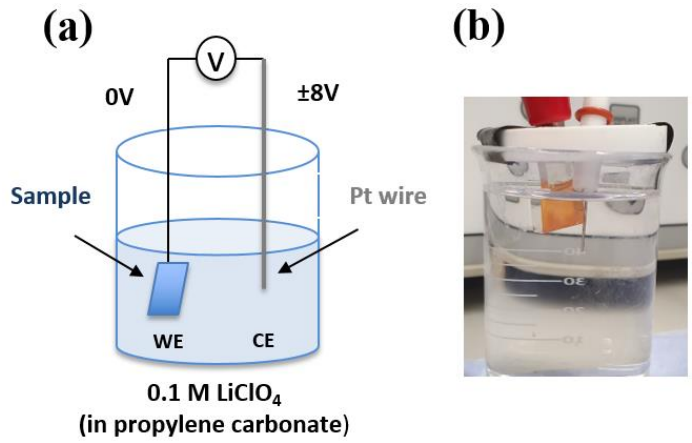

Figure 3.1 (a) Schematic of the method used for the EC poling of ferroelectric thin films and (b) relative picture of the system used in this thesis.

3.2 Material Characterization Techniques

3.2.1 Scanning Electron Microscopy

The morphology of all BTO samples, H/pBTO-5 and bare H thin films was investigated by scanning electron microscopy (SEM) on an FEI Inspect F, using an accelerating voltage of 5 kV. Both top view and cross-sectional view were acquired for all thin films. For the top view imaging, the samples were fixed onto a steel stub with a sticky double-

sided copper tape, which increases conductivity. The conductive edge of FTO glass was then connected to the copper tape. No further conductive film coating was necessary for these samples. For cross-sectional view characterization, the samples were mounted vertically on a steel stub, using sticky copper tape. This stub is equipped with a small set screw to hold the samples in the vertical position. Silver paint was additionally applied to ensure conductivity. In this case, to avoid charge buildup on the samples' surface, a palladium/gold coating was applied on the thin films in a sputter coater.

The thickness measurements from all SEM cross-sectional images of all BTO thin films, Fe_2O_3/pBTO-5 and Fe_2O_3 samples were obtained using ImageJ analysis. Moreover, the estimation of porosity in pBTO thin films from SEM images was also obtained using ImageJ analysis software, where the pore area was isolated by thresholding[12].

An energy-dispersive X-ray (EDX) spectrometer was used for elementary composition analysis of pBTO thin films, Fe_2O_3/pBTO-5 and Fe_2O_3 samples.

3.2.2 Spectroscopic Ellipsometry

To determine the overall porosity of pBTO thin films, spectroscopic ellipsometry (SE) measurements were carried out on a Semilab SE2000 ellipsometer. To perform this analysis, pBTO samples were prepared using the procedure reported in 3.1.1.2 but the films were deposited on a Si substrate without a compact TiO_2 blocking layer.

Before SE measurements, samples were placed on a hot plate (120 °C, 30 min) to remove any possible residual water molecules that remained in the pores. Application of a Bruggeman effective medium approximation (EMA) allowed accurate determination of the overall porosity of each pBTO sample[13]. To confirm ambient porosity calculations,

porous samples were infiltrated with water. Subsequently, SE measurements were fitted again using the same EMA but adding water instead of air as a medium material[14]. Absorption isotherms were obtained using an ellipsometric porosimetry chamber with controllable humidity. The Brunauer, Emmett and Teller (BET) fitting allowed the determination of the surface area for the different porosity $BaTiO_3$ samples presented here. All data analyses were performed using Semilabs SEA software (v1.6.2). The SE measurements and the relative data analysis were carried out at University College London (UCL) in the Department of Chemical Engineering, by Dr Alberto Alvarez Fernandez, Postdoctoral Research Associate in the Adaptive and Responsive Nanomaterials (AdReNa) research group.

3.2.3 X-ray Diffraction

The crystalline phase of all the samples reported in this thesis was investigated by X-ray Diffraction (XRD) using a PANalytical X'Pert Pro diffractometer, equipped with a Cu-Kα source, with 0.5° grazing incidence angle. The XRD measurements were obtained from 2ϑ = 20° to 70° with a scan speed of 0.006 °/s. The XRD measurement were carried out by Dr Richard Whiteley, XRD characterisation technician in the Department of Engineering and Materials Science at the Queen Mary University of London.

3.2.4 UV-vis spectroscopy

UV-vis spectroscopy refers to absorption spectroscopy as a function of wavelength, which gives information about the electronic transitions occurring in the sample[15].

The UV-vis spectra of all BTO samples, Fe_2O_3/pBTO-5 and Fe_2O_3 thin films, presented in this thesis, were measured using a Perkin Elmer Lambda 950 UV-vis

spectrophotometer with an integrating sphere. The spectra range was varied considering the material analysed. The optical bandgap (E_g) of all thin films was estimated using Tauc relation[16], which is known as:

$$\boldsymbol{\alpha h v = C\left(h v - E_g\right)^n} \quad 3.2$$

where C is a constant, α is absorption coefficient, *hv* is the incident photon energy, and n is related to the type of transition. The direct bandgap energy E_g of all BTO thin films, Fe_2O_3/pBTO-5 and Fe_2O_3 samples was determined by the extrapolated linear region of the plots at $(\alpha hv)^2 = 0$.

3.2.5 Raman spectroscopy

Raman spectroscopy is a spectroscopy technique based on inelastic or Raman scattering, which arises from the interaction between the incident photons and the phonons in the material. The difference in frequency between the incident and the scattered light gives information on vibrational, rotational and other low-frequency modes of a sample[17]. Thus, this technique is largely applied for the identification of molecules and chemical bonding as well as the study of phase transition in crystalline materials and the investigation of photoluminescence properties in semiconductors[18].

Raman spectroscopy measurements of all BTO thin films reported in this thesis were carried out on Renishaw inVia confocal Raman microscope, using 100 X objective and 442 nm as excitation wavelength. The Raman spectra were acquired after setting accumulation and acquisition time to 3 and 100 s, respectively, in the 100-1000 nm range.

3.2.6 X-ray Photoelectron Spectroscopy

X-ray Photoelectron Spectroscopy (XPS) is a quantitative spectroscopy technique that allows estimating the elemental composition, chemical and electronic state of the elements on the surface (up to 10 nm) of a material, upon X-ray irradiation under ultra-high vacuum (UHV). It is based on the photoemission process, where an electron is ejected from an atom after excitation by an incident photon, possessing energy at least equal to the binding energy (E_b) of the electron. The latter is known as photoelectron[17].

X-ray photoelectron spectroscopy (XPS) measurements of pBTO-air, pBTO-N_2, pBTO-O_2, Fe_2O_3/pBTO-5 and Fe_2O_3 thin films were conducted on Thermo Fisher Nexsa spectrometer, provided of monochromated Al Kα source and micro-focused to a spot size of 100 μm on the sample surface. The instrument was operated in constant analyser energy (CAE) mode. The survey and the high-resolution core-level spectra were recorded using a pass energy of 200 eV and 50 eV with a step size of 0.5 eV and 0.1 eV, respectively. To compensate for the surface charging during measurement, an electron flood gun was used. Data acquired were processed using Thermo Avantage software. Moreover, charge correction was carried out using surface adventitious carbon set to 284.8 eV.

3.2.7 Piezoresponse Force Microscopy

Piezoresponse force microscopy (PFM) is a technique developed for imaging and manipulation of ferroelectric materials at the nanoscale[19]. Figure 3.2 illustrates the standard experimental setup of PFM. During PFM measurements, a ferroelectric sample is placed between the bottom electrode and the conductive PFM tip, used as a movable top electrode. When an ac voltage is applied to the conductive tip, a periodic surface

volume change is produced in the material, inducing a force on the tip that is measured as a displacement of the PFM cantilever using a beam deflection system. This electromechanical (EC) response of the material surface constitutes the PFM response, expressed in terms of amplitude and phase, which are read out via the lock-in amplifier, as shown in Figure 3.2[20]. Specifically, the PFM amplitude and phase signals represent the magnitude of the piezoelectricity and the polarization direction, respectively[21].

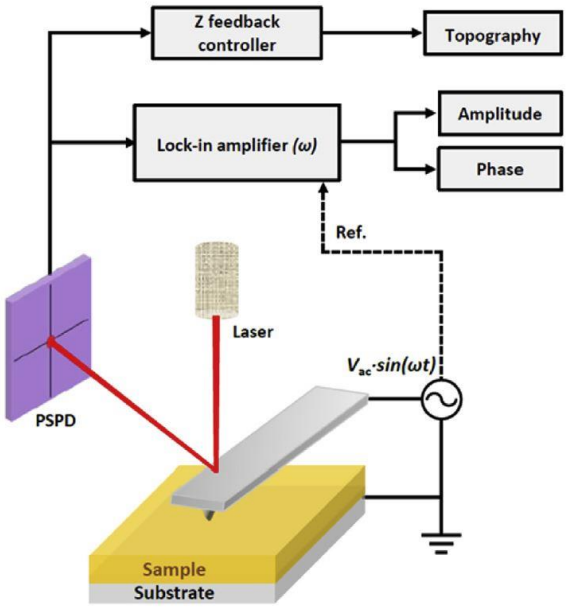

Figure 3.2 Schematic of PFM setup[20].

In this thesis, PFM images were recorded using Bruker Dimension IconXR atomic force microscope to investigate the ferroelectric domains of pBTO-0.2 and pBTO-5 thin films. PFM imaging was performed in Datacube mode (DCUBE PFM) by applying a DC voltage sweep to the tip going from -8 V to +8 V. DCUBE PFM height, phase, and amplitude signals of pBTO-0.2 and pBTO-5 were acquired off-resonance at 250 kHz and with 4 Vac. However, the PFM measurement is accurate only when the electrostatic force is zero, i.e. when the tip voltage = surface potential, therefore, hysteresis loops were

measured without electrostatic field artefacts by using Switching Spectroscopy PFM (SS-PFM) mode. SS-PFM mode allows highly accurate and sensitive characterization of a ferroelectric materials' properties at the nanoscale, reducing the electrostatic contributions that can arise using the standard PFM tecnique[22].

The acquisition of the hysteresis loops using SS-PFM involves applying a series of ('on-field') write voltage segments for each of several ('off-field') read voltages, as shown in Figure 3.3.

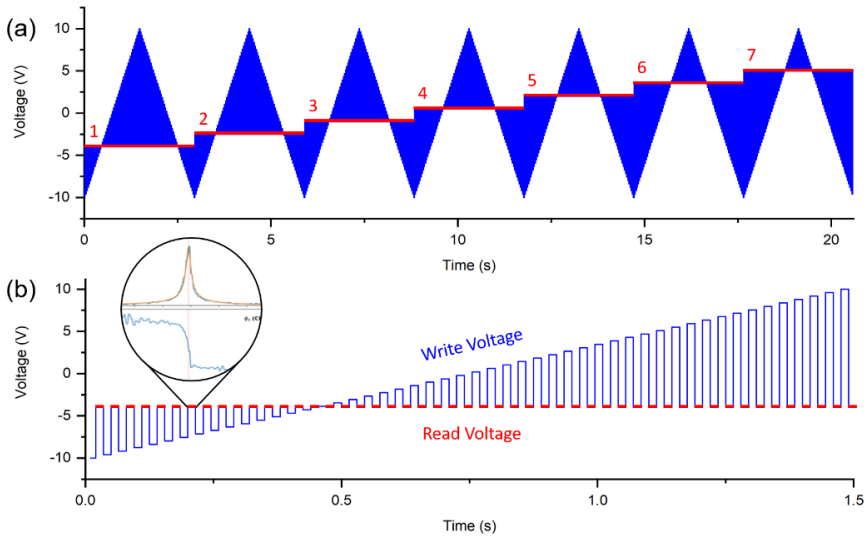

Figure 3.3 (a) The multi-segment SS-PFM script with 'write' (blue) and 'read' (red) steps. (b) For each 'read' voltage, a PFM hysteresis loop is extracted. The hysteresis loop at the sample's work function is the artefact-free one.

The purpose of the 'on-field' segments is to determine the voltage (between tip and sample) where the polarization state of the material changes. The 'off-field' segments allow characterization of the material response after each of the 'on-field' segments to look for the state change and measure the material response. By using a series of different

'off-field' voltages, it is possible to compensate for electrostatic field artefacts that arise due to the difference in contact potential between tip and sample. During each write and read voltage segment, the amplitude/phase *vs.* contact resonance frequency sweeps are performed. These are then fitted and peak amplitude, quality factor, and corresponding phase values are recorded. Plots of amplitude and phase *vs.* write voltage are extracted. The SS-PFM data were collected with minimum and maximum *write* voltage segments ranging from – 10 and +10 V, respectively, in 50 steps, going from low to high. The write time duration of each segment was 10 ms. The minimum and maximum *read* voltage segments ranged from – 4 and +5 V, respectively, in 7 steps, going from low to high. The read time duration of each segment was 20 ms.

All PFM measurements, including SS-PFM and the relative extrapolation of hysteresis loops, were carried out at Bruker in Coventry (UK) and Santa Barbara (CA) by Vishal Panchal, Bede Pittenger and Peter De Wolf.

3.2.8 Photoelectrochemical measurements

Photo-electrochemical (PEC) measurements, including Linear Sweep Voltammetry (LSV), Chronoamperometry and Mott-Schottky (MS), were conducted on all BTO thin films, Fe_2O_3/pBTO-5 and Fe_2O_3 samples using a PEC cell with a three-electrode configuration, which was connected to a potentiostat (Gamry Potentiostat Interface 1000). A solar simulator (Sciencetech, Class: ABA) was used for the illumination of all thin films. All the PEC measurements were taken at AM 1.5 G 1 sun (100 mV/cm^2). The experimental setup used for PEC testing is illustrated in Figure 3.4 a.

In this thesis, a large volume PEC cell was used, containing the selected sample as working electrode (WE), Ag/AgCl (Ag/AgCl, $E^0_{Ag/AgCl,\ sat'd\ KCl}$ = +0.197 V vs. NHE at 25 °C) or Hg/HgO ($E^0_{Hg/HgO,\ 1M\ NaOH}$ = +0.14 V vs. NHE at 25 °C) as reference electrode (RE), and a Pt wire as counter electrode (CE), immersed in 1 M NaOH solution (pH = 13.6) as electrolyte. Fe_2O_3 is usually stable at high pH, thus 1 M NaOH as basic electrolyte has been used in this thesis. Ag/AgCl RE is usually used in a wide range of pH values but the immersion in basic solutions over a long period can damage the electrode frit. Thus, in the last part of my PhD, Hg/HgO RE was used as it is more suitable for alkaline electrolytes. WE, RE, CE were connected to the potentiostat with the alligator clips (Figure 3.4 b). To connect the sample to the electrical circuit before PEC testing, a portion of FTO glass was left uncovered during the film deposition through the use of Kapton tape. For convenience, the samples were cut into 1x2 cm^2 pieces so a geometric surface area of 1 cm^2 was used for the illumination. Alternatively, a non-conductive epoxy resin was applied to delimitate the geometric surface area for illumination. The sample was then illuminated through a quartz window by the light flux coming from the lamp.

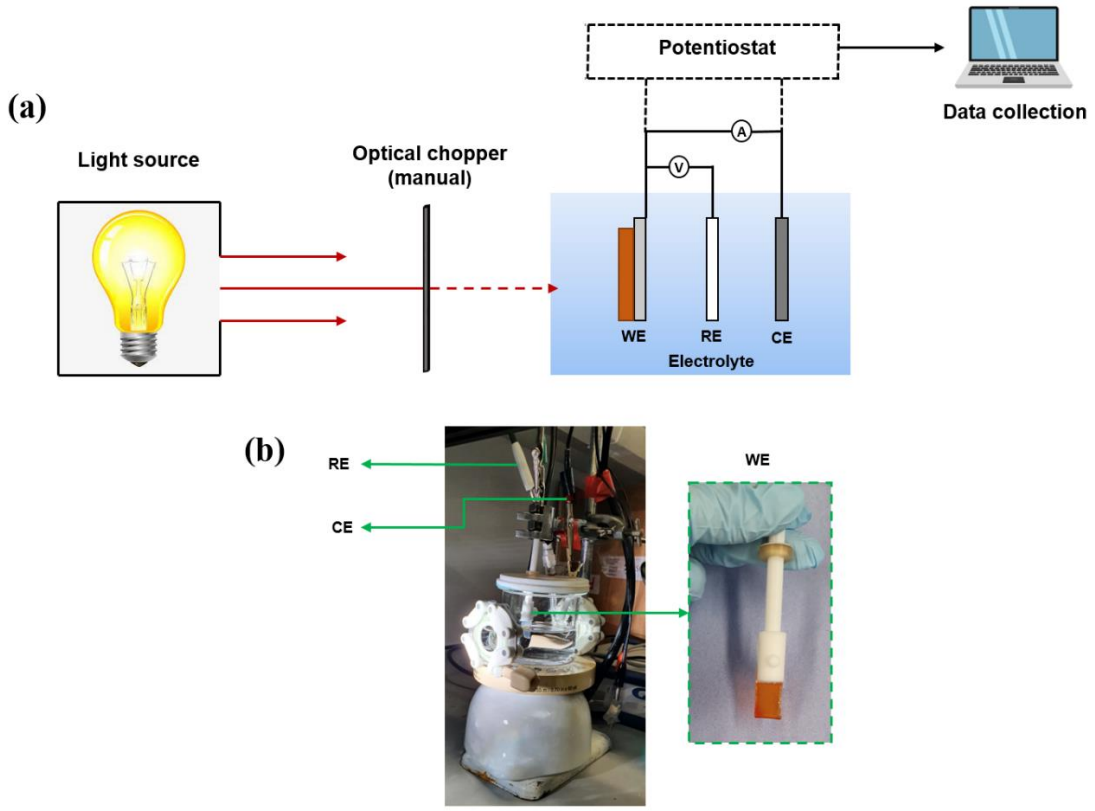

Figure 3.4 (a) Experimental setup used for PEC testing and (b) details of PEC cell.

To acquire LSV curves, the potential range was chosen according to the sample analysed and then it was swept at a rate of 10 mV/s. Chronoamperometry curves were measured under chopped illumination at the desired applied potential.

The charge separation yield of the photogenerated carriers ($P_{charge\ separation}$) and the charge injection yield to the electrolyte ($P_{charge\ injection}$) were calculated according to the following equation:

$$J_{H_2O} = J_{absorbed} \times P_{charge\ separation} \times P_{charge\ injection} \quad 3.3$$

Assuming that the charge injection yield is 100% ($P_{charge\ injection} = 1$) in the presence of a hole scavenger (H_2O_2), the photocurrent measured in the electrolyte with H_2O_2 ($J_{H_2O_2}$) can be expressed as follow:

$$\boldsymbol{J_{H_2O_2}} = \boldsymbol{J_{absorbed}} \times \boldsymbol{P_{charge\ separation}} \quad 3.4$$

Based on equations 3.3 and 3.4:

$$\boldsymbol{P_{charge\ injection}} = \frac{\boldsymbol{J_{H_2O}}}{\boldsymbol{J_{H_2O_2}}} \quad 3.5$$

$$\boldsymbol{P_{charge\ separation}} = \frac{\boldsymbol{J_{H_2O_2}}}{\boldsymbol{J_{absorbed}}} \quad 3.6$$

where J_{H_2O} is the photocurrent density in 1M NaOH, $J_{H_2O_2}$ is the photocurrent density in 1M NaOH + 0.5 M H_2O_2 and $\boldsymbol{J_{absorbed}}$ is the theoretical photocurrent density of the photoelectrode under standard AM 1.5 G solar illumination[23]. The value of $\boldsymbol{J_{absorbed}}$ was taken from ref[24].

3.2.8.1 Incident photon-to-current efficiency (IPCE)

The measurement and calculation of IPCE for bare Fe_2O_3 and Fe_2O_3/pBTO-5 were conducted by Chloe Forrester, PhD student from Joe Briscoe's research group. As introduced in 2.1.4, IPCE measurements are obtained by scanning the wavelength of a light source and then measuring the current increase from that monochromatized light at each wavelength point. Thus, the IPCE measurements were performed using a homemade PEEK (polyetheretherketone) cell with two quartz windows (area = 0.503 cm^2) held a three-electrode set-up: Ag/AgCl reference electrode, a Pt mesh counter electrode and the sample as working electrode. The Output photocurrent from the cell, obtained by using

chopped light and a lock-in amplifier, was plotted as a function of wavelength of incident light. A potential of 1.23 V vs RHE, corresponding to the oxidation potential of water, was applied by an Autolab (PG- STAT101, Metrohm) potentiostat. A 75 W xenon arc lamp was used as an illumination source which was modulated to the desired wavelength by a monochromator (OBB-2001, Photon Technology International). The intensity of incident light was measured with an optical power meter (PM 100, Thorlabs) fitted with a silicon photodiode (S120UV, Thorlabs) for wavelengths of 250-900 nm. The incident light at each calibrated wavelength was chopped three times to obtain an averaged steady-state photocurrent, which was calculated by subtracting the dark current from the total current. The IPCE as a function of incident wavelength was calculated using the equation already reported in Chapter 2.

REFERENCES

1. Tai, Q. *et al.* Efficient and stable perovskite solar cells prepared in ambient air irrespective of the humidity. *Nat. Commun.* **7**, 1–8 (2016).

2. Naoyama, T., Sakioka, Y., Noda, M., Okuyama, M. & Saito, K. A low temperature preparation of $BaTiO_3$ thin film by sol-gel-hydrothermal treatment below 210°C. *Japanese J. Appl. Physics*, **44**, 6873–6877 (2005).

3. Naoyama, T., Sakioka, Y., Noda, M., Okuyama, M. & Saito, K. A low Temperature preparation of $BaTiO_3$ thin film by Sol-Gel-Hydrothermal treatment below 210 °C. *Jpn. J. Appl. Phys.* **44**, 6873–6877 (2005).

4. Suzuki, N. *et al.* Chemical Synthesis of Porous Barium Titanate Thin Film and Thermal Stabilization of Ferroelectric Phase by Porosity-Induced Strain. *J. Vis. Exp.* 1–7 (2018).

5. Suzuki, N. *et al.* Synthesis of highly strained mesostructured $SrTiO_3/BaTiO_3$ composite films with robust ferroelectricity. *Chem. - A Eur. J.* **19**, 4446–4450 (2013).

6. Songtanasit, R., Taychatanapat, T. & Chatraphorn, S. Electrical Properties of Ultra-thin TiO_2 Compact Layer on FTO for Perovskite Solar cells. *J. Phys. Conf. Ser.* **901**, (2017).

7. Zhang, Q., Sando, D. & Nagarajan, V. Chemical route derived bismuth ferrite thin films and nanomaterials. *J. Mater. Chem. C* **4**, 4092–4124 (2016).

8. Schwartz, R., Schneller, T., Waser, R. & Dobberstein, H. Chemical solution deposition of ferroelectric thin films. *Chem. Process. Ceram. Second Ed.* **4756**, 713–742 (2005).

9. Cao, D., Wang, Z., Wen, L., Mi, Y. & Lei, Y. Switchable Charge-Transfer in the Photoelectrochemical Energy-Conversion Process of Ferroelectric $BiFeO_3$ Photoelectrodes. *Angew. Chemie - Int. Ed.* 1–6 (2014).

10. Rioult, M. *et al.* Tailoring the photocurrent in $BaTiO_3$/Nb:$SrTiO_3$ photoanodes by controlled ferroelectric polarization. *Appl. Phys. Lett.* **107**, 1–5 (2015).

11. Datta, S., Rioult, M., Stanescu, D., Magnan, H. & Barbier, A. Manipulating the ferroelectric polarization state of BaTiO3 thin films. *Thin Solid Films* **607**, 7–13 (2016).

12. Matějíček, J. *et al.* Alternative methods for determination of composition and porosity in abradable materials. *Mater. Charact.* **57**, 17–29 (2006).

13. Khardani, M., Bouaïcha, M. & Bessaïs, B. Bruggeman effective medium approach for modelling optical properties of porous silicon: comparison with experiment. *Phys. status solidi* **4**, 1986–1990 (2007).

14. Guldin, S. *et al.* Tunable mesoporous Bragg reflectors based on block-copolymer self-assembly. *Adv. Mater.* **23**, 3664–3668 (2011).

15. Chen, Z., Dinh, H. N. & Miller, E. Photoelectrochemical Water Splitting - Standards, Experimental Methods, and Protocols. Springer Briefs in Energy (2013).

16. Raciti, R. *et al.* Optical bandgap of semiconductor nanostructures : Methods for experimental data analysis. *J. Appl. Phys.* **121**, 1–9 (2017).

17. Joshi, M., Bhattacharyya, A. & Ali, S. W. Characterization techniques for nanotechnology applications in textiles. *Indian J. Fibre Text. Res.* **33**, 304–317 (2008).

18. Xu, Z. *et al.* Topic Review : Application of Raman Spectroscopy Characterization in Micro/Nano-machining. *Micromachines* **9**, 1–23 (2018).

19. Vasudevan, R. K., Balke, N., Maksymovych, P., Jesse, S. & Kalinin, S. V. Ferroelectric or non-ferroelectric: why so many materials exhibit ‘ferroelectricity’ on the nanoscale. *Appl. Phys. Rev.* **4**, 1–74 (2017).

20. Seol, D., Kim, B. & Kim, Y. Non-piezoelectric effects in piezoresponse force microscopy. *Curr. Appl. Phys.* **17**, 661–674 (2017).

21. Kalinin, S. V & Bonnell, D. A. Imaging mechanism of piezoresponse force microscopy of ferroelectric surfaces. *Phys. Rev. B* **65**, 1–11 (2002).

22. Jesse, S., Baddorf, A. P. & Kalinin, S. V. Switching spectroscopy piezoresponse force microscopy of ferroelectric materials. *Appl. Phys. Lett.* **88**, 1–4 (2006).

23. Liu, G. *et al.* A tantalum nitride photoanode modified with a hole-storage layer for highly stable solar water splitting. *Angew. Chemie - Int. Ed.* **53**, 7295–7299 (2014).

24. Murphy, A. B. *et al.* Efficiency of solar water splitting using semiconductor electrodes. *Int. J. Hydrogen Energy* **31**, 1999–2017 (2006).

4 DEVELOPMENT OF NANOSTRUCTURED BARIUM TITANATE THIN FILMS

PARTS OF THIS CHAPTER ARE REPRODUCED WITH PERMISSION FROM *ACS Appl. Mater. Interfaces* 2022, 14, 11, 13147–13157. COPYRIGHT 2022 AMERICAN CHEMICAL SOCIETY.

https://pubs.acs.org/doi/10.1021/acsami.1c17419

4.1 INTRODUCTION

One of the approaches that has been regularly adopted to improve photocatalytic activity is the fabrication of porous and nanostructured photoelectrodes. These materials present the advantage of high surface areas, which considerably enhance their reactivity at the

electrode/electrolyte interface and their light-harvesting capabilities[1,2]. Moreover, in general, at the nanoscale, a larger number of active surface sites are present at the surface of these photoelectrodes. This promotes an increase in the surface charge carrier transfer rate, which improves the overall photocatalytic performance[3].

As reported in Chapter 2, recent studies have also focused on the role of ferroelectric polarization in photo-electrocatalysis. Ferroelectric materials possess spontaneous polarization which can be reversibly switched by an external electric field[4]. This spontaneous polarization can induce opposite band-bending at the ferroelectric material's surface, facilitating electron-hole pairs' migration towards opposite directions. Thus, the spatially separated photogenerated carriers are able to participate in the oxidation and reduction reactions at different locations[5]. Indeed, it has been demonstrated that the ferroelectric phase of $BaTiO_3$ (BTO) induces the suppression of charge-carrier recombination, resulting in much higher carrier lifetimes[6].

Previous research works have reported that redox reactions can occur preferentially on the surface of $BaTiO_3$, $Pb(Zr,Ti)O_3$, and $LiNbO_3$ substrates[7–10]. For example, Giocondi *et al.*, have shown that the oxidation and reduction products of Pb^{2+} and Ag^{+} cations are selectively accumulated on the surface of BTO substrate in proximity of domains with opposite polarization[5]. This result demonstrates that the polarization from the ferroelectric substrate spatially separates charge carriers, creating consequently preferred reduction and oxidation sites. More recently, researchers have reported the enhancement of PEC performance in ferroelectric thin films with planar geometry[11–13] but only a small number of studies have focused on nanostructured ferroelectric thin films for PEC application[14–17]. Thus, this chapter discusses the impact of nanostructuring and porosity

on ferroelectric thin film photoelectrodes, which could be very favourable in photo-electrocatalysis.

Two different fabrication methods were tried to develop nanostructured BTO thin films as photoanodes. Firstly, the hydrothermal conversion of TiO_2 to BTO was used. The idea was to achieve a full morphology control of BTO nanostructure (e.g., size/shape/spacing, film thickness) for the combination of this ferroelectric film with a more efficient photocatalyst. However, the photocatalytic performance of such nanostructured BTO thin films was low, probably due to limited light absorption properties and in addition the morphology of the films obtained was not easily controlled. Therefore, in the second part of this chapter, a soft template-assisted sol-gel method, which allows large-scale coating capability and precise control of chemical composition[18,19], was used for the preparation of porous BTO thin films. Suzuki *et al.* have reported that the addition of porosity in ferroelectric thin films generates an anisotropic strain, which distorts the ferroelectric crystal lattice, promoting the stabilization of the ferroelectric phase[20]. In fact, it has been observed that porous ferroelectric thin films show a higher local piezoelectric response and an enhancement of electromechanical properties compared to dense films[21–23]. Using this facile and low-cost approach, it was possible to tune the porosity in $BaTiO_3$ thin films, while retaining ferroelectric polarization. Importantly, it was demonstrated that the photoelectrochemical performance can still be controlled via the ferroelectric polarization in porous $BaTiO_3$ thin films using electrochemical poling of the porous films. This paves the way for morphology optimization of ferroelectric photoelectrodes, improving thus their capabilities for photo-electrochemical applications.

4.2 Nanostructured BTO thin films

4.2.1 Tuning of morphology

BTO thin films were prepared using hydrothermal conversion, described in Chapter 3, which is based on the reaction of sol-gel TiO_2 films, annealed at low temperature and therefore amorphous, with $Ba(OH)_2$. In order to control the nanostructure morphology of BTO thin films, different concentrations of $Ba(OH)_2$ precursor solution and a different number of TiO_2 layers have been investigated.

The top-view SEM images reported in Figure 4.1 illustrate the morphology of BTO thin films with increasing concentration of $Ba(OH)_2$ precursor solution. For this trial, a single layer of TiO_2 was deposited on FTO glass substrate prior to $Ba(OH)_2$ treatment. It can be observed that the morphology of BTO thin films depends considerably on $Ba(OH)_2$ concentration, which is responsible for the equilibrium between the dissolution-precipitation reactions, on which the hydrothermal treatment is based[24]. In particular, the crystallization of BTO with the dissolution-precipitation reactions occur in the TiO_2 precursor thin film at a concentration of $Ba(OH)_2 > 0.2$ M, generating a morphology of a columnar BTO thin film. However, it can be noticed that when the $Ba(OH)_2$ concentration is 0.4 M, the morphology of BTO thin films assumes a denser and aggregated structure. Comparing the BTO films prepared using different concentrations of $Ba(OH)_2$ precursor solution, 0.25 M BTO thin films also possess more spacing between the BTO nanostructures which could allow a better combination with a photocatalyst. Therefore, 0.25 M BTO thin films have been used for further study.

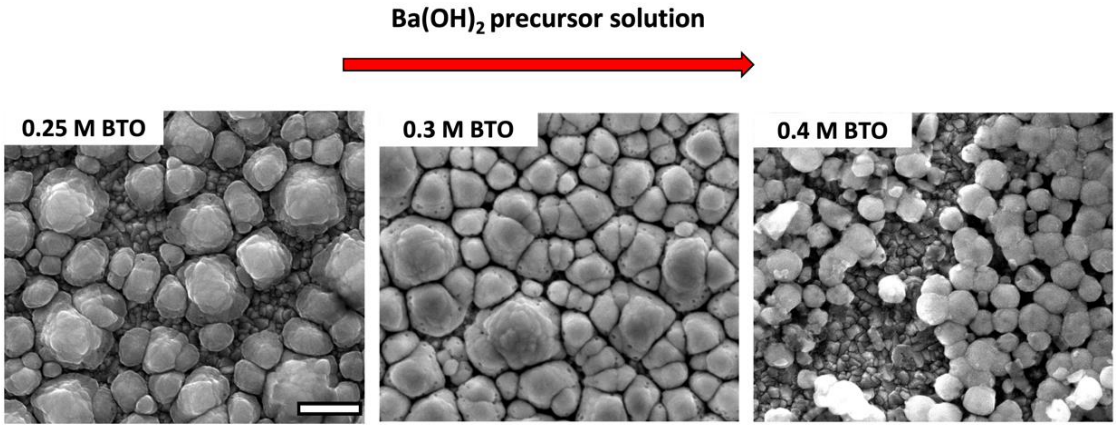

Figure 4.1 Top view SEM images of BTO thin films, prepared by increasing the $Ba(OH)_2$ concentration from 0.25 M to 0.4 M (scale bar: 500 nm) with one layer of TiO_2.

After that, 0.25 M BTO thin films have been also prepared using different number of TiO_2 layers, deposited on FTO glass by spin-coating. After this deposition process, TiO_2 films were immersed in 0.25 M $Ba(OH)_2$ solution for the hydrothermal conversion in BTO. Figure 4.2 shows that increasing the number of TiO_2 layers in 0.25 M BTO, the spacing between the BTO nanostructures is gradually reduced. Indeed, it is expected that the Ba intercalates into the amorphous TiO_2. However, variability among BTO samples prepared in the same conditions needs to be considered. For instance, under the same $Ba(OH)_2$ concentration (0.25 M), the nanostructures of BTO sample prepared using two TiO_2 layers look more spaced than that with one TiO_2 layer (Figure 4.1).

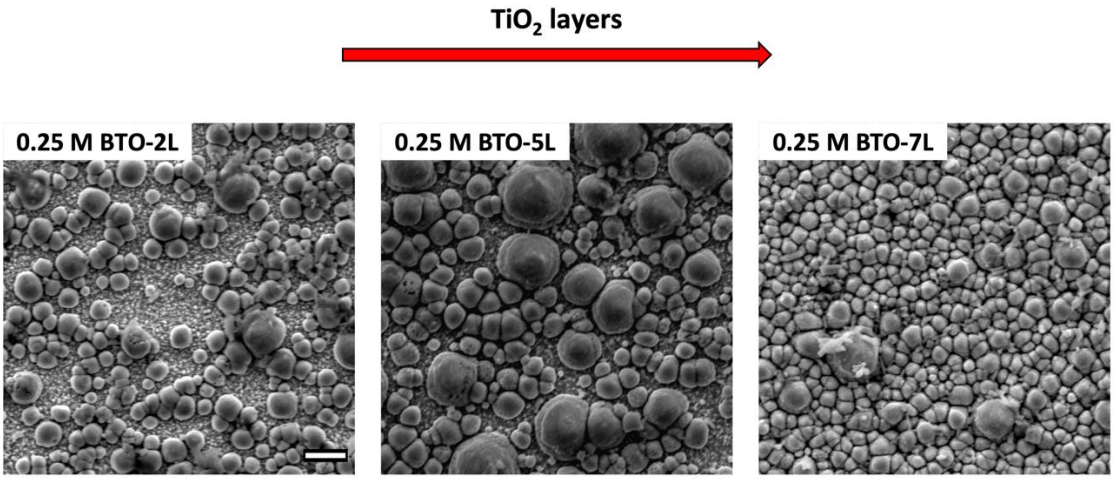

Figure 4.2 Top-view SEM images of 0.25 M BTO thin films, prepared using an increasing number of TiO_2 layers (scale bar: 1 µm).

The top-view SEM image of TiO_2 films used for the hydrothermal conversion in BTO is shown in Figure 4.3 a. In addition, the successful deposition of TiO_2 on FTO glass was monitored measuring the thickness of TiO_2 layers by Dektak profilometer. Dektak measurements were performed by Dr Lokeshwari Mohan, postdoctoral research assistant in Joe Briscoe's research group at Queen Mary University of London. Figure 4.3 b shows that the thickness of TiO_2 films is linearly proportional to the number of layers deposited on FTO glass by spin-coating (R^2=0.99). Indeed, increasing the number of TiO_2 layers from two to seven, the average thickness of TiO_2 increases from 138.40 nm to 546.63 nm.

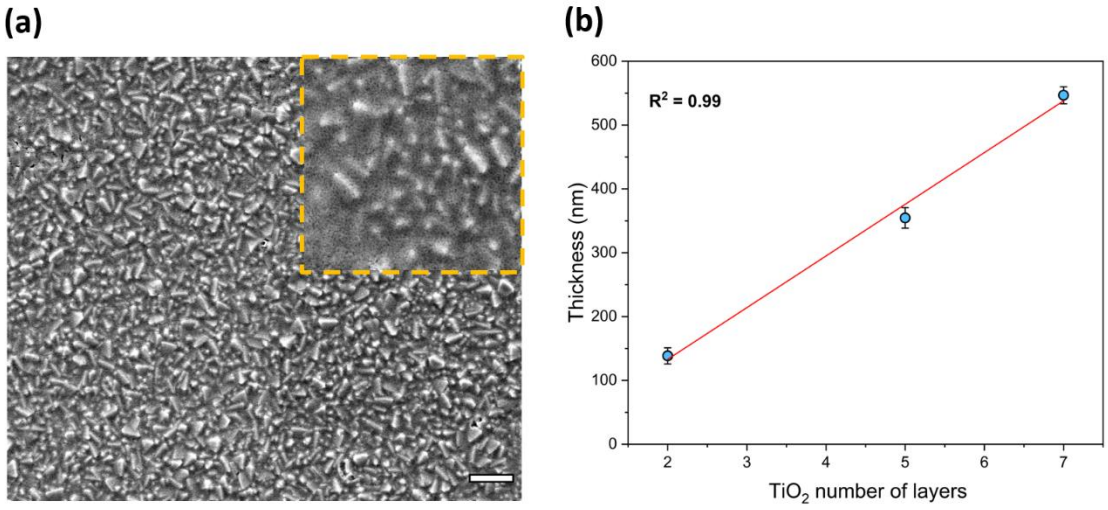

Figure 4.3 Top-view SEM image of TiO_2 film (scale bar: 1 µm) (a) and linear relationship between the number of TiO_2 layers, deposited by spin-coating on FTO glass, and their relative thickness (b).

Considering the results obtained from SEM analysis, the BTO thin films prepared with 0.25M $Ba(OH)_2$ and 2 layers of TiO_2 (0.25 M BTO-2L) seems more suitable for the fabrication of ferroelectric-photocatalyst composite film, because they could allow a complete integration of the photocatalyst within the BTO thin film.

Therefore, hereafter only 0.25 M BTO-2L thin films will be considered for further investigation. The top-view and cross-sectional SEM images of 0.25 M BTO-2L thin films show a uniform morphology with column structure (Figure 4.4 a,b). The average thickness of the film, measured from SEM cross-sectional image (Figure 4.4 b), is 380 nm.

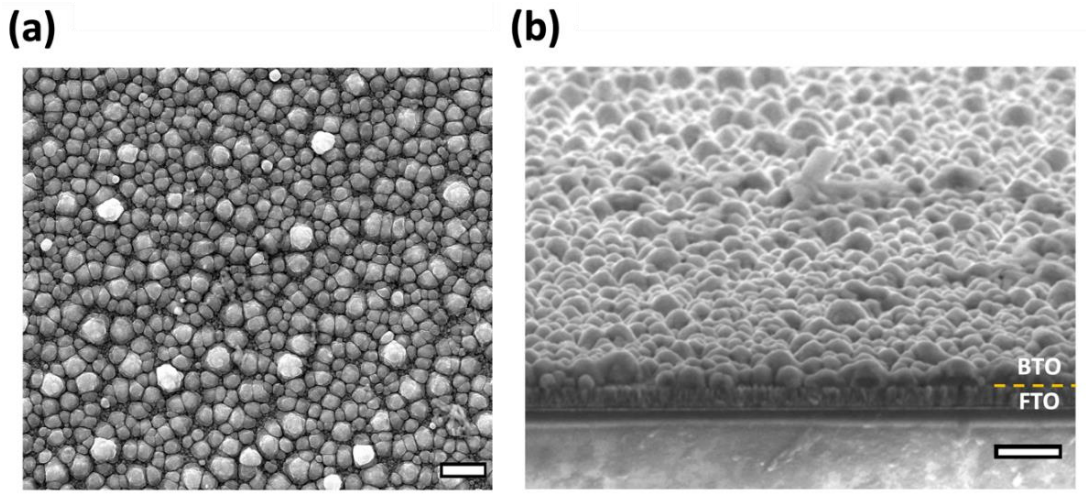

Figure 4.4 Top-view (a) and cross-sectional (b) image of 0.25 M BTO-2L thin films (scale bar: 1µm).

4.2.1.1 Optical and crystalline properties

The optical properties of 0.25 M BTO-2L thin films were investigated using UV-vis spectroscopy. The UV-vis spectrum of 0.25 M BTO-2L sample shows an absorption edge at ca. 360 nm, across the UV light range (Figure 4.5 a, inset). The optical direct bandgap energy of 0.25 M BTO-2L, estimated using the Tauc model reported in Chapter 3, is 3.87 eV, which is 0.65 eV larger than that of $BaTiO_3$ bulk[25], but in accordance with previous research works on BTO nanostructured thin films[26] (Figure 4.5 b).

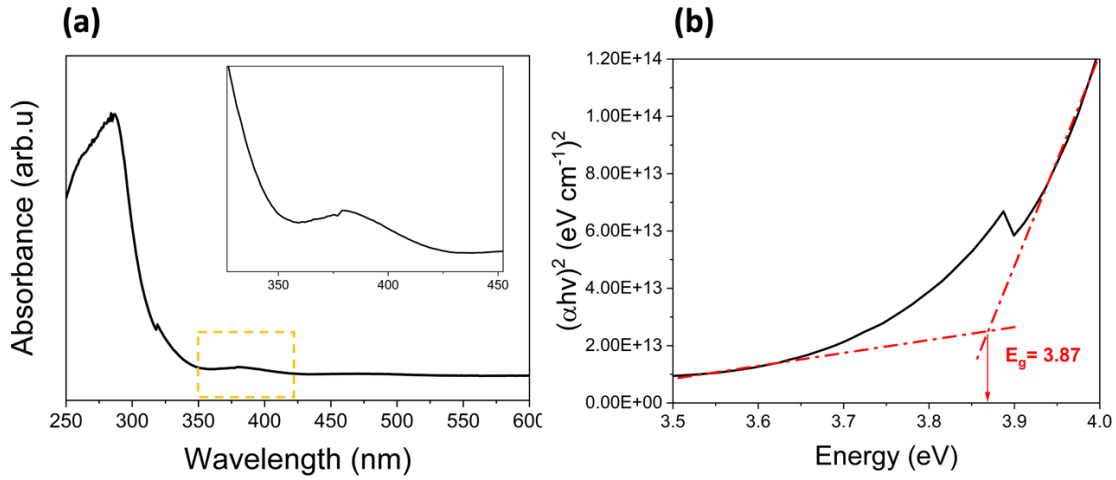

Figure 4.5 UV-vis absorption spectrum of 0.25 M BTO-2L thin films (a) and relative Tauc plot used for the determination of bandgap (b).

Furthermore, to investigate the crystalline phase, XRD analysis was performed. The XRD pattern of 0.25 M BTO-2L, reported in Figure 4.6 a, shows the peaks at 2θ = 22.2° (100), 31.5° (101), 38.9° (111), 44.8° (002), 50.7° (102), 56.1° (112), which confirm the formation of perovskite barium titanate (JCPDS No. 05-0626)[24]. There is no evident trace of the peaks referred to the TiO_2 anatase phase (JCPDS No. 00-021-1272) after the hydrothermal process other than those from the FTO glass substrate and perovskite phase of $BaTiO_3$. This result indicates that the hydrothermal conversion of TiO_2 in $BaTiO_3$ is successfully achieved.

However, using XRD analysis, the presence of the tetragonal phase, which is responsible of the ferroelectric behaviour in BTO thin films, was not confirmed. Indeed, according to the JCPDS 05-0626 reference card, in the XRD pattern of BTO tetragonal phase, it should be possible to observe the splitting of the peak at 2ϑ=45° into two peaks at 2ϑ=44.8° and 2ϑ=45.4°, corresponding to *hkl* Miller indices (002) and (200), respectively, compared to the cubic phase. Even if the presence of a slight shoulder is observed in Figure 4.6 b,

0.25 M BTO-2L does not show clear peak splitting probably because the small particle size in nanostructured $BaTiO_3$ induces inherent line broadening[27]. The presence of an amorphous hump in 0.25 M BTO-2L sample is also detected, which could be attributed to the amorphous glass substrate where the BTO films are deposited. Indeed, as observed from the SEM images of 0.25 M BTO-2L, the BTO nanostructures are separated by big gaps, which can contribute to the XRD results.

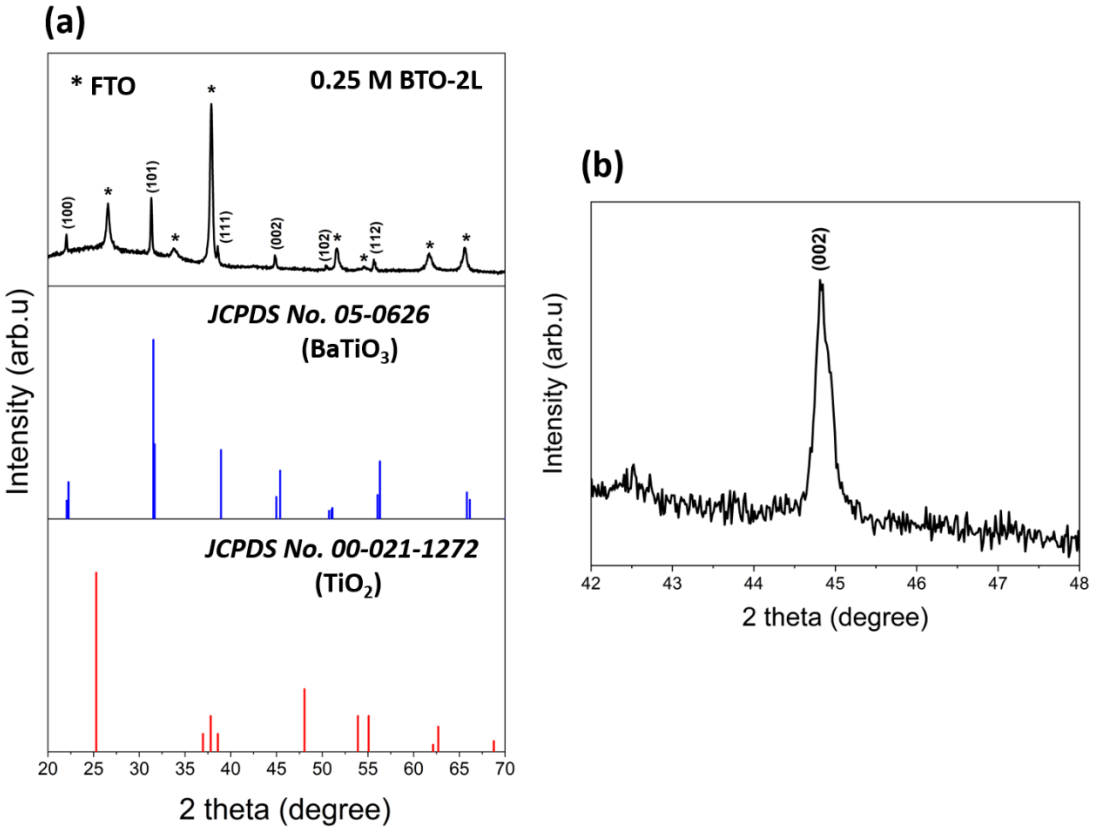

Figure 4.6 XRD pattern of 0.25 M BTO-2L thin film (a) and corresponding enlargement in 40°-50° region (b).

Considering that the transition to tetragonal phase in 0.25 M BTO-2L thin films was not confirmed using XRD analysis, Raman spectroscopy was used as technique to determine the crystalline phase. A commercial BTO powder, annealed at 1200 °C for 12 h, was used

as reference sample. The BTO powder shows the peaks at 275, 305, 520, and 720 cm^{-1}, which are assigned to the [A1(TO)], [B1 + E (TO + LO)], [E(TO) + A1(TO)], and [E(LO) + A1(LO)] Raman active modes, corresponding to the tetragonal phase of BTO[28]. The tetragonality of BTO commercial powder was verified using temperature-dependent Raman spectroscopy. Increasing the temperature up to 300 °C, the Raman peaks relative to the tetragonal phase decrease gradually in BTO commercial powder, consistent with the ferroelectric-paraelectric phase transition[27] (Figure 4.7).

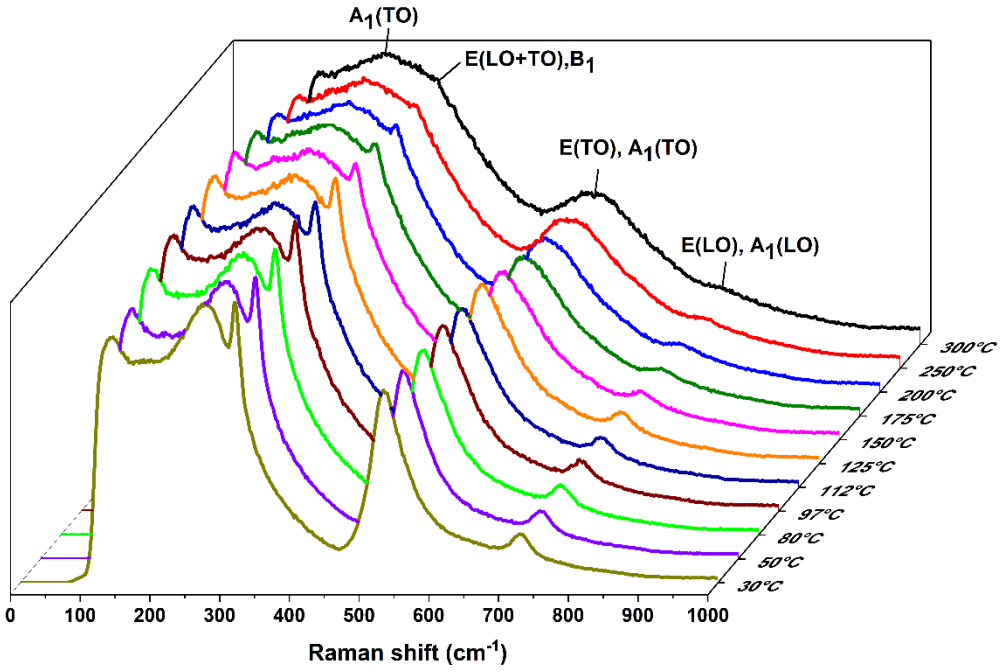

Figure 4.7 Raman spectra of BTO powder (1200 °C, 12h), acquired by increasing the temperature from 30 °C to 300 °C, in order to demonstrate the tetragonality of this reference sample.

Comparing 0.25 M BTO-2L thin film with BTO powder (Figure 4.8), three broader peaks at 275 cm^{-1} [A1(TO)], 520 cm^{-1} [E(TO)+A1(TO)] and 720 cm^{-1} [E(LO)+A1(LO)] are observed in 0.25 M BTO-2L thin films while the peak at 305 cm^{-1} [B1+E(TO+LO)] is not clearly detected. In particular, the increase in the peak width and the drop in the peak intensity of 305 cm^{-1} are the main two characteristics, indicating the tetragonal-cubic phase transition[27,29].

It has been observed that surface-related strain in BTO samples can stabilize the cubic phase at room temperature in small size particles[30]. Thus, it can be inferred that probably the cubic (paraelectric) and tetragonal (ferroelectric) phases coexist at room temperature in 0.25 M BTO-2L thin films, with a dominant cubic (paraelectric) phase.

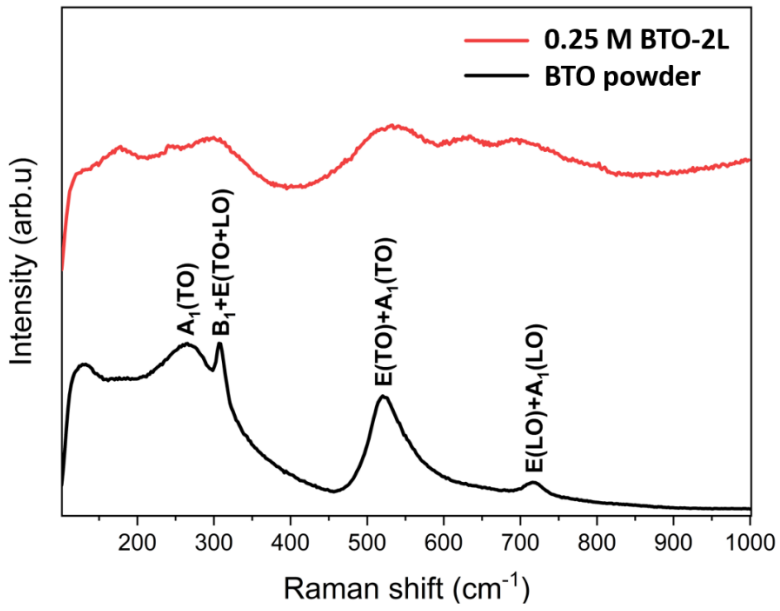

Figure 4.8 Raman spectra of 0.25 M BTO-2L thin films compared to the reference BTO powder.

4.2.1.2 Photoelectrochemical performance

Figure 4.9 shows current density *vs.* applied potential plot of 0.25 M BTO-2L thin film, acquired under dark, light and chop conditions in 1 M NaOH as electrolyte, using the photoelectrochemical cell system reported in Figure 3.4. The photoelectrochemical (PEC) performance of 0.25 M BTO-2L sample is quite low, giving 0.5 μA/cm^2 as maximum photocurrent value at 1.6 V vs RHE. This result could be related to the limited light absorption properties of this sample due to the wide bandgap as well as the poor crystallinity.

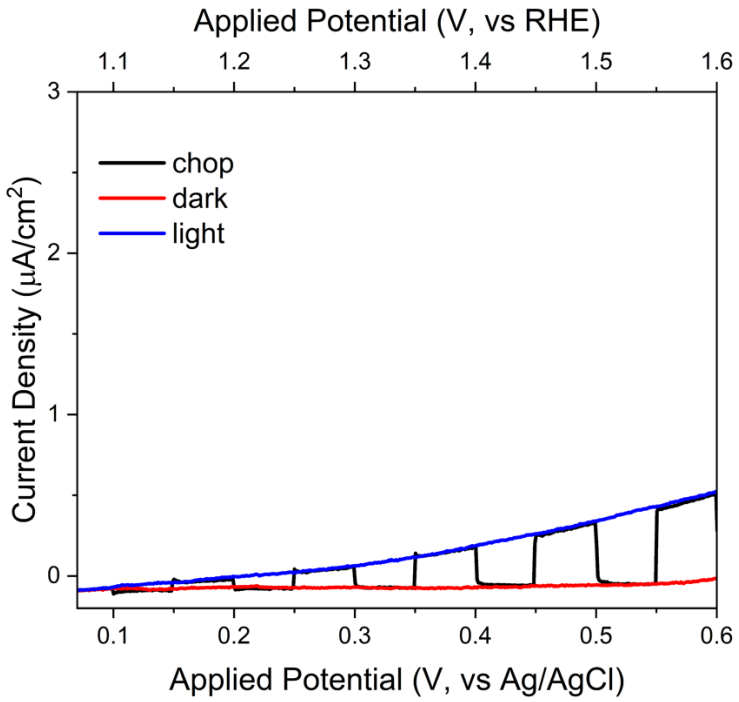

Figure 4.9 Linear sweep voltammetry (LSV) curves of 0.25 M BTO-2L, measured under dark, chop and light conditions in 1 M NaOH as electrolyte.

Therefore, it was decided to use an alternative method for the preparation of nanostructured BTO thin films, considering that the hydrothermal conversion process was

difficult in terms of control of BTO morphological properties (e.g., spacing between nanostructured, particles' size) and it generated a photoelectrode with a very low photocatalytic activity. In addition, the tetragonal (ferroelectric) phase of 0.25 M BTO-2L was not successfully confirmed.

4.2.2 Porous BTO thin films

4.2.2.1 Control of porous structure

Porous BTO (pBTO) thin films were prepared following the so-called soft template-assisted sol-gel method, using the experimental procedure reported in Chapter 3. An overview of the fabrication method is shown in Figure 4.10**.** To this end, block copolymer (BCP) micelles were mixed in solution with the inorganic sol-gel precursors and deposited on FTO substrates. In a subsequent step, the hybrid composites were transformed into the final porous BTO film by thermal calcination. This is in line with previous studies, where controllable porous materials were synthesized using BCPs as sacrificial structure-directing agents. Indeed, following this approach pore size can be tuned by controlling the BCP molecular weight[31] or by the addition of swelling agents to the hybrid solution,[32] while total sample porosity directly relies on the final organic-inorganic ratio[33].

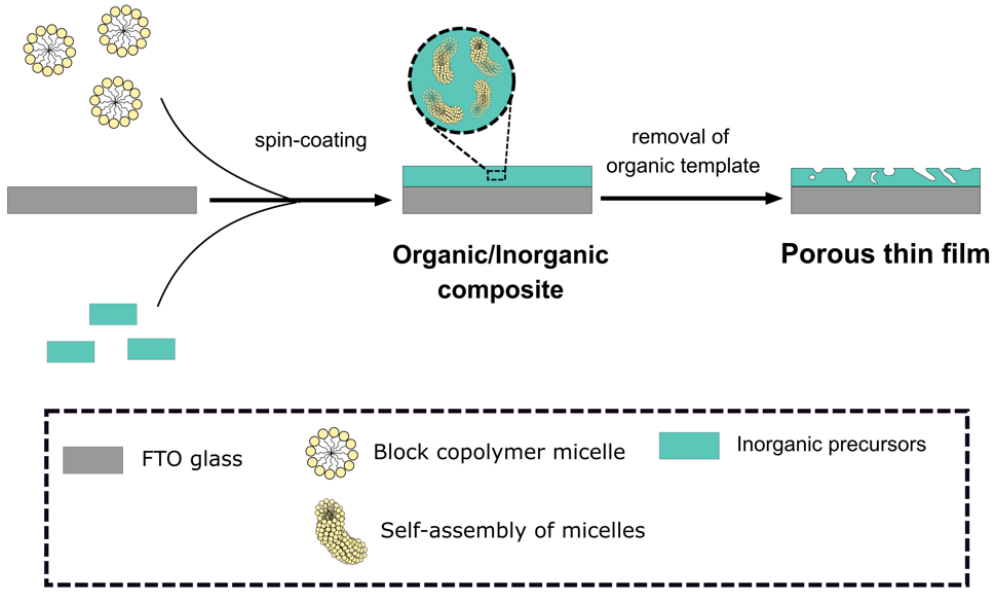

Figure 4.10 Soft template-assisted sol-gel method, used for the preparation of BTO thin films. The procedure involves the following steps: preparation of BTO precursor solution, where inorganic component and block copolymer (BCP) agent are combined, and the hydrolysis/polycondensation reaction takes place; after that, the BTO precursor solution is deposited on cleaned FTO glass by spin-coating and the organic/inorganic hybrid film is obtained. Finally, the deposited film is annealed (750°C, 10 min) to remove the organic template and to allow the BTO crystallization, promoting the formation of porous BTO (pBTO) thin films.

SEM top-view images confirm the porous structure of pBTO thin films **(**Figure 4.11 a). In particular, the films show a solid matrix with interconnected pores. Furthermore, it is possible to observe that by increasing the amount of P123 BCP from 0.2 g to 5 g in pBTO thin films (pBTO-0.2, pBTO-2, pBTO-3.5 and pBTO-5) the pore area gradually increases (Figure 4.11 a). The morphological features are also investigated through cross-sectional SEM images, where the grains are vertically stacked, and the gaps between them are the

pores (Figure 4.11 a). Moreover, the thickness of pBTO thin films is linearly proportional to the P123 BCP concentration, calculated as the quantity of BCP over the total volume of the precursor solution (R^2= 0.971). This is expected as the volume occupied by the organic sacrificial template present in the thin films deposited by spin-coating is higher in pBTO-5 compared to pBTO-0.2. For this reason, the pBTO-5 thin film is thicker (Figure 4.11 b).

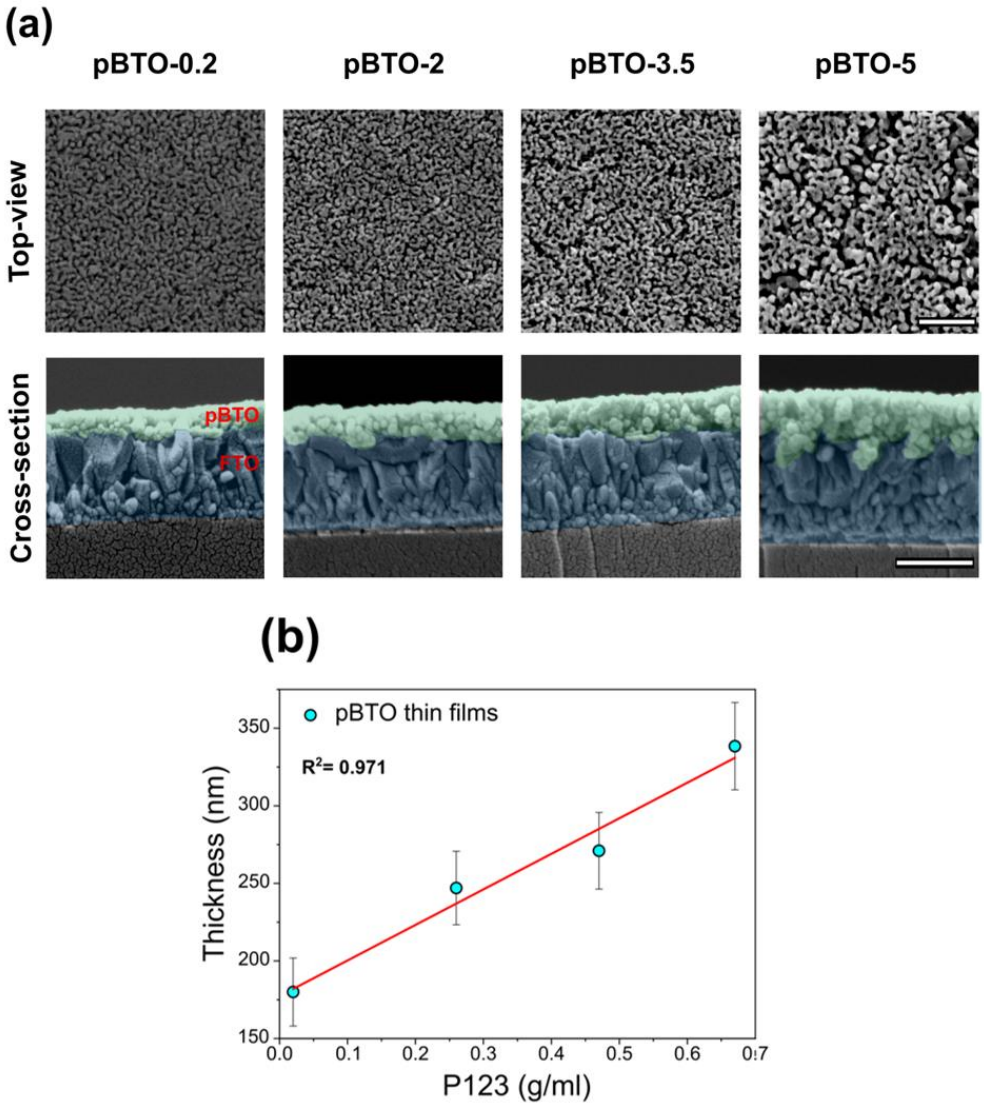

Figure 4.11 Top-view and cross-sectional SEM images of pBTO thin films, prepared with different amounts of P123 block-copolymer 0.2g-5g (scale bar: 500 nm) (a);

Linear relationship between the thickness of pBTO thin films and the concentration (g/ml) of P123 block-copolymer (b).

Ellipsometric assessment of pBTO thin films presented in this work was conducted to verify the control of porosity according to P123 BCP concentration. The spectroscopic ellipsometry (SE) measurements and the corresponding data analysis were performed by Dr Alberto Alvarez Fernandez, Postdoctoral Research Associate in the Adaptive and Responsive Nanomaterials (AdReNa) research group at University College London (UCL).

Figure 4.12 shows a schematic of the different steps followed in the ellipsometric characterization of the fabricated samples. In a first step, a non-porous BTO (npBTO) thin film is used to establish the optical characteristics (n and k) of the pristine material (Figure 4.12 i).

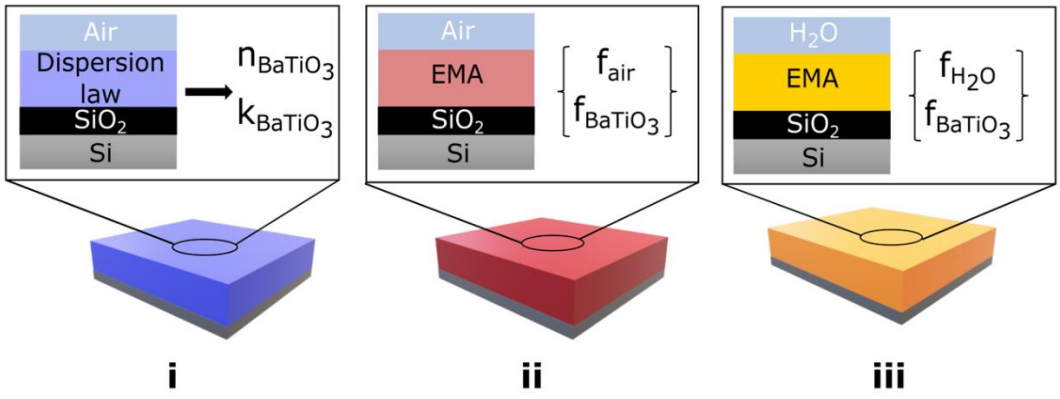

Figure 4.12 Schematic on the different steps involved in SE for the calculation of porosity in pBTO thin films (figure made by Dr Alberto Alvarez Fernandez). Firstly, the optical characteristics (n and k) of the pristine material are obtained using npBTO (i); after that, a homogeneous flat layer with a certain volume fraction of

$BaTiO_3$ (f_{BaTiO_3}) and air (f_{air}) is established, allowing the estimation of porosity in pBTO samples by application of Bruggeman Effective Medium Approximation (EMA) (ii); analogously, an appropriate volume fraction of $BaTiO_3$ (f_{BaTiO_3}) and water (f_{H_2O}) is used to confirm the porosity values obtained (iii).

The application of a Cauchy dispersion model displayed a reasonable fit with optical parameters acquired for the npBTO film (Figure 4.13 b, c). The obtained refractive index of the film (1.98 at 632 cm^{-1}) is slightly lower than the one reported in previous literature (2.33)[34]. This small variation can be explained taking into account the presence of certain intrinsic porosity, probably due to the material deposition process by spin-coating, and visible in the corresponding SEM image, reported in Figure 4.13 a. Considering that all BTO samples present in this study are deposited in the same conditions, this residual porosity can be neglected. The optical parameters of npBTO are used as reference values to determine porosity in all porous pBTO thin films.

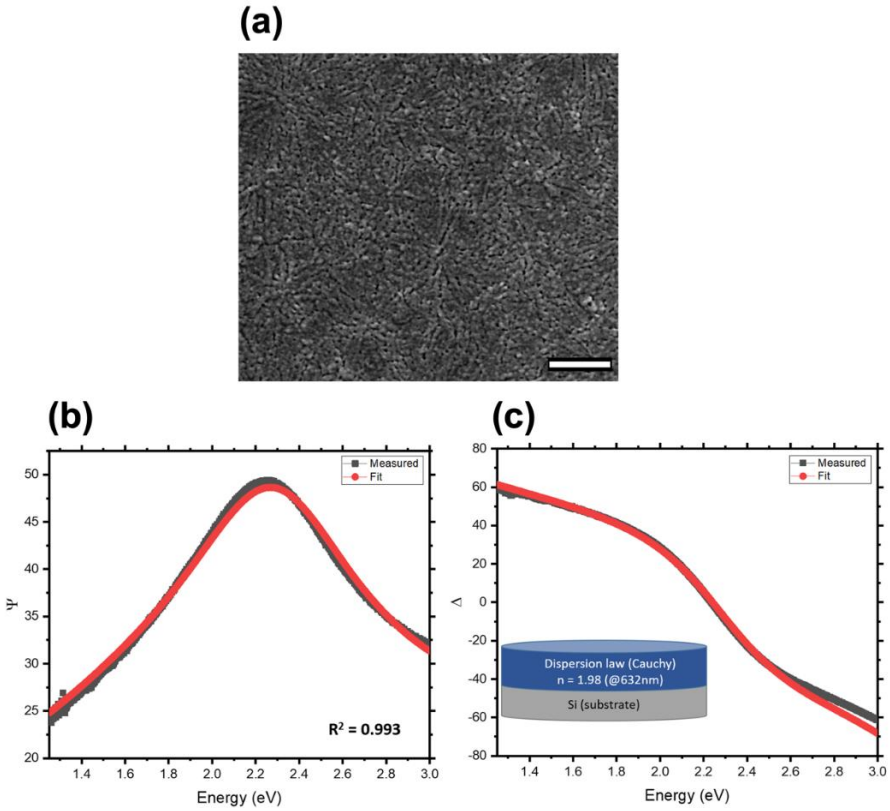

Figure 4.13 Top-view SEM image of npBTO sample used as reference (scale bar: 500 nm) (a); ellipsometric angles Ψ (b) and Δ (c) referred to npBTO thin films obtained by application of Cauchy dispersion model.

In a second step, pBTO-0.2, pBTO-2, pBTO-3.5, and pBTO-5 samples were characterized following the same SE protocol. In all these cases, ellipsometer angles (Ψ and Δ) were fitted using a Bruggeman EMA to extrapolate the overall porosity of each pBTO sample (Figure A1 in Appendix). Thus, a homogeneous flat layer with a certain volume fraction of each component ($BaTiO_3$ and air) was established (Figure 4.12 ii). In the final step, pBTO samples were infiltrated with water to confirm the porosity values previously obtained (Figure 4.12 iii). In this case, a homogeneous flat layer with a certain volume fraction of $BaTiO_3$ and water was used as starting point for the modelling. Similar to the previous case, ellipsometer angles (Ψ and Δ) were fitted using a Bruggeman EMA

to determine the overall porosity of each pBTO sample (Figure A2 in Appendix).The porosity of pBTO thin films obtained using SE-air, SE-H_2O, and SEM analysis is summarized in Table 4.1.

Table 4.1 Porosity (%) obtained using SE-ai, SE-H_2O, and SEM analysis for pBTO thin films (0.2-5).

	SE-air	SE-H_2O	SEM analysis	Surface areas
pBTO thin films	Porosity (%)	Porosity (%)	Porosity (%)	m^2/cm^3
0.2	44	36	24	524
2	49	47	33	481
3.5	52	50	40	413
5	58	60	48	340

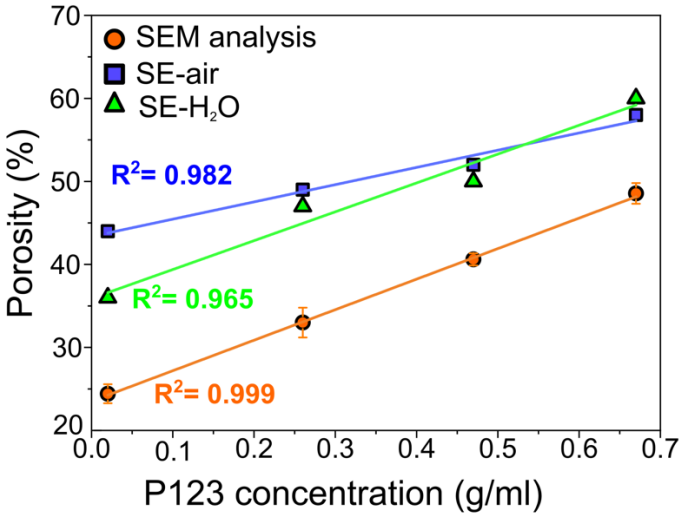

Figure 4.14 Comparison between porosity (%) values obtained using SEM analysis, SE-air, and SE-H_2O for pBTO thin films with different P123 BCP concentrations.

The porosity values acquired by SE-air and SE-H_2O show a linear dependence with P123 BCP concentration, in agreement with the ones estimated from image analysis of the SEM micrographs (Figure 4.14). However, in all cases, the porosity values obtained by SE are higher compared to the ones obtained by SEM. It needs to be considered that the estimation of porosity from SEM images only refers to the surface of the samples, contrary to SE, where the whole film thickness is analyzed[35], which would account for this systematic underestimation of porosity by SEM analysis.

Porosity values obtained after infiltration (SE-H_2O) show a good reproducibility when compared with the ones obtained for ambient measurements (SE-air), showing in both cases similar values for high and medium P123 BCP concentrations (Figure 4.14). However, for low organic content (pBTO-0.2), SE results show a slight discrepancy (36 vs. 44 %), as evidenced in Table 4.1. A likely reason for the discrepancy in the pBTO-0.2 sample may be incomplete water infiltration due to limited pore accessibility due to the lower porosity and pore size compared to the rest of the pBTO thin films. Moreover, the surface area (S) of pBTO thin films has been determined from the ellipsometric adsorption isotherms by applying the BET method. The BET plots obtained for the samples presented in this Chapter are shown in the Appendix, Figure A3. By fitting the experimental values in the linear range ($0.05 \leq p/p_0 \leq 0.3$) the corresponding surface areas were calculated. As shown in Table 4.1, a clear reduction in the surface area can be identified with the increase in the concentration of the P123 BCP in the starting solution from pBTO-0.2 (524 m^2/cm^3) to pBTO-5 (340 m^2/cm^3). This can be explained by taking into account the increase in the pore area detected in the top-view SEM images (Figure 4.11 a). Thus, the higher the BCP concentration, the bigger the pores in the final inorganic structure and therefore the lower the surface area.

4.2.2.2 Optical properties

The transmittance spectra of pBTO thin films show band edges within 350-380 nm across the UV light range, as depicted in Figure 4.15 a. The bandgap energies estimated from the Tauc plot are in the range 3.3 to 3.6 eV (Figure 4.15 b), which is close to the value reported for bulk samples (3.2 eV)[36] and it is in accordance with values previously reported for BTO thin films prepared by the sol-gel method (3.7 e V)[37].It has been found that the preparation technique can induce variations in the stoichiometry and defect distribution of the films, leading to differences in the estimated bandgap energies [37]. In addition, the slight variation between the estimated bandgap energy values of pBTO thin films could be correlated to scattering effects which can arise in porous samples. This has previously been demonstrated to lead to an apparent absorption enhancement due to light scattering, which influences the measured transmittance spectra, including the position of the absorption onset used to determine the bandgap[38].

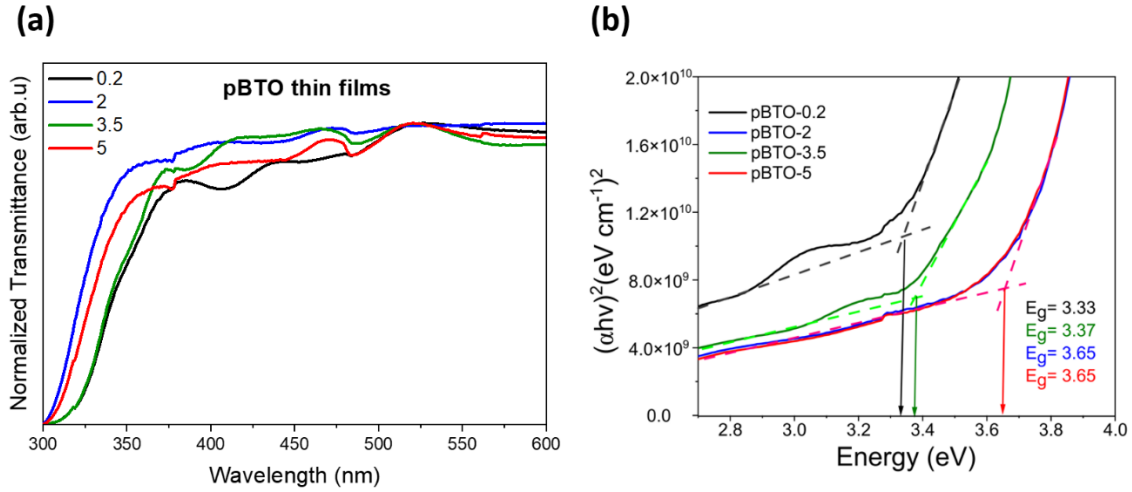

Figure 4.15 Transmittance spectra of pBTO thin films (0.2-5) (a) and relative Tauc plots, which allow the estimation of their bandgap energies (b).

4.2.2.3 Crystalline properties

To investigate the crystalline phase, XRD analysis was performed on pBTO thin films, which clearly show the peaks referred to BTO crystals. However, as discussed in section 4.2.1.1, it is difficult to discriminate between the cubic (paraelectric) and the tetragonal (ferroelectric) phase using XRD. For the pBTO thin films, the presence of the peak splitting at $2\vartheta = 45°$, which is correlated to the transition cubic-tetragonal phase, is not distinctly observable, probably because the polycrystalline nature of the film broadened the peak width[39] (Figure 4.16 a). In addition, the peak at $2\vartheta = 45°$ in pBTO-5 shows a lower intensity compared to pBTO-0.2. Indeed, when increasing the concentration of P123 BCP, the volume fraction occupied by BTO inorganic precursor present in the film deposited by spin coating is lower. Therefore, the signal at $2\vartheta = 45°$ referred to pBTO-5 is weaker (Figure 4.16 b).

To further investigate the crystalline phase, Raman spectroscopy was performed on the pBTO-5 thin film and compared with a commercial BTO powder, which clearly show the tetragonal (ferroelectric) phase of BTO, as reported in Figure 4.7. In the pBTO-5 thin film, the presence of the peaks relative to the Raman modes of tetragonal BTO is confirmed except for the splitting of [A_1(TO)] mode. This can be attributed to the in-plane compressive strain induced by porosity, which enhances the stability of the ferroelectric phase[40]. The porosity in BTO thin films is expected to induce elongation of the crystal lattice toward the c-axis, generating further dislocation of Ti^{4+} from the center of the lattice and consequently in-plane compressive strain in the (001) surface, enhancing the ferroelectricity in BTO thin films[20]. Thus, it is possible to conclude that the pBTO-5 thin films are in the tetragonal, ferroelectric phase. In addition, the Raman active mode

detected at 639 cm^{-1} in the pBTO-5 thin film is most likely attributed to the anatase phase of TiO_2[41] blocking layer, deposited on FTO glass prior to BTO (Figure 4.16 c).

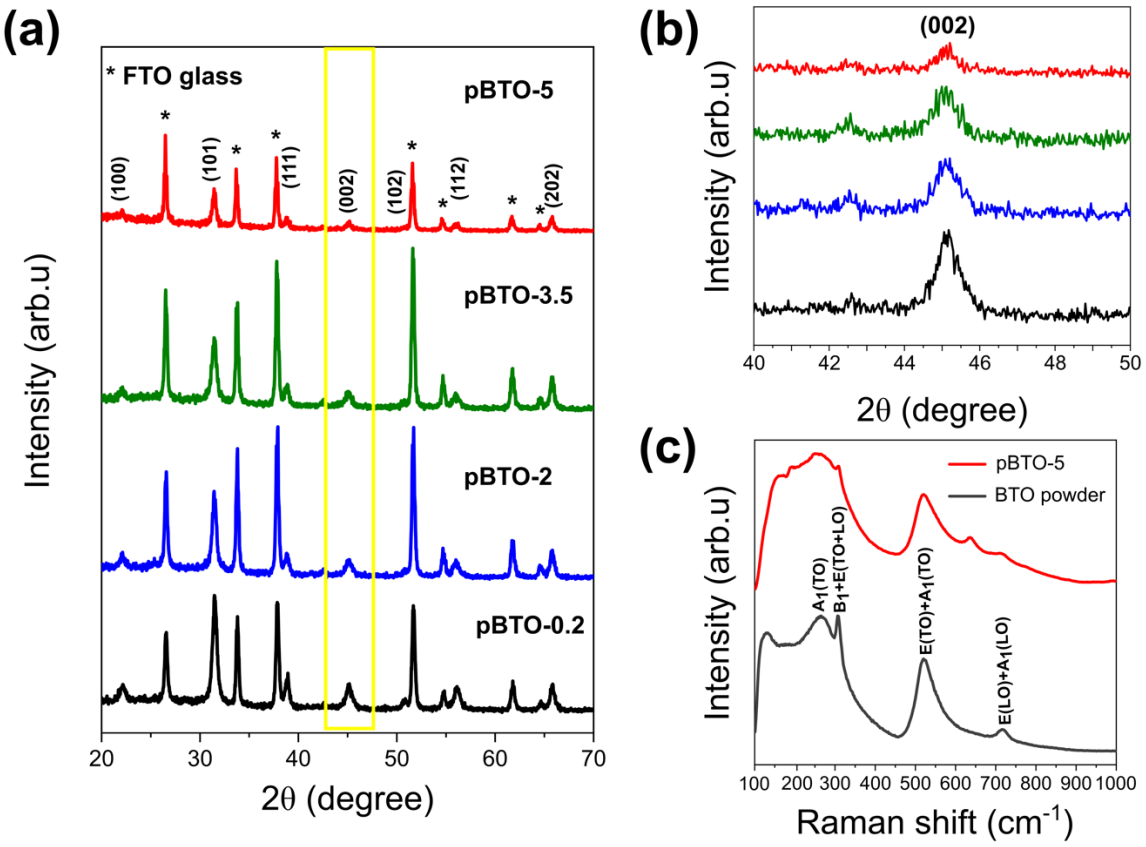

Figure 4.16 XRD patterns of pBTO thin films (0.2-5) (a) and corresponding enlargement in 40°-50° region (b); Raman spectra of pBTO-5 compared to the reference BTO tetragonal powder (c).

4.2.2.4 Photoelectrochemical performance of pBTO thin films with different porosity

After confirming the crystalline phase of pBTO thin films, the photoelectrochemical properties of pBTO thin films were tested under chopped illumination in 1 M NaOH as electrolyte. All pBTO thin films show higher photocurrent density than the non-porous

BTO (npBTO) samples, suggesting that the inclusion of porosity is beneficial (Figure 4.17).

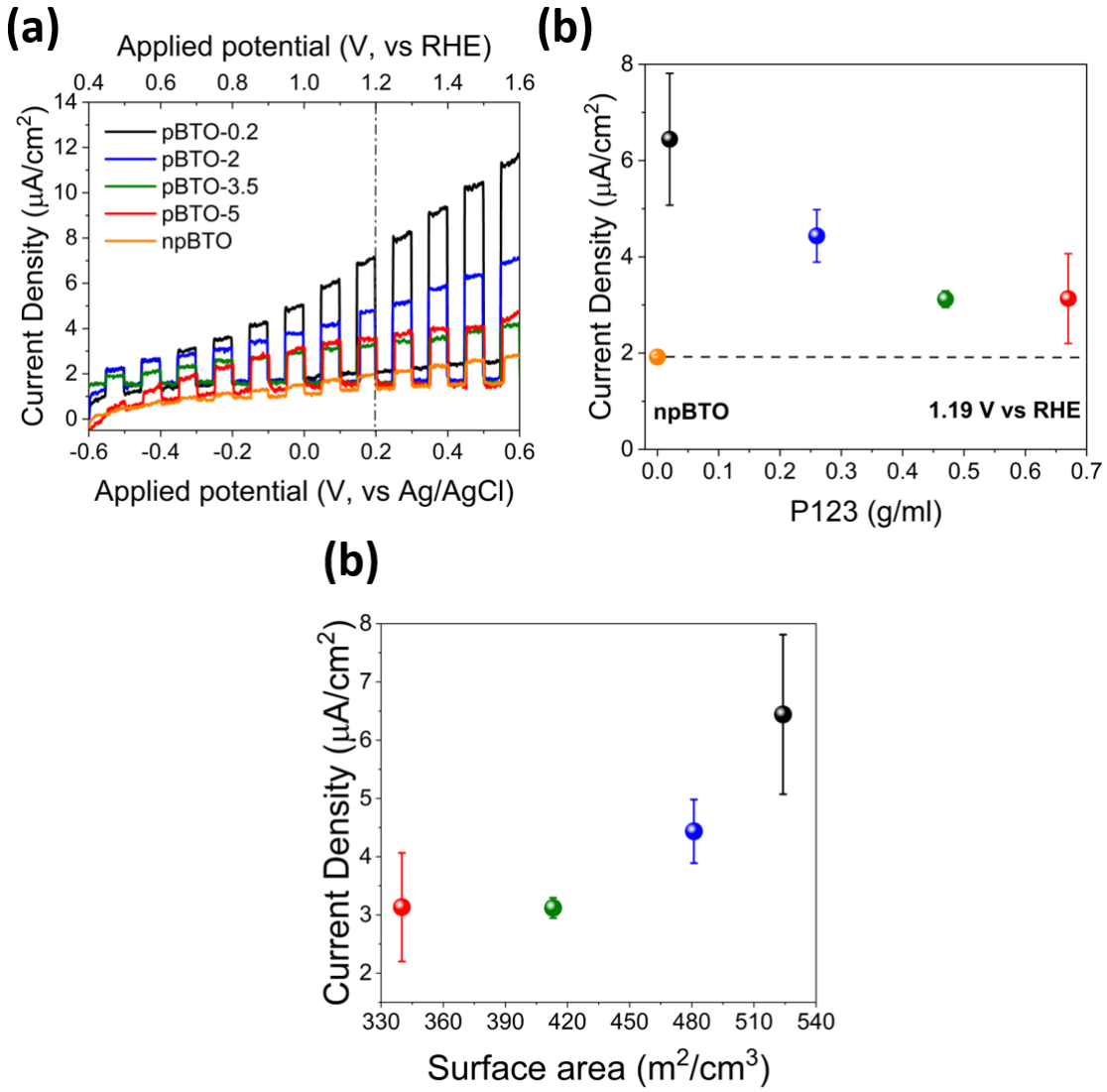

Figure 4.17 LSV measurements of BTO thin films (a) and relative current density values extrapolated at 1.19V vs RHE as a function of the concentration of block copolymer P123 (g/ml) in pBTO films (b), acquired under chopped illumination in 1M NaOH as electrolyte; correlation between current density and surface area values of pBTO-0.2, pBTO-2, pBTO-3.5 and pBTO-5 (c).

For fair comparison to the pBTO films, the npBTO films used for these tests were deposited on FTO glass with a compact TiO_2 hole-blocking layer. The presence of TiO_2 layer can prevent short-circuiting of the electrolyte to the FTO. It also can induce a favourable band bending in the BTO layer, leading to efficient electron transport towards the FTO through the TiO_2 layer. Combined with the hole-mirroring effect of the TiO_2 layer, this can effectively suppress charge recombination. Similar to the films on Si substrate, those films still demonstrated a non-porous structure when using these substrates (Figure 4.18 a), except for the small amount of nanoporosity attributed to the material deposition process by spin coating. Moreover, the LSV curve of the compact TiO_2 blocking layer is shown in Figure 4.18 b, confirming that no additional contribution in the PEC performance arises from this layer.

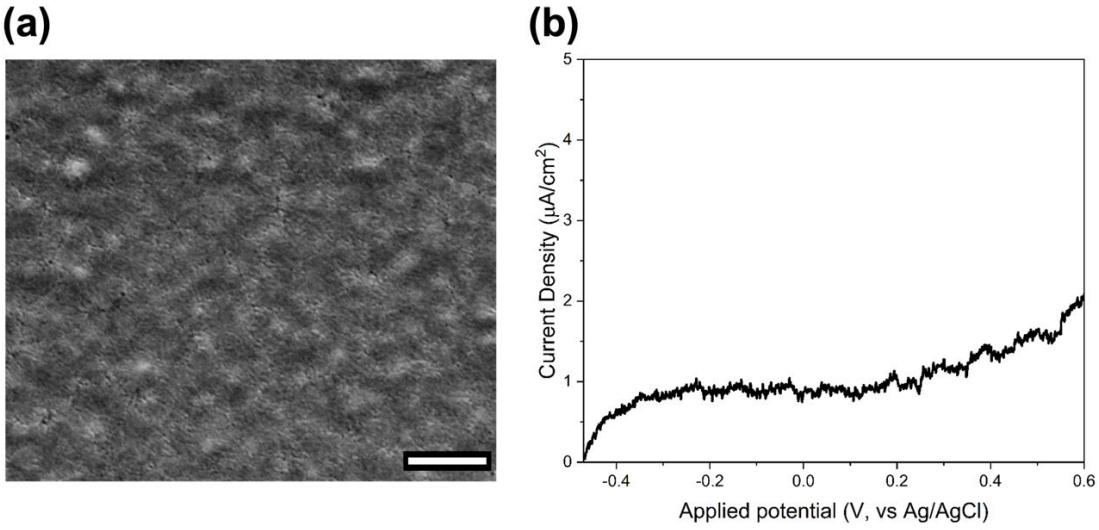

Figure 4.18 Top-view SEM image of non-porous BTO (npBTO) thin film, deposited on FTO glass (scale bar: 1μm) (a) and LSV measurement under light-chopped illumination of compact TiO_2 ($cTiO_2$) blocking layer, acquired in 1 M NaOH as

electrolyte (b), showing a negligible PEC response, and thus it does not contribute to the photoelectrochemical performance of pBTO films.

Furthermore, from the current density-voltage (J-V) curves of pBTO thin films, it is possible to observe that when increasing the concentration of P123 BCP the measured current density gradually decreases (Figure 4.17 a), with pBTO-3.5 and pBTO-5 displaying very similar values. Extrapolating the photocurrent values obtained across a range of samples at 1.19 V vs RHE, which is close to the oxidation potential of water (1.23 V vs RHE), this trend can be seen more clearly (Figure 4.17 b), and it can be seen that the pBTO-3.5 and pBTO-5 indeed show comparable values of photocurrent density within the spread of error across the measured samples. Nevertheless, it is evident that at 1.19 V vs RHE, pBTO-0.2 shows an enhancement of the photocurrent of about 3 $\mu A/cm^2$ compared to pBTO-5 (Figure 4.17 b).

This result could be related to the presence of a high number of smaller pores in pBTO-0.2, according to the SEM analysis, which leads to higher surface area and consequently improvement of PEC performance. On the contrary, although pBTO-5 shows greater overall porosity, this is comprised of larger pores, which results in a lower surface area overall and a decrement of overall PEC response. This is confirmed by the measured surface area values of pBTO thin films discussed above and reported in the Appendix, Figure A3. From Figure 4.17 c, it can be seen that the photocurrent density at 1.19 V vs RHE shows a good correlation with the surface area of the samples.

Therefore, it can be concluded that the introduction of porosity into a BTO photoanode does indeed improve the PEC photocurrent, but that a basic increase in overall porosity *via* inclusion of increasing quantities of BCP does not necessarily increase PEC photocurrent further. Instead, careful consideration must be given to the morphology of

the porous photoelectrode, where a greater number of smaller pores is preferable, as it leads to an overall increase of interfacial area in contact with the electrolyte.

4.2.2.5 Ferroelectric behaviour

4.2.2.5.1 Microscopic poling: Piezoresponse Force Microscopy (PFM)

To study the ferroelectric response of pBTO thin films, PFM was obtained for pBTO thin films with lower (pBTO-0.2) and higher (pBTO-5) porosity. All PFM measurements were performed at Bruker in Coventry (UK) and Santa Barbara (CA) by Vishal Panchal, Bede Pittenger and Peter De Wolf. The topographic images show the grain structure of the pBTO films where the presence of pores is further confirmed. However, the pores are not well-defined, probably because of the use of PFM contact mode, which is not particularly suitable for the resolution of film topography. Moreover, it is possible to observe that the BTO grain structure is larger in pBTO-5 than in pBTO-0.2, in agreement with SEM images (Figure 4.19).

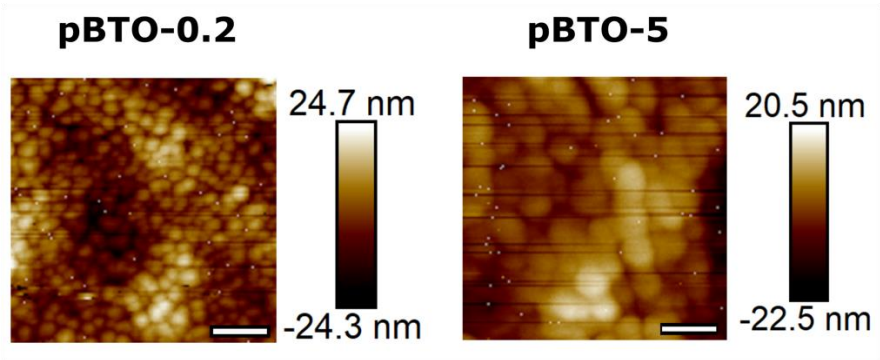

Figure 4.19 Topography of pBTO-0.2 and pBTO-5 obtained by PFM (scale bar: 200 nm).

The PFM phase images of pBTO-0.2 and pBTO-5 show clear regions in the samples with different contrast, which reflect the grains randomly split into domains of opposite

polarities (Figure 4.20 a). The dark areas correspond to domains with polarisation oriented toward the substrate (P_{down}). In contrast, the bright regions are domains with polarisation terminated at the free surface of the film (P_{up}). pBTO-5 shows more P_{down} as grown, compared to pBTO-0.2. As the DC voltage was increased from - 8 V to +8 V, the domains switched their polarity in both samples. This behaviour is also observed in the PFM amplitude images (Figure 4.21 a).

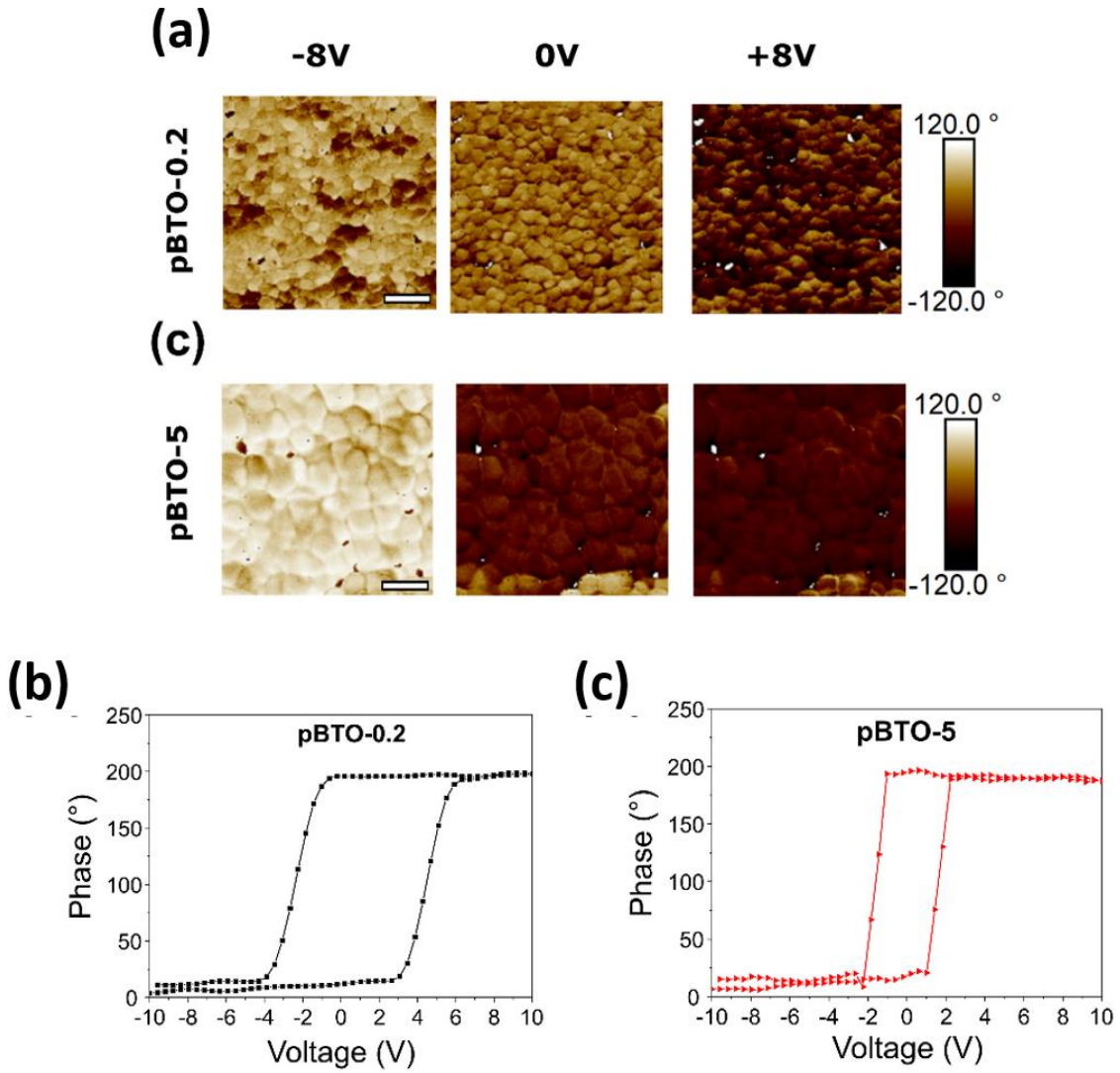

Figure 4.20 PFM phase signals of pBTO-0.2 and pBTO-5 obtained at - 8 V, 0 V and +8 V (scale bar: 200 nm) (a) and the corresponding phase-voltage curves of pBTO-0.2 (b) and pBTO-5 (c) acquired using SS-PFM.

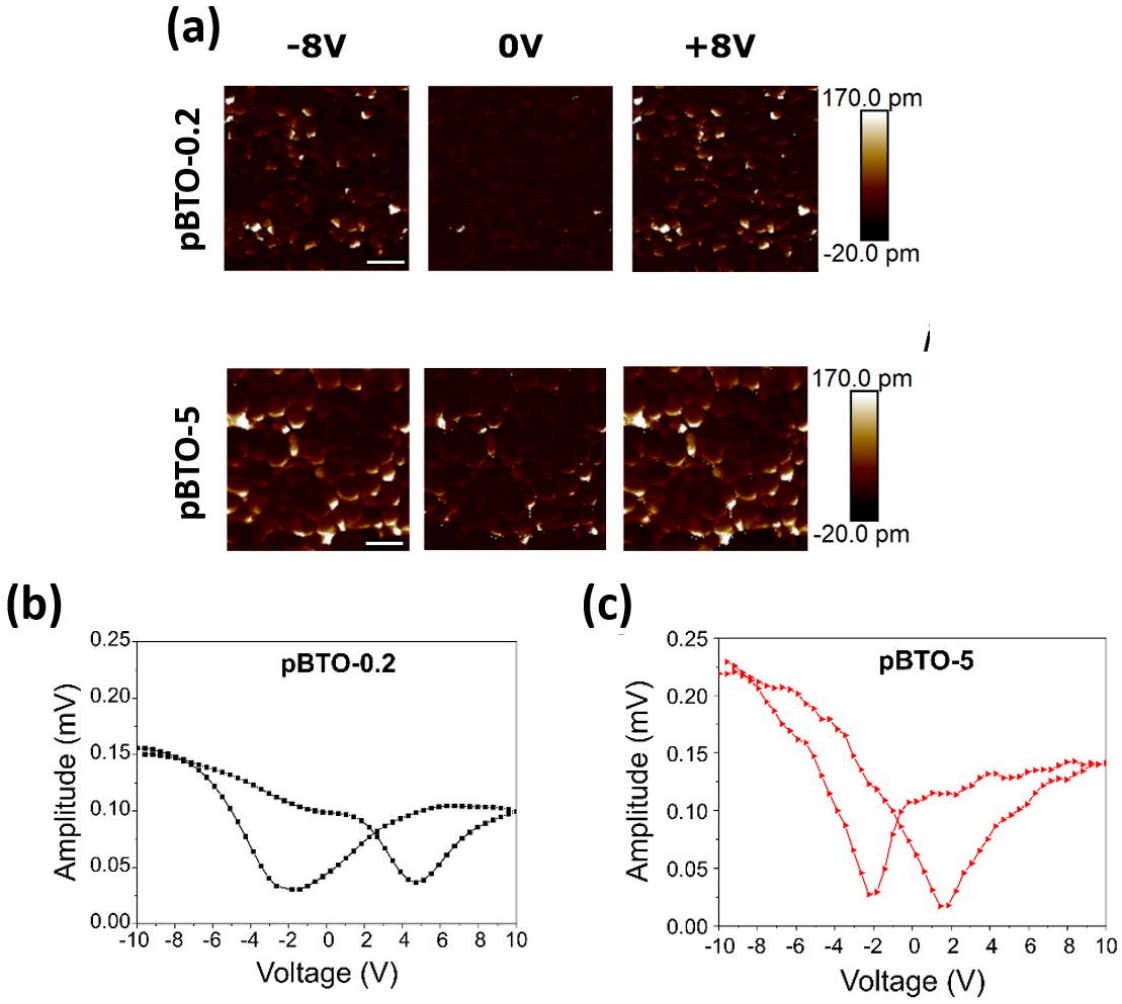

Figure 4.21 PFM amplitude signals of pBTO-0.2 and pBTO-5, obtained at – 8 V, 0 V, +8 V (a) (scale bar: 200 nm) and the corresponding amplitude-voltage curves of pBTO-0.2 (b) and pBTO-5 (c) acquired using SS-PFM.

Analysing the PFM phase signals in more detail (Figure 4.20 a), the switching of the domains appears more complete for pBTO-5 compared to pBTO-0.2. This evidence could

be related to the relationship between grain size and piezoresponse. According to previous research[42,43], larger grains usually exhibit stronger piezoresponse signals compared to smaller grains. Therefore, as a consequence, small grains could be more difficult to switch in polarity, with respect to large grains. This result is also reflected in the PEC performance after EC poling procedure, which is discussed further in 4.2.2.5.2.

However, it has been found that surface charging and electrostatic interaction between the tip and the sample can contribute to create contrast in PFM images, which can be unrelated to the presence of ferroelectricity[44,45]. Thus, as explained in Chapter 3, to confirm the ferroelectric behaviour of pBTO thin films, SS-PFM, which removes electrostatic contributions that can affect the signals measured by traditional PFM modes[46], was performed. Figure 4.20 b,c and Figure 4.21 b,c show the PFM phase and amplitude hysteresis loops, respectively, acquired using SS-PFM. The phase loops show clear switching with a phase difference of close to 180°, as expected for $BaTiO_3$, and the amplitude loops show a clear 'butterfly' shape. These results clearly confirm the ferroelectric properties of the pBTO samples of both high and low porosity. The phase loop is also narrower for pBTO-5 samples indicating a smaller coercive field, in agreement with the more complete domain switching seen in the PFM images for these samples.

Therefore, it can be concluded that the PFM phase and amplitude signals obtained demonstrate spontaneous polarisation switching by applying an electric field in pBTO-0.2 and pBTO-5 thin films and the SS-PFM hysteresis loops, in combination with Raman spectroscopy, showing the tetragonal (ferroelectric) phase and electrochemical (EC) poling results, that will be discussed further below, give strong evidence in support of the ferroelectricity of these samples.

4.2.2.5.2 Macroscopic poling: Electrochemical (EC) poling

As previously reported, one of the beneficial and fascinating properties of ferroelectrics as photocatalysts is the ability to switch their photocurrent response via controlling the polarisation orientation[47]. Therefore, to investigate the effect of ferroelectric polarization on PEC response, electrochemical (EC) poling on pBTO thin films at lower (pBTO-0.2) and higher (pBTO-5) porosity was performed, and then J-V curves were measured after the poling pre-treatment. Compared to the unpoled state, the +8 V EC poling induces an improvement of PEC performance in both pBTO-0.2 and pBTO-5 (Figure 4.22 a,b).

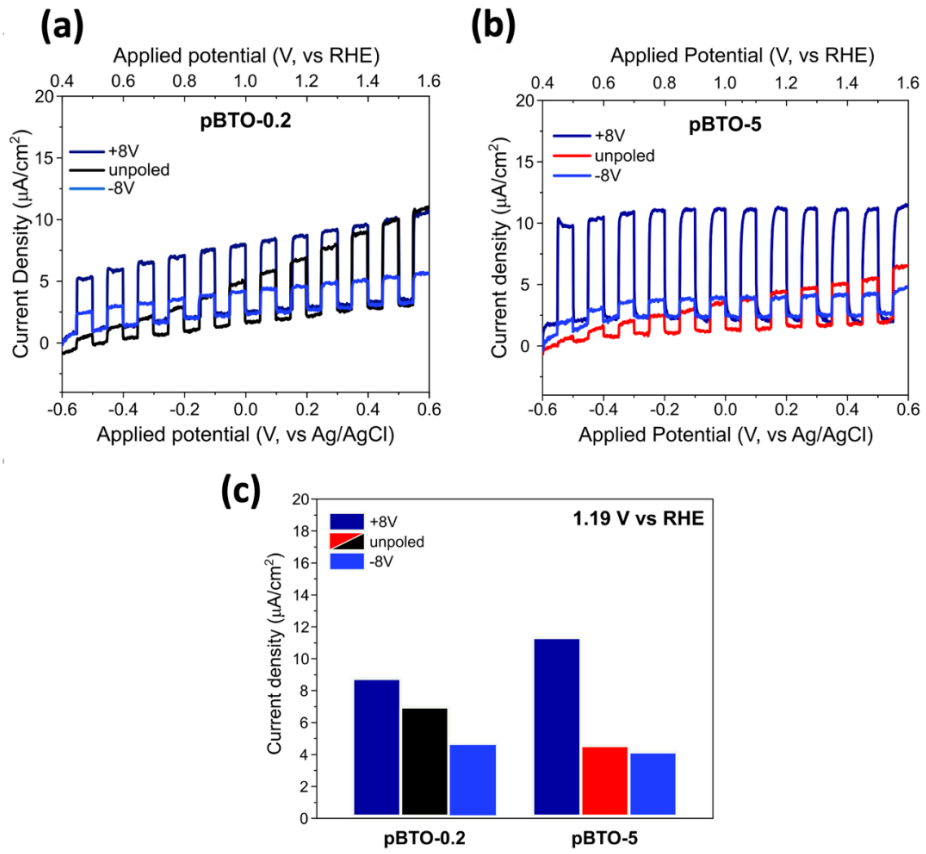

Figure 4.22 LSV curves of pBTO-0.2 (a) and pBTO-5 (b) obtained under chopped illumination in 1M NaOH before and after EC poling and relative comparison of the current density values obtained at 1.19 V vs RHE (c).

This enhancement in the photoelectrochemical response can be related to the band-bending at the pBTO/electrolyte interface with electric field polarization. When pBTO is exposed to illumination, electron-hole (e^--h^+) pairs are generated and e^- will migrate to the C^+ surface while h^+ will move on C^- surface, according to the polarization direction where C^+ and C^- corresponds to the ferroelectric domains that show upward and downward polarization, respectively. During positive poling, the applied field in pBTO points towards the substrate, aligning the ferroelectric domains with polarization downward from the surface (C^-), which in turn induces the formation of an internal depolarization field ($\mathbf{E}_{dep}$) that opposes the polarization direction. To obtain charge compensation, $\mathbf{E}_{dep}$ promotes hole accumulation at the surface of pBTO, leading to upward band-bending. Therefore, positive poling enhances hole transfer from the ferroelectric surface to the electrolyte to participate in the water oxidation reaction, favouring the performance of pBTO as photoanodes as observed (Figure 4.23).

However, the effect of positive poling is more evident in pBTO-5 compared to pBTO-0.2. Indeed, at 1.19 V vs RHE, +8 V EC poled pBTO-5 shows an increment of the photocurrent density of about 7 $\mu A/cm^2$ compared to the unpoled counterpart. On the other hand, the +8 V EC poling state of pBTO-0.2 shows a higher photocurrent density (8.6 $\mu A/cm^2$ at 1.19 V vs RHE) than the unpoled state (6.8 $\mu A/cm^2$ at 1.19 V vs RHE), but the increase of PEC response is not as significant as in pBTO-5 (Figure 4.22 c). This suggests that the PEC performance cannot be changed drastically using EC poling from the as-produced state in the pBTO-0.2 sample.

This evidence can be correlated to the PFM results previously reported for pBTO-5 and pBTO-0.2 thin films. In pBTO-5 thin film, the almost complete domains switching

observed is reflected in a greater enhancement in the PEC performance after positive poling, compared to pBTO-0.2, where the smaller pores and grains of pBTO-0.2 may make polarisation switching more difficult.

After -8 V EC poling, pBTO-0.2 exhibits a reduced photocurrent density (4.5 µA/cm^2 at 1.19 V vs RHE) compared to the unpoled state (6.8 µA/cm^2 at 1.19 V vs RHE), as shown in Figure 4.22 c. Indeed, during negative poling, the applied electric field points to the pBTO surface, generating the formation of opposite $\mathbf{E}_{dep}$ which will create electron accumulation at the surface of pBTO and consequently downward band-bending. This leads to the presence of more electrons available for the water reduction reaction but suppresses hole injection and therefore photocurrent under anodic bias (Figure 4.23). This trend in terms of PEC response is also observed in pBTO-5 which shows slightly lower photocurrent density after -8V EC poling (4 µA/cm^2 at 1.19 V vs RHE), compared to the unpoled state (4.4 µA/cm^2 at 1.19 V vs RHE) (Figure 4.22 c).

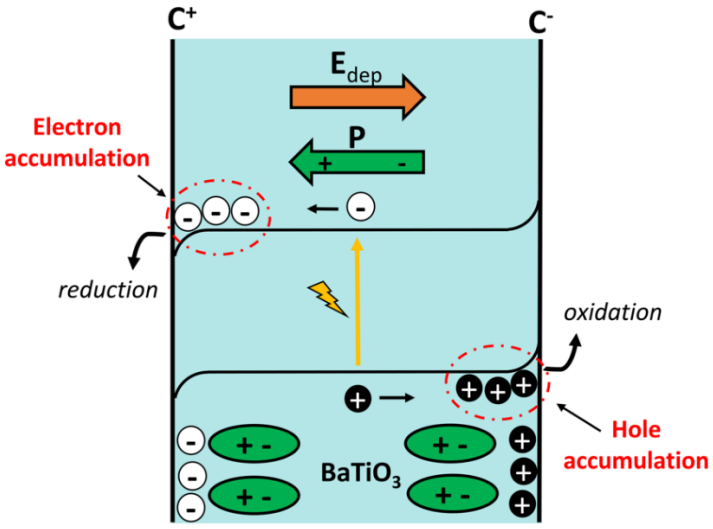

Figure 4.23 Schematic of band-bending, which occurs at pBTO/electrolyte interfaces depending on the polarisation orientation.

In the case of pBTO-5 this decrement of photocurrent with -8 V EC poling is only slight, again correlating with PFM measurements, where a greater level of P_{down} imprint was observed in the as-prepared sample, therefore less change in photocurrent would be expected after negative poling, as observed.

4.3 Summary

This chapter has outlined the development and study of nanostructured BTO thin films, which can be promising candidates as photoanodes for the improvement of PEC performance thanks to their ferroelectric polarization. Two different approaches were used to produce such nanostructured films. Firstly, the hydrothermal conversion of TiO_2 to $BaTiO_3$ was investigated. However, such nanostructured BTO thin films failed to show a good photocatalytic performance probably due to their insufficient light absorption properties and poor crystallinity. Moreover, it was not possible to achieve accurate control of the morphological features in nanostructured BTO thin films. Therefore, a soft template-assisted sol-gel method, using different amounts of P123 organic sacrificial template, was used as second approach for the preparation of porous BTO (pBTO) thin films.

For the pBTO thin films, the concentration-dependent tuning of the porosity was evidenced by SEM analysis and ellipsometry technique, using air and water as mediums. The combination of these analyses indeed demonstrated the linear dependence of the porosity with the amount of P123 block-copolymer. XRD analysis and Raman spectroscopy were performed to confirm the tetragonal phase of the pBTO thin films, which is responsible for the ferroelectric behaviour of BTO. In addition, using PFM, the

switching of spontaneous polarization in pBTO thin films was verified and it was observed that it appears more complete in pBTO-5 than pBTO-0.2. Owing to their controllable porosity, pBTO thin films resulted promising candidates as photoanodes, with all pBTO samples displaying enhanced photocurrent compared to a non-porous BTO film. It was also observed that when the quantity of P123 block copolymer was increased, the PEC response gradually decreased, and this evidence was related to the lower surface area in pBTO-5, compared to pBTO-0.2. Moreover, after performing +8 V EC poling, a clear improvement in the PEC performance of pBTO-5 compared to pBTO-0.2 was evidenced, which is in accordance with the PFM results obtained. This suggests that positive poling is very favourable when pBTO is used as a photoanode.

Thus, the controlled PEC response of a porous ferroelectric film via electrochemical poling has been demonstrated, which opens up opportunities to tune and optimize the morphology of ferroelectric films for photoelectrochemical applications while still maintaining the advantages conferred by ferroelectric polarization.

REFERENCES

1. Sun, M. H. *et al.* Applications of hierarchically structured porous materials from energy storage and conversion, catalysis, photocatalysis, adsorption, separation, and sensing to biomedicine. *Chem. Soc. Rev.* **45**, 3479–3563 (2016).

2. Li, Y., Fu, Z. Y. & Su, B. L. Hierarchically structured porous materials for energy conversion and storage. *Adv. Funct. Mater.* **22**, 4634–4667 (2012).

3. Zhang, Z., Wang, C. C., Zakaria, R. & Ying, J. Y. Role of particle size in nanocrystalline TiO_2-based photocatalysts. *J. Phys. Chem. B* **102**, 10871–10878 (1998).

4. Lines, M. E. & Glass, A. M. Principles and Applications of Ferroelectrics and Related Materials. (Oxford University Press, 1997).

5. Giocondi, J. L. & Rohrer, G. S. Spatial separation of photochemical oxidation and reduction reactions on the surface of ferroelectric $BaTiO_3$. *J. Phys. Chem. B* **105**, (2001).

6. Morris, M. R., Pendlebury, S. R., Hong, J., Dunn, S. & Durrant, J. R. Effect of Internal Electric Fields on Charge Carrier Dynamics in a Ferroelectric Material for Solar Energy Conversion. *Adv. Mater.* **28**, 7123–7128 (2016).

7. Kalinin, S. V. *et al.* Atomic Polarization and Local Reactivity on Ferroelectric Surfaces: A New Route toward Complex Nanostructures. *Nano Lett.* **2**, 589–593 (2002).

8. Inoue, Y., Yoshioka, I. & Sato, K. Polarization effects upon adsorptive and catalytic properties. 1. CO oxidation over Pd deposited on $LiNbO_3$ ferroelectrics. *J. Phys. Chem.* **88**, 1148–1151 (1984).

9. Burbure, N. V., Salvador, P. A. & Rohrer, G. S. Photochemical reactivity of titania films on $BaTiO_3$ substrates: Origin of spatial selectivity. *Chem. Mater.* **22**, 5823–5830 (2010).

10. Burbure, N. V., Salvador, P. A. & Rohrer, G. S. Photochemical reactivity of titania films on $BaTiO_3$ substrates: Influence of titania phase and orientation. *Chem. Mater.* **22**, 5831–5837 (2010).

11. Cheng, X., Dong, W., Zheng, F., Fang, L. & Shen, M. Enhanced photocathodic behaviors of $Pb(Zr_{0.20}Ti_{0.80})O_3$ films on Si substrates for hydrogen production. *Appl. Phys. Lett.* **106**, 0–4 (2015).

12. Rioult, M. *et al.* Tailoring the photocurrent in $BaTiO_3$/Nb:$SrTiO_3$ photoanodes by controlled ferroelectric polarization. *Appl. Phys. Lett.* **107**, 1–5 (2015).

13. Cao, D., Wang, Z., Wen, L., Mi, Y. & Lei, Y. Switchable Charge-Transfer in the Photoelectrochemical Energy- Conversion Process of Ferroelectric $BiFeO_3$ Photoelectrodes. *Angew. Chemie - Int. Ed.* 1–6 (2014).

14. Singh, S., Sangle, A. L., Wu, T., Khare, N. & MacManus-Driscoll, J. L. Growth of Doped $SrTiO_3$ Ferroelectric Nanoporous Thin Films and Tuning of Photoelectrochemical Properties with Switchable Ferroelectric Polarization. *ACS Appl. Mater. Interfaces* **11**, 45683–45691 (2019).

15. Singh, S. & Khare, N. Electrically tuned photoelectrochemical properties of ferroelectric nanostructure $NaNbO_3$ films. *Appl. Phys. Lett.* **110**, (2017).

16. Das, S. *et al.* High performance $BiFeO_3$ ferroelectric nanostructured photocathodes. *J. Chem. Phys.* **153**, 1–8 (2020).

17. Li, S. *et al.* Manipulation of charge transfer in vertically aligned epitaxial ferroelectric $KNbO_3$ nanowire array photoelectrodes. *Nano Energy* **35**, 92–100 (2017).

18. Khan, M. A., Kurchania, R., Corkovic, S., Zhang, Q. & Milne, S. J. Compaction of lead zirconate titanate sol-gel coatings. *Mater. Lett.* **60**, 1463–1465 (2006).

19. Zhang, Q., Corkovic, S., Shaw, C. P., Huang, Z. & Whatmore, R. W. Effect of porosity on the ferroelectric properties of sol-gel prepared lead zirconate titanate thin films. *Thin Solid Films* **488**, 258–264 (2005).

20. Suzuki, N. *et al.* Chemical Synthesis of Porous Barium Titanate Thin Film and Thermal Stabilization of Ferroelectric Phase by Porosity-Induced Strain. *J. Vis. Exp.* 1–7 (2018).

21. Matavž, A., Bradeško, A., Rojac, T., Malič, B. & Bobnar, V. Self-assembled porous ferroelectric thin films with a greatly enhanced piezoelectric response. *Appl. Mater. Today* **16**, 83–89 (2019).

22. Castro, A., Ferreira, P., Rodriguez, B. J. & Vilarinho, P. M. The role of nanoporosity on the local piezo and ferroelectric properties of lead titanate thin films. *J. Mater. Chem. C* **3**, 1035–1043 (2015).

23. Ferreira, P. *et al.* Nanoporous piezo- and ferroelectric thin films. *Langmuir* **28**, 2944–2949 (2012).

24. Naoyama, T., Sakioka, Y., Noda, M., Okuyama, M. & Saito, K. A low Temperature preparation of $BaTiO_3$ thin film by Sol-Gel-Hydrothermal treatment below 210°C. *Jpn. J. Appl. Phys.* **44**, 6873–6877 (2005).

25. Wemple, S. H. Polarization Fluctuations and the Optical-Absorption Edge in $BaTiO_3$. *Phys. Rev. B* **2**, 2679 (1970).

26. Singh, M., Yadav, B. C., Ranjan, A., Kaur, M. & Gupta, S. K. Synthesis and characterization of perovskite barium titanate thin film and its application as LPG sensor. *Sensors Actuators, B Chem.* **241**, 1170–1178 (2017).

27. Smith, M. B., Page, K., Siegrist, T. & Et, A. Crystal structure and the paraelectric-to-ferroelectric phase transition of nanoscale $BaTiO_3$. *J. Am. Chem. Soc.* **130**, 6955–6963 (2008).

28. Zhang, W. H. *et al.* Raman study of barium titanate with oxygen vacancies. *Phys. B Condens. Matter* **406**, 4630–4633 (2011).

29. Xiao, C. J., Jin, C. Q. & Wang, X. H. Crystal structure of dense nanocrystalline $BaTiO_3$ ceramics. *Mater. Chem. Phys.* **111**, 209–212 (2008).

30. Cui, Y., Briscoe, J. & Dunn, S. Effect of ferroelectricity on solar-light-driven photocatalytic activity of $BaTiO_3$ - Influence on the carrier separation and stern layer formation. *Chem. Mater.* **25**, 4215–4223 (2013).

31. Alvarez-Fernandez, A. *et al.* Fractionation of block copolymers for pore size control and reduced dispersity in mesoporous inorganic thin films. *Nanoscale* **12**, 18455–18462 (2020).

32. Reid, B., Alvarez-Fernandez, A., Schmidt-Hansberg, B. & Guldin, S. Tuning Pore Dimensions of Mesoporous Inorganic Films by Homopolymer Swelling. *Langmuir* **35**, 14074–14082 (2019).

33. Lokupitiya, H. N., Jones, A., Reid, B., Guldin, S. & Stefik, M. Ordered Mesoporous to Macroporous Oxides with Tunable Isomorphic Architectures: Solution Criteria for Persistent Micelle Templates. *Chem. Mater.* **28**, 1653–1667 (2016).

34. Wemple, S. H., Didomenico, M. & Camlibel, I. Dielectric and optical properties of melt-grown $BaTiO_3$. *J. Phys. Chem. Solids* **29**, 1797–1803 (1968).

35. Alvarez-Fernandez, A. *et al.* Structural Characterization of Mesoporous Thin Film Architectures: A Tutorial Overview. *ACS Appl. Mater. Interfaces* **12**, 5195–5208 (2020).

36. Wemple, S. H. Polarization Fluctuations and the Optical-Absorption Edge in $BaTiO_3$. *Phys. Rev. B* **2**, 2679–2689 (1970).

37. Sharma, H. B. Structural and optical properties of sol-gel derived barium titanate thin film. *Int. J. Mod. Phys. B* **21**, 1837–1849 (2007).

38. Vaněček, M., Poruba, A., Remeš, Z., Beck, N. & Nesládek, M. Optical properties of microcrystalline materials. *J. Non. Cryst. Solids* **227**–**230**, 967–972 (1998).

39. Suzuki, N. *et al.* Chemical synthesis of porous barium titanate thin film and thermal stabilization of ferroelectric phase by porosity-induced strain. *J. Vis. Exp.* **2018**, 1–7 (2018).

40. Suzuki, N., Osada, M., Billah, M., Alothman, Z. A. & Bando, Y. Origin of thermally stable ferroelectricity in a porous barium titanate thin film synthesized through block copolymer templating. *APL Mater.* **5**, 076111 (2017).

41. Solis, D. & Vigueras, E. Textural , structural and electrical properties of TiO_2 nanoparticles using Brij 35 and P123 as surfactants. *Sci. Technol. Adv. Mater.* (2008).

42. Zeng, H. R. *et al.* Piezoresponse force microscopy studies of nanoscale domain structures in ferroelectric thin film. *Mater. Sci. Eng. B Solid-State Mater. Adv. Technol.* **120**, 104–108 (2005).

43. Melo, M., Araújo, E. B., Shvartsman, V. V., Shur, V. Y. & Kholkin, A. L. Thickness effect on the structure, grain size, and local piezoresponse of self-polarized lead lanthanum zirconate titanate thin films. *J. Appl. Phys.* **120**, (2016).

44. Neumayer, S. M. *et al.* Piezoresponse amplitude and phase quantified for electromechanical characterization. *J. Appl. Phys.* **128**, 1–11 (2020).

45. Balke, N. *et al.* Exploring local electrostatic effects with scanning probe microscopy: Implications for piezoresponse force microscopy and triboelectricity. *ACS Nano* **8**, 10229–10236 (2014).

46. Jesse, S., Baddorf, A. P. & Kalinin, S. V. Switching spectroscopy piezoresponse force microscopy of ferroelectric materials. *Appl. Phys. Lett.* **88**, 1–4 (2006).

47. Li, Y., Li, J., Yang, W. & Wang, X. Implementation of ferroelectric materials in photocatalytic and photoelectrochemical water splitting. *Nanoscale Horizons* **5**, 1174–1187 (2020).

5 ROLE OF OXYGEN VACANCIES IN THE POLING OF $BATIO_3$ PHOTOANODES

5.1 INTRODUCTION

One of the most effective strategies recently used in a PEC water splitting system to improve charge separation is the tuning of internal electric field, which appear at semiconductor/electrolyte interface[1,2]. Among various materials which exploit the internal electric field to enhance water splitting performance, ferroelectrics can be ideal candidates. They possess spontaneous dipole moments without applying stress, producing

spontaneous polarisation which can facilitate the separation of electron-hole pairs, driving them towards the opposite direction[3].

As shown in the Chapter 4, the introduction of mesopores in $BaTiO_3$ as ferroelectric material can generate new opportunities in photo-electrocatalysis, thanks to the inclusion of new functionalities in the same material[4,5,6]. In particular, this is due to the higher surface-area-to-volume ratio, as the fraction of surface atoms in mesoporous materials increases compared to the bulk and this affects the surface activity[7]. Suzuki *et al*. have also demonstrated that the presence of porosity in $BaTiO_3$ thin films can directly introduce strain, which leads to the thermal stabilization of ferroelectric phase[8].

In perovskite oxide ferroelectric materials (*e.g.* barium titanate (BTO), potassium niobate (KNO), lead zirconate titanate (PZT)), oxygen vacancies are known as the most common mobile point defects, which considerably affect their ferroelectric behaviour due to the oxygen vacancies migration and redistribution[9]. These defects are usually created by the removal of an oxygen atom from the crystalline structure, which consequently remains charged with two extra electrons[10]. The formation of these oxygen vacancies can be associated either with treatments altering the chemical environment of perovskite oxide material (*e.g* sintering temperature[11], annealing under different atmospheres[12]) or with the introduction of dopants into the perovskite lattice[13].

To study the effect of ferroelectric polarization for photocatalytic applications, different procedures have been reported, such as poling in an electrolyte[14,15,16] or using a top electrode on the surface[17,18,19,20]. However, the possible chemical modification induced by electric polarization of ferroelectric materials, particularly the effect on mobile ionic species such as oxygen vacancies, was not considered in detail in these research works.

Recently, Magnan *et al.* reported an alternative soft poling method in electrolyte which involves modulated low potential to preserve the chemical composition of the sample. Indeed, the authors confirmed by XPS analysis that the intensity and shape of photoemission peaks are almost unchanged after the poling procedure, suggesting that this process does not alter the film. However, even if it was demonstrated that the ferroelectric polarisation can be reversed in these films, by applying different successive poling, the photocurrent values were not completely reversible using this method[21].

Thus, this chapter explores the influence of the electrochemical (EC) poling process on the surface oxygen vacancies concentration of porous $BaTiO_3$ (pBTO) thin films, prepared in O_2, air and N_2 atmospheres, which are correlated to different contents of oxygen vacancies. The choice of porous thin films, which present an enhanced surface activity with respect to the bulk, can maximize the potential effect of EC poling, allowing the study of the pBTO surface in greatest detail. It is demonstrated that the photoelectrochemical response of pBTO photoanodes can still be tuned via ferroelectric polarisation using an EC poling procedure, provided the concentration of oxygen vacancies in the films is not considerably high. Interestingly, the mutual effect of ferroelectric polarisation and oxygen vacancies can further improve the photoelectrochemical performance of the porous ferroelectric films. However, in ferroelectric thin films with higher oxygen vacancies concentration, the higher diffusion of oxygen vacancies greatly influences the EC poling procedure, giving very unpredictable results.

5.2 Porous BTO thin films in different annealing conditions

5.2.1 Morphological structure and elemental composition

Porous BTO (pBTO) thin films were synthesized following the soft template-assisted sol-gel method, illustrated in Chapter 4, under different annealing atmospheres (O_2, air, N_2), using the experimental procedure described in Chapter 3. The top-view SEM images, reported in Figure 5.1 a, confirm the porous structure of the obtained pBTO thin films prepared in O_2, air and N_2 conditions (pBTO-O_2, pBTO-air, pBTO-N_2). As observed in Figure 5.1 b, the porosity and thickness of pBTO-O_2, pBTO-air and pBTO-N_2, estimated from the top-view and cross sectional SEM images, respectively, show comparable values, suggesting that the use of different annealing conditions does not affect those parameters considerably.

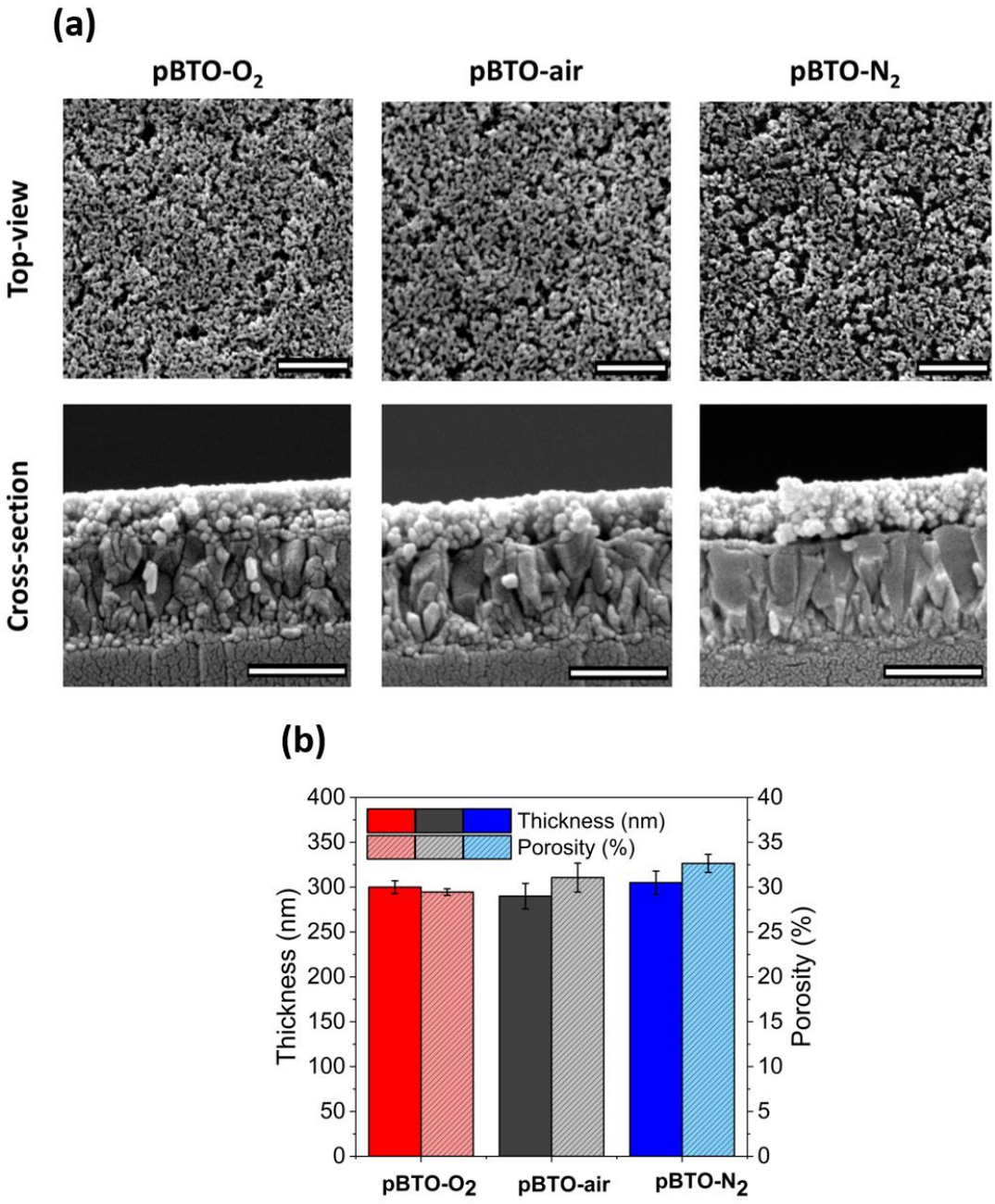

Figure 5.1 SEM top view and cross-sectional SEM images of pBTO-5 thin films, prepared in different annealing atmosphere O_2, air, N_2 (scale bar: 500 nm) (a); estimation of thickness and porosity of pBTO-5 O_2, pBTO-5 air, pBTO-5 N_2 (b).

Moreover, Figure 5.2 a,b,c show the EDX spectra of pBTO-O_2, pBTO-air and pBTO-N_2 samples, where the high intensity peaks corresponding to the Ba, Ti, and O elements are

clearly observed. The presence of Si and Sn elements is also noticed due to the FTO glass substrate, where the pBTO thin films were deposited. In addition, even if the concentration of oxygen as a light element is not detected accurately by EDX analysis, comparing O/Ba ratio of all samples, a decrease in the oxygen content, which could be related to oxygen vacancies, is observed in pBTO-O_2 (44.33), pBTO-air (42.51), pBTO-N_2 (38.81) (Figure 5.2 d).

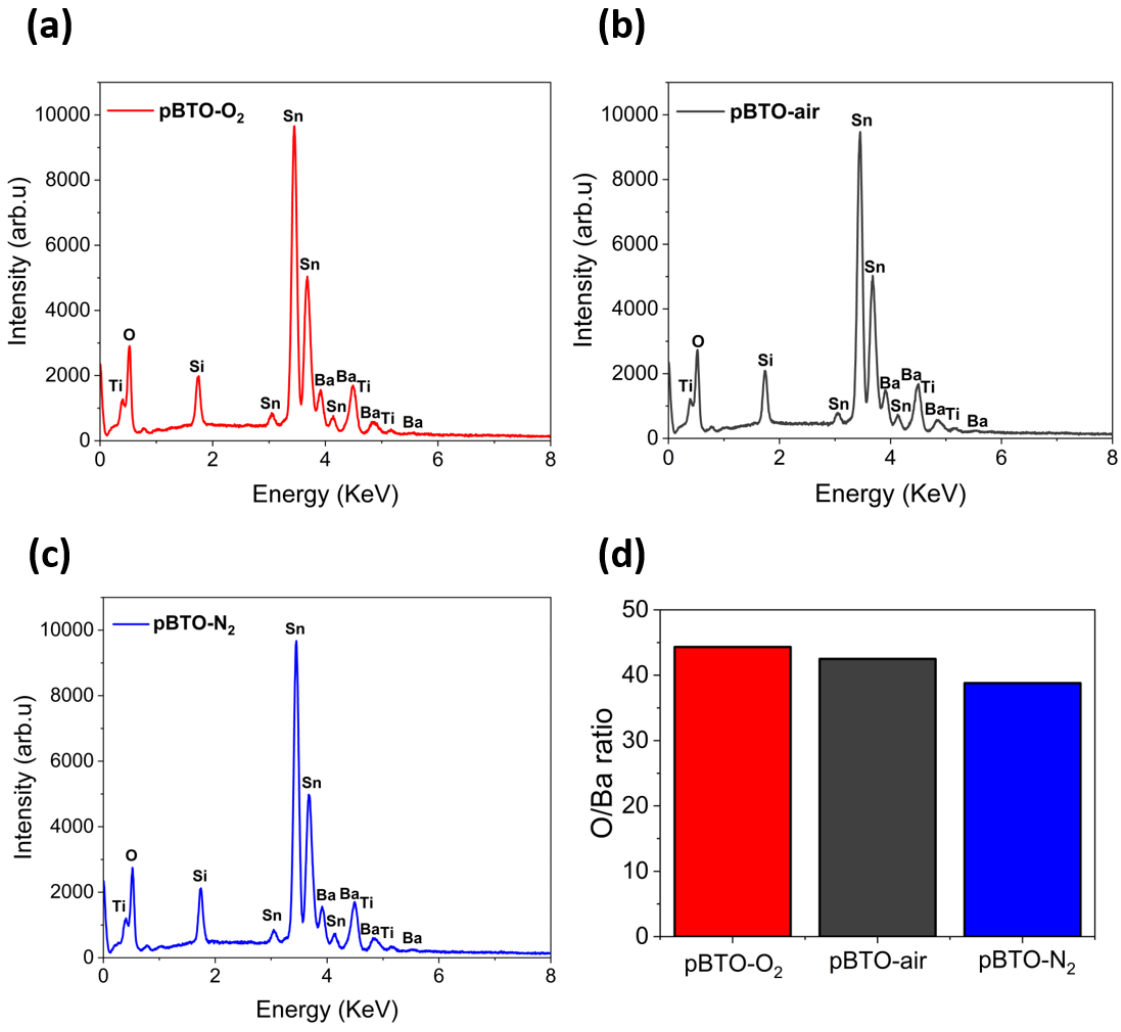

Figure 5.2 EDX spectra of pBTO-O_2 (a), pBTO-air (b), pBTO-N_2 (c) and corresponding O/Ba ratio detected in the films (d).

5.2.2 Optical properties

The transmittance spectra of pBTO samples show band edges in the UV region at a wavelength of 350-380 nm (Figure 5.3). The optical bandgaps energies of pBTO-O_2, pBTO-5 air and pBTO-N_2 thin films, estimated using Tauc relation, are found to be in the range of 3.68 to 3.57 eV, which is in agreement with values previously reported for BTO thin films, synthesized by the sol-gel method (3.7 eV))[22] (Figure 5.3 inset). Sharma *et. al.* has shown that the preparation technique can create differences in the stoichiometry and defect distribution of the films, inducing variations in the calculated bandgap energies[22], compared to bulk BTO samples (3.4 eV)[23]. As observed in Figure 5.3, the shifting of light absorption onset in the visible light region in pBTO-N_2 leads to a decrease in its optical bandgap, which could be associated to sub bandgap defects created by the annealing in N_2 atmosphere[24]. Moreover, it has been found that porosity in thin films can affect the scattering of light from the surface, leading to apparent absorption enhancement, which influence the measured transmittance spectra[25]. Consequently, the presence of porosity and sub bandgap defects can both mutually contribute to the variations in the estimated bandgap energies of the pBTO thin films.

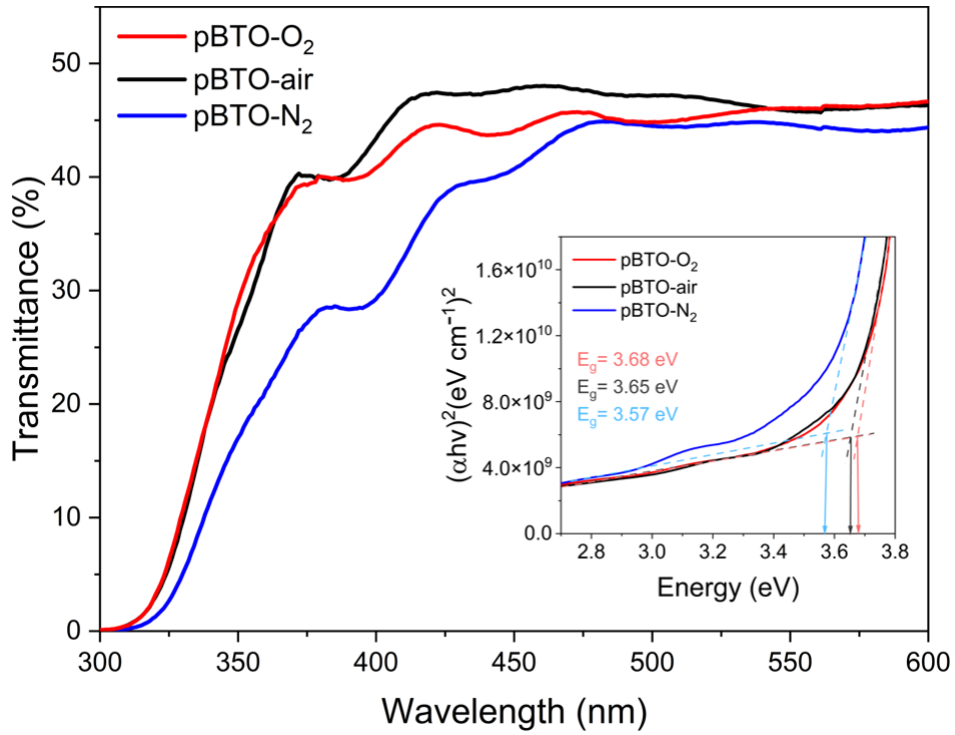

Figure 5.3 Transmittance spectra of pBTO-5 O_2, pBTO-5 air and pBTO-5 N_2 and corresponding bandgap energies, estimated from Tauc plots (inset).

5.2.3 Crystallographic structure

XRD patterns of pBTO-O_2, pBTO-air and pBTO-N_2, acquired to investigate the crystalline phase of the samples, confirm the formation of perovskite barium titanate. However, comparing the XRD diffractograms obtained with the respective JCPDS card No. 00-066-0829 referred to BTO tetragonal (ferroelectric) phase, the peak splitting at 2ϑ= 45° into two peaks at 2ϑ= 44.8° and 2ϑ=45.4°, corresponding to *hkl* Miller indices (002) and (200), is not clearly visible (Figure 5.4 a). This is confirmed by the high resolution XRD patterns, shown in Figure 5.4 b. Indeed, it has been reported that the polycrystalline nature of the films broadened the peak width, leading to a not clearly observable peak splitting[26]. Moreover, previous research works have demonstrated that

the presence of strain can stabilize the cubic (paraelectric) phase regardless of the tetragonal (ferroelectric) phase, which is the most thermodynamically stable at room temperature[27,28]. However, the ferroelectricity of pBTO thin films, prepared using the same preparation technique, was demonstrated in Chapter 4, showing PFM amplitude and phase signals as well as SS-PFM hysteresis loops, in combination with Raman spectroscopy, which confirm their tetragonal (ferroelectric) phase, and ferroelectric switching behaviour[4].

Moreover, analysing the XRD patterns of pBTO thin films shown in this work in more detail, one can note that the area ratio of (101)/(002) peaks gradually increases in pBTO-O_2 (1.09), pBTO-air (1.56) and pBTO-N_2 (1.85) (Figure 5.4 b). It indicates that the pBTO-5 thin films show increasing (001) preferred orientation when the oxygen concentration of annealing atmosphere drops. Therefore, this result suggests that competitive growth among various orientations may take place in different annealing conditions: indeed, previous research works have reported a similar phenomenon in other ferroelectric materials, sintered in N_2 atmosphere[12,29,30]. The different orientation may be ascribed to the anisotropy of nucleation and growth rates in different directions when the samples are annealed in different atmospheres, which contributes to a change in the predominant orientation[29]. It is not clear whether this is driven directly by a difference in the crystallisation kinetics or chemical pathway in different atmospheres, or whether the increased inclusion of oxygen vacancies in N_2-annealed films may slightly alter the relative orientation preference during crystallisation, as this was not reported in previous work. It would be challenging to differentiate these effects in the samples prepared in this thesis as they are polycrystalline films grown on non-epitaxial substrates. Therefore, a future study of the growth mechanisms of samples annealed in different atmospheres

when deposited on epitaxial substrates could be an interesting route to shed light on this phenomenon.

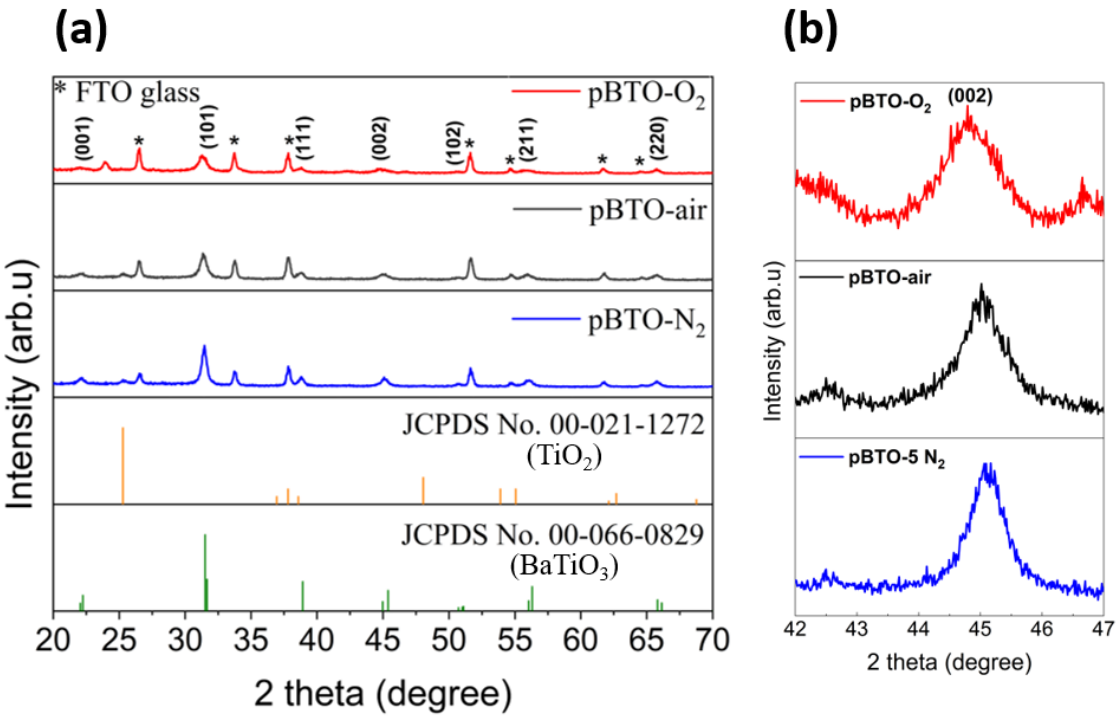

Figure 5.4 XRD patterns of pBTO-O2, pBTO-air, pBTO-N2 thin films (a) and corresponding enlargement in the region 42-47° (b).

5.2.4 Surface structure investigation

To study the effect of the different annealing conditions on the surface chemistry of pBTO thin films, XPS analysis was carried out. Figure 5.5 shows the survey spectra of pBTO-O2, pBTO-air and pBTO-N2, where the presence of C on the surface of all the samples is observed. However, the C1s signal is weaker than O1s intensity, suggesting that C contamination does not affect the XPS measurements significantly.

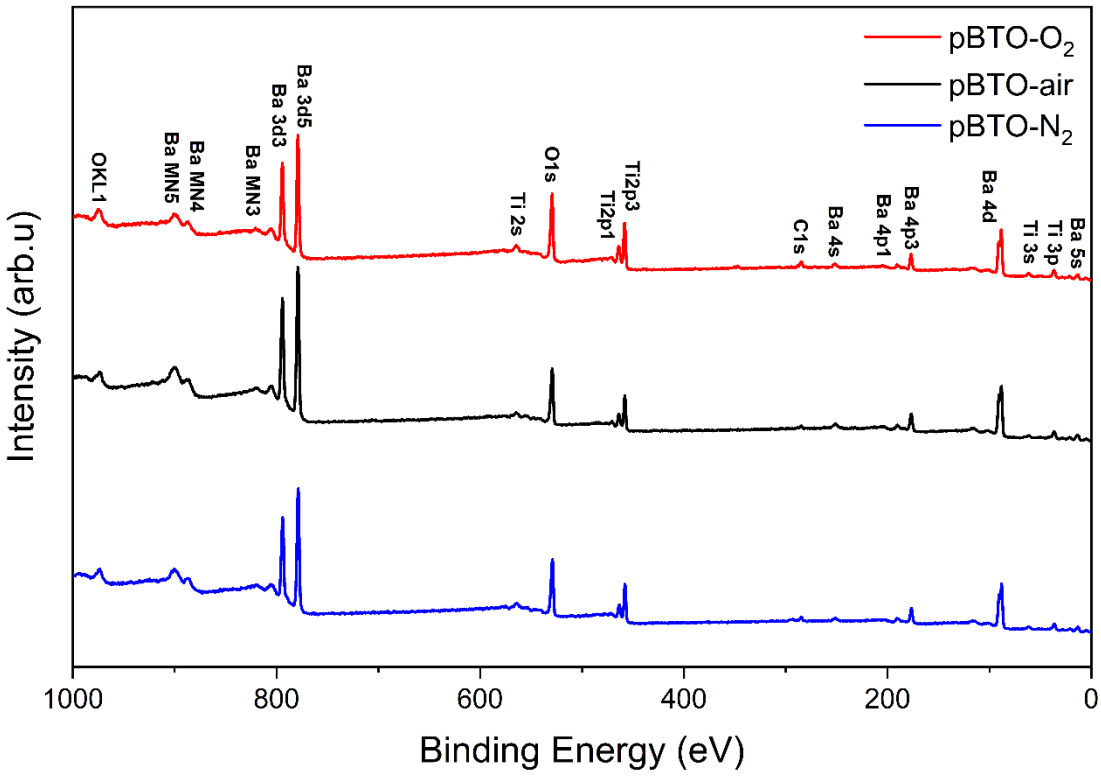

Figure 5.5 XPS survey spectra of pBTO thin films, prepared in different annealing atmosphere (O_2, air, N_2).

The Ba 3d, Ti 2p and O 1s high-resolution spectra of pBTO-O_2, pBTO-air and pBTO-N_2 are reported in Figure 5.6. The O1s high resolution XPS peak of pBTO films can be consistently fitted by two different Gaussian sub-peaks, indicated as O1s (I) and O1s (II). In particular, the main peak O1s (I) (529.31 eV) is attributed to the lattice oxygen ions (O^{2-}), which are bonded with barium (Ba^{2+}) and titanium (Ti^{4+}) ions in BTO while the broad peak O1s (II) (530.95 eV) is associated with the oxygen ions (O_2^-/O^-) in a different environment due to the oxygen vacancies[12]. Comparing the O1s XPS peak of pBTO-O_2, pBTO-air and pBTO-N_2, the contribution of O1s (II) sub-peak gradually increases, suggesting an increment in the content of oxygen vacancies concentration, expressed in terms of $O_{vacancy}/O_{lattice}$ area ratio (Figure 5.6 b). Indeed, the $O_{vacancy}/O_{lattice}$ area ratio value

obtained for pBTO-N_2 (1.49) is higher than both pBTO-air (0.50) and pBTO-O_2 (0.32), respectively (Figure 5.6 bi, ii, iii). This evidence indicates that the annealing in oxygen-enriched ambient induces a decrease in the oxygen vacancy content[12].

Ba $3d_{5/2}$ (I) and Ba $3d_{3/2}$ (I) peaks, which are associated with a binding energy of 778 eV and 793.3 eV respectively, correspond to Ba^{2+} state in the BaO moiety of perovskite BTO[13]. In addition, the presence of Ba 3d (II) shoulders at 779.4 eV and 794.6 eV is observed[31]. The exact attribution of these second peaks is still unclear and remains under debate: they have been previously correlated to Ba vacancy defects, surface $BaCO_3$ contamination and oxygen vacancy from the surface-layer of Ba ions. In Figure 5.6, it can be noted that the peak area of both 779.4 eV and 794.6 eV increases from pBTO-O_2 to pBTO-N_2, suggesting that these peaks are caused by oxygen vacancies. In particular, it has been reported that during the generation of oxygen vacancies, the displaced O atoms, which are removed from the sample surface, can be trapped in the vicinity of BaO moiety, forming BaO_2 with +2 state for Ba and -1 for O. The peak associated with a binding energy of 779.4 eV can be correlated to the formation of BaO_2[32,33]. It can be observed that the peak area of BaO_2 gradually increases from pBTO-O_2 to pBTO-N_2, according to the oxygen vacancy content (Figure 5.6 a i, ii, iii).

Moreover, the high-resolution spectra of Ti 2p show the presence of $Ti2p_{3/2}$ (I) and $Ti2p_{1/2}$ (I) peaks, located at 457.7 eV and 464.4 eV respectively, related to Ti bonding in BTO perovskite structure with valency of 4+. In pBTO-air and pBTO-N_2, two small Ti 2p (II) components are also visible due to the reduced valence state of Ti (3+), associated with the formation of oxygen vacancies after annealing in air and N_2 conditions, in order to gain charge neutrality[34] (Figure 5.6 c i, ii, iii).

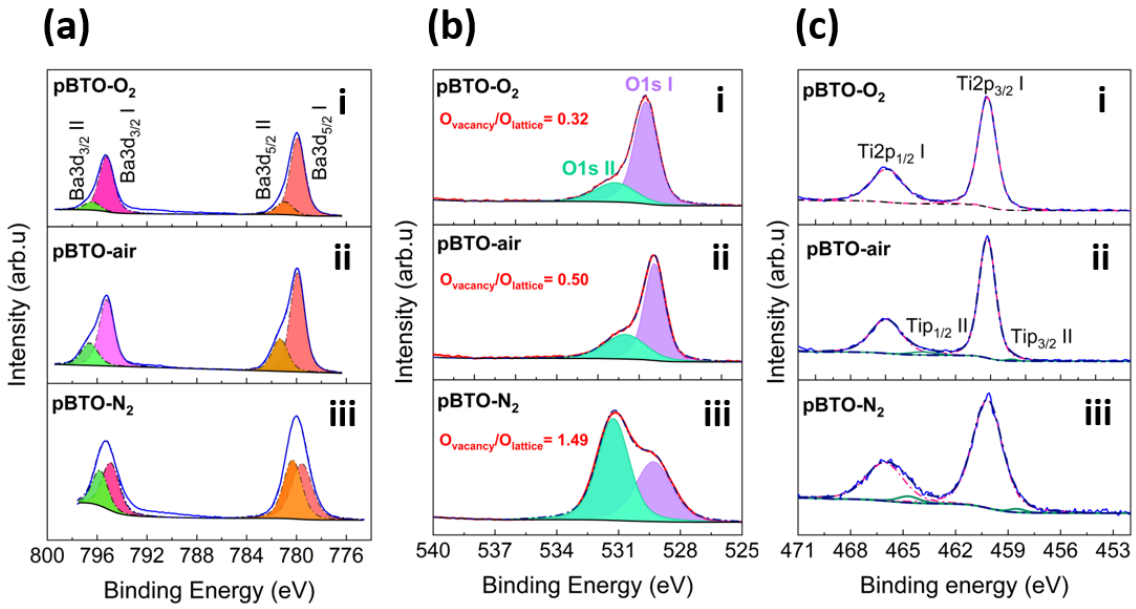

Figure 5.6 Ba 3d (a), O 1s (b) and Ti 2p (c) high resolution XPS spectra, relative to pBTO-O_2 (i), pBTO-air (ii) and pBTO-N_2 (iii); LSV chop curves of pBTO-O_2, pBTO-air, pBTO-N_2 (d) and relative current density values extrapolated at 0.19 V vs Ag/AgCl (e).

5.2.5 Photoelectrochemical performance

After confirming the effect of annealing condition on the oxygen vacancies content in pBTO thin films, their photoelectrochemical performance under chopped illumination was investigated. From the current density-voltage (J-V) curves, it is possible to observe that pBTO-N_2 shows higher photocurrent density than pBTO-air and pBTO-O_2 thin films, respectively, suggesting that the gradual increment in the oxygen vacancies concentration, induced by the different atmospheres, is beneficial for the PEC performance of pBTO thin films (Figure 5.7 a). Considering the photocurrent values extrapolated at 0.19 V vs Ag/AgCl and acquired across a range of samples, this trend can be confirmed and it can be observed that pBTO-N_2 show an enhancement of the

photocurrent of about 7.6 μA/cm^2 and 2.3 μA/cm^2 compared to pBTO-O_2 and pBTO-air, respectively (Figure 5.7 b). The presence of oxygen vacancies may have a double-sided effect on the PEC performance: the oxygen vacancies can create new energy levels, which facilitate the electron transition from valence band to conduction band, using less activating energy. In addition, oxygen vacancies can act as donors, increasing the carrier concentration and, consequently, the photoelectrochemical response[35]. This result is in good agreement with previous research works, which have investigated the relationship between oxygen vacancies and PEC properties in different semiconductor materials[10]: Gan *et al.* have reported that oxygen vacancies, generated in In_2O_3 nanocubes after annealing, provide a more efficient charge carrier transfer process, promoting enhanced PEC performance[33]. In addition, Corby *et al.* have shown that the appropriate modulation of oxygen vacancies in nanostructured WO_3 films can significantly reduce the bulk recombination, improving electron transport and charge separation, which maximizes the photocurrent response[36].

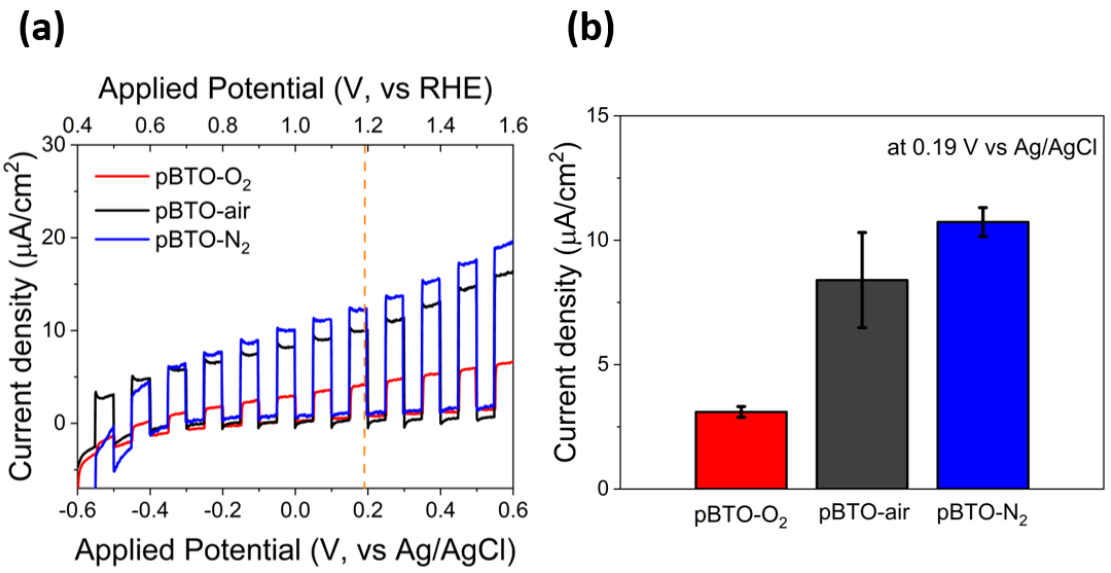

Figure 5.7 LSV chop curves of pBTO-O_2, pBTO-air, pBTO-N_2 (a) and relative current density values extrapolated at 0.19 V vs Ag/AgCl (b).

5.2.6 Tuning of photoelectrochemical response via electrochemical poling

To investigate the relationship between oxygen vacancies and poling process, which can be used to control the photocurrent response of pBTO thin films as demonstrated in Chapter 4, electrochemical (EC) poling was carried out on pBTO-O_2, pBTO-air and pBTO-N_2 thin films and the current density-voltage (J-V) and chronoamperometry (J-t) curves after this poling pretreatment were measured. Thus, to study the effect of ferroelectric polarization on the PEC response of pBTO thin films, J-t curves under chopped light illumination at 1.23 V vs RHE (oxidation potential of water), before and after EC poling were measured. The chronoamperometry curves show that the +8 V EC poling leads to an enhancement of the PEC performance in pBTO-O_2, pBTO-air and pBTO-N_2 thin films, compared to their unpoled states (Figure 5.8 a,b). These results are also consistent with the J-V curves of pBTO-O_2, pBTO-air and pBTO-N_2 samples, reported in Figure 5.9 a,b.

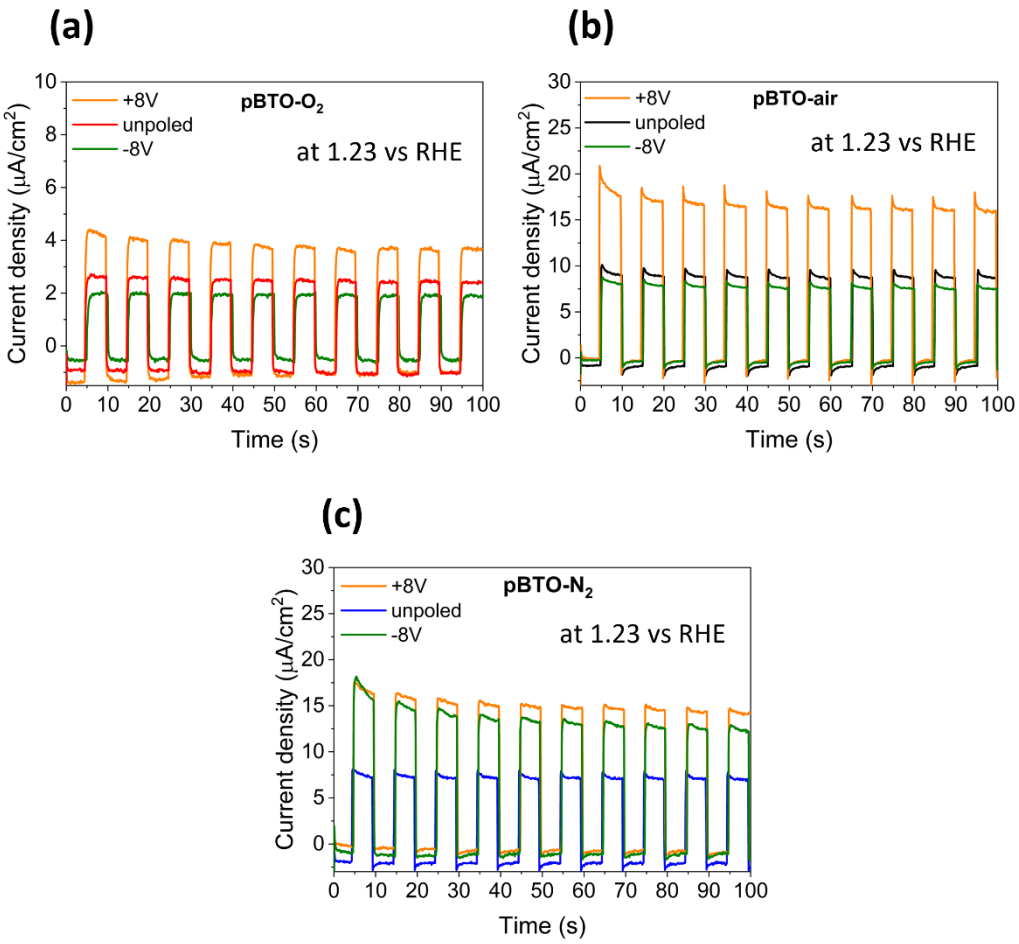

Figure 5.8 Chronoamperometry curves of pBTO-O_2 (a), pBTO-air (b), pBTO-N_2 (c), acquired in the upoled, +8 V and -8 V poled states under chopped illumination.

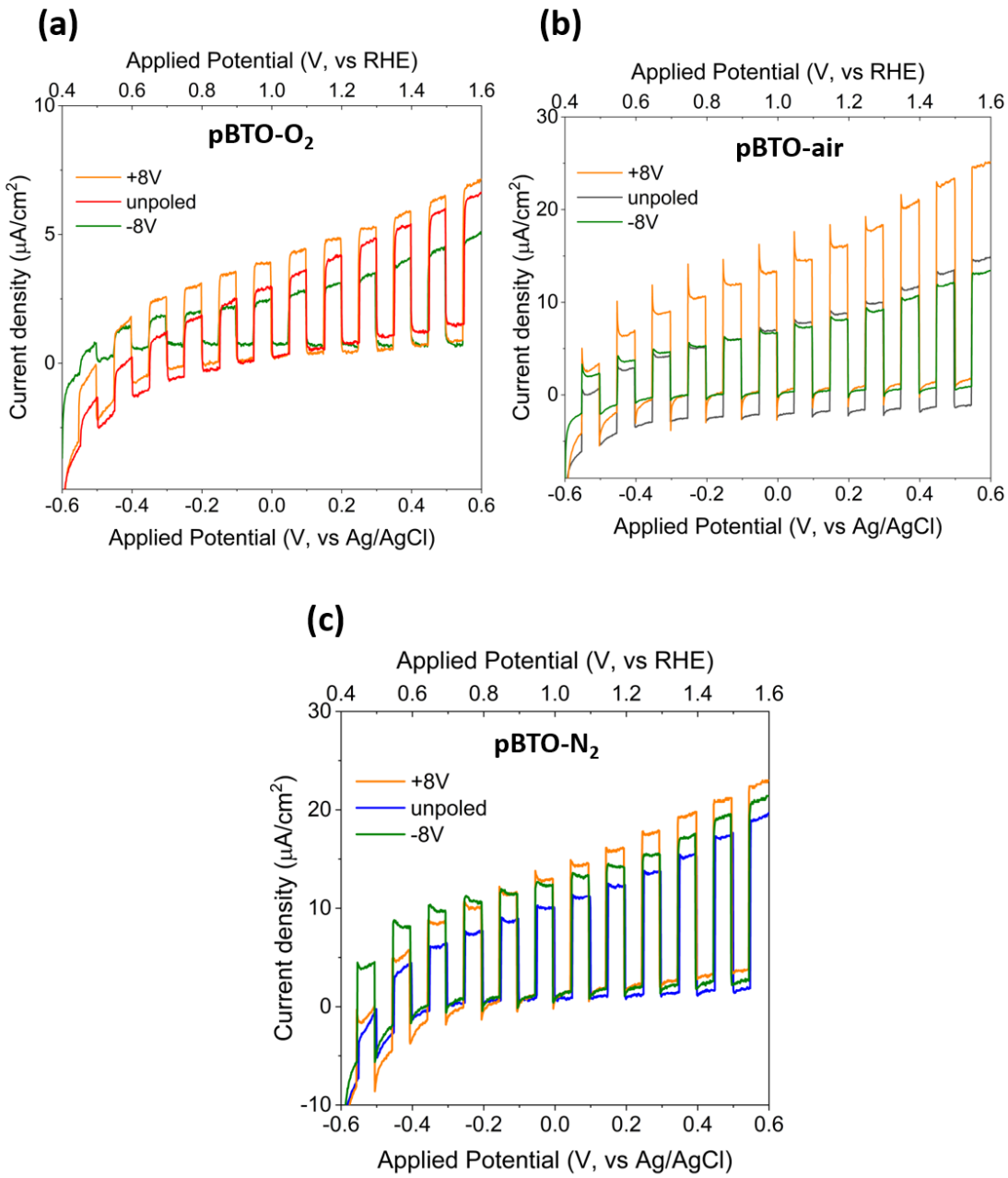

Figure 5.9 LSV curves under chopped illumination of pBTO-O_2 (a), pBTO-air (b) and pBTO-N_2 (c) after +8 V, -8 V EC poling and relative unpoled counterpart.

As reported in Chapter 4, this improvement in the photoelectrochemical response can be attributed to the band-bending at pBTO/electrolyte interface, induced by electric field polarization. When pBTO thin films are positively poled, the applied field in pBTO,

pointing towards FTO glass substrate, induces the alignment of ferroelectric domains with polarization downward from the pBTO/electrolyte interface, which in turn generates an internal depolarization field (E_{dep}), opposing the polarization direction. To gain charge compensation, this E_{dep} favours hole accumulation at pBTO/electrolyte interface, as shown in Figure 5.10 a (positive poling). As consequence, it increases the upward band-bending, producing a wider space charge region at the pBTO/electrolyte interface. Considering the favorable band-bending the photogenerated electron-hole (e^--h^+) pairs will be separated more effectively in pBTO thin films, improving consequently the photoelectrochemical performance. Therefore, it can be noticed that positive poling enhances hole transfer from the surface of pBTO to the electrolyte to participate in the water oxidation reaction, promoting the use of pBTO as photoanodes as noticed from J-V and J-t results.

On the contrary, after -8 V EC poling, the J-t curves of pBTO-O_2 and pBTO-air show a decrement in the photocurrent density compared to their unpoled states (Figure 5.8 a,b), which is in agreement with the relative J-V measurements results, shown in Figure 5.9 a,b. Indeed, when pBTO thin films are negatively poled, the macroscopic ferroelectric polarization, generated by the applied electric field, pointing to pBTO surface, induces the formation of opposite E_{dep}, which will lead to electron accumulation at the surface of pBTO and consequently downward band-bending. This downward band-bending at pBTO/electrolyte interface and upward band-bending at pBTO/FTO interface will suppress the transfer of photogenerated electrons to FTO substrate and photogenerated holes to the electrolyte, which is against the water oxidation reaction and consequently reduces the photoelectrochemical response (Figure 5.10 b, negative poling).

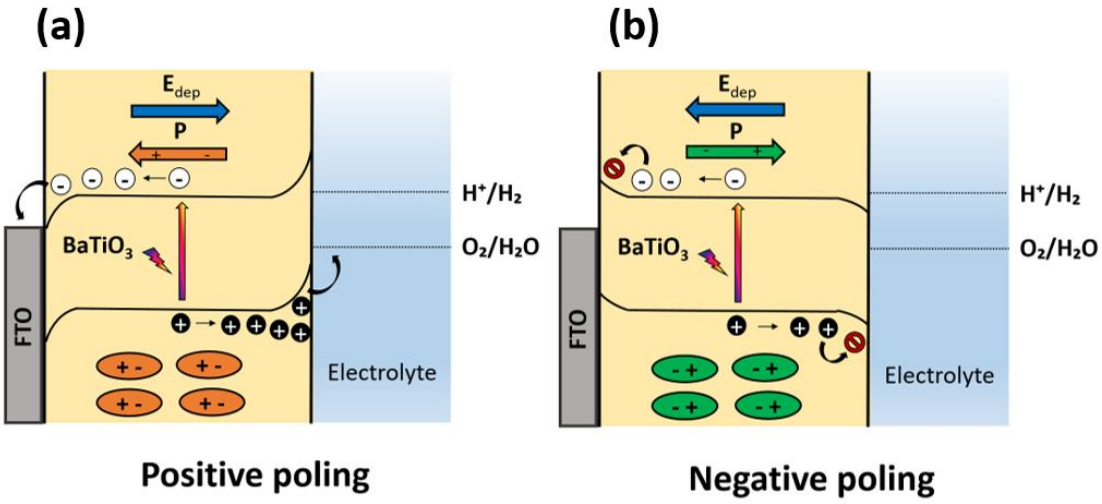

Figure 5.10 Schematic of band-bending at pBTO/electrolyte interface, after positive poling (e) and negative poling (f).

However, the pBTO-N_2 thin film does not show the same trend after -8V EC poling, as reported in Figure 5.8 c and Figure 5.9 c. Considering the PEC response of pBTO-O_2, pBTO-air and pBTO-N_2, extrapolated at 0.19 V vs Ag/AgCl and obtained across a range of samples, this result can be seen more clearly (Figure 5.11): on one hand, within error, there is effectively no change in the photocurrent values of pBTO-N_2 sample before and after EC poling. On the other hand, pBTO-O_2 and pBTO-air samples show a consistent increment/decrement of PEC performance after +/-8 V EC poling. However, the effect of positive poling is more pronounced in pBTO-air compared to pBTO-O_2. Indeed, at 0.19 V vs Ag/AgCl, an enhancement of the photocurrent density of about 10.3 $\mu A/cm^2$ compared to the unpoled counterpart is observed in pBTO-air sample. pBTO-O_2 shows higher photocurrent density (4.8 $\mu A/cm^2$) than the unpoled state (3.2 $\mu A/cm^2$) but the PEC performance improvement due to ferroelectric polarization is not as substantial as in pBTO-air thin film. According to the XPS results reported in Figure 5.6, this evidence suggests that a mutual effect between the interface charges arising at pBTO/electrolyte

interface from ferroelectric polarization and the higher content of oxygen vacancies may greatly enhance the photoelectrochemical response in pBTO-air compared to pBTO-O_2. Indeed, it has been previously reported that the combination of ferroelectric polarization and oxygen vacancies improves the PV response in $BiFeO_3$ thin films[37]. On the other hand, the as-described PEC trend is not clearly observed in pBTO-N_2 and this result could be related to a more significant alteration in the oxygen vacancies content after EC poling procedure compared to the pBTO-O_2 and pBTO-air samples, where the oxygen vacancies concentration is lower, as detected from XPS analysis. Indeed, the high concentration of oxygen vacancies in pBTO-N_2 films confirmed by XPS analysis may have a significant impact on the control of PEC response via EC poling, producing unpredictable results[34]. As previously shown in Figure 5.9 c, the photocurrent values of pBTO-N_2 does not effectively change before and after EC poling, compared to pBTO-O_2 and pBTO-air samples.

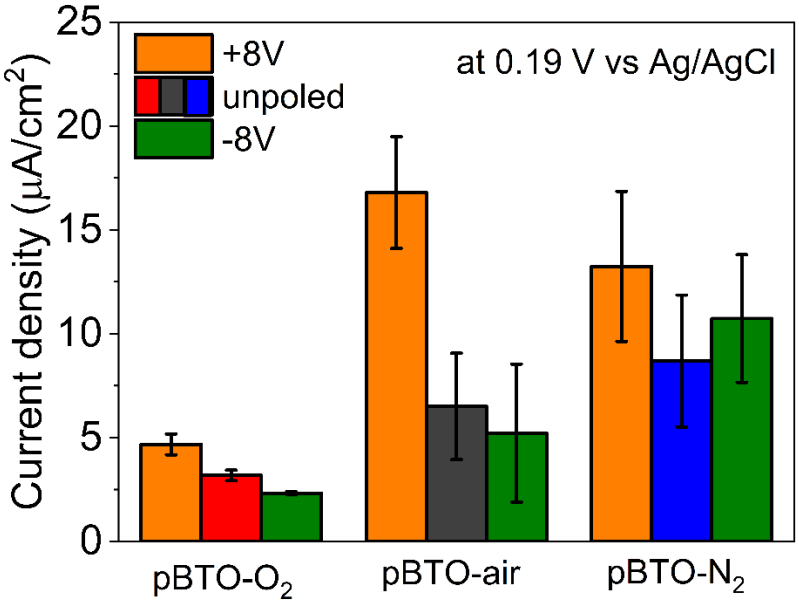

Figure 5.11 Comparison between photocurrent density values of pBTO-O_2, pBTO-air and pBTO-N_2, obtained before and after poling at 0.19 V vs Ag/AgCl.

5.2.7 Influence of electrochemical poling on porous BTO films

Therefore, to study the effect of the poling pretreatment on pBTO films, their chemical composition after EC poling was investigated using XPS analysis. The XPS results are summarized in Table 5.1 and Figure 5.12, where the variation of surface oxygen vacancies detected in pBTO-O_2, pBTO-air and pBTO-N_2 after positive and negative poling is clearly observed.

Table 5.1 Comparison between $O_{vacancy}/O_{lattice}$ area ratio values of pBTO-O_2, pBTO-air and pBTO-N_2, determined from XPS analysis for the unpoled, positive poled and negative poled state.

Peaks	$O_{vacancy}/O_{lattice}$ (area ratio)		
	+8 V	unpoled	- 8 V
pBTO-O_2	0.34	0.32	0.32
pBTO-air	0.71	0.50	0.55
pBTO-N_2	1.37	1.49	0.52

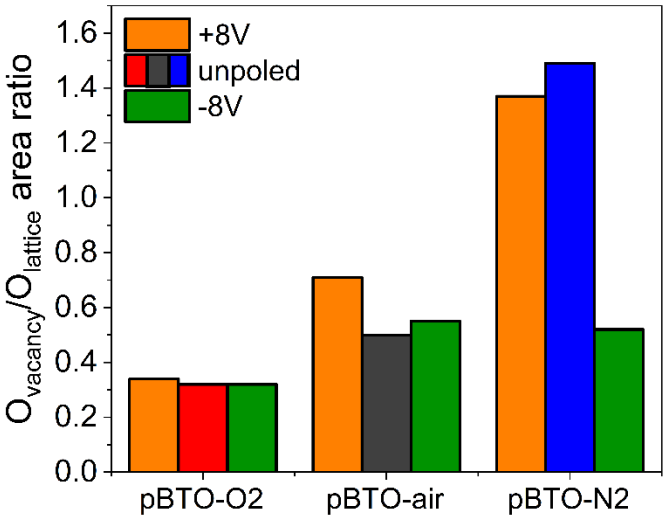

Figure 5.12 Bar graph showing $O_{vacancy}/O_{lattice}$ area ratio values of pBTO-O_2, pBTO-air and pBTO-N_2, before and after poling.

As observed from the high resolution XPS spectra shown in Figure 5.13 a,b, the shape of O1s photoemission peaks in both pBTO-O_2 and pBTO-air is almost unchanged after +/- 8 V EC poling, suggesting that the EC poling procedure does not alter the surface composition of the films. Moreover, the pBTO-O_2 film does not show a significant modification of the $O_{vacancy}/O_{lattice}$ area ratio value before (0.32) and after +8 V (0.34) and -8 V (0.32) EC poling, indicating that the poling pretreatment does not affect the mobility and content of oxygen vacancies in this film (Figure 5.13 a). On the other hand, in pBTO-air sample the $O_{vacancy}/O_{lattice}$ area ratio value estimated is slightly higher after +8 V EC poling (0.71) compared to the unpoled counterpart while it remains almost unchanged after -8 V EC poling (0.55) (Figure 5.13 b). This result can be explained considering the possible oxygen vacancies migration within the BTO layer: when pBTO-air sample is positively poled, the positively charged oxygen vacancies will also experience the driving force from the E_{dep} and thus, they may migrate toward the sample surface, superimposing their contribution on the accumulated holes derived from ferroelectric polarization. This

leads to a much wider space charge region at pBTO/electrolyte interface, where the photogenerated electron-hole pairs can be more effectively separated, generating consequently markedly enhanced PEC response. This evidence can be correlated to the PEC results previously shown for pBTO-O_2 and pBTO-air samples. In pBTO-air, the higher $O_{vacancy}/O_{lattice}$ area ratio value after +8 V EC poling, due to possible oxygen vacancies migration, is reflected in a greater increment of PEC response after +8 V EC poling, compared to pBTO-O_2, where the improvement of the PEC performance mainly arises from ferroelectric polarization as the oxygen vacancies concentration is lower. Thus, the effect of the oxygen vacancies migration can be associated to the enhancement of PEC performance in pBTO-air. On the contrary, when pBTO-air sample is negatively poled, it may be expected that the oxygen vacancies will move away from the sample surface, according to the driving force from the E_{dep}. However, there are probably already less oxygen vacancies at pBTO-air sample surface as-prepared, thus they don't diffuse away from the sample surface during negative poling. Indeed, pBTO-air sample shows almost comparable $O_{vacancy}/O_{lattice}$ area ratio values before (0.50) and after -8 V EC poling (0.55), which is in agreement with the PEC performance after negative poling, as previously reported. As evidenced previously, the $O_{vacancy}/O_{lattice}$ area ratio value is also unchanged after negative poling in pBTO-O_2, with respect to the unpoled counterpart.

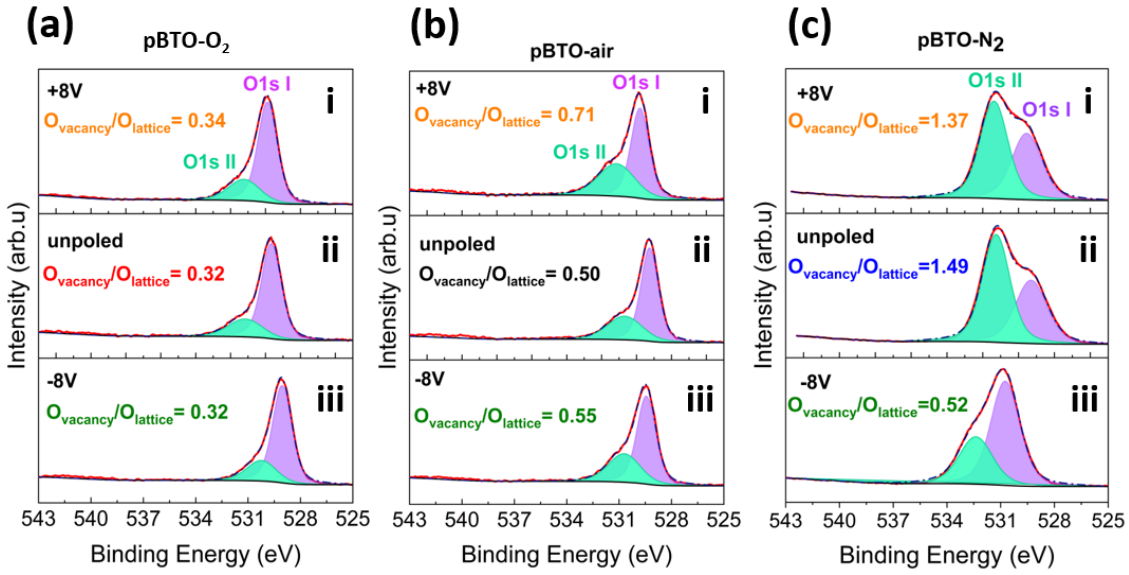

Figure 5.13 O1s high-resolution scans of pBTO-O_2 (a), pBTO-air (b), pBTO-N_2 (c) after +8 V poling (i), -8 V poling (iii) and in the unpoled state (ii) and relative $O_{vacancy}/O_{lattice}$ area ratio values obtained, summarized in the table (d) and in the bar graph (e).

However, a change in the shape of O1s peaks of pBTO-N_2 sample is appreciable, and in particular the O1s (II) peak area referred to the oxygen vacancies is more significantly affected by the EC poling procedure compared to both pBTO-air and pBTO-O_2 samples (Figure 5.13 c). Specifically, in pBTO-N_2 film, the $O_{vacancy}/O_{lattice}$ area ratio value obtained after +8 V EC poling is slightly lower (1.37), compared to the corresponding unpoled state (1.49). As discussed above for pBTO-air sample, it may be expected that the positive poling induces the migration of the oxygen vacancies to the sample surface. However, based on the contrary argument presented for pBTO-air, there are already more oxygen vacancies at the surface of pBTO-N_2 as-made, thus they do not move towards the sample surface during +8 V EC poling. On the other hand, according to the discussion above, in the case of negative poling, the oxygen vacancies may migrate from the sample

surface toward the FTO substrate, consequently reducing the concentration of oxygen vacancies present at the pBTO/electrolyte interface. This is clearly confirmed by XPS analysis of pBTO-N_2 films, where the $O_{vacancy}/O_{lattice}$ area ratio value detected is considerably decreased after -8 V EC poling (0.52) compared to the relative unpoled state (1.49). The migration of surface oxygen vacancies in pBTO-N_2 sample can also explain the slight change in the photocurrent response after both types of EC poling, as shown in Figure 5.8c and Figure 5.9c. However, considering the PEC performance of pBTO-N_2 measured across a range of samples (Figure 5.11), no variation in the photocurrent density is observed within error after EC poling compared to the unpoled state.

Thus, it can be concluded from XPS and PEC results that the EC process in pBTO-N_2 sample leads to oxygen vacancy migration, which limits the ability to control these films *via* ferroelectric polarisation.

5.3 Summary

The present chapter investigated the effect of EC poling pre-treatment on porous $BaTiO_3$ thin films, prepared by soft template-assisted sol-gel method in different atmospheres (O_2, air and N_2).

The annealing of pBTO thin films in O_2, air and N_2 conditions induced an increase of oxygen vacancies content from pBTO-O_2 to pBTO-N_2 sample. This was verified by the combination of UV-vis spectroscopy, XPS analysis and PEC testing. SEM and EDX analysis were performed to confirm the porous structure and the elemental composition of pBTO-O_2, pBTO-air and pBTO-N_2 thin films. The formation of perovskite $BaTiO_3$ structure was verified by XRD analysis. Owing to the promising ferroelectric properties

of pBTO thin films for photoelectrochemical applications, an EC poling procedure was performed on pBTO thin films to control their PEC response *via* ferroelectric polarisation. The +8 V EC poling of pBTO-O_2 and pBTO-air samples induced a clear enhancement in the PEC response of those films, compared to the -8 V EC poling. This indicates that the positive poling is very favourable when pBTO is used as a photoanode. However, the improvement in the PEC performance was more significant in pBTO-air compared to pBTO-O_2 sample. Indeed, the cooperative effect between the interface charges derived from the ferroelectric polarisation and the surface oxygen vacancies enhances greatly the PEC response in pBTO-air compared to pBTO-O_2, as confirmed by XPS and PEC analysis. On the other hand, the PEC trend of pBTO-N_2 films obtained after EC poling was not as clear as in pBTO-O_2 and pBTO-air films. This evidence in combination with the XPS results suggests that the high concentration of oxygen vacancies induces their enhanced migration within the pBTO-N_2 sample, which limits the ability of these films to be controlled *via* poling. Indeed, as previously reported, the high diffusion of oxygen vacancies has a large influence on the sample instability: it was found that the state after removing the poling field in ferroelectric materials with higher oxygen vacancies concentration was unstable, considering that the hopping electrons could recombine with the oxygen vacancies[38].

Thus, it was demonstrated that the EC poling process can still be adopted to control the PEC response in a porous ferroelectric thin film with low and intermediate concentrations of oxygen vacancies, without affecting their chemical states. In particular, the synergic effect of ferroelectric polarisation and oxygen vacancies may be beneficial for the enhancement of PEC performance due to the increase in carrier concentration caused by Vo combined with enhanced separation due to the polarisation. However, an excess of

oxygen vacancies may trap the photogenerated electrons and thus they can act as recombination centers. This study opens the route for further enhancing the PEC response based on defect engineering using oxygen vacancies in nanostructured ferroelectric thin films. However, when the concentration of oxygen vacancies is higher, the EC poling procedure could be difficult to control in the porous ferroelectric films leading to very unpredictable results.

REFERENCES

1. Li, Y., Li, J., Yang, W. & Wang, X. Implementation of ferroelectric materials in photocatalytic and photoelectrochemical water splitting. *Nanoscale Horizons* **5**, 1174–1187 (2020).

2. Li, S. *et al.* Recent Advances of Ferro-, Piezo-, and Pyroelectric Nanomaterials for Catalytic Applications. *ACS Appl. Nano Mater.* **3**, 1063–1079 (2020).

3. Chen, F., Huang, H., Guo, L., Yihe, Z. & Ma, T. The role of polarization in photocatalysis. *Angew. Chemie - Int. Ed.* doi:10.1002/anie.201901361.

4. Augurio, A. *et al.* Controlled Porosity in Ferroelectric $BaTiO_3$ Photoanodes. *ACS Appl. Mater. Interfaces* acsami.1c17419 (2022).

5. Castro, A., Ferreira, P., Rodriguez, B. J. & Vilarinho, P. M. The role of nanoporosity on the local piezo and ferroelectric properties of lead titanate thin films. *J. Mater. Chem. C* **3**, 1035–1043 (2015).

6. Ferreira, P. *et al.* Nanoporous Piezo- and Ferroelectric Thin Films. *Langmuir* **28**, 2944–2949 (2012).

7. Detsi, E. *et al.* On the specific surface area of nanoporous materials. *Acta Mater.* **59**, 7488–7497 (2011).

8. Suzuki, N. *et al.* Chemical Synthesis of Porous Barium Titanate Thin Film and Thermal Stabilization of Ferroelectric Phase by Porosity-Induced Strain. *J. Vis. Exp.* 1–7 (2018).

9. Tyunina, M. Oxygen vacancies in perovskite oxide piezoelectrics. *Materials (Basel).* **13**, 1–11 (2020).

10. Fernández-Climent, R., Giménez, S. & García-Tecedor, M. The role of oxygen vacancies in water splitting photoanodes. *Sustain. Energy Fuels* **4**, 5916–5926 (2020).

11. Zhang, W. H. *et al.* Raman study of barium titanate with oxygen vacancies. *Phys. B Condens. Matter* **406**, 4630–4633 (2011).

12. Cai, W. *et al.* Effects of oxygen partial pressure on the electrical properties and phase transitions in (Ba,Ca)(Ti,Zr)O_3 ceramics. *J. Mater. Sci.* **55**, 9972–9992 (2020).

13. Sun, Q. *et al.* Crystalline Structure , Defect Chemistry and Room Temperature Colossal Permittivity of Nd-doped Barium Titanate. *Nat. Publ. Gr.* 1–8 (2017) doi:10.1038/srep42274.

14. Rioult, M. *et al.* Tailoring the photocurrent in $BaTiO_3$/Nb:$SrTiO_3$ photoanodes by controlled ferroelectric polarization. *Appl. Phys. Lett.* **107**, 1–5 (2015).

15. Datta, S., Rioult, M., Stanescu, D., Magnan, H. & Barbier, A. Manipulating the ferroelectric polarization state of $BaTiO_3$ thin fi lms. *Thin Solid Films* **607**, 7–13 (2016).

16. Cao, D., Wang, Z., Wen, L., Mi, Y. & Lei, Y. Switchable Charge-Transfer in the Photoelectrochemical Energy- Conversion Process of Ferroelectric $BiFeO_3$ Photoelectrodes. *Angew. Chemie - Int. Ed.* 1–6 (2014).

17. Huang, W. *et al.* Epitaxial Bi_2FeCrO_6 Multiferroic Thin-Film Photoanodes with Ultrathin p-Type NiO Layers for Improved Solar Water Oxidation. *ACS Appl. Mater. Interfaces* **11**, 13185–13193 (2019).

18. Zhang, C. C. *et al.* Polarized Ferroelectric Polymers for High-Performance Perovskite Solar Cells. *Adv. Mater.* **31**, 1–11 (2019).

19. Singh, S., Sangle, A. L., Wu, T., Khare, N. & MacManus-Driscoll, J. L. Growth of Doped $SrTiO_3$ Ferroelectric Nanoporous Thin Films and Tuning of Photoelectrochemical Properties with Switchable Ferroelectric Polarization. *ACS Appl. Mater. Interfaces* **11**, 45683–45691 (2019).

20. Wu, F. *et al.* Simultaneous Enhancement of Charge Separation and Hole Transportation in a TiO_2–$SrTiO_3$ Core–Shell Nanowire Photoelectrochemical System. *Adv. Mater.* **29**, 1–7 (2017).

21. Magnan, H. *et al.* Tuning the Charge Carriers Migration in Epitaxial $BaTiO_3$ Thin-Film Photoanodes. *J. Phys. Chem. C* **124**, 10315–10323 (2020).

22. Sharma, H. B. Structural and optical properties of sol-gel derived barium titanate thin film. *Int. J. Mod. Phys. B* **21**, 1837–1849 (2007).

23. Wemple, S. H. Polarization Fluctuations and the Optical-Absorption Edge in BaTiO3. *Phys. Rev. B* **2**, 2679–2689 (1970).

24. Maneeshya, L. V. *et al.* Influence of annealing temperature and oxygen atmosphere on the optical and photoluminescence properties of $BaTiO_3$ amorphous thin films prepared by sol-gel method. *J. Mater. Sci. Mater. Electron.* **24**, 848–854 (2013).

25. Vaněček, M., Poruba, A., Remeš, Z., Beck, N. & Nesládek, M. Optical properties of microcrystalline materials. *J. Non. Cryst. Solids* **227**–**230**, 967–972 (1998).

26. Suzuki, N. *et al.* Chemical synthesis of porous barium titanate thin film and thermal stabilization of ferroelectric phase by porosity-induced strain. *J. Vis. Exp.* **2018**, 1–7 (2018).

27. Uchino, K., Sadanaga, E. & Hirose, T. Dependence of the Crystal Structure on Particle Size in Barium Titanate. **90**, 1–4 (1989).

28. Begg, B. D., Vance, E. R. & Nowotny, J. Effect of Particle Size on the Room-Temperature Crystal Structure of Barium Titanate. *J. Am. Ceram. Soc.* **77**, 3186–3192 (1994).

29. Yang, C., Sui, H., Wu, H. & Hu, G. $Na_{0.5}Bi_{0.5}(Ti_{0.98}Zr_{0.02})O_3$ thin film with improved performance by modifying annealing atmosphere and Zr doping content. *J. Alloys Compd.* **637**, 315–320 (2015).

30. Zhang, F. *et al.* The effect of sintering atmospheres on the properties of CSBT-0.15 ferroelectric ceramics. *Ceram. Int.* **44**, 13502–13506 (2018).

31. Pancotti, A. *et al.* X-ray photoelectron diffraction study of relaxation and rumpling of ferroelectric domains in $BaTiO_3$(001). *Phys. Rev. B - Condens. Matter Mater. Phys.* **87**, 1–10 (2013).

32. Chakrabarti, S. *et al.* Negative voltage modulated multi-level resistive switching by using a Cr/BaTiOx/TiN structure and quantum conductance through evidence of H_2O_2 sensing mechanism. *Sci. Rep.* **7**, 1–13 (2017).

33. Siemek, K., Olejniczak, A., Korotkov, L. N., Konieczny, P. & Belushkin, A. V. Investigation of surface defects in $BaTiO_3$ nanopowders studied by XPS and positron annihilation lifetime spectroscopy. *Appl. Surf. Sci.* **578**, 151807 (2022).

34. Wu, W., Liu, Z., Gu, Y., Yue, Z. & Li, Y. Thermally stimulated depolarization current study on barium titanate single crystals. *AIP Adv.* **8**, 0–6 (2018).

35. Gan, J. *et al.* Oxygen vacancies promoting photoelectrochemical performance of In_2O_3 nanocubes. *Sci. Rep.* **3**, 1–7 (2013).

36. Corby, S., Francàs, L., Kafizas, A. & Durrant, J. R. Determining the role of oxygen vacancies in the photoelectrocatalytic performance of WO_3 for water oxidation. *Chem. Sci.* **11**, 2907–2914 (2020).

37. Matsuo, H., Kitanaka, Y., Inoue, R., Noguchi, Y. & Miyayama, M. Cooperative effect of oxygen-vacancy-rich layer and ferroelectric polarization on photovoltaic properties in $BiFeO_3$ thin film capacitors. *Appl. Phys. Lett.* **108**, (2016).

38. Guo, Y., Guo, B., Dong, W., Li, H. & Liu, H. Evidence for oxygen vacancy or ferroelectric polarization induced switchable diode and photovoltaic effects in $BiFeO_3$ based thin films. *Nanotechnology* **24**, (2013).

6 FERROELECTRIC-PHOTOCATALYST NANOCOMPOSITE FILMS

6.1 Introduction

Photoelectrochemical (PEC) systems based on semiconductors are one of the most attractive solutions adopted for the production of clean energy due to their potential high efficiency and simplicity. However, the development of highly efficient and stable photocatalytic materials is still quite challenging.

Many research studies focused on various n-type semiconductor photoanodes, such as TiO_2, WO_3, and Fe_2O_3, have been reported, aiming to achieve a high PEC response[1–3].

Among them, Fe_2O_3, a highly Earth-abundant and low-cost material, has a narrow optical band gap (E_g= 2.2 eV), environmental consistency and excellent chemical stability[4–6]. Consequently, this material, also well-known by its mineral name hematite, is one of the most promising candidates for the fabrication of robust and efficient PEC systems. However, the application of Fe_2O_3-based photoanodes in photoelectrocatalysis is hampered by its poor charge transfer, short hole-diffusion length and low conductivity[7].

Different strategies have been adopted to improve the PEC performance of hematite, including nanostructuring[8], element doping[9] and cocatalyst loading[10]. Nevertheless, PEC systems based on Fe_2O_3-photoanodes used for hydrogen production show efficiencies that are still much lower than the theoretical limit. Thus, alternative approaches for the enhancement of the efficiencies in Fe_2O_3-based PEC systems need to be explored.

In this context, UV light and visible light absorbing ferroelectric materials, such as $SrTiO_3$ (3.25 eV), $BaTiO_3$ (3.2 eV), $PbTiO_3$ (3.18 eV), and $BiFeO_3$ (2.4 eV), have been recently exploited as PEC photoanodes thanks to their spontaneous polarization effect[11–13]. Indeed, as demonstrated in Chapter 4 and Chapter 5 for ferroelectric $BaTiO_3$ thin films, the ferroelectric polarisation can induce the migration of photogenerated electron-hole pairs towards opposite directions, leading to their fast separation, which is responsible for an enhancement of the PEC response. Owing to the beneficial properties of ferroelectric materials, they have been also used in ferroelectric/photocatalyst heterostructures, aiming to reach a further PEC improvement[14]. For example, it has been reported that a $BiVO_4/BiFeO_3$ composite photoanodes shows a photocurrent density ~4 times higher than the bare $BiVO_4$, accompanied by a negative shift in the onset potential of ~400 mV[15]. Here, the coating of $BiFeO_3$ on $BiVO_4$ by surface passivation has a bifunctional effect: it

significantly boosts the PEC performance due to ferroelectric polarization of $BiFeO_3$, which improves charge separation and transfer as well as it acts as passivation layer which reduces self-photocorrosion of the film. Yang *et al.* showed that $TiO_2/BaTiO_3$ core/shell nanowires (NWs) have a photocurrent density, which is 67 % higher than that of the bare TiO_2 NWs[16]. The BTO enhances separation of the charges that are photogenerated in the TiO_2 by absorption of UV light. Moreover, a Fe_2O_3/PZT photoanode exhibited a remarkable enhancement in the photocurrent density, reaching a value of 1 mA/cm^2 at 1.23 V vs RHE, which was 10 times that of the bare Fe_2O_3 film[17]. More examples of ferroelectric/photocatalyst heterostructures have been previously detailed in Chapter 2. However, only a small number of studies have been reported on ferroelectric semiconductors and Fe_2O_3-based heterostructures.

Thus, this chapter discusses the beneficial effect derived by the combination of ferroelectric $BaTiO_3$ with photocatalyst Fe_2O_3 for the enhancement of PEC activity. In particular, a Fe_2O_3/BTO composite photoanode was successfully obtained by hydrothermal growth of Fe_2O_3 within the pores and on the surface of porous BTO thin films, which were prepared and studied in more detail in Chapter 4 and Chapter 5. The morphology, optical and crystalline properties, elemental composition and photoelectrochemical performance of Fe_2O_3/BTO thin films are investigated. A significant enhancement in the PEC response and charge transfer of Fe_2O_3/BTO composite film was demonstrated compared to both bare Fe_2O_3 and BTO thin films, which is correlated to the ferroelectricity of BTO. More importantly, it was proven that the photoelectrochemical performance can still be easily and effectively regulated by controlling the ferroelectric polarization orientation in BTO thin films using

electrochemical poling pretreatment, which did not significantly alter the film chemistry, as confirmed by XPS results.

This study suggests that when Fe_2O_3 is combined with BTO, hematite can potentially maximize its capabilities through the enhancement of its PEC performance and the charge separation and transport properties simultaneously.

6.1.1 Combination of ferroelectric $BaTiO_3$ with photocatalyst Fe_2O_3

Fe_2O_3 nanorods were grown on $BaTiO_3$ thin films by hydrothermal method, using the experimental procedure detailed in Chapter 3 (Figure 6.1). Indeed, considering that $BaTiO_3$ is a UV light absorber material, the combination of $BaTiO_3$ with Fe_2O_3 (Fe_2O_3/pBTO-5) offers the opportunity to exploit the beneficial properties of both materials: the enhanced spatial charge separation induced by ferroelectric $BaTiO_3$ and the visible light absorption and good photochemical stability of Fe_2O_3 as photocatalyst. For the formation of this non-ferroelectric/ferroelectric heterostructure, pBTO-5 has been used as ferroelectric material because its larger pores are more suitable for the integration with the Fe_2O_3 photocatalyst. Hematite was grown by Qian Guo, a PhD student from Ana Sobrido's research group, in the shape of nanorods because, thanks to their high aspect ratios and large surface areas, they can improve charge carrier separation, consequently maximizing the photoelectrochemical (PEC) performance[4] of the composite film.

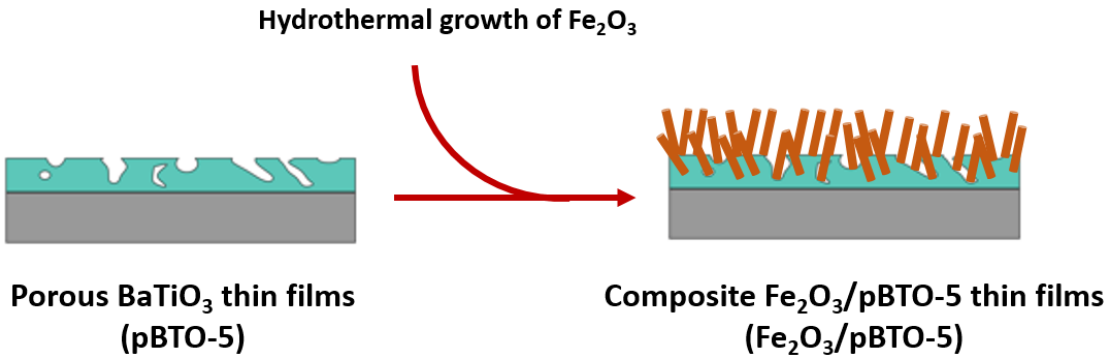

Figure 6.1 Schematic on the combination of ferroelectric $BaTiO_3$ with Fe_2O_3 as photocatalyst (Fe_2O_3/pBTO-5).

6.1.1.1 Morphological structure and elemental analysis

The morphologies of pBTO-5, Fe_2O_3/pBTO-5 and Fe_2O_3 thin films, investigated by SEM analysis, are reported in Figure 6.2. The porous structure of pBTO-5 thin film, shown in Figure 6.2 a, is in agreement with the results detailed in Chapter 3. The bare Fe_2O_3 photoanode exhibit randomly aligned nanorods grown on FTO substrate with diameters of 90-100 nm, as shown in Figure 6.2 b. After hydrothermal growth of Fe_2O_3 on pBTO-5 films, hematite nanorods in Fe_2O_3/pBTO-5 sample appear to be straighter than the ones in the bare Fe_2O_3 thin film, accompanied by a decrease in the diameter of the nanorods (50-70 nm) (Figure 6.2 c). This is likely related to the confinement effect from the pBTO underlayer, which is similar to the function of SiO_2 in the fabrication of mesoporous Fe_2O_3 reported by Sivula *et al.*[18]. This observation is also in agreement with previously reported hematite photoanodes using underlayers[19,20]. The average thickness of the hematite layer above pBTO-5 is ~ 145 nm, as observed from the cross-sectional SEM image of a different Fe_2O_3/pBTO-5 sample, prepared in the same experimental conditions (Figure 6.2 d).

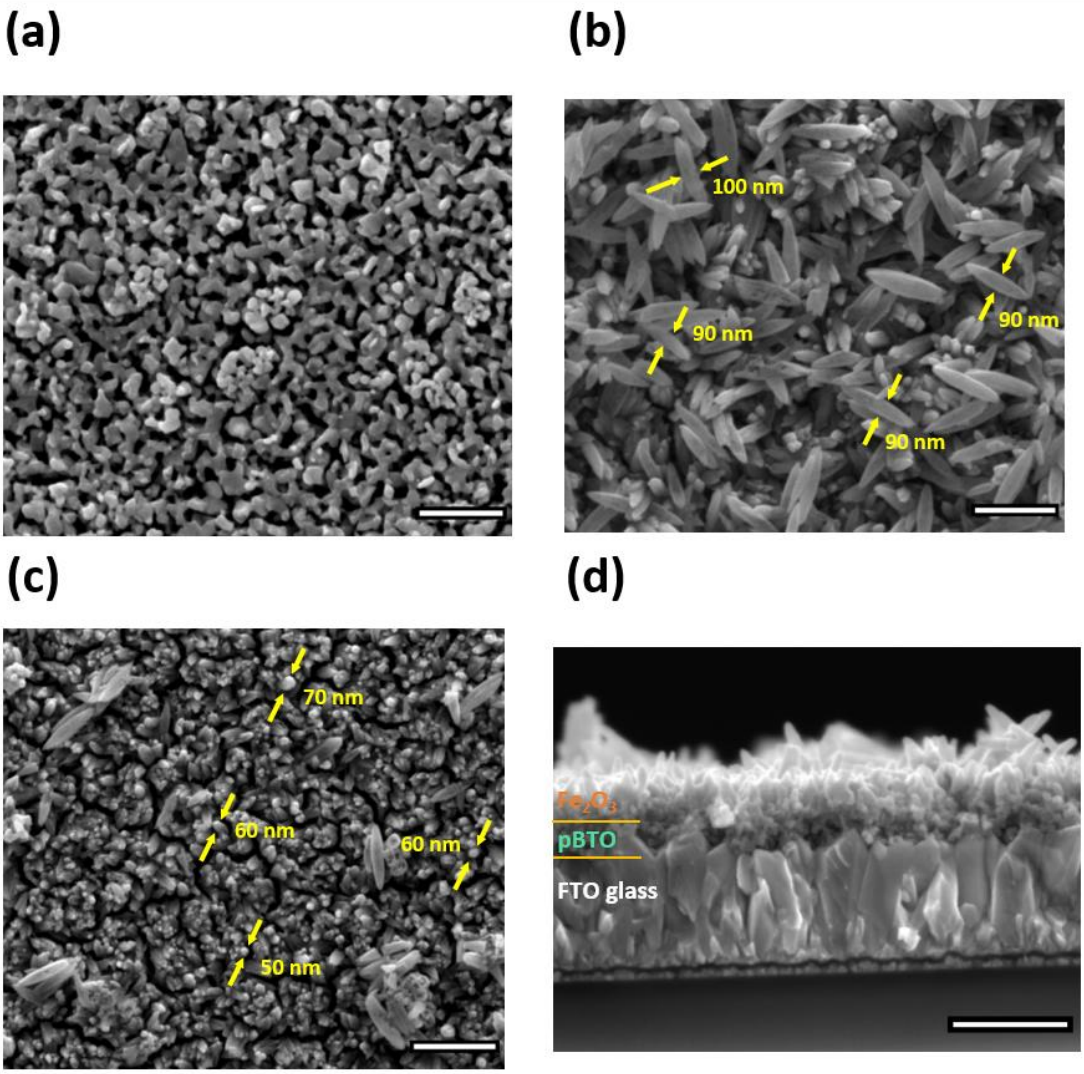

Figure 6.2 Top view SEM image of (a) pBTO-5, (b) Fe_2O_3, (c) Fe_2O_3/pBTO-5 and corresponding cross-section (d) (scale bar: 500 nm).

The presence of Ba, Ti, O, Fe was confirmed by EDX analysis, indicating the successful growth of Fe_2O_3 on pBTO-5 thin films. The elemental maps of O, Fe, Ti, Ba have the same spatial distribution which indicates a uniform distribution of elements in the synthesized Fe_2O_3/pBTO-5 films at the micron length scale, and thus complete filling/coverage of the pBTO film by Fe_2O_3. Moreover, the presence of Sn and Si elements is observed, which is due to the FTO glass substrate where the films are

deposited (Figure 6.3 a). The elemental content is also observed from the EDX spectrum of Fe_2O_3/pBTO-5 thin films (Figure 6.3 b,c).

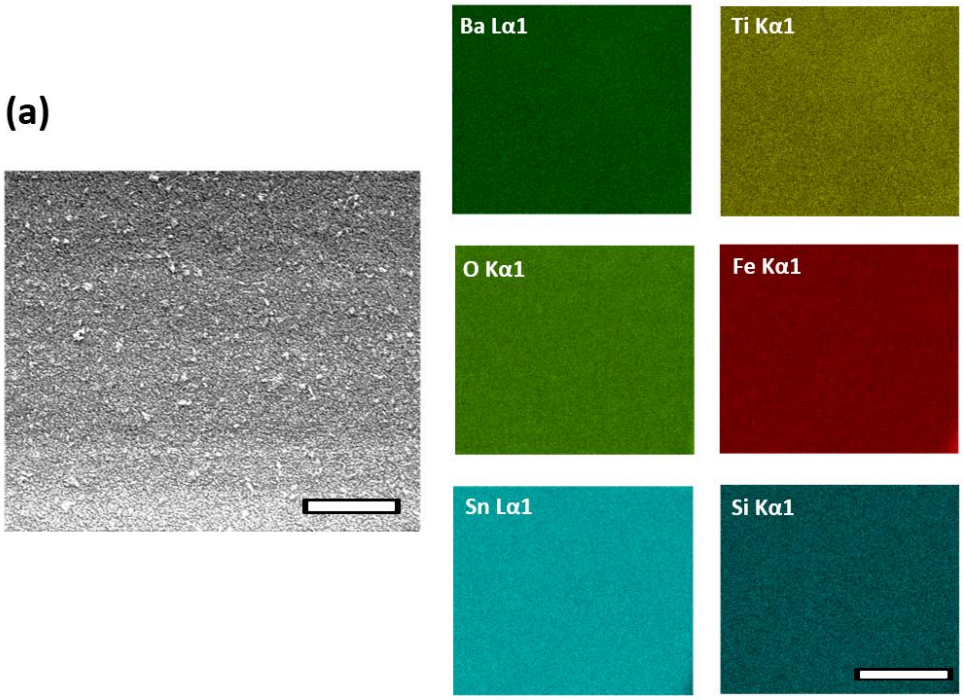

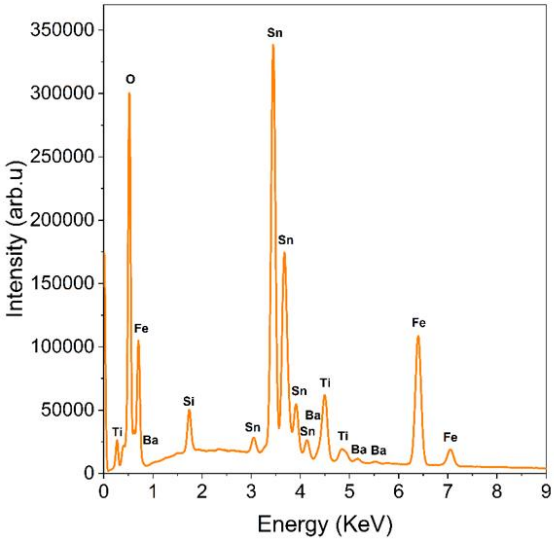

(c)

Element	Weight %
O	42.6
Sn	36.8
Fe	13.1
Ba	4.2
Ti	2.4
Si	1

Figure 6.3 SEM micrograph of Fe_2O_3/pBTO-5 thin film and the EDX mapping pattern of the element distribution: Ba, Ti, O, Fe, Sn, Si (a); the EDX spectrum of

Fe_2O_3/pBTO-5 (b) and the relative elemental quantification in weight (%) (c) (scale bar: 5 µm).

6.1.1.2 Crystalline phase

To investigate the crystalline phase of Fe_2O_3/pBTO-5 thin film, XRD analysis was performed. Comparing the XRD pattern of Fe_2O_3/pBTO-5 with that of both bare Fe_2O_3 and $BaTiO_3$ thin films, the characteristic XRD peaks belonging to α-phase Fe_2O_3 (JCPDS No. 33-0664) are detected in the composite film. However, only the (202) peak can clearly be ascribed to α-phase Fe_2O_3. The rest of the XRD peaks belonging to α-phase Fe_2O_3 [(104), (214)] may be present, but overlap with the XRD peaks from the FTO glass substrate therefore cannot be unequivocally assigned to α-phase Fe_2O_3. Thus, the formation of Fe_2O_3 on pBTO can be confirmed using XRD analysis, but the preferred orientation cannot be confirmed due to overlap with substrate peaks. Moreover, the XRD peaks referred to crystalline $BaTiO_3$ are clearly observed, even if it is difficult to discriminate between the cubic (paraelectric) and the tetragonal (ferroelectric) phases using XRD, as discussed in more detail in Chapter 4 and Chapter 5. Beside the XRD peaks corresponding to Fe_2O_3 and $BaTiO_3$, the presence of XRD peaks of FTO glass, used as substrate for the films' deposition, can be noted (Figure 6.4).

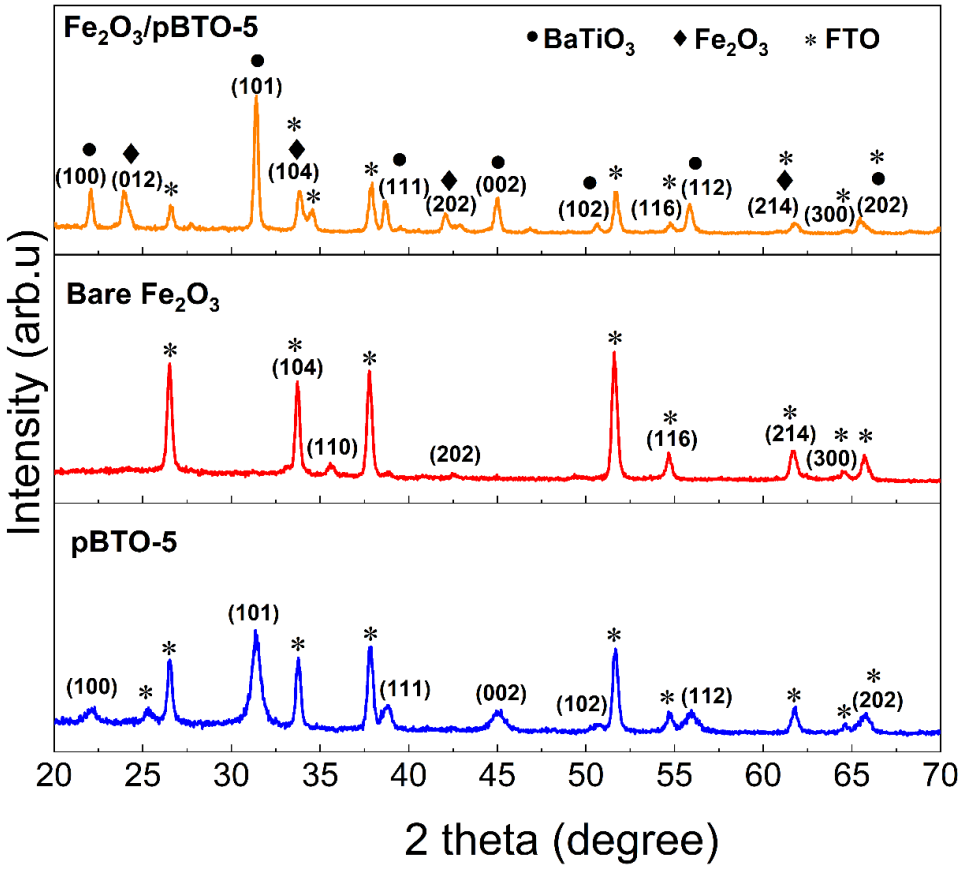

Figure 6.4 XRD patterns of Fe_2O_3/pBTO-5, bare Fe_2O_3 and pBTO-5 thin films.

6.1.1.3 Optical properties

The absorption spectra of Fe_2O_3/pBTO-5 and bare Fe_2O_3 thin films show an absorption onset from ~600 nm to ~400 nm, which is in agreement with previous research works[21,19] (Figure 6.5). However, the absorbance intensity of the composite Fe_2O_3/pBTO-5 thin film is higher in the UV region than that of the bare Fe_2O_3 sample. This could be correlated to the presence of BTO, which shows an absorption edge in the UV region, as previously reported in Chapter 4 and Chapter 5. Besides the contribution of the BTO layer, it can be possibly explained considering that the presence of multiple interfaces in the composite Fe_2O_3/pBTO-5 thin film can increase the light scattering, which leads to an enhancement of light absorption[22]. The direct bandgap energies of Fe_2O_3/pBTO-5 and bare Fe_2O_3

estimated from the Tauc plots are 2.15 and 2.17 e V respectively, which are in agreement with values reported by previous research work[23,24] (inset of Figure 6.5). The slight variation between the estimated bandgap energy values of Fe_2O_3/pBTO-5 and bare Fe_2O_3 thin films could be attributed to scattering effects which can arise in the composite ferroelectric/photocatalyst film due to multiple interfaces.

The inset of Figure 6.5 shows the corresponding pictures of Fe_2O_3/pBTO-5 and bare Fe_2O_3 samples, confirming that the colour intensity and transparency of the two films are quite similar.

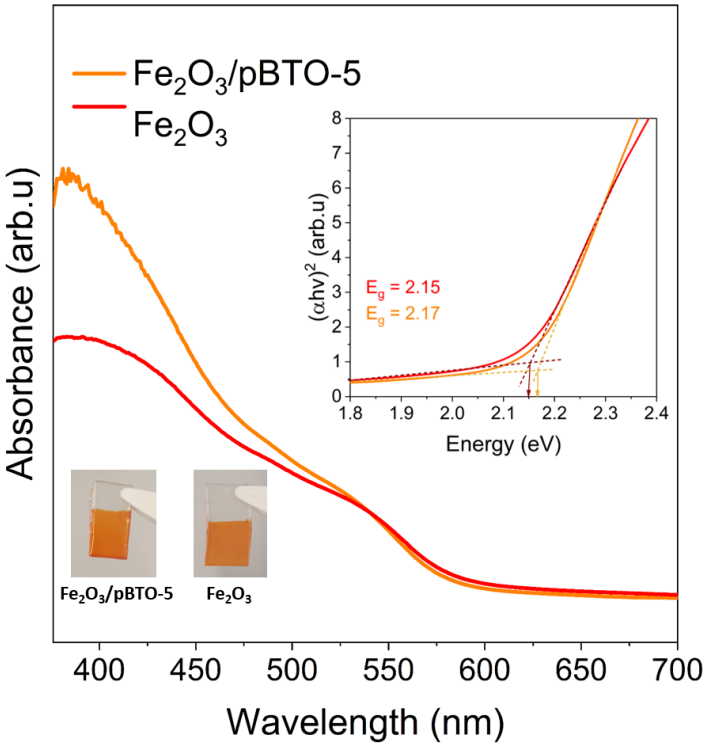

Figure 6.5 UV-vis absorption spectra of composite Fe_2O_3/pBTO-5 and bare Fe_2O_3 thin films; Insets: Tauc plots of the Fe_2O_3/p BTO-5 and Fe_2O_3 samples and photos of the corresponding Fe_2O_3/pBTO-5 and bare Fe_2O_3 films.

6.1.1.4 Photoelectrochemical (PEC) performance

Linear sweep voltammetry (LSV) measurements were performed to investigate the effect of combining Fe_2O_3 with $BaTiO_3$ photoanode on the overall PEC performance of the composite ferroelectric/photocatalyst thin film.

The photoresponse of pBTO-5 shows a maximum photocurrent of 14.4 μA/cm^2, which is considerably lower than both bare Fe_2O_3 (181.6 μA/cm^2) and Fe_2O_3/pBTO-5 thin films (383 μA/cm^2) (Figure 6.6 b,c). This is ascribed to the sluggish oxygen evolution reaction (OER) kinetics, UV light absorption and low conductivity of $BaTiO_3$, which depends on the oxygen vacancy concentration. Comparing the LSV light and chopped curves of the composite film with the bare Fe_2O_3, it is possible to see a clear increment in the PEC performance in the composite film, as shown in Figure 6.6 b and c. In particular, upon sweeping the potential from 0.7 V to 1.623 V vs RHE to probe the photocurrent onset and trend with increasing potential, the composite film shows an onset of water oxidation photocurrent at 1.011 V vs RHE and a maximum photocurrent of 383 μA/cm^2, which is two times higher than bare Fe_2O_3. The choice of the voltage ranges depends on the reference electrode and the pH of the electrolyte solution used as well as the conductivity type (n or p) of the semiconductor material. In the case of pBTO/Fe_2O_3, below 0.7 V vs RHE cathodic current begins to occur, which can damage the sample, and this voltage range allows both the onset potential and photocurrent at and above the water oxidation potential (1.23 V vs RHE) to be observed. This enhancement in the PEC response can be correlated to the presence of $BaTiO_3$. Indeed, the combination of pBTO-5 with Fe_2O_3 sample can move the energy band of the Fe_2O_3 upward and widen its depletion region, promoting the movement of the photogenerated holes from the Fe_2O_3 layer to the electrolyte.

It is also possible to observe a slight anodic shift of the photocurrent onset in the composite film compared to the bare Fe_2O_3 sample (0.988 V vs RHE). This anodic shift indicates a slightly inferior water oxidation kinetics compared to bare Fe_2O_3, which could be due to possible surface trapping states resulting from the confinement effect from the pBTO underlayer[18], i.e. the restricted growth of the Fe_2O_3 within the BTO pores could lead to an increase of surface traps. The presence of these surface trap states, which can lead to carrier recombination, is a critical factor that influences the photocurrent onset potential of Fe_2O_3 as photoanode.

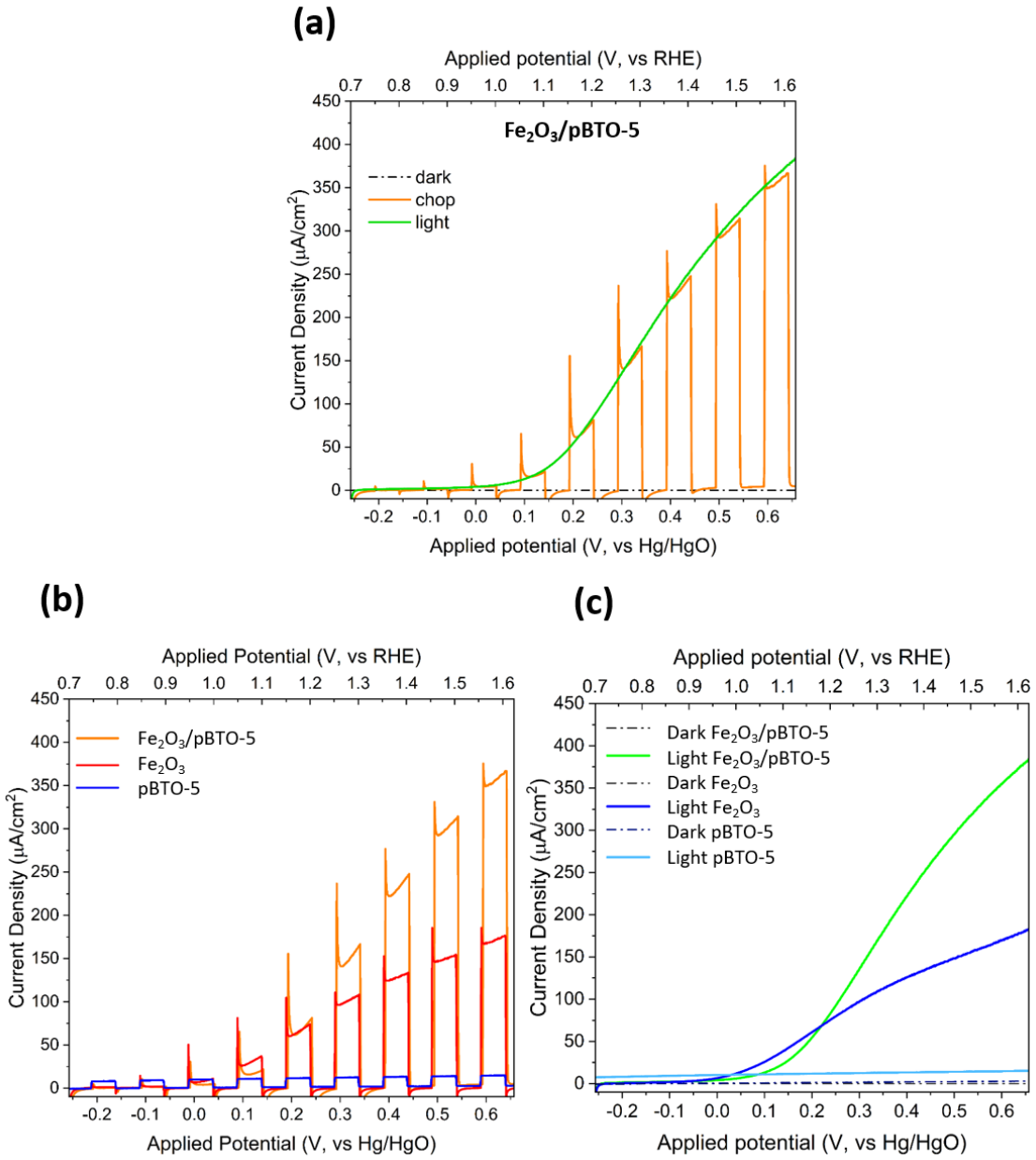

Figure 6.6 LSV curves of Fe_2O_3/pBTO-5 (a); comparison between chopped (b) and light (c) LSV curves of Fe_2O_3/pBTO-5, Fe_2O_3, pBTO-5 samples.

The chronoamperometry (J-t) curves of Fe_2O_3/pBTO-5, Fe_2O_3, pBTO-5 samples at 1.27 V vs RHE are analysed to investigate the PEC performance improvement and the repetitive light response of the ferroelectric/photocatalyst thin film. As shown in Figure

6.7 a, the Fe_2O_3/pBTO-5 photoanode exhibits an enhanced PEC response compared to both bare Fe_2O_3 and pBTO-5 samples, which is consistent with the above LSV measurements. The J-t curve was also used to study the stability of Fe_2O_3/pBTO-5 photoanode. Figure 6.7 b shows that there is not a significant loss of the photocurrents during the test for 1 h after initial stabilisation, indicating good stability of Fe_2O_3/pBTO-5 thin film as photoanode under full sunlight illumination. Thus, both LSV and chronoamperometry results demonstrate that the combination of ferroelectric $BaTiO_3$ with photocatalyst Fe_2O_3 improves the separation of photogenerated charges, maintaining a repetitive light response and longer-term stability.

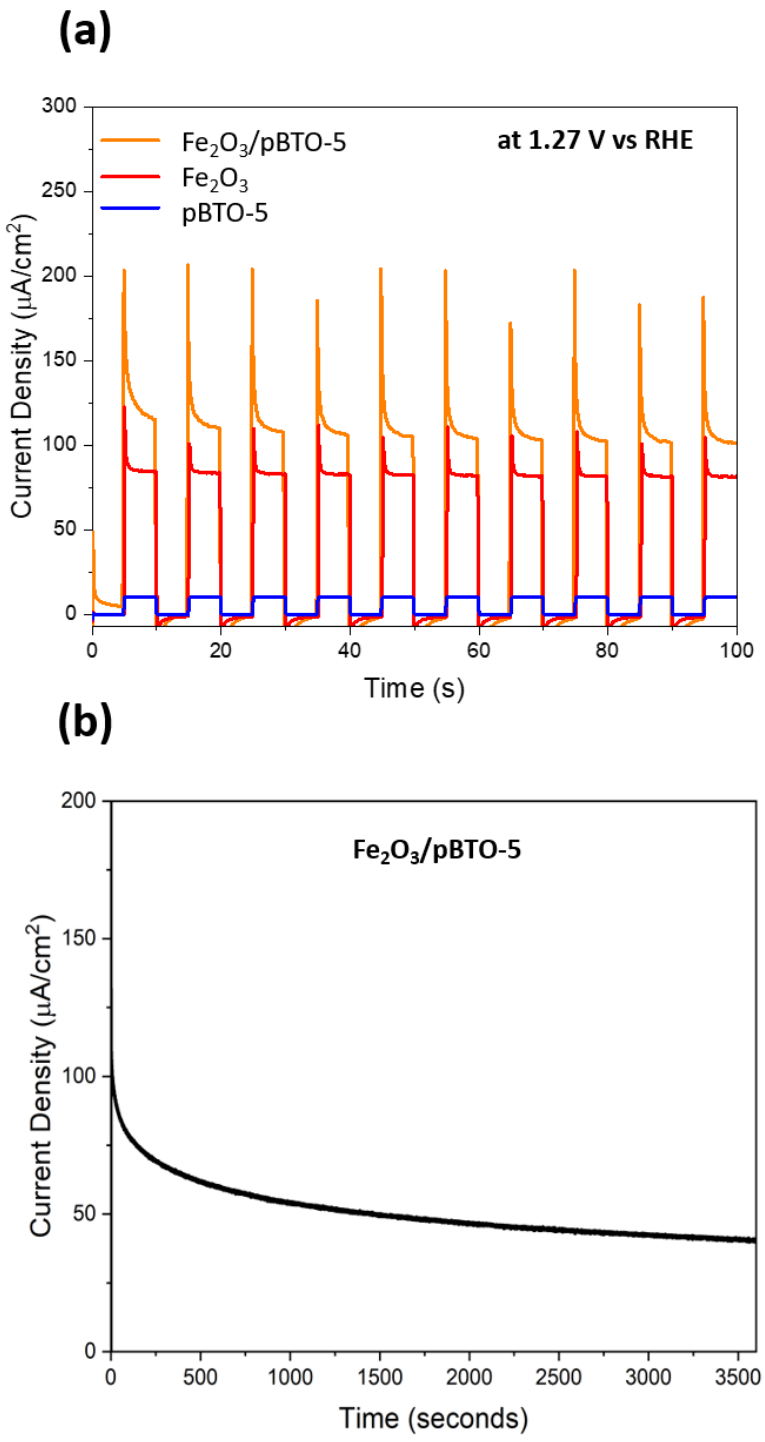

Figure 6.7 Chronoamperometry measurements of Fe_2O_3/pBTO-5, Fe_2O_3, pBTO-5 under chopped illumination over 100 s (a); Stability test of Fe_2O_3/pBTO-5 thin film under illumination at 1.2 V vs RHE for 1 h (b).

In addition to its increased performance compared to bare Fe_2O_3, obvious transient photocurrent peaks are observed in the chopped light chronoamperometry curves of Fe_2O_3/pBTO-5 when the light is turned on and off. It has been previously reported that such peaks are related to a variation in the rates of carrier extraction at the semiconductor interface[25,26]. To investigate this in more detail, the PEC performance of Fe_2O_3/pBTO-5 thin film was measured after adding a typical hole-scavenger, H_2O_2, into the electrolyte solution. H_2O_2 is an ideal hole scavenger because of its much higher rate constant for oxidation than water (10 to 100 times), accompanied by a relatively negative reduction potential than that of water (E^0 = +0.68 V vs RHE for the O_2/H_2O_2 couple, instead of E^0 = +1.23 V vs RHE for the O_2/H_2O couple)[26]. Indeed, it is known that the 4-hole oxidation of water to molecular oxygen has sluggish kinetics, because an excess of photoexcited holes are generated over the rate of extraction to complete the electrochemical reaction[27]. The electrochemical current obtained with H_2O_2 is mostly a product of the following reactions:

$$H_2O_2 + 2H^+ + e^- \rightarrow OH^- + OH^* + 2H^+ \rightarrow 2H_2O + h^+ \quad 6.1$$

$$H_2O_2 + 2h^+ \rightarrow 2H^+ + O_2 \quad 6.2$$

Equation 6.1 leads to a rise of the cathodic dark current as well as inducing photocurrent enhancement for electron injection with some p-type semiconductors. On the other hand, equation 6.2 generally gives rise to anodic dark current and photocurrents with n-type semiconductors. Thus, the addition of a hole scavenger can facilitate the reaction of the accumulated holes at the electrode/electrolyte interface, reducing back electron-hole recombination considerably. Figure 6.8 a,b shows the chopped and light LSV curves of Fe_2O_3/pBTO-5, tested using two different electrolytes: 1 M NaOH and 1M NaOH + 0.5

M H_2O_2. As illustrated in Figure 6.8 b, the introduction of H_2O_2 to the electrolyte changes the onset potential of the photocurrent to 0.75 V vs RHE. Moreover, a drastic reduction of the transient photocurrents associated with the non-equilibrium extraction of holes and electrons is observed upon the addition of H_2O_2 and a significant increment in the PEC response is recorded (512 μA/cm^2 at 1.27 V vs RHE) compared to the corresponding measurements in the electrolyte solution without a hole-scavenger (141 μA/cm^2 at 1.27 V vs RHE). Thus, the results obtained demonstrate that the generation of transient photocurrents can be suppressed after addition of a hole scavenger. The latter can offer an alternative oxidation pathway with faster kinetics, promoting the reaction of accumulated holes at the electrode/electrolyte interface and consequently avoiding back electron-hole recombination. This demonstrates that the PEC performance of Fe_2O_3/pBTO-5 photoanode could be further enhanced, for example by combination with a co-catalyst. Moreover, the LSV curves of the bare Fe_2O_3 sample under light and chopped illumination are measured in 1 M NaOH and 1 M NaOH + 0.5 M H_2O_2 electrolytes as comparison. Also in this case, after addition of H_2O_2 as hole scavenger, the PEC performance of the bare Fe_2O_3 is improved (188 μA/cm^2 at 1.27 V vs RHE) compared to the measurements without hole-scavenger (97 μA/cm^2 at 1.27 V vs RHE), as shown in Figure 6.8 c,d.

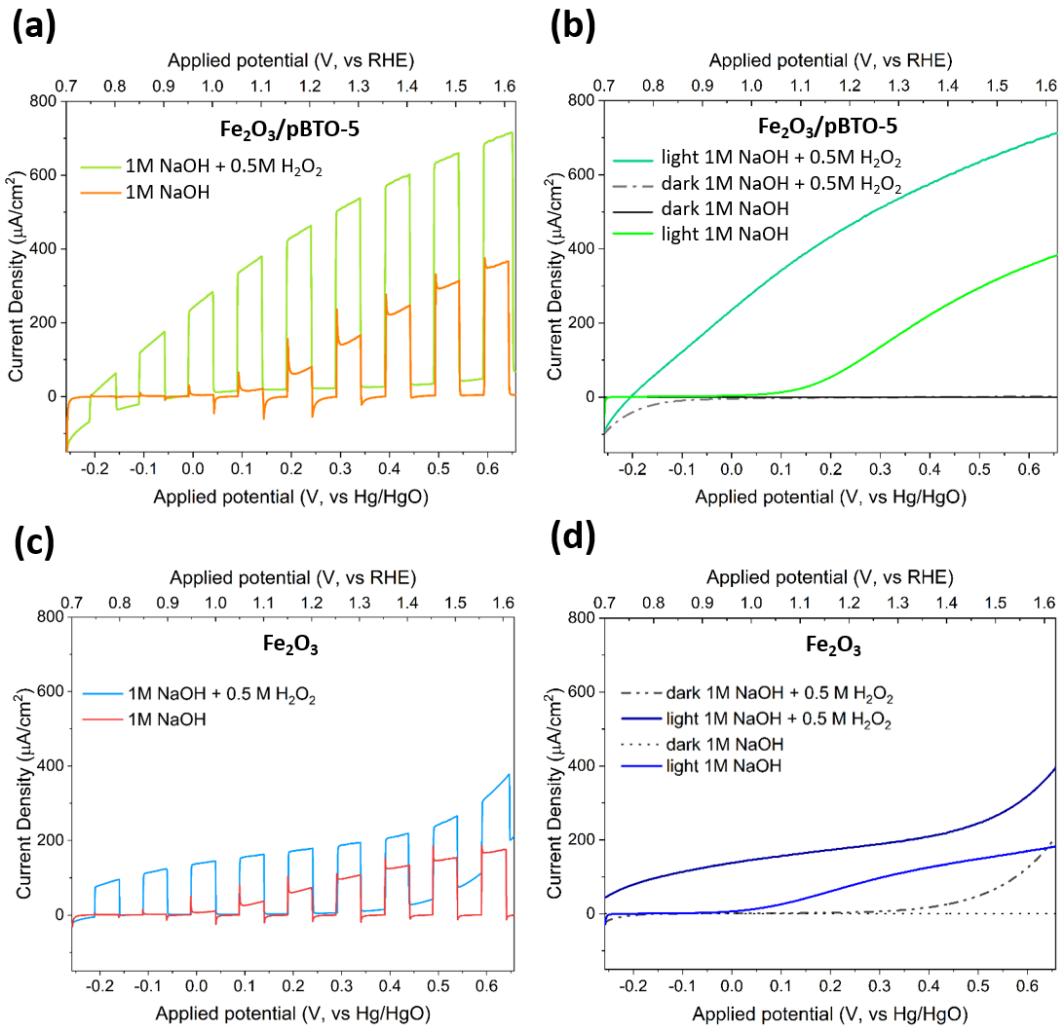

Figure 6.8 LSV curves under chopped illumination and illumination for Fe_2O_3/pBTO-5 (a,b) and Fe_2O_3 photoanode (c,d) with and without hole scavenger (H_2O_2).

However, the composite Fe_2O_3/pBTO-5 film shows a much better PEC response compared to the bare Fe_2O_3 sample upon addition of H_2O_2 and this gives strong evidence that ultimately a large enhancement in the PEC performance can be gained in the composite film (Figure 6.9).

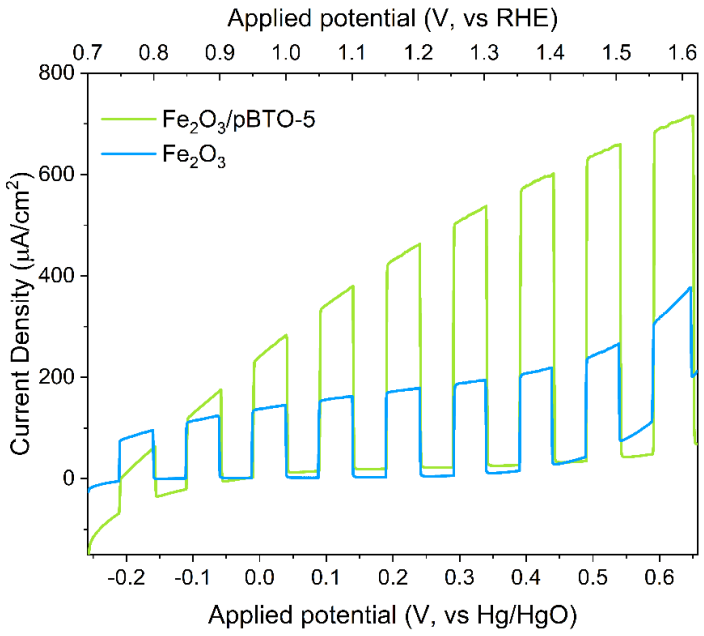

Figure 6.9 Comparison between LSV curves of Fe_2O_3/pBTO-5 and Fe_2O_3 sample under chopped illumination with hole scavenger (H_2O_2).

Moreover, to further investigate the beneficial effect on the PEC performance derived by the combination of the ferroelectric $BaTiO_3$ with the photocatalyst Fe_2O_3, the charge transfer properties are analysed. The charge injection efficiency and the charge separation efficiency were calculated using the following equations:

$$J_{H_2O} = J_{absorbed} \times P_{charge\ separation} \times P_{charge\ injection} \quad 6.3$$

Assuming that the charge injection yield is 100 % ($P_{charge\ injection} = 1$) in the presence of a hole scavenger (H_2O_2), the equation 6.3 can be expressed as follow:

$$J_{H_2O_2} = J_{absorbed} \times P_{charge\ separation} \quad 6.4$$

Based on equations 6.3 and 6.4:

$$P_{charge\ injection} = \frac{J_{H_2O}}{J_{H_2O_2}} \quad 6.5$$

$$P_{charge\ separation} = \frac{J_{H_2O_2}}{J_{absorbed}} \quad 6.6$$

Additional details about equations 6.3-6.6 are reported in Chapter 3[28,17]. Figure 6.10 a shows that the charge injection efficiency (%) is significantly improved in Fe_2O_3/pBTO-5, reaching a maximum value of 51 % at 1.6 V vs RHE compared to bare Fe_2O_3 and pBTO-5 thin films. This suggests that the combination of Fe_2O_3 with $BaTiO_3$ can facilitate charge injection between the Fe_2O_3/electrolyte interface. In addition, the charge separation efficiency of Fe_2O_3/pBTO-5 (56 % at 1.6 V vs RHE) is considerably higher than that of bare Fe_2O_3 (27 % at 1.6 V vs RHE) and pBTO-5 (16 % at 1.6 V vs RHE), suggesting that in the composite film the presence of ferroelectric $BaTiO_3$ could enhance charge transfer from Fe_2O_3 to its surface, leading to a reduction in electron-hole recombination (Figure 6.10 b).

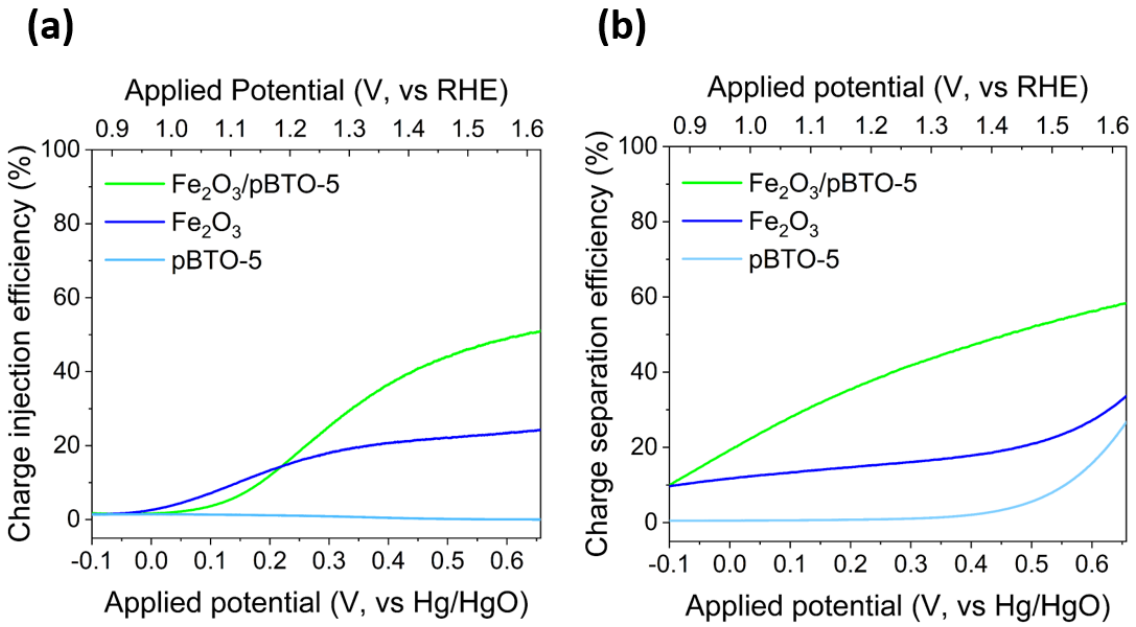

Figure 6.10 Charge injection efficiency (a) and charge separation efficiency (b) of Fe_2O_3/pBTO-5, Fe_2O_3 and pBTO-5 thin films.

6.1.1.5 Energy conversion efficiency of ferroelectric/photocatalyst film

To further understand the enhancement of PEC performance in Fe_2O_3/pBTO-5 thin films, the photon-to-current conversion efficiency was measured using IPCE. The IPCE measurements were conducted on different Fe_2O_3/pBTO-5 and Fe_2O_3 thin films from those used to obtain the above results, but which were prepared in the same experimental conditions. The measurement and calculation details of IPCE for both Fe_2O_3/pBTO-5 and bare Fe_2O_3, reported in Chapter 3, were performed by Chloe Forrester, a PhD student from Joe Briscoe's research group. The results obtained confirm the conversion from adsorbed photons with different energies to photocurrents. As shown in Figure 6.11, higher IPCE values in both UV and visible region are obtained for the composite Fe_2O_3/pBTO-5 film at 1.23 V vs RHE (peak value is ~ 4.5 %) compared to the bare Fe_2O_3 sample (peak value ~ 1.4 %). This result demonstrates an improvement of photon-to-current conversion efficiency in the Fe_2O_3/pBTO-5 film, probably correlated to a more efficient charge separation, resulting in a low recombination rate as well as a faster charge transfer in the composite ferroelectric/photocatalyst film.

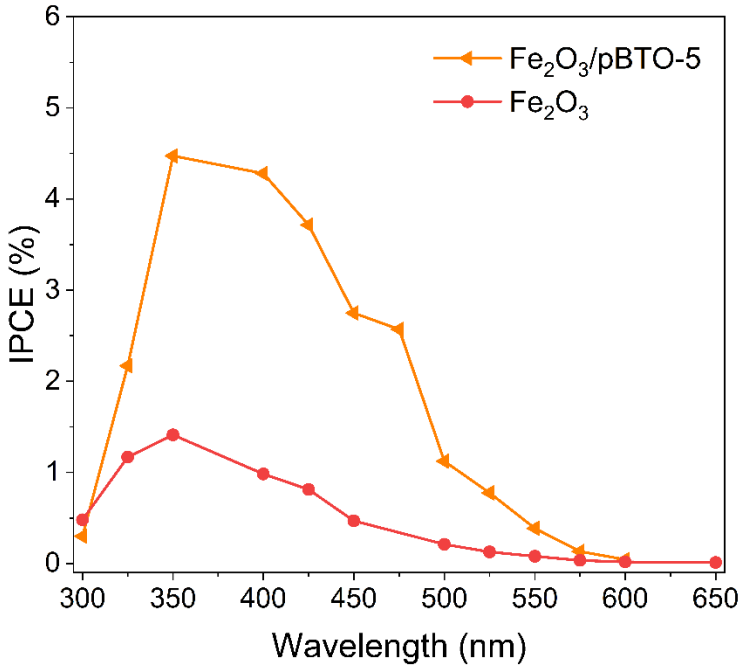

Figure 6.11 IPCE spectra of Fe_2O_3/pBTO-5 and Fe_2O_3 at 1.23 V vs RHE.

6.1.2 Tuning of photoelectrochemical performance *via* ferroelectric polarization

To further study the influence of ferroelectric polarisation on the PEC response of the Fe_2O_3 layer in the ferroelectric/photocatalyst composite film, the Fe_2O_3/pBTO-5 photoanode was poled using the electrochemical poling procedure, detailed in Chapter 3, and J-V curves were measured after poling pretreatment. The electrochemical poling pretreatment was also performed on bare Fe_2O_3 used as control sample.

6.1.2.1 Photocurrent density measurements after electrochemical (EC) poling

Figure 6.12 a,b report the LSV curves of Fe_2O_3/pBTO-5 sample under chopped and continuous illumination after positive and negative poling. The +8 V EC poling induces an obvious enhancement of the PEC performance in Fe_2O_3/pBTO-5 (821.4 µA/cm^2 at 1.623 V vs RHE) compared to the unpoled counterpart (383 µA/cm^2 at 1.623 V vs RHE).

This improvement in the PEC response can be correlated to the upward band-bending at the semiconductor/electrolyte interface with electric field polarisation, as described in more detail for pBTO thin films in Chapter 4 and 5. In contrast, the photocurrent density is lower for the unpoled Fe_2O_3/pBTO-5 sample (383 μA/cm^2 at 1.623 V vs RHE) with respect to the -8 V EC poled state (424 μA/cm^2 at 1.623 V vs RHE). However, as observed in Figure 6.12 a,b, at lower applied potentials, the PEC response is decreased in the -8 V EC poled sample compared to the unpoled counterpart. This is related to the downward band-bending at the semiconductor/electrolyte interface, as reported in Chapter 4 and 5. The schematic of Fe_2O_3/$BaTiO_3$ system in parallel structure after positive and negative poling is illustrated in Figure 6.13. As shown in Figure 6.13 a, when the Fe_2O_3/pBTO-5 film is +8 V EC poled, the spontaneous polarisation from ferroelectric pBTO-5 will induce internal screening, driving the holes from pBTO-5 to the film/electrolyte interface to neutralize the ferroelectric polarisation. Consequently, the hole accumulation in pBTO-5 leads to an enhancement in upward band bending, pulling the Fe_2O_3 bands in the same direction as the pBTO-5 because of the Fe_2O_3/$BaTiO_3$ parallel structure. This internal screening generated in pBTO-5 films can offer an additional driving force to improve the charge separation efficiency and consequently boosts the overall PEC performance of the composite photoanode (Figure 6.13 a). On the contrary, if -8 V EC poling is performed, the ferroelectric polarisation will induce electron accumulation at the film/electrolyte interface, which consequently generates downward band bending in both pBTO-5 and Fe_2O_3. This downward band bending will hamper the transfer of electrons to the electrolyte because it is against the water oxidation reaction and thus a decrease in the PEC response of Fe_2O_3/pBTO-5 as photoanode is observed (Figure 6.13 b). This is in agreement with the LSV results reported.

The photocurrent density of bare Fe_2O_3 thin films shows a decrease after both positive and negative EC poling, indicating that the application of high voltages may generate chemical changes in Fe_2O_3 film or even its dissolution in the electrolyte and this may induce variation in the PEC response (Figure 6.12 c). Thus, the chemical composition of Fe_2O_3 layer will be analysed and discussed in more detail in the following section. Nevertheless, compared to bare Fe_2O_3 film, Fe_2O_3/pBTO-5 shows a clear PEC trend after positive and negative poling, suggesting that the PEC response of Fe_2O_3/pBTO-5 thin films can still be tuned by controlling the orientation of ferroelectric polarization. (Figure 6.12 b, c).

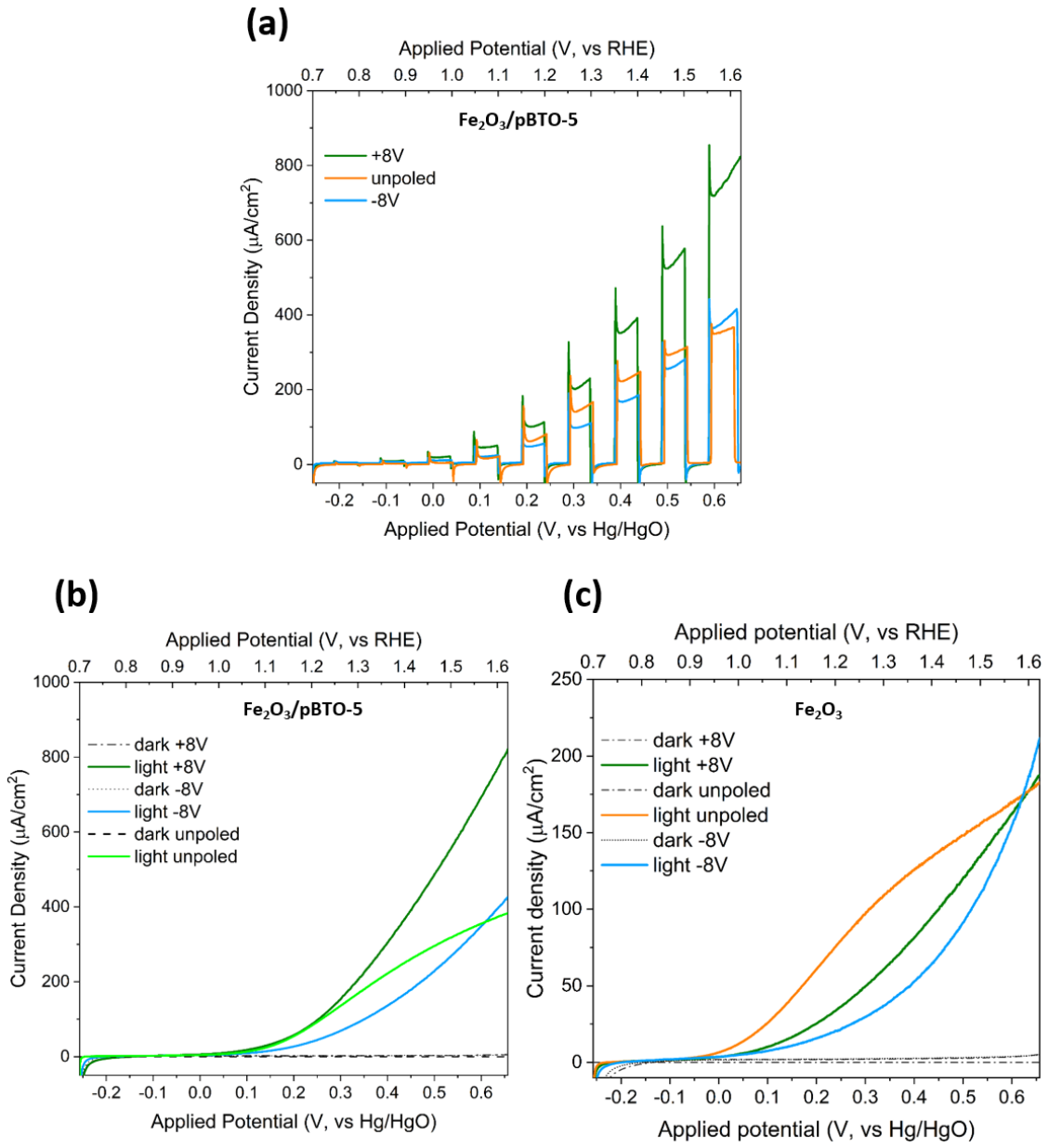

Figure 6.12 LSV under chopped illumination of Fe_2O_3/pBTO-5 sample after positive and negative poling (a); LSV curves under continuous illumination of Fe_2O_3/pBTO-5 (b) and bare Fe_2O_3 sample (c) after positive and negative poling.

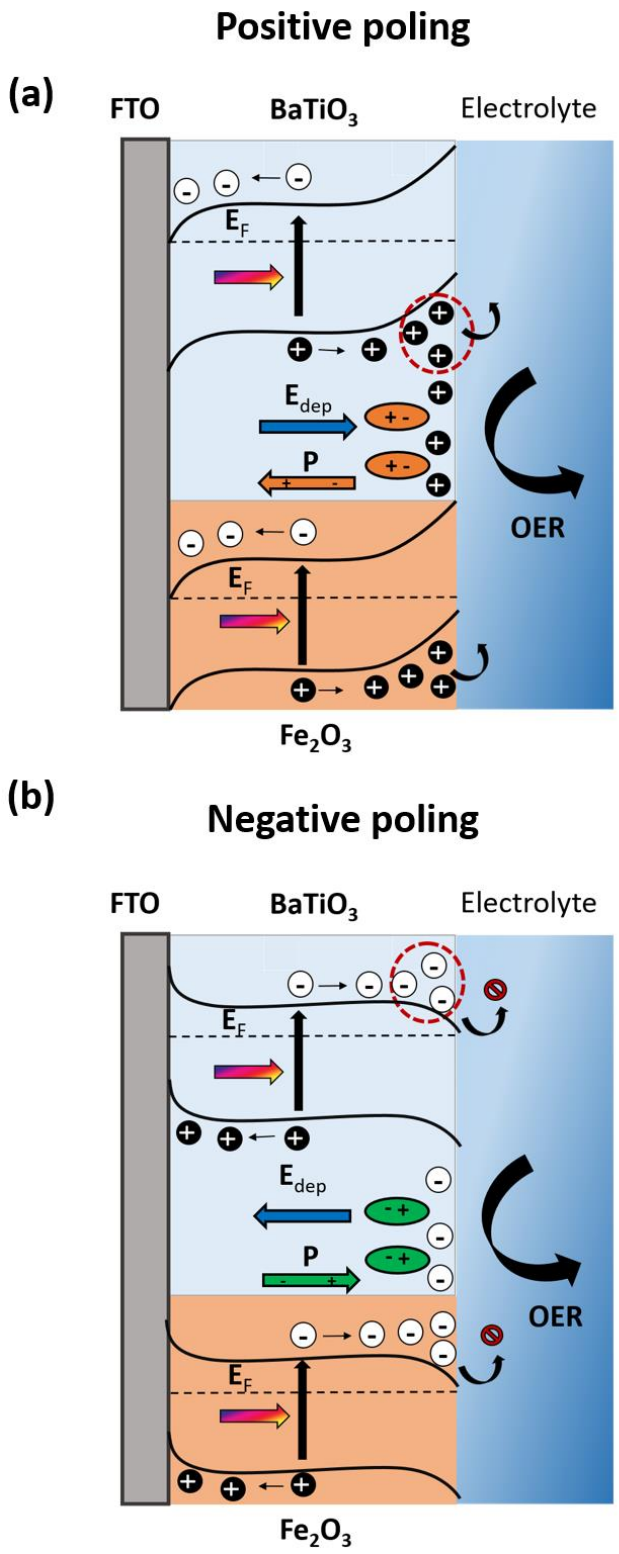

Figure 6.13 Schematic mechanism of controlling PEC performance in Fe_2O_3/pBTO-5 sample via ferroelectric polarisation, after positive (a) and negative (b) poling.

6.1.2.2 XPS analysis after electrochemical (EC) poling

To further investigate the effect of poling pretreatment on Fe_2O_3/pBTO-5 sample and investigate any chemical changes that may contribute to the changes in PEC performance discussed above, the elemental composition after EC poling was investigated using XPS analysis. Figure 6.13 shows the survey spectra of Fe_2O_3/pBTO-5 thin film unpoled, +8 V poled and -8 V poled. The presence of Fe and O signals along with Ba and Ti peaks are detected in Fe_2O_3/pBTO-5 photoanode, confirming the successful growth of Fe_2O_3 on the $BaTiO_3$ film. As shown in Figure 6.13, Fe_2O_3/pBTO-5 sample has not experienced overcurrent effects since the intensity of the peaks before and after poling is only marginally varied compared to the unpoled counterpart[29]. Moreover, the C1s signal is observed in Fe_2O_3/pBTO-5 sample before and after EC poling, but its intensity is weaker than that of O1s signal, indicating that C contamination does not influence the XPS measurements significantly, and it does not vary greatly between samples, indicating the presence of surface organic species does not vary greatly.

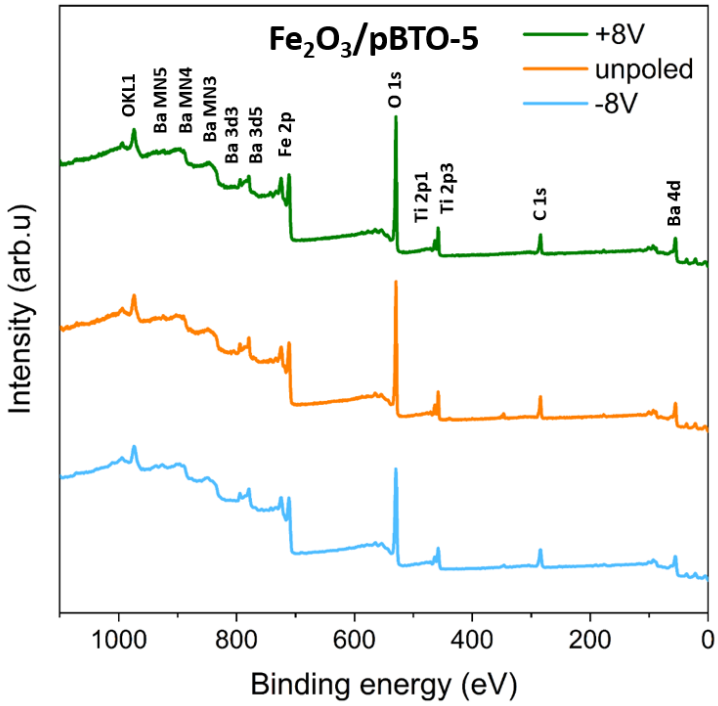

Figure 6.14 XPS survey spectra of Fe_2O_3/pBTO-5 thin films unpoled, +8 V EC poled and -8 V EC poled.

To analyse the effect of EC poling on the elemental composition of Fe_2O_3 layer in more detail, XPS scans at high resolution over smaller energy windows were collected. Figure 6.14 a shows the Fe 2p high resolution XPS spectra of Fe_2O_3/pBTO-5 film before and after poling, where the peaks at 724.2 and 710.9 eV belong to Fe 2p 1/2 and Fe 2p 3/2, respectively. In addition, the two satellite peaks of the Fe 2p main line are observed, revealing the presence of the Fe^{3+} oxidation state in the Fe_2O_3/pBTO-5 sample[30,31]. Moreover, the O 1s XPS peak can be attributed to lattice oxygen in the crystalline $BaTiO_3$ and Fe_2O_3 layer at a binding energy of 529.9 eV[32], as reported in Figure 6.14 b. Comparing both Fe 2p and O 1s signals before and after EC poling, the +8 V poled sample shows almost the same surface atomic content of oxygen and iron ions observed in the unpoled counterpart, as reported in Table 6.1, in the same chemical environment. This is

confirmed by the shapes and intensities of the Fe 2p and O 1s signals, which remain unchanged after +8 V EC poling (Figure 6.14 a,b). In the -8 V EC poled sample, a slight decrease in the surface atomic content of iron and oxygen ions can be noted compared to the unpoled sample, as shown in Table 6.1. It is accompanied by a slight attenuation of the Fe and O peaks intensity as well as a slight shift of the O 1s peak position toward higher binding energy after negative poling. This shifting could be related to a global surface charge effect[29,33]. Nevertheless, this evidence is not sufficiently significant to indicate a sample alteration. Therefore, it can be concluded that the EC poling of the Fe_2O_3/pBTO-5 sample does not considerably change the surface composition of the Fe_2O_3 layer, including the oxygen vacancies content, and thus the change in PEC response of the poled Fe_2O_3/pBTO-5 sample can be attributed to the influence of the ferroelectric polarisation.

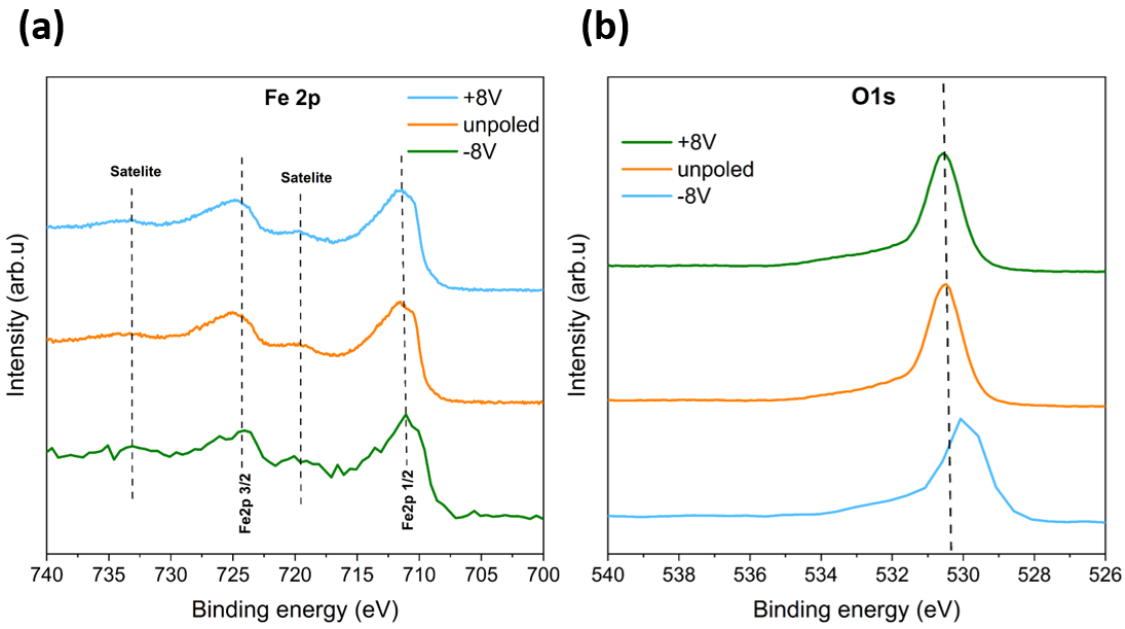

Figure 6.15 Fe2p (a) and O1s (b) high resolution XPS spectra of Fe_2O_3/pBTO-5 sample before and after EC poling.

Table 6.1 Surface atomic content (%) of iron and oxygen in Fe_2O_3/pBTO-5 sample before and after +/- 8 V EC poling.

	Surface atomic content (%)		
	-8V	unpoled	+8V
Fe 2p3	1.05	1.42	1.44
Fe 2p1	0.32	0.33	0.38
O1s	13.63	14.35	14.49

6.2 Summary

In this chapter, the development and study of a novel ferroelectric/photocatalyst system, obtained by hydrothermal growth of Fe_2O_3 within the pores and on the surface of ferroelectric porous $BaTiO_3$ (pBTO-5) thin films has been reported. The SEM, EDX, XRD and XPS analysis confirm the successful combination of F_2O_3 with $BaTiO_3$ sample. The as-obtained Fe_2O_3/pBTO-5 photoanode revealed a significant enhancement in the photoelectrochemical (PEC) response under solar illumination, compared to bare Fe_2O_3 and pBTO-5 thin films. In particular, the Fe_2O_3/pBTO-5 film showed a maximum photocurrent density of 383 $\mu A/cm^2$ which is two times higher than that of bare Fe_2O_3 and considerably improved with respect to the bare pBTO-5 sample. This remarkable improvement in the PEC performance in Fe_2O_3/pBTO-5 films and its long-term stability

was attributed to the ferroelectric polarisation, which induces free carrier redistribution at the Fe_2O_3/electrolyte interface, leading to a reduction in charge carrier recombination. Indeed, the injection and separation of photogenerated charges in Fe_2O_3/pBTO-5 film is clearly improved compared to both bare Fe_2O_3 and pBTO-5 films. In addition, it was demonstrated that the Fe_2O_3/pBTO-5 film possesses a switchable PEC response by tuning the ferroelectric polarisation orientation of $BaTiO_3$, using electrochemical (EC) poling pretreatment. As proved by XPS analysis, the EC poling procedure did not significantly alter the surface composition of the Fe_2O_3 layer. Thus, in this chapter, the beneficial effect on the PEC response of Fe_2O_3/pBTO-5 films derived by their combination to form a ferroelectric/photocatalyst heterostructure has been demonstrated. The possibility to enhance the PEC performance of ferroelectric/photocatalyst film by adjusting ferroelectric polarisation could be a promising strategy to adopt in photoelectrocatalysis, which combined with the optimization of photocatalyst's structure and chemistry, could open up further opportunities.

REFERENCES

1. Roger, I., Shipman, M. A. & Symes, M. D. Earth-abundant catalysts for electrochemical and photoelectrochemical water splitting. *Nat. Rev. Chem.* **1**, (2017).

2. Saraswat, S. K., Rodene, D. D. & Gupta, R. B. Recent advancements in semiconductor materials for photoelectrochemical water splitting for hydrogen production using visible light. *Renew. Sustain. Energy Rev.* **89**, 228–248 (2018).

3. Sivula, K. & Van De Krol, R. Semiconducting materials for photoelectrochemical energy conversion. *Nat. Rev. Mater.* **1**, (2016).

4. Tamirat, A. G., Rick, J., Dubale, A. A., Su, W. N. & Hwang, B. J. Using hematite for photoelectrochemical water splitting: A review of current progress and challenges. *Nanoscale Horizons* **1**, 243–267 (2016).

5. Li, C., Luo, Z., Wang, T. & Gong, J. Surface, Bulk, and Interface: Rational Design of Hematite Architecture toward Efficient Photo-Electrochemical Water Splitting. *Adv. Mater.* **30**, 1–23 (2018).

6. Grave, D. A., Yatom, N., Ellis, D. S., Toroker, M. C. & Rothschild, A. The "Rust" Challenge: On the Correlations between Electronic Structure, Excited State Dynamics, and Photoelectrochemical Performance of Hematite Photoanodes for Solar Water Splitting. *Adv. Mater.* **30**, 1–10 (2018).

7. Wang, X. *et al.* Efficient photo-electrochemical water splitting based on hematite nanorods doped with phosphorus. *Appl. Catal. B Environ.* **248**, 388–393 (2019).

8. Hiralal, P. *et al.* Nanostructured hematite photoelectrochemical electrodes prepared by the low temperature thermal oxidation of iron. *Sol. Energy Mater. Sol. Cells* **95**, 1819–1825 (2011).

9. Kong, T. T., Huang, J., Jia, X. G., Wang, W. Z. & Zhou, Y. Selective doping of titanium into double layered hematite nanorod arrays for improved photoelectrochemical water splitting. *Appl. Surf. Sci.* **486**, 312–322 (2019).

10. Fan, K. *et al.* Immobilization of a Molecular Ruthenium Catalyst on Hematite Nanorod Arrays for Water Oxidation with Stable Photocurrent. *ChemSusChem* **8**, 3242–3247 (2015).

11. Song, J. *et al.* Domain-engineered $BiFeO_3$ thin-film photoanodes for highly enhanced ferroelectric solar water splitting. *Nano Res.* **11**, 642–655 (2018).

12. Lv, J., Chen, X., Chen, S., Li, H. & Deng, H. A visible light induced ultrasensitive photoelectrochemical sensor based on $Cu_3Mo_2O_9/BaTiO_3$ p–n heterojunction for detecting oxytetracycline. *J. Electroanal. Chem.* **842**, 161–167 (2019).

13. Cao, D., Wang, Z., Wen, L., Mi, Y. & Lei, Y. Switchable Charge-Transfer in the Photoelectrochemical Energy- Conversion Process of Ferroelectric $BiFeO_3$ Photoelectrodes. *Angew. Chemie - Int. Ed.* 1–6 (2014).

14. Wang, F. *et al.* Interfacial multiferroics of $TiO_2/PbTiO_3$ heterostructure driven by ferroelectric polarization discontinuity. *ACS Appl. Mater. Interfaces* **9**, 1899–1906 (2017).

15. Xie, J. *et al.* Bi-functional ferroelectric $BiFeO_3$ passivated $BiVO_4$ photoanode for efficient and stable solar water oxidation. *Nano Energy* **31**, 28–36 (2017).

16. Yang, W. *et al.* Ferroelectric Polarization-Enhanced Photoelectrochemical Water Splitting in TiO_2-$BaTiO_3$ Core-Shell Nanowire Photoanodes. *Nano Lett.* **15**, 7574–7580 (2015).

17. He, X. *et al.* Novel Fe_2O_3/PZT nanorods for ferroelectric polarization-enhanced photoelectrochemical water splitting. *Energy and Fuels* **34**, 16927–16935 (2020).

18. Brillet, J., Grätzel, M. & Sivula, K. Decoupling feature size and functionality in solution-processed, porous hematite electrodes for solar water splitting. *Nano Lett.* **10**, 4155–4160 (2010).

19. Guo, Q. *et al.* The role of carbon dots-derived underlayer in hematite photoanodes. *Nanoscale* **12**, 20220–20229 (2020).

20. Tang, P. *et al.* Enhanced photoelectrochemical water splitting of hematite multilayer nanowire photoanodes by tuning the surface state via bottom-up interfacial engineering. *Energy Environ. Sci.* **10**, 2124–2136 (2017).

21. Zong, X. *et al.* A scalable colloidal approach to prepare hematite films for efficient solar water splitting. *Phys. Chem. Chem. Phys.* **15**, 12314–12321 (2013).

22. Schröder, S. *et al.* Origins of light scattering from thin film coatings. *Thin Solid Films* **592**, 248–255 (2015).

23. Sivula, K. *et al.* Photoelectrochemical water splitting with mesoporous hematite prepared by a solution-based colloidal approach. *J. Am. Chem. Soc.* **132**, 7436–7444 (2010).

24. Lohaus, C., Steinert, C., Brötz, J., Klein, A. & Jaegermann, W. Systematic Investigation of the Electronic Structure of Hematite Thin Films. *Adv. Mater. Interfaces* **4**, 2–9 (2017).

25. Dotan, H., Sivula, K., Grätzel, M., Rothschild, A. & Warren, S. C. Probing the photoelectrochemical properties of hematite (α-Fe_2O_3) electrodes using hydrogen peroxide as a hole scavenger. *Energy Environ. Sci.* **4**, 958–964 (2011).

26. Le Formal, F., Sivula, K. & Grätzel, M. The transient photocurrent and photovoltage behavior of a hematite photoanode under working conditions and the influence of surface treatments. *J. Phys. Chem. C* **116**, 26707–26720 (2012).

27. Sivula, K. Metal oxide photoelectrodes for solar fuel production, surface traps, and catalysis. *J. Phys. Chem. Lett.* **4**, 1624–1633 (2013).

28. Luo, Z. *et al.* Dendritic Hematite Nanoarray Photoanode Modified with a Conformal Titanium Dioxide Interlayer for Effective Charge Collection. *Angew. Chemie - Int. Ed.* **56**, 12878–12882 (2017).

29. Datta, S., Rioult, M., Stanescu, D., Magnan, H. & Barbier, A. Manipulating the ferroelectric polarization state of $BaTiO_3$ thin films. *Thin Solid Films* **607**, 7–13 (2016).

30. Tang, P. *et al.* Enhanced photoelectrochemical water splitting of hematite multilayer nanowire photoanodes by tuning the surface state via bottom-up interfacial engineering. *Energy Environ. Sci.* **10**, 2124–2136 (2017).

31. Tang, P. Y. *et al.* Synergistic effects in 3D honeycomb-like hematite nanoflakes/branched polypyrrole nanoleaves heterostructures as high-performance negative electrodes for asymmetric supercapacitors. *Nano Energy* **22**, 189–201 (2016).

32. Sun, Q. *et al.* Crystalline Structure , Defect Chemistry and Room Temperature Colossal Permittivity of Nd-doped Barium Titanate. *Nat. Publ. Gr.* 1–8 (2017) doi:10.1038/srep42274.

33. Rioult, M. *et al.* Tailoring the photocurrent in $BaTiO_3$/Nb:$SrTiO_3$ photoanodes by controlled ferroelectric polarization. *Appl. Phys. Lett.* **107**, 1–5 (2015).

34. Li, Y., Li, J., Yang, W. & Wang, X. Implementation of ferroelectric materials in photocatalytic and photoelectrochemical water splitting. *Nanoscale Horizons* **5**, 1174–1187 (2020).

7 CONCLUSIONS AND OUTLOOK

7.1 Conclusions

This thesis aimed to investigate the effect of ferroelectric polarisation on the improvement of photoelectrochemical (PEC) performance of bare $BaTiO_3$ photoanode and when combined with Fe_2O_3 as a more efficient photocatalyst.

The first stage was to develop ferroelectric thin films, suitable for the integration with a more efficient photoactive material. Thus, nanostructured ferroelectric $BaTiO_3$ thin films have been prepared, owing to the high surface area that enhances their capabilities. The first trial for the production of nanostructured $BaTiO_3$ thin films involved a hydrothermal sol-gel method whereby TiO_2 gel films previously deposited on FTO glass substrate were converted to $BaTiO_3$ films. Although the full chemical conversion was successfully

obtained, the nanostructured $BaTiO_3$ thin films did not show a good PEC performance probably due to poor crystallinity and wide bandgap. In addition, the morphology of nanostructured $BaTiO_3$ thin films was difficult to control. Therefore, the preparation method was changed to a soft template-assisted sol-gel method, using different amounts of an organic sacrificial template to produce porous $BaTiO_3$ (pBTO) thin films with controllable porosity. The effect of different porosity on the ferroelectric and photoelectrochemical properties of pBTO thin films was explored. The linear dependence of the porosity with the amount of block-copolymer was verified by SEM and ellipsometry technique. PFM analysis, in combination with XRD and Raman spectroscopy, confirmed the ferroelectric behaviour of pBTO thin films, although the switching of spontaneous polarisation was more complete in the pBTO sample with higher porosity and larger particles than that with lower porosity and smaller particles. Moreover, all pBTO thin films showed an improvement in the PEC response compared to the corresponding non-porous BTO film and a correlation between surface area and PEC performance of pBTO films was observed. In addition, the tuning of PEC response using ferroelectric polarisation was obtained by performing electrochemical (EC) poling. Indeed, a clear enhancement in the photocurrent density values was observed after positive poling, making pBTO thin films promising candidates as photoanodes.

The next stage was to evaluate the influence of oxygen vacancies on the ability to pole pBTO thin films *via* EC poling. Hence, pBTO thin films were prepared in O_2, air and N_2 annealing atmospheres (pBTO-O_2, pBTO-air and pBTO-N_2), which produce different amounts of oxygen vacancies, as demonstrated by UV-vis spectroscopy, XPS analysis and PEC testing. Considering the favourable ability of ferroelectric thin films to control their PEC performance via ferroelectric polarisation, EC poling was conducted on all

pBTO thin films and in particular, as expected, the positive poling showed a clear improvement in the PEC performance of pBTO-O_2 and pBTO-air compared to the negative poling. Nevertheless, the mutual effect between interface charges generated by ferroelectric polarisation and the surface oxygen vacancies induced a more significant enhancement in the PEC performance in pBTO-air compared to pBTO-O_2, as demonstrated by XPS and PEC analysis.

On the contrary, the PEC results for the pBTO-N_2 sample after EC poling were not as consistent as in pBTO-O_2 and pBTO-air thin films. As supported by XPS and PEC analysis, the high concentration of oxygen vacancies induced high migration of oxygen vacancies within the p BTO-N_2 film, which limited its ability to be controlled by poling and this consequently generated very unpredictable results.

Finally, porous $BaTiO_3$ thin films with higher porosity (pBTO-5) were combined with Fe_2O_3 as nanocomposite photocatalyst (Fe_2O_3/pBTO-5). The Fe_2O_3 was grown by hydrothermal method within the pores and on the surface of pBTO-5 sample. This was confirmed by the combination of SEM, EDX, XRD and XPS analysis. Upon illumination, the Fe_2O_3/pBTO-5 photoanode showed a considerable increase in the PEC response compared to the bare Fe_2O_3 and pBTO-5 films, reaching a maximum photocurrent density of 383 $\mu A/cm^2$. Moreover, upon the addition of H_2O_2 as a hole scavenger, a significant increment in the PEC response was obtained (512 $\mu A/cm^2$ at 1.27 V vs RHE) compared to the corresponding measurements in the electrolyte solution without a hole-scavenger (141 $\mu A/cm^2$ at 1.27 V vs RHE). This suggested that by combination with a co-catalyst, ultimately a greater enhancement in the PEC performance could be gained in the ferroelectric/photocatalyst composite film. The credit for the remarkable enhancement in

the PEC performance in Fe_2O_3/pBTO-5 films and its long-term stability was given to the ferroelectric polarisation of pBTO-5. The latter generated free carrier redistribution at the Fe_2O_3/electrolyte interface, favouring a reduction in charge carrier recombination, as demonstrated by IPCE results and the injection and separation of photogenerated charges in Fe_2O_3/pBTO-5 film, which were clearly improved. In addition, the tuning of PEC response according to the switchable ferroelectric polarisation orientation in $BaTiO_3$, controlled by EC poling was achieved in Fe_2O_3/pBTO-5 film, without significantly affecting the surface composition of the film, as confirmed by XPS analysis. Thus, the PEC performance of the ferroelectric/photocatalyst composite system was further improved after positive poling, generating a maximum photocurrent response of 821.4 $\mu A/cm^2$, which is ca. two times higher than the unpoled counterpart (383 $\mu A/cm^2$).

In conclusion, the influence of ferroelectricity on the photoelectrochemical performance in both single ferroelectric $BaTiO_3$ and composite Fe_2O_3/$BaTiO_3$ photoanode has been demonstrated. The beneficial effect of ferroelectric polarisation on the PEC properties of the composite Fe_2O_3/$BaTiO_3$ film could be further enhanced by optimizing the design structure of the ferroelectric-photocatalyst system. Besides, this work suggested different characterisation methods to assess nanoscale ferroelectrics and to exploit ferroelectricity in photoelectrocatalysis, which can advantage future studies on ferroelectrics for photocatalysis.

7.2 Future work

- Preparation of well-ordered porous $BaTiO_3$ films

In this work, pBTO thin films were prepared by soft template-assisted sol-gel method, which allows the tuning of porosity in the porous films, using different amounts of sacrificial organic template. However, the pore diameter and size distribution control could be improved using a different synthetic approach. For example, inverse opal $BaTiO_3$ films could be a valid alternative for the preparation of highly ordered and uniform porous films, where the pore size can be easily tuned, changing the diameter of the polystyrene sphere template, which directly influences the actual pore dimension and the interconnecting space between pores. This could allow better integration with Fe_2O_3 as photocatalyst in the following step. Preliminary results showing the inverse opals $BaTiO_3$ films structure are reported in Figure 7.1.

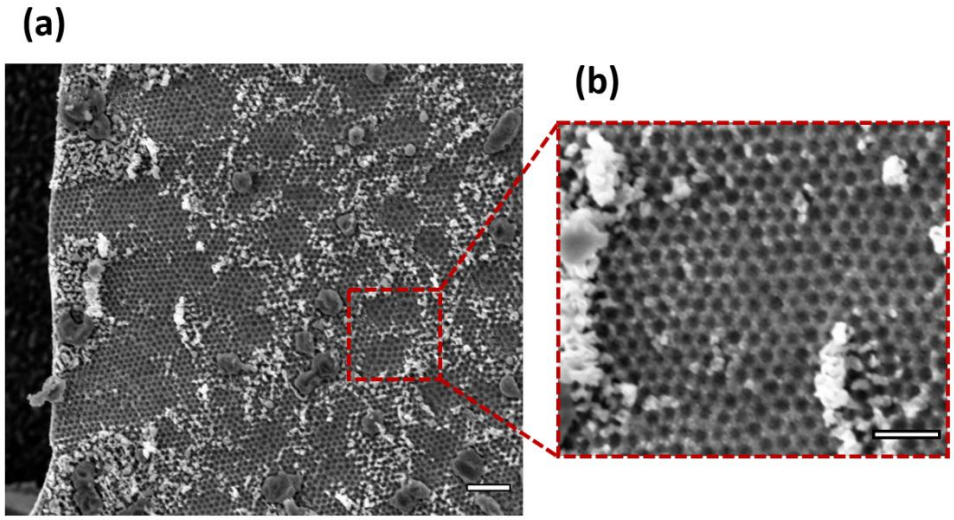

Figure 7.1 Top-view SEM image of inverse opal $BaTiO_3$ films (scale bar: 1 µm) (a) and corresponding magnification of smaller film area (scale bar: 0.5 µm) (b).

- Alternative method for poling of ferroelectric thin films

This thesis demonstrated that EC poling pre-treatment is a suitable method to control ferroelectric polarisation in bare pBTO and Fe_2O_3/pBTO composite system. Nevertheless, corona poling could be explored as alternative method. Corona poling has gained considerable attention for the poling of ferroelectric thin films[1-3]. As shown in Figure 7.2, this technique is based on placing the sample under the corona discharge, deriving from a tip held at a high potential. The film to be poled is usually grounded on a plate. Using this method, it is possible to pole a film without the application of a top electrode[2], and it is also possible to pole nanostructured or porous films.

Compared to the EC poling pre-treatment, the main advantages of corona poling are: (1) good potential for scale-up, (2) higher fields can be achieved (3) thin films can be poled in spite of defects, considering that breakdowns are limited only to small sample areas. Thus, corona poling may give improved results for bare pBTO and Fe_2O_3/pBTO compared to EC poling.

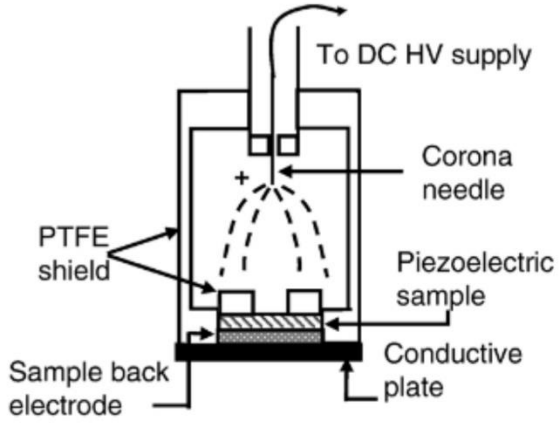

Figure 7.2 Schematic of corona poling set-up[2].

- Addition of co-catalyst on ferroelectric/photocatalyst composite film

As demonstrated in the previous chapter, the PEC response of Fe_2O_3/pBTO-5 film was further improved upon by adding H_2O_2 as a hole scavenger. Thus, the addition of co-catalysts ~~such as Co-Pi~~ on the photoanode surface is expected to improve the photocurrents greatly and this could also maximize the PEC performance of the composite film after poling pre-treatment. Among different cocatalysts, cobalt phosphates (Co-Pis) have gained great interest because they are earth-abundant, ion permeable, easily created on the surfaces of different semiconductors and they can also be used to catalyse water splitting over a wide pH range (1-14). Thus, Co-Pi cocatalysts are promising alternatives to noble-metal-based cocatalysts[4].

- Alternative method for the preparation of Fe_2O_3 photocatalyst

A different approach for the synthesis of Fe_2O_3 on porous $BaTiO_3$ films could be adopted to have better control over the thickness and particle size of Fe_2O_3 and to improve the interaction between Fe_2O_3 and $BaTiO_3$, which could allow a further improvement of PEC response after EC poling. Electrochemical deposition could be a suitable method for the preparation of Fe_2O_3 film. Compared to the hydrothermal method, it allows better control of the composition, crystallinity and film deposition property by properly adjusting electrodeposition process parameters.

REFERENCES

1. Park, S. *et al.* A ferroelectric photocatalyst for enhancing hydrogen evolution: Polarized particulate suspension. *Phys. Chem. Chem. Phys.* **16**, 10408–10413 (2014).

2. J.M. Marshall, Q. Zhang, R.W. Whatmore, Corona poling of highly (001)/(100)-oriented lead zirconate titanate thin films. *Thin Solid Films* **15**, 4679-4684 (2008).

3. Markus Kohli & Paul Muralt, Poling of ferroelectric thin films, *Ferroelectrics*, 155-162 (1999).

4. Xu, X. T., Pan, L., Zhang, X., Wang, L. & Zou, J. J. Rational Design and Construction of Cocatalysts for Semiconductor-Based Photo-Electrochemical Oxygen Evolution: A Comprehensive Review. *Adv. Sci.* **6**, (2019).

8 APPENDIX

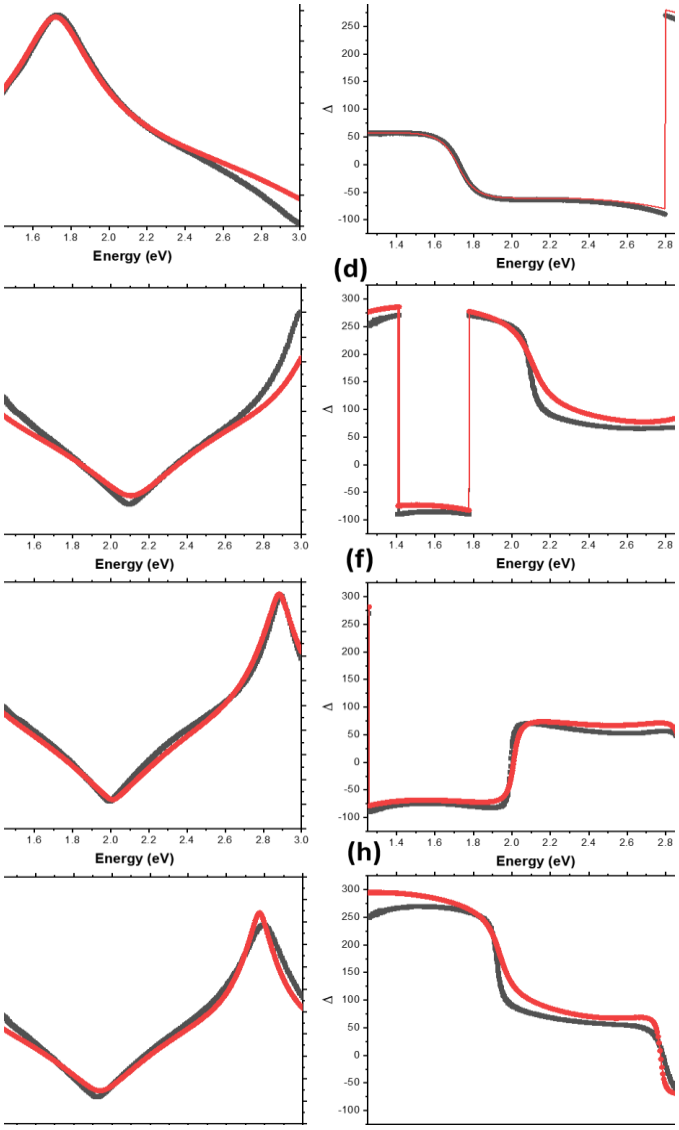

Figure A1 Fitting of ellipsometric angles Ψ and Δ obtained for pBTO-0.2 (a-b), pBTO-2 (c-d), pBTO-3.5 (e-f), and pBTO-5 (g-h), obtained by application of Bruggeman EMA, using air as medium.

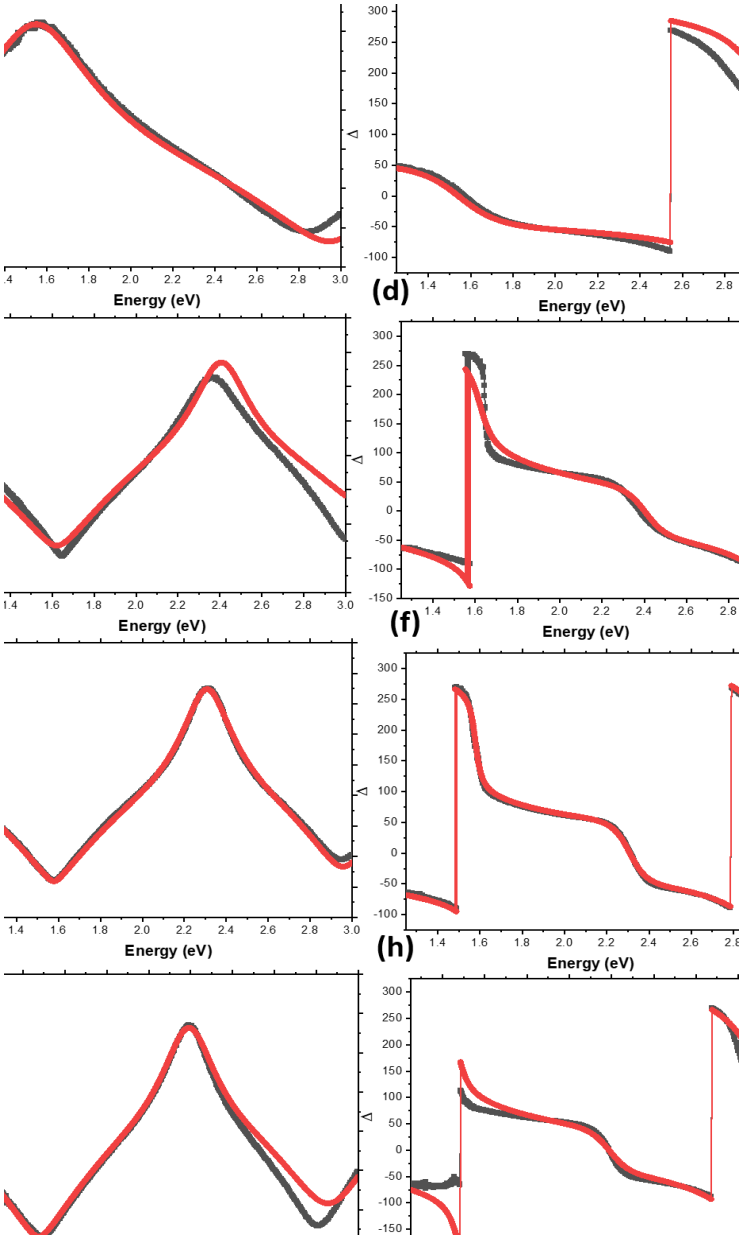

Figure A2 Fitting of ellipsometric angles Ψ and Δ obtained for pBTO-0.2 (a-b), pBTO-2 (c-d), pBTO-3.5 (e-f), and pBTO-5 (g-h), obtained by application of Bruggeman EMA, using water as medium.

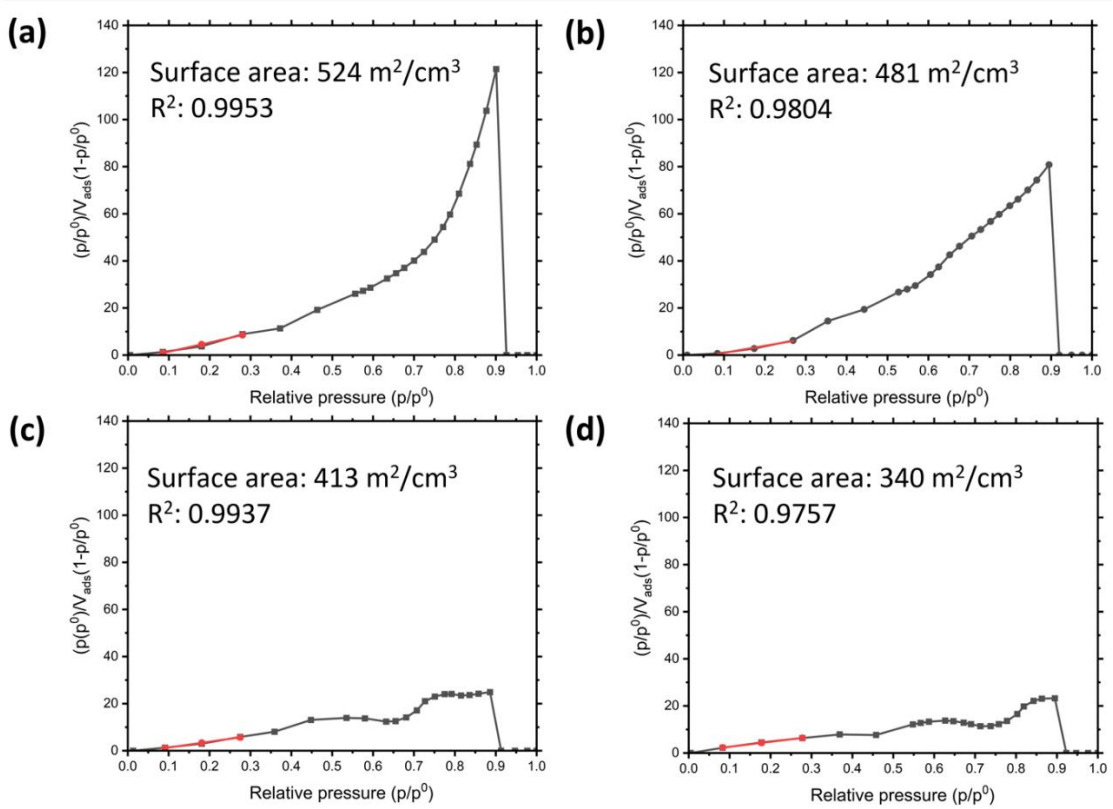

Figure A3 BET plots of pBTO-0.2 (a), pBTO-2 (b), pBTO-3.5 (c) and pBTO-5 (d), where the surface area values are obtained by fitting the linear region of the ellipsometric adsorption isotherms.

9 PERMISSION

9.1 Proof of permission from ACS for first author publication

Chapter 4 was reproduced/adapted according to *ACS Appl. Mater. Interfaces* 2022, 14, 11, 13147–13157 (https://pubs.acs.org/doi/10.1021/acsami.1c17419). Permission to reproduce this manuscript has been granted by ACS Publications Support:

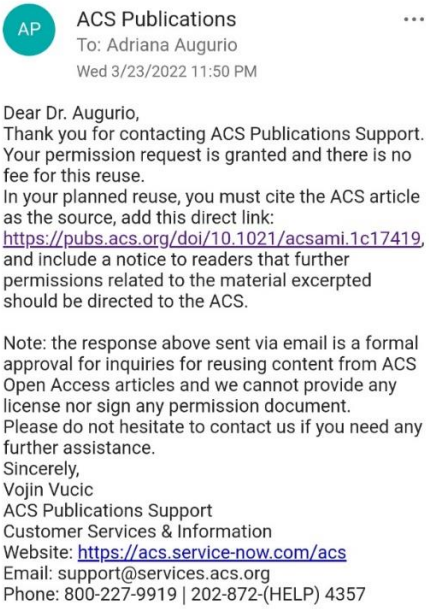

AP

ACS Publications

To: Adriana Augurio

Wed 3/23/2022 11:50 PM

Dear Dr. Augurio,
Thank you for contacting ACS Publications Support.
Your permission request is granted and there is no fee for this reuse.
In your planned reuse, you must cite the ACS article as the source, add this direct link: https://pubs.acs.org/doi/10.1021/acsami.1c17419, and include a notice to readers that further permissions related to the material excerpted should be directed to the ACS.

Note: the response above sent via email is a formal approval for inquiries for reusing content from ACS Open Access articles and we cannot provide any license nor sign any permission document.
Please do not hesitate to contact us if you need any further assistance.
Sincerely,
Vojin Vucic
ACS Publications Support
Customer Services & Information
Website: https://acs.service-now.com/acs
Email: support@services.acs.org
Phone: 800-227-9919 | 202-872-(HELP) 4357